Microstructure Evolution in Dilute and Concentrated Multi-Component Alloys under Irradiation

by

Anshul Kamboj

A dissertation submitted in partial fulfillment
of the requirements for the degree of
Doctor of Philosophy
(Materials Science and Engineering)
in the University of Michigan
2023

Doctoral Committee:

Professor Emmanuelle Marquis, Chair
Assistant Professor Yue Fan
Professor Amit Misra
Associate Professor Liang Qi

Anshul Kamboj

kamboj@umich.edu

ORCID iD: 0009-0001-2576-5478

Dedication

Honoring the memory of my late grandfather, Shri Raj Pal,

who instilled in me the value of humility.

Acknowledgements

During my five-year Ph.D. program, I have been blessed to receive unparalleled support and guidance from numerous individuals, but before acknowledging their significant contributions, I want to express my heartfelt gratitude to my family. My immensely supportive parents, Sh. Rakesh Kumar and Smt. Sneh Lata, and my loving brother Mayank have been my pillars of strength throughout my research journey, especially during challenging times. The unconditional love and support from my grandparents and great-grandparents, namely Smt. Kamla Devi, late Sh. Rajpal Kamboj, and Smt. Karti Devi, kept me rooted during exciting moments. My uncle Sh. Naresh Kumar and aunt Smt. Sunita Devi have always motivated me to overcome any setbacks in life. My cousins, Manvi and Ashit, have always kept me engaged in fun conversations. I am profoundly grateful for their unwavering support, which has enabled me to navigate through the challenges and reach new heights in my academic journey.

I am immensely grateful to my advisor, Prof. Emmanuelle Marquis, for being an outstanding mentor who has supported me throughout my academic journey. Under her mentorship, uncovering new knowledge has been a truly enriching experience. Our discussions have challenged me to delve deeper into my research findings and address pertinent questions. I cannot thank her enough for the enormous amount of time and effort she invested in my work. Her constructive feedback and mentorship have played a pivotal role in shaping me into the researcher that I am today, and her dedication and work ethic will continue to motivate and inspire me for years to come. One of the most significant takeaways from my time with Prof. Marquis is the

realization that our mental constructs can serve as our limitations. This lesson has not only transformed the way I approach research but has also impacted all aspects of my life.

I would also like to extend my sincere appreciation to my dissertation committee members, Professors Amit Misra, Liang Qi, and Yue Fan, for their valuable guidance, insightful suggestions, and unwavering support throughout my thesis journey. Their expertise and feedback have been instrumental in shaping my research and ensuring its rigor and quality. Additionally, I am grateful for the technical support and camaraderie provided by my lab mates, both past, and present, in the Marquis Research Group at the University of Michigan. Their support and friendship have made this journey not only productive but also enjoyable. I especially want to thank Thomas Valenza and Nina Perry, who provided invaluable support in data collection and offered insightful discussions throughout my research. I would also like to express my heartfelt gratitude to all the staff at the Michigan Center for Materials Characterization and the Michigan Ion Beam Laboratory for their technical advice and assistance throughout my graduate studies. Their support and expertise have been invaluable in helping me conduct my research and analyze my results. In particular, I would like to thank Dr. Allen Hunter, Dr. Tao Ma, Dr. Bobby Kerns, Dr. Ovidiu Toader, and Dr. Zhijie Jiao for their important contributions and thoughtful conversations during my experimental work and data collection. Their guidance and support have played a critical role in the success of my research, and I am truly grateful for their help.

I am sincerely grateful for our collaboration with Professor Robert Odette and Dr. Nathan Almirall at the University of California, Santa Barbara. I am also grateful to Dr. Mukesh Bachhav at the Idaho National Laboratory for giving me an internship opportunity during my PhD. I would like to acknowledge funding and support for this thesis work from U.S. Department of Energy's Integrated Research Project award [grant number DE-NE0000639], DOE's Basic Energy

Science program [grant number DE-SC0022980], Rapid Turnaround Experiment (RTE) award by the DOE Nuclear Science User Facilities (NSUF) Program, and travel support for conferences provided through the Rackham Graduate School at the University of Michigan.

I cannot express enough gratitude for the unwavering support and camaraderie of my friends during my graduate school experience. Shivani, Ayush, Mohit, Vishwas, Pratyush, Thomas, Arshdeep, Kaushal, and countless others have been a constant source of motivation, laughter, and inspiration. They have stood by me during difficult times, celebrated with me during milestones, and helped me create unforgettable memories that I will cherish forever. Their friendship has enriched my life in immeasurable ways, and I am forever grateful for their unwavering presence in my life. Additionally, I am deeply grateful to my badminton partners Abhinav, Meet, Swapnil, Prateek, Puneet, Shiv, and Burt. Beyond providing a therapeutic outlet, they have taught me valuable lessons on managing pressure, the importance of resilience, and instilled in me a "never give up" attitude that has been invaluable both in my academic and personal life.

Finally, I am deeply grateful for the impact that Dr. Satinder Sartaaj's music has had on my life. As a Punjabi poet and singer, he has a unique talent for crafting powerful and emotional lyrics that resonated deeply with me. His music has been a constant source of comfort and inspiration for me during difficult times, helping me to process my emotions and find solace in his words. Through his colorful and evocative writings, he has instilled a range of emotions in me, from joy and hope to sadness and contemplation. His music has helped me to gain a deeper understanding of the world around me and has enriched my life in countless ways.

Table of Contents

List of Tables

List of Figures

List of Appendices

Abstract

The development of sustainable energy sources that minimize greenhouse gas emissions such as nuclear energy lessens the world's dependence on fossil fuels while addressing climate change and longer-term sustainability. The designs of the next generation of nuclear reactors focus on high efficiency and versatility, which will require structural materials to be able to sustain much harsher environments than in current nuclear reactors. Consequently, there is an urgent need to understand the shortcomings of current materials and improve their properties as well as design more performant materials. In this two-part thesis, I am addressing the roles of alloying elements and dose rate on the irradiation response of dilute steels used in light water reactor pressure vessels (RPV) and of multi principal element alloys (MPEAs) that have shown promise as radiation resistant materials.

The first part of the thesis presents a systematic experimental approach to investigate the effects of P and Ni alloying elements, and dose rate on the irradiation response of dilute RPV steels. The study revealed that P, similar to Cu, causes early nucleation of Mn-Ni-Si precipitates in neutron-irradiated RPV model steels, leading to hardening and embrittlement at early fluence. In addition, to accelerate the understanding of precipitation mechanisms in RPV surveillance steels, high dose rate ion irradiation is increasingly used, which enables the end-of-life dose (0.2 dpa) to be reached in a matter of hours to several days, compared to years required in lower dose rate test reactors. By comparing the microstructure of several RPV surveillance steels under high dose rate ion irradiation and lower dose rate neutron irradiation at similar dose levels, the study

found lower precipitate number density and larger size in the case of neutrons, while the precipitate volume fraction and composition remained remarkably similar.

The second part of the thesis presents the effect of composition and dose rate on the microstructure evolution of Ni-based MPEAs under irradiation and thermal aging. While prior literature claimed that $Cr_{0.6}FeNiMn$ and equiatomic CrFeNiCoPd possess excellent phase stability under irradiation, it is shown here that microstructure stability is controlled by dose rate, whereby phase decomposition takes place at low dose rate irradiation but is suppressed by cascade mixing at high dose rates. Furthermore, to clarify the mechanisms of phase decomposition under irradiation, phase stability under thermal conditions during aging at 500 ^{o}C was also elucidated and quantified. Furthermore, prior literature also showed high swelling resistance and suppressed damage evolution in CrFeNi-based MPEAs as compared to the less concentrated alloys under high dose rate environment (>10^{-3} dpa/s). To understand the effect of dose rates on the irradiation behavior of MPEAs, the microstructural responses of a series of Ni-based alloys of increasing compositional complexity were investigated after ion irradiation at the relatively low dose rates of 10^{-4} dpa/s and 10^{-5} dpa/s. The findings suggested that the effect of composition on dislocation loops and cavity swelling significantly decreased with decreasing dose rates.

Chapter 1 Introduction

1.1 Motivation and background

Earth's climate is changing rapidly at a pace never observed in the history of modern civilization [1]. This change has been primarily driven by the industrial production of greenhouse gasses like CO_2 and CH_4 [2]. Reversing the course of climate change quickly requires lowering greenhouse gas emissions by limiting the use of fossil fuels, which are the primary contributors of greenhouse gasses [3]. So-called "green" alternatives to fossil fuel energy include solar, wind, hydro, biomass, and nuclear energy. Among these, nuclear energy offers several advantages that include low costs, continuous energy production, and high efficiency [4]. Currently, nuclear energy only accounts for 20% of the total power generated in the United States [5]. It has the potential to contribute a greater fraction provided structural materials can be designed to sustain the harsher conditions of modern reactors.

Existing nuclear power plants that extract energy from nuclear fission are classified based on the type of coolant used. Common reactor designs include the light water reactor (LWR), graphite-moderated reactor, gas-cooled thermal reactor, pressurized heavy-water reactor, liquid-metal cooled reactor, and molten-salt reactor. All these reactors operate in extreme environments consisting of relatively high temperatures (300 – 600 ^{o}C), high stresses (7-15 MPa), and high irradiation fluence (up to 60 dpa) [6]. However, the next generation of reactors, generation IV, are designed to operate under more extreme conditions. Generation IV reactors include very high

temperature reactors, sodium fast reactors, super-critical water-cooled reactors, gas cooled fast reactors, and lead cooled fast reactors, which are designed to use fuel more efficiently, reduce waste production, be economically competitive, and meet stringent safety standards. Consequently, parts of these modern reactors and materials will experience higher temperatures (510 – 1000 ^{o}C), higher pressures (22 MPa) and higher doses (1-200 dpa) [7]. Yet, structural materials used in current nuclear reactors are limited in their ability to sustain such harsh conditions without significant microstructural and mechanical property degradation. Therefore, there is a need to understand and develop existing materials and design new advanced structural materials that possess high-temperature and irradiation resistance, excellent mechanical properties, and appropriate resistance to corrosion and oxidation.

Current structural materials employed in nuclear applications include low-alloy steels used in reactor pressure vessel (RPV) in light-water reactors, which exhibit good mechanical and chemical properties [8]. The RPV is a massive cylindrical structure containing the reactor coolant, core shroud, and the reactor core. The integrity of RPVs is one of the key factors in determining the lifetime of a nuclear power plant [9]. The chemistry of RPV steels typically consists of (in units of at. %), C (0.2–1.8%), Mn (0.7–1.6%), Mo (0.2–0.3%), Ni (0.2– 1.3%), Si (0.4–1.2%), and Cr (0.05–0.5%). Over time, irradiation induces precipitation in the form of nanoscale precipitates typically containing Mn, Ni, Si, and Cu depending on the steel composition [10]. The high number density and volume fraction of these precipitates result in hardening and embrittlement, with increased brittle-to-ductile transition temperature shifts (ΔT) [11], which is a concern as it may limit the service life of RPV, eventually affecting the life extension of light-water reactors (LWR) [12,13]. Life extension of LWRs require that RPVs operate within the safety margins set by predicting the change in fracture toughness under long-term irradiation. Several models such as

engineering trend curves (ETC) [14], mechanistically based correlations (MBC) [15], multiscale models (MSM), Avrami based models [16,17], the Eason-Odette-Nanstad-Yamamoto (EONY) model and Odette-Wells-Almirall-Yamamoto (OWAY) model [18] have been developed to predict ΔT [11]. These models are generally accurate for predicting low flux ΔT up to intermediate fluence ($< \sim 5 \times 10^{19}$ n/cm^2); but some significantly underpredict ΔT at higher fluence, pertinent to extended life conditions (up to $\sim 10^{20}$ n/cm^2) [11]. To increase the accuracy of embrittlement prediction models at higher fluence, further understanding of microstructural evolution as alloy composition (Cu, Mn, Ni, Si, and P) at high fluence, low/high flux conditions is needed.

Parallel to continuing studies on existing alloys used in current reactors, there is also a push to develop new materials with enhanced irradiation resistance in addition to mechanical and chemical properties. These materials include ferritic-martensitic steels [19–21], compositionally tailored austenitic steels [22], ODS ferritic steel [23–25], SiC/SiC composites [26,27], nano-engineered austenitic stainless steels [28], Vanadium alloys [29,30], and multi-principal element alloys (MPEAs) [31]. All these materials are designed to achieve a specific microstructure with improved irradiation resistance. For instance, ODS steels are designed to maximize sink density, which helps in eliminating interstitials and vacancies produced during irradiation [32]. Among all these alloys, MPEAs are of particular interest due to the promise of high recombination and presumed sluggish diffusion via composition complexity [33,34]. Recent work showed that several MPEAs exhibit significant delay in cavity-swelling resistance, low hardening, and phase stability under ion, neutrons, and electron irradiation [35,36]. However, more research is needed to validate the mechanisms causing high irradiation resistance and phase stability.

Given the existing challenges in the understanding of precipitation in RPV steels, and irradiation response and phase stability in MPEAs, this thesis discusses the development of

radiation damage and phase decomposition in these two classes of materials. Specifically, the questions addressed in this thesis are the following:

1) What is the effect of dose rate, and Cu and Ni concentrations on the microstructure of RPV steels under intermediate dose rate ion and low dose rate neutron irradiation?
2) What is the effect of phosphorous (P) on the precipitation mechanism in RPV steels under low dose rate neutron irradiation?
3) Are CrFeNi-based MPEAs microstructurally stable under irradiation?
4) What is the dependence (if any) on the nature of elements in MPEAs and their irradiation behavior under high and intermediate dose rate ion irradiation?
5) What are the mechanisms of phase decomposition of the studied MPEAs under thermal aging?

1.2 Thesis structure

This dissertation thesis is divided into eight main chapters. Following the introduction, Chapter 2 provides a review of the literature on factors influencing the irradiation behavior of RPV steels and MPEAs, and discussions of gaps in the current knowledge of mechanisms of irradiation damage in these materials. Chapter 3 focuses on the effect of P on the precipitation mechanism in RPV steels. Chapter 4 focuses on the role of dose rate, and Cu and Ni on the precipitation mechanism in RPV steels under intermediate dose rate ion and low dose rate neutron irradiation. Chapter 5 and Chapter 6 investigate the mechanisms of phase decomposition in CrFeNi-based MPEAs under ion irradiation and thermal aging. Chapter 7 investigates the effect of composition and dose rate on evolution of dislocation, and cavity swelling in Ni-based MPEAs. Finally, Chapter

8 summarizes the conclusions for this work and gives suggestions for future investigations. Appendices contain additional details on sample preparation, experimental data collection, and supplemental data for the main chapters.

Chapter 2 Literature Review

In this chapter, we examine the impact of thermal aging and irradiation on the microstructure of RPV steels and nickel based MPEAs. We begin by reviewing the current literature on the evolution of solute clusters and precipitates in RPV steels during prolonged thermal aging, discussing the various parameters that influence them. Next, we investigate the microstructural response of RPV steels to irradiation, exploring how different irradiation and material parameters affect the evolution of these phases. Next, we review the current literature on thermal and irradiation studies of CrFeNi-based MPEAs.

2.1 Response of RPV Steels under thermal aging

Thermal aging is a process by which materials are exposed to high temperatures for a prolonged period, leading to changes in their microstructure, morphology, and composition. For RPV steels, studying thermal aging is crucial as it provides insights into the expected equilibrium phases. In nuclear applications, RPV steels are subjected to both irradiation and thermal aging, as they typically operate at a temperature range of 300-400 °C for at least 40 years [37]. The impact of thermal aging is an engineering concern for RPV steels, as it can cause embrittlement and degrade their mechanical properties [38]. This embrittlement is primarily caused by the formation of precipitates in the matrix and grain boundaries, resulting from solute segregation [39]. Therefore, understanding the microstructural response of RPV steels to thermal aging is essential for maintaining the safety and reliability of nuclear power plants.

The typical chemistry of RPV steels includes (in units of at. %), C (0.2–1.8%), Mn (0.7–1.6%), Mo (0.2–0.3%), Ni (0.2– 1.3%), Si (0.4–1.2%), and Cr (0.05–0.5%) [11]. Going forward, RPV steels will be categorized based on their Cu and Ni content, with the following designations: Cu-free/low Cu (<0.1 at. % Cu), medium Cu (0.1-0.3 at. % Cu), high Cu (>0.3 at. % Cu), low Ni (<0.3 at. % Ni), medium Ni (0.3-0.7 at. % Ni), and high Ni (>0.7 at. % Ni). This section will outline the mechanism of precipitate formation in RPV steels under thermal aging and discuss the parameters that control the resulting microstructure.

2.1.1 Precipitation mechanism under thermal aging

During thermal ageing, the microstructure of RPV steels consist of precipitates enriched with Cu, Mn, Ni, Si, and P atoms, with Cu-enriched cores and Mn, Ni, Si, and occasionally P segregated at the Cu-Fe interfaces. These precipitates are termed Cu-MNS and form inside grains (matrix), on grain boundaries, and on dislocations (Figure 2.1**)**. At operational temperatures of light water reactors ~ 290 ^{o}C, Cu is supersaturated beyond 0.02 wt.% according to Fe-Cu phase diagram [40–42]. However, the presence of alloying elements in RPV steels can extend the solubility of Cu to 0.06 wt.% [41,43,44]. Therefore, in RPV steels with >0.06 wt.% Cu, the supersaturated Cu is the likely driving force behind the nucleation of Cu-rich precipitates (CRPs). Once the CRPs are nucleated, they likely provide heterogeneous nucleation sites for the segregation of Ni, Mn and Si; a mechanism confirmed by several studies on multiple alloys including Fe-Cu-Ni, Fe-Cu, Fe-Cu-Ni-Mn, and RPV steels in the temperature range of 330-360 ^{o}C and for time periods from 100 to 100,000 hrs. using a variety of characterization techniques that included small angle neutron scattering (SANS), transmission electron microscopy (TEM), energy dispersive X-ray spectroscopy (EDS), and atom probe tomography (APT) [41,42,45–54]. The

precipitate morphology appears to be core-shell, with a Cu-rich core surrounded by a shell of Mn, Ni, and Si atoms as illustrated in Figure 2.2. Furthermore, several modelling studies using Gibbs isotherms suggested that the segregation of Ni, Mn, and Si on the CRP interface reduced the interfacial energy by 10-145 mJ/m^2 in RPV steels in a temperature range of 330-360 ^{o}C [39,50,52,55–57].

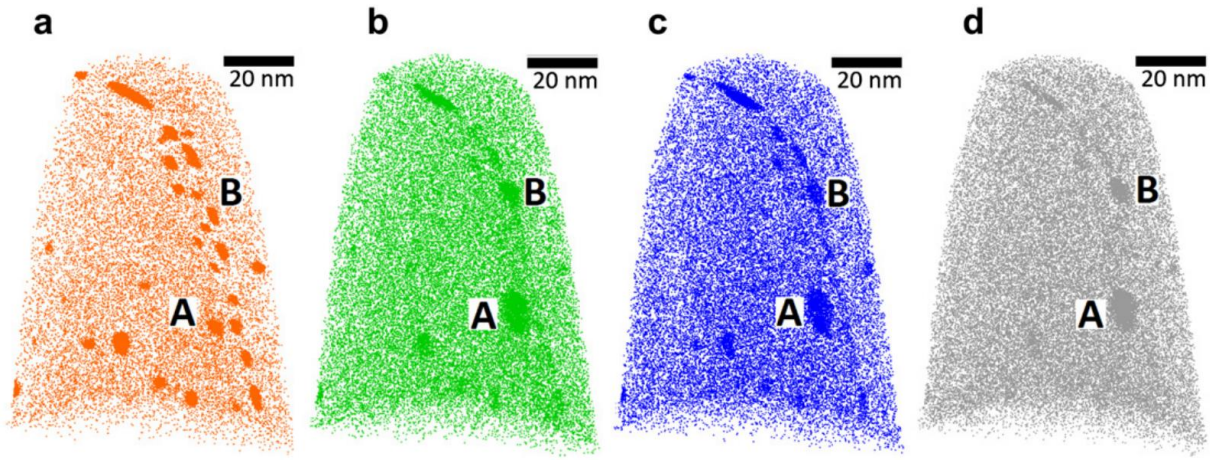

Figure 2.1**:** Distributions of Cu, Ni, Mn and Si in precipitates in the matrix and at a grain boundary aged for 50,000 h at 365 ^{o}C. a) Cu atoms, b) Ni atoms, c) Mn atoms, d) Si atoms. The Cu-MNS precipitate in the matrix and MNS precipitate on grain boundary is labeled as A and B, respectively [39].

Although the core of the precipitates consists mainly of copper (80 ± 5 %) with smaller amounts of manganese, nickel, and silicon (20 ± 5 at. %), the interface has been found to be rich in nickel, manganese, and silicon with a composition closer to the G phase and Γ2 phase field in the Mn-Ni-Si ternary phase diagram [39,52,55,58]. The G phase is a complex intermetallic phase with a stoichiometric composition of ($Mn_6Ni_{16}Si_7$) [59]. The Γ2 phase field is represented by the composition of ($Mn(Ni_xSi_{1-x})_2$) [60]. Γ2 phase has a constant 33.3 at. % Mn composition and a range of Si from 12.7 to 20.7 at. % and a corresponding Ni range of 46.0–54.0 at. %. At the beginning of precipitation, KLMC simulation results showed that MNS phase forms as an ordered

B2 structure (Ni and Mn occupy the two sublattices and Si randomly replacing some Mn atoms) [44,60]. The coherent ordered structure B2 transforms to the intermetallic G/Γ2 phase when the precipitates grow to large size [61–63]. However, these predictions are yet to be confirmed experimentally. In high-Ni samples, the interface composition is generally closer to the G phase, while in low and medium-Ni samples, it is closer to the Γ2 phase field [39,52,55]. However, in some exceptional cases, the trends were found to be reversed. These findings suggest that the G phase and Γ2 phase field are thermodynamically stable phases in RPV steels at a service temperature of around 300 °C.

In addition to Cu-MNS precipitates, Mn-Ni-Si (or MNS) precipitates were also observed during thermal ageing [39] (Figure 2.1). MNS precipitates were observed at grain boundaries, through heterogeneous nucleation and promoted by these fast diffusion paths [39]. The compositions of Cu-MNS and MNS precipitates measured by APT varied across studies likely due to differences in alloy composition, aging time, and temperatures. However, at relevant RPV operational temperatures (330-365 ^{o}C), the precipitates consisted of 28-40 at. % Cu, 4-19 at. % Ni, 5-16 at. % Mn, <5 at. % Si, and the rest as Fe. Notably, most of the Fe atoms detected in the precipitates are likely the result of APT evaporation artifacts [64].

In addition to precipitation, multiple studies also reported the segregation of C, Mo, Mn, Cr, Ni and P at grain boundaries, possibly due to co-segregation effect [65–67], and it was hypothesized that C segregation improves the cohesion of the grain boundaries. In addition, C exhibits strong affinity for Mo, Mn, and Cr and therefore drives them to the grain boundaries. Furthermore, Mo possesses a strong affinity for P and drives it to the grain boundary. However, Si has repulsive interaction with C and weak attraction towards Ni and Mn, which could explain the small segregation level of Si observed at grain boundaries [65–67].

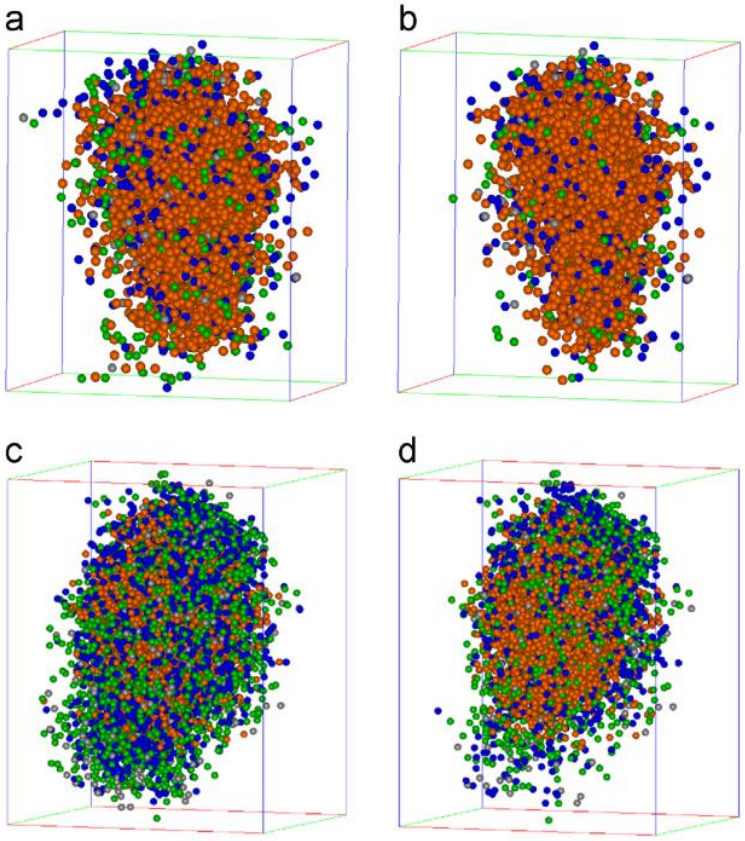

Figure 2.2**:** Atom maps showing a cluster from the high-Cu low-Ni (a), (b) and high-Cu high-Ni (c), (d) RPV steels after ageing at 365 ℃ for 90,000 hrs. and 100,000 hrs., respectively. Dimensions of the box are 8x8x8 nm^3 (a) and (b), and 10x10x10 nm^3 (c) and (d). Cu atoms – orange, Ni – green, Mn – blue, Si – grey [52].

2.1.2 Effect of steel composition on precipitation under thermal aging

The evolution of matrix precipitates appears to be controlled by the composition of RPV steel, and time and temperature of aging. During thermal ageing, precipitation is strongly dependent on the concentration of individual solute atoms. Most studies focused on the effect of Cu and Ni, but there is limited information about the effects of Si and Mn. With increasing Cu content, an increase in the number density of precipitates has been observed, which was attributed to the increased supersaturation proving higher driving force for precipitation [47,48,55]. With increasing Ni content, the number density of matrix CRPs also increased [47,49,55], which was

hypothesized to the higher Ni content allowing a greater amount of Ni to segregate on the CRPs and stabilizing them by reducing the interfacial energy. This hypothesis was also consistent with first principal simulations [50] and MC simulations [51] in Fe-Cu-Ni alloy.

2.1.3 Effect of time and temperature on microstructure under thermal aging

Aging time and temperature also influence the evolution of precipitates. At a given temperature, with increase in time, studies on various high-Cu, low and high-Ni RPV steels at 330-360 ^{o}C for 50,000-100,000 hrs. showed an increase in precipitate number density and size followed by a decrease in number density and increase in size [41,55]. This behavior is consistent with classical theory of nucleation and growth, and coarsening of precipitates in metals [68]. Furthermore, with increase in time, these studies also showed a saturation in size of Cu-core and an increase in the width of the interface corresponding to a higher amount of Ni, Mn, and Si in the interface thereby widening it [39,55,65]. Notably, a small amount of Cu is found to be associated with the interface after all aging conditions, likely due to the Cu diffusing from matrix through the interface to Cu rich core. With an increase in aging temperature, the driving force for precipitation decreases but the kinetics of precipitate formation become faster. As a result, the coarsening regime is observed at an early time period and more precipitates were observed at the dislocations as compared to the matrix [41,55].

2.2 Evolution of RPV steels under irradiation

In light water reactors, RPV steels operate under extreme environment consisting of pressures up to 14 MPa at 290 ^{o}C, and a constant flux of neutrons leading to fluence of 10^{20} n cm^{-2} over a lifespan of 60 years [7]. As a result, RPV steels are susceptible to embrittlement, which can limit the life extensions of these reactors [12,13]. The embrittlement is primarily caused by solute-defect cluster complexes and nm-scale precipitates that evolves during the quenching stage of cascade evolution [10,11,18]. The mechanism of irradiation hardening, and embrittlement is briefly summarized here.

Neutron irradiation create primary knock on atoms that produce displacement cascades and result in excess interstitials and vacancies, which leads to defect-solute clustering and radiation-enhanced diffusion (RED) [69]. RED is responsible for accelerating the precipitation rates that are normally limited by slow kinetics at the RPV operational temperatures (300 ^{o}C). The high number density and volume fraction of solute-defect clusters and precipitates can increase the yield strength by pinning dislocations [70]. The increase in yield strength leads to a corresponding embrittlement, which is manifested as ductile to brittle transition temperature shifts [11]. This section will outline the mechanism of precipitate formation in RPV steels under irradiation and discuss the parameters that control the resulting microstructure.

2.2.1 Precipitation mechanism under neutron irradiation

Under irradiation, solute elements (Cu, Mn, Ni, Si, and P) in RPV steels precipitate, and segregate to dislocation loops [71,72]. Irradiation-enhanced precipitation is observed in the form of Cu-Mn-Ni-Si (Cu-MNS) and Mn-Ni-Si (MNS) precipitates in the matrix, at dislocations, and on grain boundaries as illustrated in Figure 2.3. Prior studies have reported pure MNS precipitates

without any Cu in steels with Cu < 0.06 at. %, whereas, both Cu-MNS and MNS precipitates were found in steels with Cu > 0.06 at. % [44,73]. Depending upon the irradiation conditions, Cu-MNS precipitates evolve into either a core shell morphology or an appendage morphology. The core shell morphology consists of Cu atoms forming the core and Mn, Ni and Si atoms distributed in a shell around the Cu-rich core. In the appendage morphology, Mn, Ni, and Si are preferentially clustered next to a Cu-rich region. The core-shell and appendage morphologies are illustrated in Figure 2.4. Unlike the Cu-MNS precipitates, the MNS precipitates always evolve into a spherical morphology.

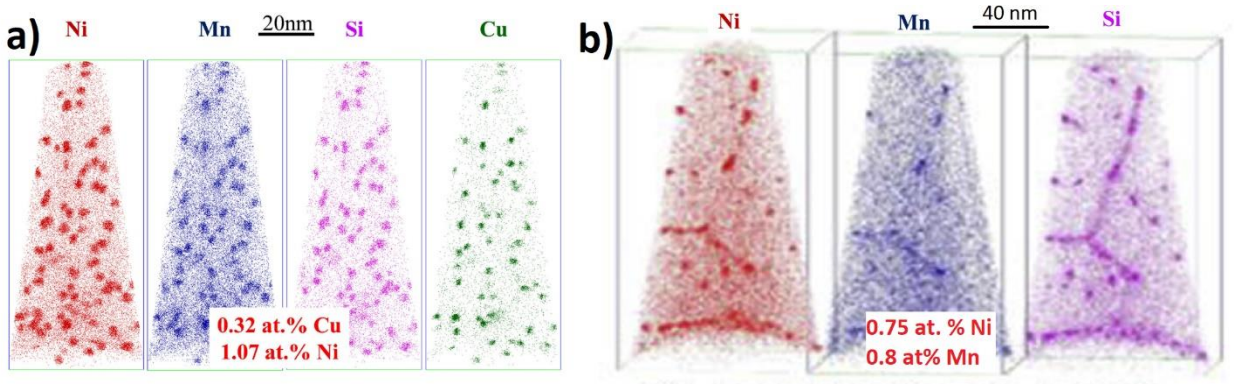

Figure 2.3: Solute maps for neutron irradiated alloys a) high-Cu high-Ni, and b) Cu-free medium-Ni RPV steels after 0.2 dpa [44,74].

The MNS precipitates in Cu-free steel and MNS shell/appendage in Cu-containing steels form ordered phases, which often closely resembles with G (also known as T3) and Γ2 (also known as T6) phases and are consistent with thermal aging studies. However, depending upon the steel composition, the ordered MNS precipitates could also belong to other phases such as T7, T8, T9, and T10 as predicted by CALPHAD in the Fe-Mn-Ni-Si system at relevant RPV operational temperatures (300 ^{o}C) as shown in Figure 2.5 [60]. In addition to precipitation, segregation of solute elements is observed in the form of uniform segregation of Cu, Mn, Ni, Si, and P on

dislocations and grain boundaries [10,60,75–77]. The extent and nature of precipitation and segregation depend on the steel composition, i.e., concentration of Cu, Mn, Ni, Si, and P, and on the irradiation parameters, namely type of irradiating particle, flux, fluence, and temperature.

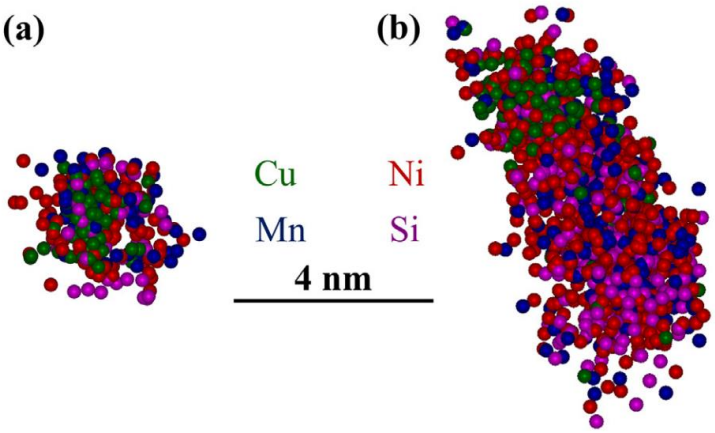

Figure 2.4: APT maps of typical precipitates in the high-Cu, high-Ni RPV steels showing a) core-shell morphology after 0.4 dpa, and b) appendage morphology after 3.1 dpa under neutron irradiation [44].

2.2.2 Effect of composition on microstructure under neutron irradiation

In steels with Cu < 0.06 at. %, Ni is primarily responsible for driving precipitation in the absence of Cu, while Mn and Si play lesser roles [44,72]. The formation of MNS precipitates is hypothesized to evolve from solute–defect cluster complexes present in the matrix and formed during displacement cascades [10,78–81]. MNS precipitates nucleate via homogeneous and heterogeneous nucleation mechanisms depending upon the Ni content in the steel. According to cluster dynamic (CD) simulations [73], a large free energy difference drives precipitation via homogeneous nucleation mechanism in steels with Ni > 1.5 at. %, while a heterogeneous nucleation mechanism is critical for the nucleation of MNS precipitates in low Cu steels with Ni < 1.5 at. %. These simulation results were backed by experimental studies showing MNS

precipitates nucleating heterogeneously on network dislocations and irradiation induced dislocation loops in low and medium-Ni steels as compared to homogeneous nucleation of precipitates in the matrix in high-Ni steels [74]. Furthermore, the number densities and volume fraction of MNS precipitates in neutron-irradiated both medium and high-Ni steels increased with increasing Ni concentration [44,74]. Once precipitates have nucleated, their growth takes place by radiation-enhanced diffusion (RED). At a given dose, the size and volume fraction of MNS precipitates increase with increasing concentration of solute elements [44]. Typically, the observed MNS precipitate composition is closer to Γ_2 phase in Cu-free steels [44,60].

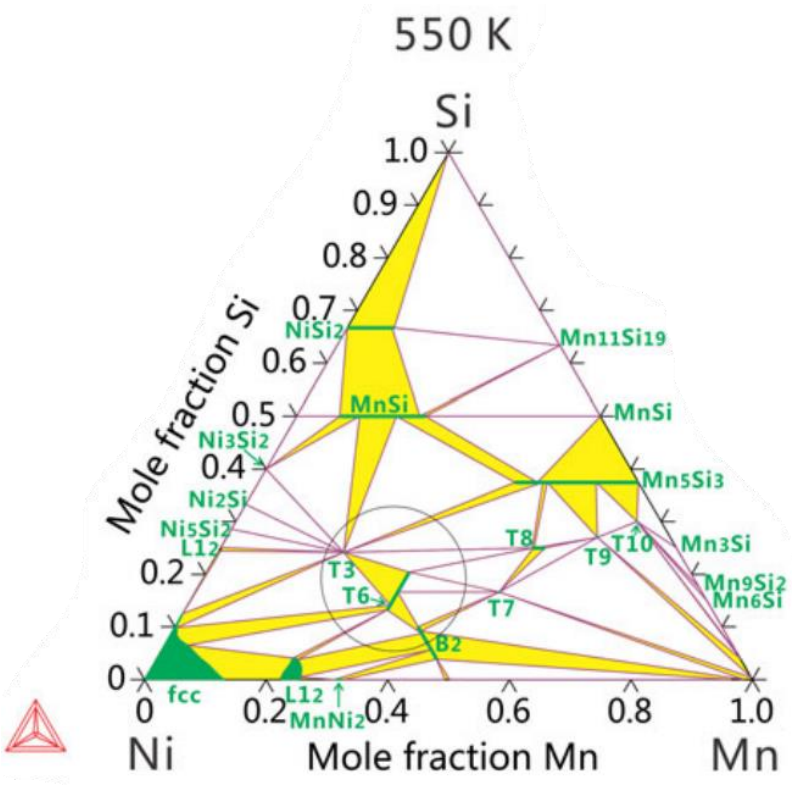

Figure 2.5: Isothermal section of the MNS system at 550 K showing various expected phases in RPV steels [73].

In steels with Cu > 0.06 at. %, Cu and Ni concentrations appear to have the strongest effect on precipitation. The number density and size of precipitates was found to be significantly higher in high-Cu steels (10^{23} - 10^{24} m^{-3}) as compared to low-Cu steels (10^{22} - 10^{23} m^{-3}) as the driving force for precipitation increases with Cu concentration [44,82,83]. At levels more than 0.06 at. %, the supersaturation drives the nucleation of Cu rich precipitates [16]. In the early stages of precipitate formation (low dose), precipitates have a Cu rich core with a thin shell of MNS atoms, known as core-shell morphology [84]. The core-shell morphology arises because the interfacial energy of the Fe-Cu interface ($\gamma_{Fe\text{-}Cu}$) is significantly higher than the combined energies of the Fe-MNS ($\gamma_{Fe\text{-}MnNiSi}$) and Cu-MNS ($\gamma_{Cu\text{-}MnNiSi}$) interfaces [73,85,86]. The segregation of Mn, Ni, and Si atoms at the interface lowers the interfacial energy for all major crystallographic orientations promoting a total wetting and formation of thin, disordered, and dense shell of MNS at the Cu-Fe interface [87]. At high dose levels (>0.2 dpa), the MNS shell become ordered and resembles the G phase or Γ2 phase field. In the precipitates, the Cu rich core consists of ~83 ±5 at. % Cu [88], which grows until Cu is fully depleted from the matrix (< 0.03 at. %) at very high dose (>1 dpa) [44]. The depletion of other solute atoms (Ni, Mn, and Si) is slower due to their lower diffusivities. The thermal diffusion coefficients of Cu, Ni, Mn, and Si are summarized in Table 2.1. Once a significant amount of Cu is depleted from the matrix (>1 dpa), Ni drives the precipitation and cause the existing Cu-MNS precipitates to grow by incorporating more Ni, Mn, and Si at the interface. In addition, starting from high dose levels (0.2 dpa), the excess Ni also causes nucleation of MNS precipitates in the matrix, which are smaller in size by roughly 0.3 nm as compared to Cu-MNS, suggesting late nucleation of MNS due to lower driving force for their nucleation. These MNS precipitates continue to grow alongside MNS shell on CRPs until the matrix is fully depleted of the solutes at very high dose levels (3-4 dpa).

Apart from Cu and Ni, Mn, Si, and P can also influence the precipitation in RPV steels. The Mn and Si concentration doesn't affect the number density of MNS precipitates, however with increasing Mn and Si content, a slight increase in the precipitate size and volume fraction has been reported [44,74]. While P is a minor constituent, the presence of P was found to correlate with an increase in the number density of CRPs and a decrease in the average CRP radius [89]. The mechanism for this effect of P is yet to be established.

Table 2.1: Thermal diffusion coefficient of Cu, P, Mn, Ni, and Si in pure Fe at 300 ^{o}C [90].

Element	**Diffusion coefficient (m^2/s)**
Cu	2.78×10^{-24}
P	6.78×10^{-25}
Mn	6.38×10^{-26}
Ni	5.93×10^{-27}
Si	5.65×10^{-26}

2.2.3 Effect of dose on microstructure under neutron irradiation

At RPV operational dose rates ($\ll 10^{-7}$ dpa/s), the precipitate morphology evolves from core-shell to appendage morphologies with increasing dose in medium and high Cu steels [84]. At high dose, Ni is the only influencer as Cu approaches full depletion [44]. With increasing dose (>0.2 dpa), the precipitate number density decreases and size and volume fraction increases [44,74,82], which signifies a coarsening regime created at RPV operational conditions. In terms of morphology, the shell of Mn, Ni, and Si atoms does not thicken uniformly. Instead ordered nuclei, or appendage, form on <001> facets due to its lowest interfacial energy [87] and grow on one side of the Cu rich core [84]. The MNS appendages result from a decrease in MNS ordering energy, which is the energy required to form an ordered phase [84]. Further growth of the ordered MNS phase occurs by supply of Mn, Ni, and Si through the available diffusion paths. These

diffusion paths include the Mn, Ni, and Si rich interface, bulk diffusion through matrix, and the Cu-rich core. It was hypothesized that the Cu-rich core may be an efficient diffusion path due to the lower vacancy formation energy in the bcc Cu phase compared to the Fe matrix allowing a higher vacancy concentration [91]. The evolution of core shell morphology into appendage morphology is illustrated in Figure 2.6. Despite the Mn, Ni, and Si contribution to the appendage via interfacial diffusion, the interface remains rich in these atoms as there is a large free energy penalty if all the Mn, Ni, Si atoms from the shell join the MNS ordered appendage and completely exposing the Cu/Fe interface. Therefore, with increasing in dose, the core shell morphology transform into appendage morphology [44,82].

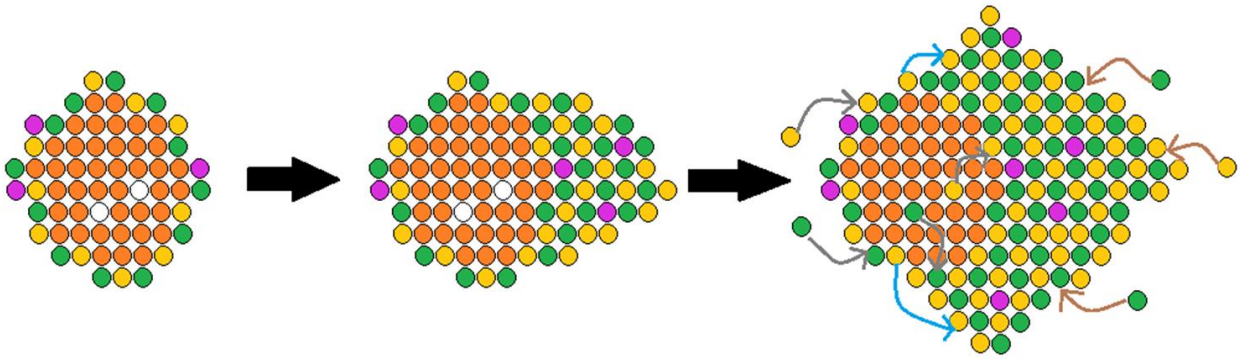

Figure 2.6: Schematic showing the evolution of precipitate morphology with increasing dose. a) core shell morphology with Cu rich core (green) surrounded by disordered Mn (yellow), Ni (green), Si (yellow), and Fe (pink) atoms, b) formation of ordered MNS nucleus, c) growth of MNS nucleus via three diffusion paths i.e., via matrix (brown arrows), interface (blue arrows), and Cu-rich core (grey arrows).

2.2.4 Effect of dose rate on microstructure under irradiation

Studying the microstructural evolution in RPV steels under actual operating environment is time and cost intensive due to the low neutron dose rates. In nuclear reactors, the surveillance samples of sensitive steels located on the inner wall of the RPV are periodically tested to monitor embrittlement. However, the low neutron dose rate (~10^{-10} dpa/s) in commercial reactors make the process time intensive. Consequently, test reactors use accelerated neutron fluxes (~10^{-7} dpa/s) [44,92] to develop correlations that can predict end-of-life dose of RPV steels. Despite the higher dose rates of test reactors compared to commercial reactors, it can take years to reach end of life dose levels. Alternatively, ion irradiation, which can produce very high dose rates (10^{-3} - 10^{-6} dpa/s) can reach the end-of-life dose typically in days and has been used to study precipitation in RPV steels [93,94].

Dose rates can significantly influence precipitate evolution. When using neutrons or ions, cascade mixing promotes athermal dissolution of precipitates [95–98] whereas RED tends to accelerate precipitation by enhancing diffusion via an excess concentration of mobile point defects [92,99]. Competition between these two processes results in one of three different microstructural evolution regimes, i.e. solid solution, nanoscale patterning, and coarsening [100]. The solid solution regime prevails at high dose rates, where cascade mixing dominates, and no precipitation is observed. The patterning regime is observed at intermediate dose rates, where cascade mixing and RED are comparable, and a steady precipitate number density and size is observed. A pattering regime has been observed under ion irradiation in Fe-Cu, Fe-Cu-Mn alloys (at 290 ^{o}C at 10^{-5} dpa/s) [43]. A coarsening regime has been observed under neutron irradiation (at 290 ^{o}C at 10^{-6} - 10^{-10} dpa/s) in RPV steels [44,74,82], Fe-Cu, and Fe-Cu-Mn alloys [43,101].

2.2.5 Characterization techniques utilized to study precipitation in RPV Steels

Various material characterization techniques have been employed to examine the microstructure of RPV steels following irradiation and thermal aging, including small angle neutron scattering (SANS), transmission electron microscopy (TEM), positron annihilation spectroscopy (PAS), and atom probe tomography (APT). APT, in particular, provides unique capabilities for 3-D data visualization and chemical composition measurement, with 0.1-0.3 nm in-depth resolution and 0.3-0.5 nm lateral resolution [102,103]. However, APT has its limitations. In RPV steels, APT data often contain artifacts such as variations in the reconstructed atomic density and solute concentration dependence on crystallographic orientation. During APT data collection, several mechanisms such as long-range surface diffusion under laser mode [104], non-uniform evaporation due to differences in evaporation fields between the matrix and precipitates [102,105], detection bias against multiple events [106], trajectory overlaps close to the matrix-precipitate interface [107], and localized hopping of atoms prior to evaporation [108], can significantly impact the spatial and chemical accuracy of APT data. These inaccuracies can be reflected in the form of reconstruction artifacts in RPV datasets such as significant presence of Fe in precipitates [64] and inaccurate compositions due to the loss of low solubility elements Cu and P to pre-pulse evaporation [109]. Furthermore, the overlap of Fe and Ni peaks pose additional challenges to spatial and chemical accuracy of APT data [64]. The user-defined mass spectrum ranging can also be a non-negligible source of variability in the detection of clusters [110]. Despite these challenges, APT remains a widely used method for characterizing the microstructure of RPV steels due to its ability to quantify precipitate number density, radius, volume fraction, and composition, which are unmatched by other techniques.

Several cluster analysis algorithms have been utilized to define the precipitate volume in APT data, such as maximum separation method (MSM) [111], Combined HDBSCAN and DeBaCl (CHD) [112], k-means, gaussian mixture model [113], Delaunay tessellation algorithm [114], and Voronoi cells methods [115], etc. have been used. Among these algorithms, MSM is the most commonly used due to its accuracy in defining the cluster boundaries, its ability to handle large datasets, and its commercial availability though IVAS and ApSuite softwares. However, MSM has limitations, as it only works in datasets with high concentration contrast between precipitates and matrix [112] and is sensitive to parameter selection [110] and cluster shape [112].

2.3 Response of MPEAs during thermal aging

Traditional alloys typically consist of one principal element diluted with other elements to achieve desired properties. In contrast, concentrated solid solution alloys (CSAs) consist of more than one principal element. A special category of CSAs is referred to as multi-principal element alloys (MPEAs), which comprise of four or more metallic elements and form single-phase solid solutions. MPEAs have generated significant interest for a wide range of applications due to their promising properties [116]. In the context of nuclear applications, a number of studies suggested that CrFeNi-based MPEAs, specifically equiatomic CrFeNiCo, $Cr_{0.6}$FeNiMn, equiatomic CrFeNiCoMn, and equiatomic CrFeNiCoPd, may exhibit superior irradiation properties, including high swelling resistance [117], delayed energy dissipation [33,118], and suppressed damage accumulation [119] when compared to stainless steels [120–122] and simpler concentrated alloys [33–36]. While homogenization at 1100°C results in solid solution for these MPEAs, it is necessary for them to exhibit phase stability between 400-600°C to be effectively employed at high temperatures or under irradiation conditions.

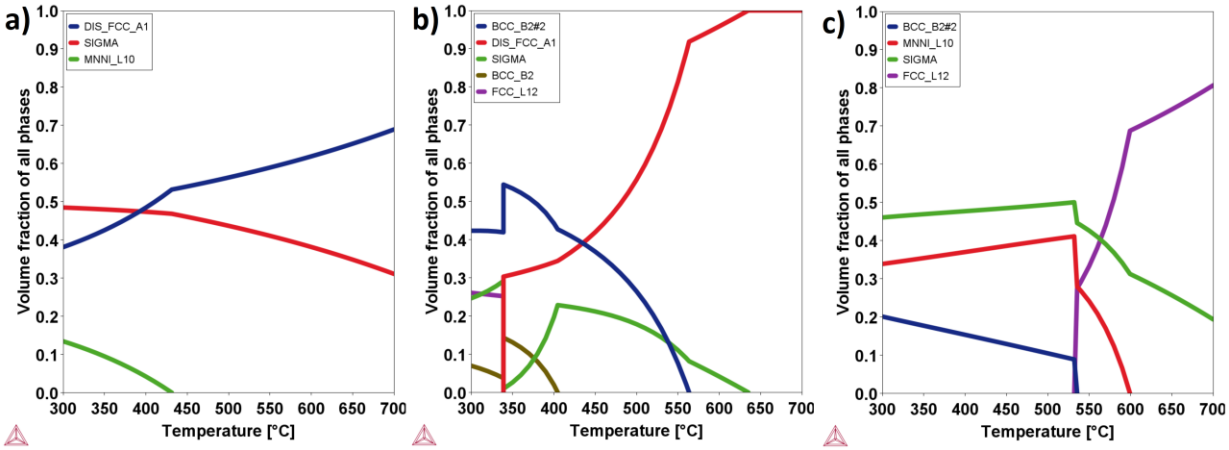

Figure 2.7: Volume fraction of phases in a) $Cr_{0.6}FeNiMn$, b) equiatomic CrFeNiCo, and c) equiatomic CrFeNiCoMn predicted by CALPHAD using TCHEA6 database in Thermocalc.

2.3.1 Simulation studies

Relatively limited data on the phase stability of CrFeNi-based MPEAs is available from thermodynamic simulations and thermal aging experiments. Atomistic simulations predicted the formation of the $L1_0$ Ni-Mn phase in $Cr_{0.6}FeNiMn$ [123], which is present in the most recent CALPHAD modeling that includes a $L1_0$ ordered phase below 450 ^oC, sigma phase below 1000 ^oC, and remaining FCC matrix (Figure 2.7 and Table 2.2). In addition, CALPHAD predicted B2 Fe-Co phase below 560 ^oC, sigma phase below 640 ^oC, and FCC matrix in CrFeNiCo and $L1_0$ ordered phase below 600 ^oC, sigma phase below 820 ^oC, and remaining ordered FCC matrix in equiatomic CrFeNiCoMn. No modelling or simulation data is available for equiatomic CrFeNiCoPd alloy.

Table 2.2 Composition (at. %) of different phases at 450-550 °C in CrFeNi-based MPEAs calculated using CALPHAD.

Phases	**Alloy**	**Cr**	**Fe**	**Ni**	**Co**	**Mn**
$L1_0$ Ni-Mn	$Cr_{0.6}$FeNiMn	9.7	8.1	50.1		32.1
Sigma		38.5	27.8	7.7		25.9
FCC matrix		8.5	28.1	36		27.5
B2 Fe-Co	Equiatomic CrFeNiCo	8.4	41.8	11.9	37.9	
Sigma		55.5	13.6	5.3	25.5	
FCC matrix		20	20	39	20.7	
$L1_0$ Ni-Mn	Equiatomic CrFeNiCoMn	1.8	14	45.2	17.4	21.5
Sigma		36.3	18.6	2.7	20.4	22.1
B2 Fe-Co		3.5	48.5	9.4	37.7	1
$L1_2$ Ni-Mn		8.8	29.4	27	20.6	14.2

2.3.2 Thermal aging experiments

Experimental studies have reported phase decomposition in $Cr_{0.6}$FeNiMn and equiatomic CrFeNiCoMn MPEAs under thermal aging. A Cr-rich bcc phase was observed in the matrix of $Cr_{0.6}$FeNiMn after long term aging at 700 °C [124,125]. In equiatomic CrFeNiCoMn, ordered $L1_0$-NiMn, Cr rich bcc, and ordered B2-FeCo phases were observed in the matrix and at grain boundaries after annealing between 300 and 700 °C [126–132] as shown in Figure 2.8. At 700 °C, only the Cr rich sigma phase was found at grain boundaries and no phase decomposition was noted upon further increasing the temperature to 900 °C [127,129]. No results from thermal aging studies were found for equiatomic CrFeNiCo and equiatomic CrFeNiCoPd. Due to the limited thermal aging data available for CrFeNi-based MPEAs, further long-term aging studies are needed to validate the phases predicted by CALPHAD and determine the mode of phase decomposition in these alloys, including nucleation and growth, spinodal decomposition, discontinuous precipitation, and other potential mechanisms.

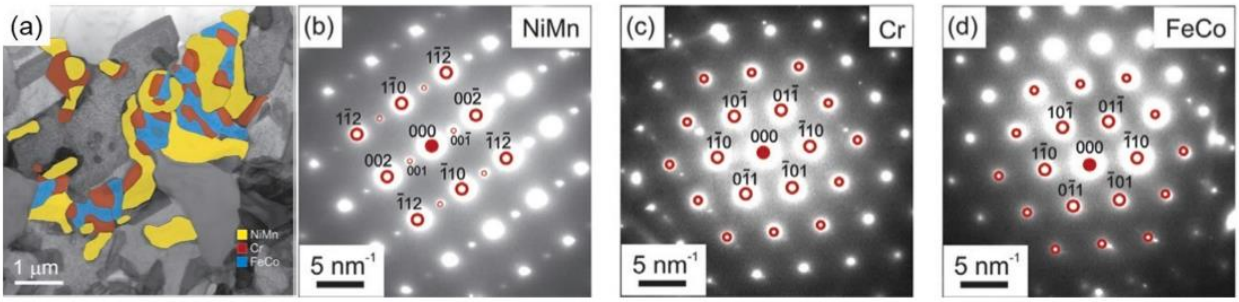

Figure 2.8: a) EDX maps superimposed on a STEM BF image of $Cr_{0.6}FeNiMn$ after aging at 500 °C for 500 days with three different phases. Corresponding SAED patterns superimposed with simulated diffraction patterns (red circles) of (b) $L1_0$-NiMn, (c) bcc Cr-rich, and (d) B2-FeCo phases.

2.3.3 Potential mechanisms of phase decomposition in MPEAs

Phase decomposition in the form of nanoscale precipitates can take place by two modes i.e., spinodal decomposition or nucleation and growth. Spinodal decomposition occurs in materials with a miscibility gap. The material undergoes a spontaneous, thermally driven phase separation, resulting in the formation of a fine-scale microstructure of alternating regions of the two phases [133]. It starts with homo-phase concentration fluctuations with a diffused interface, which evolves into a sharp interface with time. Whereas classical nucleation mode initiates with a distinct precipitate composition characterized by a sharp interface [134]. The final microstructure product by both modes of phase decomposition can look similar. Spinodal decomposition has been observed in Al and Cu alloyed equiatomic CrFeNiCo MPEA [135–138].

Another possible mechanism of phase decomposition is discontinuous precipitation (DP), which occurs at grain boundaries and proceeds inwards into a supersaturated matrix through the cellular growth of two alternating layers of phases behind a moving grain boundary [139]. Although, not yet observed in CrFeNi-based MPEAs, DP has been observed in other Al, Ti, and Cu alloyed MPEAs such as $(CoCrFeNi)_{94-x}Al_3Ti_3Nb_x$ [140], $(CoCrNi)_{94}Al_3Ti_3$ [141],

$Ni_{33}Co_{33}Cr_{24.3}Al_9$ [142], $Al_{0.2}Ti_{0.3}Co_{1.5}CrFeNi_{1.5}$ [143], $Al_{3.31}Co_{27}Cr_{18}Fe_{18}Ni_{27.27}Ti_{5.78}$ [144], $Ni_{30}Co_{30}Fe_{13}Cr_{15}Al_6Ti_6B_{0.1}$ [145], $(FeCoNiCr)_{100-x-y}Ti_xAl_y$ (where x = 1–3, y = 4–9 at. %) [146], $Fe_{40.4}Ni_{11.3}Mn_{34.8}Al_{7.5}Cr_6$ [147], $Al_{0.3}CoCrFeNi$ [148]. DP is different from continuous precipitation (CP) [139]. From a diffusional aspect, CP is controlled by bulk diffusion, whereas DP is controlled by grain boundary diffusion. DP is typically observed at low to intermediate temperatures, where bulk diffusion is too slow for continuous precipitation but grain boundary diffusion is still sufficient to permit allotriomorph formation, as shown in Figure 2.9 [149]. The driving force behind DP is hypothesized to be either a high lattice misfit between precipitate and matrix phases (>1%), where the matrix strain energy drives DP or the change of grain boundary energy with solute segregation, where the increase in grain boundary energy induces its migration to decrease its energy [150]. The initiation of DP depends on two factors i.e., the occurrence of heterogeneous grain boundary precipitation and the ability of the grain boundary to move. The precipitation on grain boundaries can be influenced by the inclination and misorientation of the boundary, as well as the orientation of the grain boundary plane with the habit plane of precipitate [139]. DP has not been observed on twin boundaries. Once the precipitates are nucleated on grain boundary, growth occurs by grain boundary migration towards the supersaturated matrix leaving behind phases in alternating sequence aligned normally to the reaction front. The growth of DP is supported by higher solute diffusivities along the migrating grain boundary [151–153] and in some cases through lattice diffusion of solutes characterized by bulk concentration gradient ahead of reaction front [142,154,155].

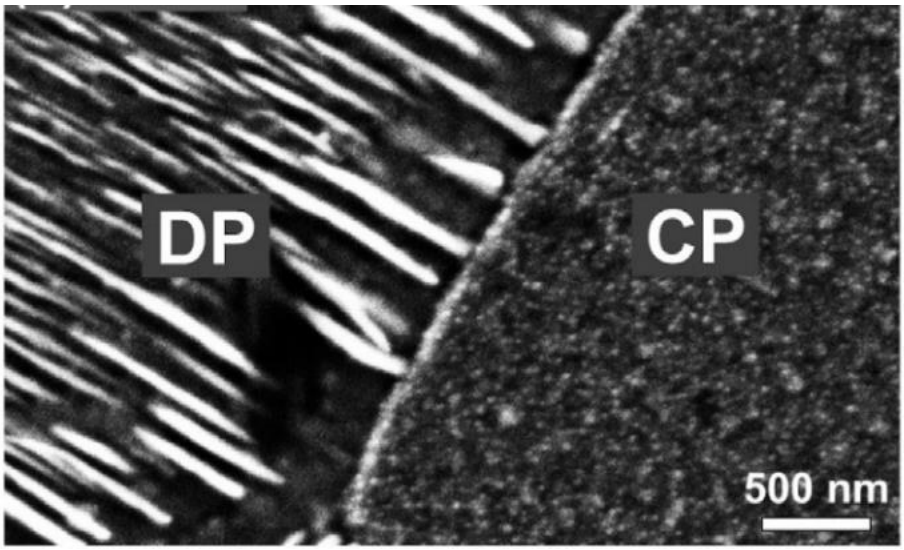

Figure 2.9: Schematic showing the occurrence of discontinuous precipitation in the form of alternating phases, and continuous precipitation in the form of γ' precipitates in $(CoCrFeNi)_{94-x}Al_3Ti_3Nb_x$ at 800 ^oC [140].

2.4 Evolution of MPEAs during irradiation

The microstructural response of CrFeNi-based MPEAs under irradiation is observed in the form of interstitial (i), and vacancy (v) type defect structures, segregation/depletion at defect sinks, and phase decomposition. Due to the FCC matrix, the i-type defects include ½<110> perfect loops and 1/3<111> faulted loops [156]. The v-type defects include {111} stacking fault tetrahedron and voids [33,118]. In addition, radiation-induced segregation (RIS) causes segregation and depletion of elements at these i-type and v-type defects [157].

2.4.1 Mechanism of irradiation damage in materials

During irradiation, incoming particles interact with lattice atoms, transferring their kinetic energy and creating primary knock-on atoms (PKAs). These PKAs then transfer their energy to other atoms, causing a chain reaction of displacements, resulting in displacement cascades surrounded by vacancies and interstitials [158]. The evolution of these cascades can be divided into four stages, which are illustrated in Figure 2.10:

Collisional - When the incoming particle imparts enough energy to displace atoms (E_d), the PKA lattice atom is knocked from its position, resulting in the formation of more knock-on atoms. This creates a cascade of displacive collisions until no atom has enough energy to cause further displacements. This stage occurs rapidly, from the creation of PKA at 10^{-6} ps until 0.1 ps, and results in displaced atoms and vacancies.

Thermal spike - After the displaced atoms can no longer cause further displacements, the remaining energy dissipates as heat among neighboring atoms, causing thermal spikes. For simplicity, regions with freshly generated thermal spikes can resemble molten metal. The thermal spike occurs just after 0.1 ps. For reference, the estimated temperature of the spike under 10 keV Ar ions irradiation in pure iron is 5800 K [159].

Quenching - Within 10 ps, the molten zone created by the thermal spike cools by the recombination of vacancies and interstitials, leaving only a small fraction of defects observed in the collisional stage. Stable point defect structures begin to form in this stage.

Annealing – The residual concentration of vacancies and interstitials after quenching stage is significantly higher than the thermal concentration of these defects. Therefore, these access defects enhance atomic mobility or diffusion, which is referred to as radiation enhanced diffusion (RED). These surviving defects initiate long-range migration via thermally activated diffusion and lead to

the interaction and recombination of interstitial-vacancy pairs, as well as the formation of extended defects via clustering, such as dislocation loops, cavities, etc. Some remaining defects may be annihilated at sinks such as grain boundaries, precipitates, and dislocations. The continuous loss of point defects to sinks, recombination, and extended defects causes their concentration to reach a steady state. The timescale of this stage can range from nanoseconds to months, depending on the irradiation conditions. This stage links the damage cascade with the extended defects observed after irradiation.

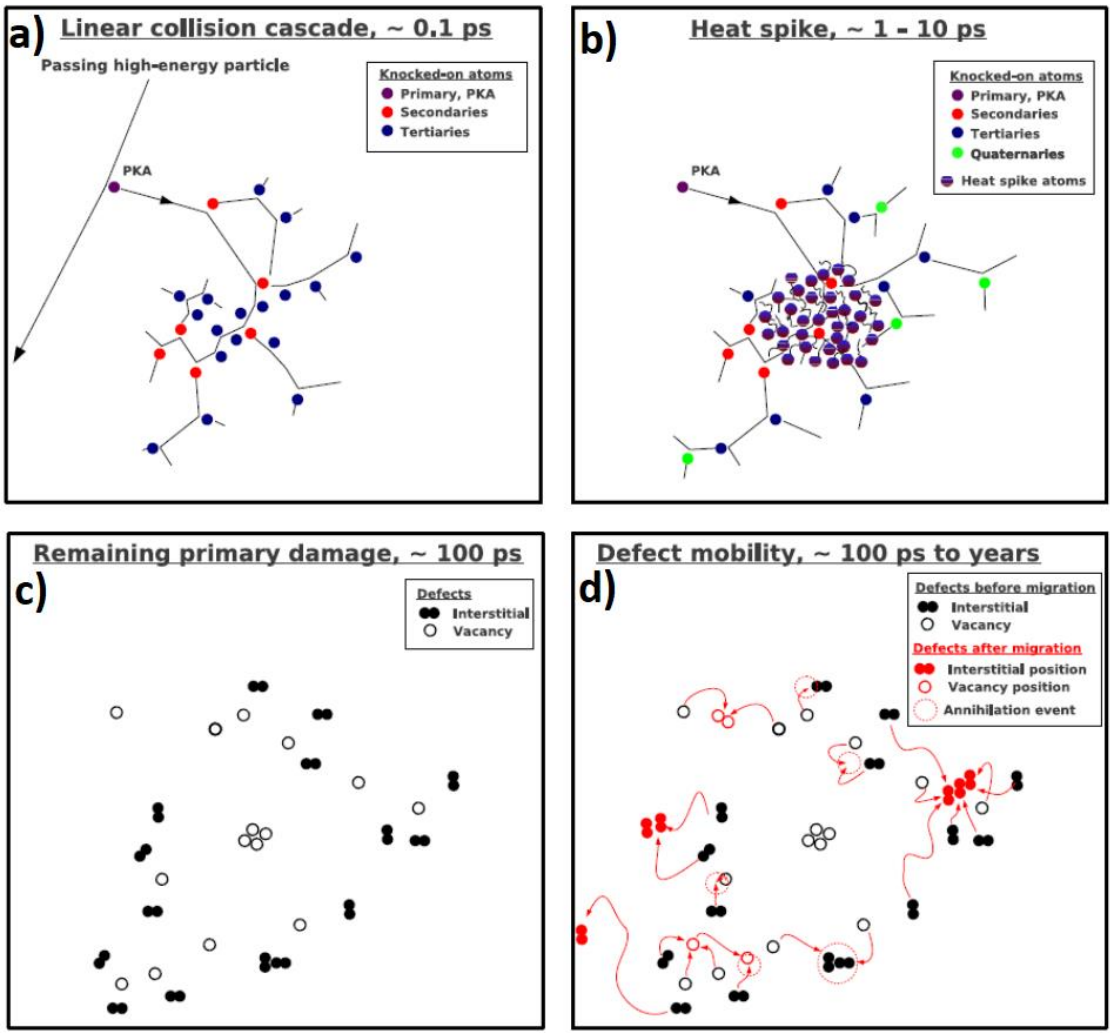

Figure 2.10: Evolution of cascades showing a) Collisional, b) thermal spike, c) quenching, and d) annealing stages [160].

2.4.2 Energy and mass transport in MPEAs

The energy transport in MPEAs is controlled by their electrical, thermal, and magnetic properties, which are correlated to an extent and have shown to significantly influence their irradiation behavior. The chemical disorder in MPEAs may lead to disorder in electronic, magnetic, and lattice structure causing a loss of translation symmetry in the crystal. Consequently, the electronic band structure was shown to smear out in reciprocal space, using ab initio Korringa-Kohn-Rostoker Coherent-Potential-Approximation (KKR-CSA) calculations [33,118]. The extent of smearing is dependent on the magnetic properties of individual alloying elements. Elements such as Ni, Fe, and Co are ferromagnetic whereas Cr is antiferromagnetic. In MPEAs, if all alloying elements are ferromagnetic, ab initio calculation showed that smearing only takes place in the minority spin near Fermi level whereas, a mixture of both ferromagnetic and antiferromagnetic elements showed significantly higher smearing in both majority and minority spin at Fermi level. The same ab-initio calculations also showed that the smearing in electronic structure results in a smaller mean free path for electrons, which is hypothesized to cause higher experimentally measured electrical resistivity of MPEAs. Therefore, equiatomic CrNiCo, equiatomic CrFeNiCo, equiatomic CrFeNiCoMn, and equiatomic CrFeNiCoPd alloys exhibited significantly higher electrical resistivity as compared to Ni, equiatomic NiCo, equiatomic NiFe, and equiatomic NiFeCo at room temperature as shown in Figure 2.11a [161]. Similar to electrical resistivity, the experimentally measured thermal resistivity of MPEAs is also higher than the less concentrated binary and ternary alloys (Figure 2.11b). In addition, the nature of elements in MPEAs also influenced the thermal conductivity as the Cr containing alloys exhibited lower thermal conductivity. This is hypothesized to the lower mean free paths of electrons in MPEAs keeping the electron-electron interactions local and resulting in lower heat conductivities [118].

Therefore, depending upon the nature of alloying elements, the energy dissipation in MPEAs could be slower as compared to the less concentrated alloys.

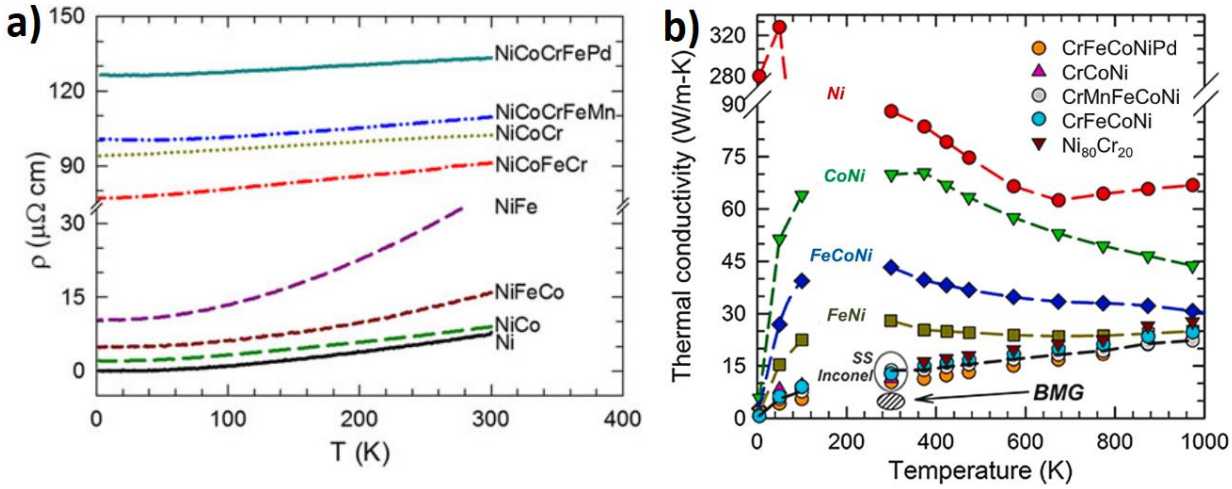

Figure 2.11: a) Electrical resistivity and b) thermal conductivity of Ni-based alloys as a function of temperature measured experimentally [36,161].

Mass transport in MPEAs is also important to understand the evolution of radiation damage. Diffusion in MPEAs was claimed to be "sluggish" and termed as one of the four core properties of MPEAs [116,162]. In pure metals and dilute alloys, diffusion is relatively simple as the neighborhood is roughly uniform across each atom, which results in a defined value of defect migration energy. However, in MPEAs, chemical complexity results in a large number of possible neighborhoods for each atom, yielding a range of defect migration energies. Several modelling studies showed that the non-uniform neighborhood can result in a large fluctuation of lattice potential energy (LPE) between lattice sites and hindering diffusion of atoms by creating a distribution of defect migration energies [163–165]. Using ab initio calculations, the migration energy barriers of interstitials and vacancies were estimated for Ni, equiatomic NiFe, equiatomic CrNiCo, and equiatomic CrFeNiCo as shown Figure 2.12. With increasing composition

complexity, a statistical distribution with an overlap between migration energies of vacancies and interstitial instead of single value was observed. The interstitials in equiatomic NiFe, equiatomic CrNiCo, and equiatomic CrFeNiCo showed higher migration barriers and lower diffusion coefficients whereas the vacancies showed slightly smaller migration barriers than in pure Ni [166,167]. The migration of vacancies was facilitated by Fe in equiatomic NiFe, Cr in both equiatomic CrNiCo and equiatomic CrFeNiCo. In addition, in-situ TEM during irradiation and MD simulations found the migration of interstitial clusters to occur in 3-D rather than 1D as in pure Ni and consequently be more localized in equiatomic NiCo and equiatomic NiFe [117,168,169]. Nonetheless, the claims of "sluggish diffusion" are only experimentally supported by observations of defect evolution under high dose rate heavy ion irradiation. Tracer diffusion experiments did not provide evidence to support sluggish diffusion in MPEAs and casted a doubt on its existence [116,170–179]. Furthermore, several studies also suggested that the interdiffusion of individual elements may not always be slow in MPEAs compared to simpler alloys [180–182].

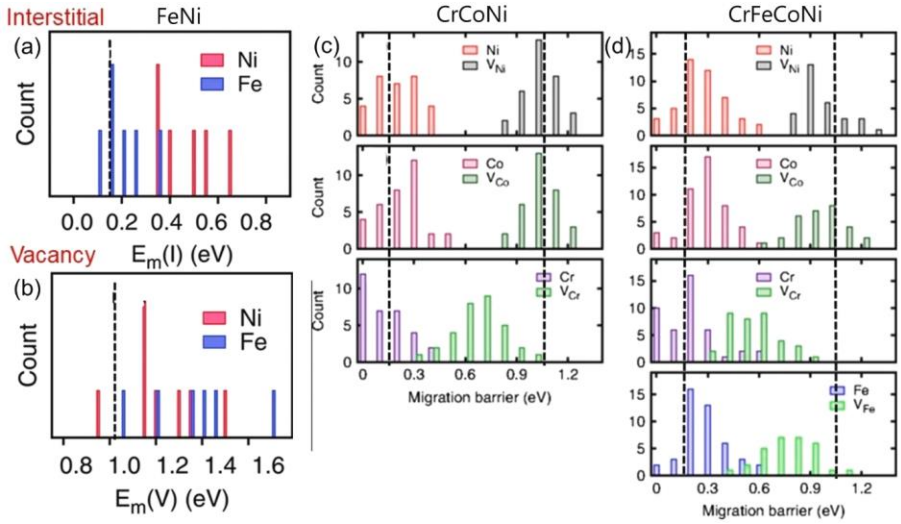

Figure 2.12: Ab initio calculation of migration energy of (a) an interstitial (b) a vacancy in equiatomic FeNi; migration energy of an interstitial and a vacancy in (c) equiatomic CrCoNi and (d) equiatomic CrFeCoNi. The migration energies of interstitials and vacancies in pure Ni is represented by a black dashed line [164,165].

2.4.3 Dislocations and cavities evolution in MPEAs under irradiation

The slow energy and mass transport in MPEAs is claimed to significantly influence their microstructure under irradiation [33–36,183]. It was hypothesized that the combined effects of reduced thermal conductivity and orders of magnitude reduction in the mean free path of electrons lead to less efficient heat conduction in MPEAs, resulting in prolonged thermal spike in displacement cascades that may increase vacancy-interstitial recombination rate and decrease defect density [33,118]. In addition, the overlaps in the defect migration energy of interstitials and vacancies, and 3-D motion of interstitial-clusters in MPEAs can lead to higher rates of recombination and reduce the interstitial mobility [163–165]. Therefore, the decreased defect density and sluggish interstitial migration in MPEAs should result in their superior irradiation behavior. This hypothesis was validated by multiple ion irradiation studies conducted at high dose rates (> 10^{-3} dpa/s), where MPEAs exhibited higher dislocation loop density, smaller loop radius, and smaller cavity swelling as compared the less concentrated alloys (Figure 2.13 and Figure 2.14). A higher number density and smaller size of loops was observed in equiatomic CrFeNiCo (2 x 10^{21} m^{-3}, 50nm) and equiatomic CrFeNiCoMn (1 x 10^{22} m^{-3}, 25 nm) as compared to equiatomic NiFe (1.2 x 10^{-21} m^{-3}, 75 nm) alloy under Ni ions (at 500 ^{o}C at 40 dpa, 2 x 10^{-3} dpa/s) [157]. Rutherford backscattering spectroscopy revealed a lower damage in equiatomic CrFeNiCo alloy as compared to pure Ni and equiatomic NiFe under Ar ion (at -257 ^{o}C at 0.2-0.8 dpa). Equiatomic CrFeNiCo and equiatomic CrFeNiCoMn MPEAs exhibited lower swelling (0.2% and 0.3%, respectively) as compared to equiatomic NiCoCr (1.1%), equiatomic NiFe (0.3%), equiatomic NiCo (3.5%), and pure Ni (6.7%) during Ni ion irradiation (at 500 ^{o}C at 53 dpa, 0.003 dpa/s) [117]. A similar trend in the swelling behavior was observed by another study using Ni ions at 500 ^{o}C at

60 dpa [168]. Therefore, these studies suggest that MPEAs exhibit superior irradiation resistance than simpler concentrated alloys under high dose rate ion irradiation.

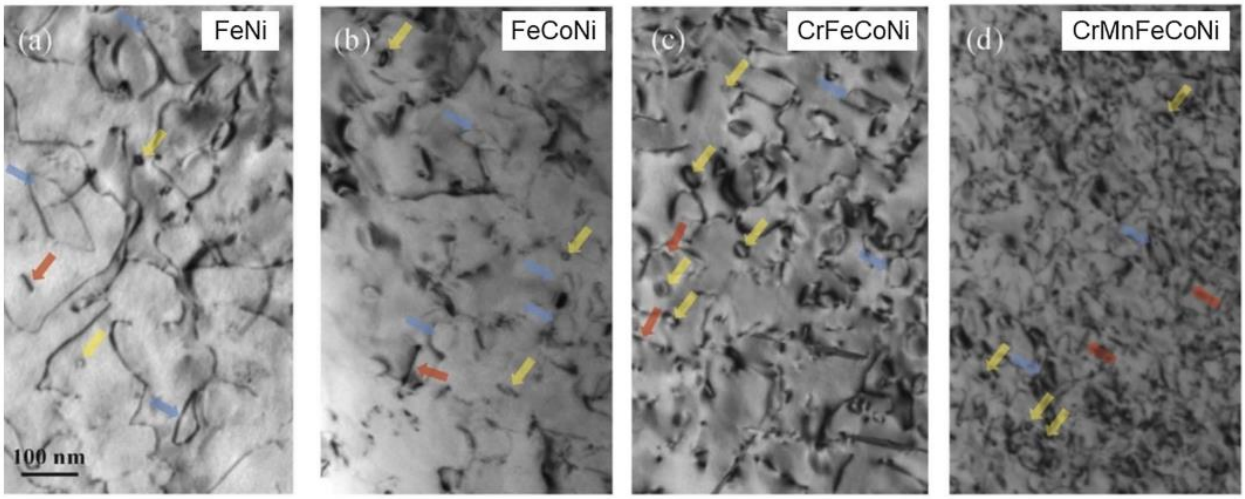

Figure 2.13: BF TEM images showing differences in dislocation loops size and density in irradiated a) equiatomic FeNi, b) equiatomic FeCoNi, c) equiatomic CrFeCoNi, and d) equiatomic CrMnFeCoNi alloys using 3 MeV Ni ions at 773K at 35 ± 5 dpa [157].

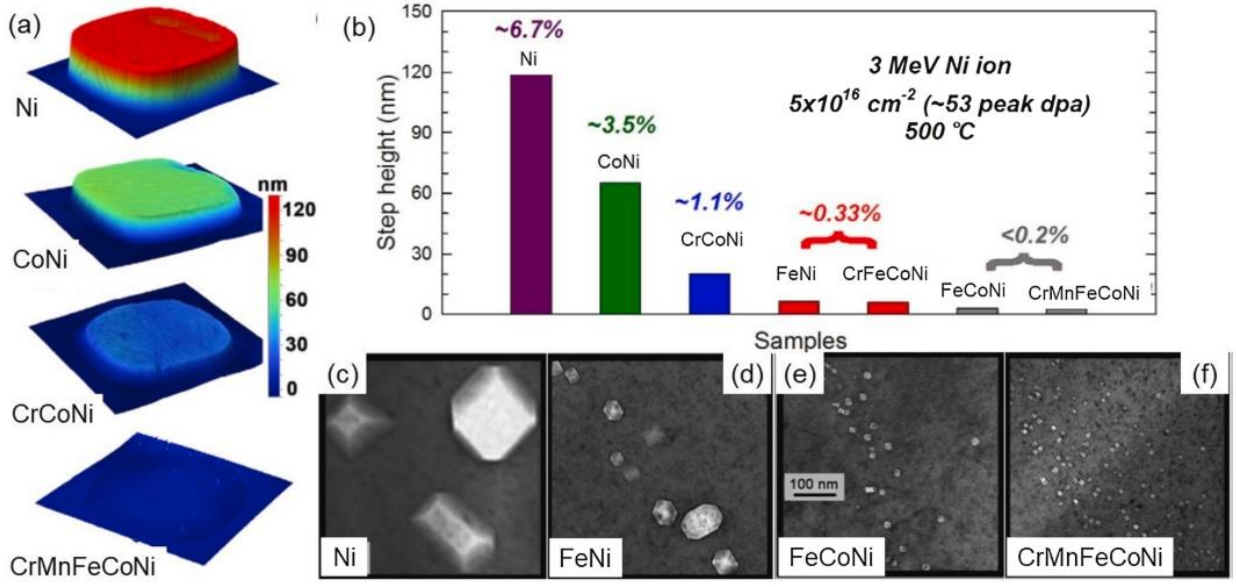

Figure 2.14: a) Optical profilometer measurements of cavity swelling in Ni, equiatomic CoNi, equiatomic CrCoNi, equiatomic CrMnFeCoNi, b) step height change in each alloy after irradiation, and c) TEM images showing the distribution of cavities in the irradiated region [117].

Within CrFeNi-based MPEAs, there were attempts to link the irradiation behavior to the number and nature of the alloying elements. Prior studies reported better irradiation behavior while increasing the number of alloying elements from 4 to 5, though this effect may simply be due to the alloying with Mn. Equiatomic CrFeNiCoMn possessed higher dislocation loop number density and lower loop size (1 x 10^{22} m^{-3}, 25 nm) compared to equiatomic CrFeNiCo MPEA (2 x 10^{21} m^{-3}, 50 nm) during Ni ion irradiation (at 500 ^{o}C at 40 dpa, 0.002 dpa/s) [157]. Equiatomic CrFeNiCoMn also exhibited lower swelling of 0.2% as compared to 0.33% in equiatomic CrFeNiCo during Ni ion irradiation (at 500 ^{o}C at 53 dpa, 0.003 dpa/s) [117]. Alloying with other elements can further change the irradiation response. For example, equiatomic CrFeNiCoPd exhibited lower swelling of 0.29% as compared to 0.37% in equiatomic CrFeNiCoMn during Ni ion irradiation (at 580 ^{o}C at 60 dpa, 0.002 dpa/s) [184]. The better irradiation resistance was attributed to enhanced recombination due to the increase in electrical resistivity after the addition of Mn or Pd in equiatomic CrFeNiCo MPEA [36] and to the higher atomic distortion caused by the addition of oversized atoms of Mn or Pd, which may slow diffusion and result in a higher number density and smaller size of defects [184].

Figure 2.14 further illustrates that instead of the number of alloying elements but rather their chemistry is relevant to understand irradiation resistance, equiatomic NiCoFe ternary alloy exhibited lower swelling compared to equiatomic CrFeNiCo MPEA during Ni ion irradiation (at 500 ^{o}C at 53 dpa, 0.003 dpa/s) [117] and similar swelling compared to equiatomic CrFeNiCoMn MPEA during Ni ion irradiation (at 500 ^{o}C using 0.003 dpa/s) at 53 dpa, [117] and at 60 dpa [168]. Furthermore, equiatomic NiCoFe also possessed higher dislocation loop number density and lower loop size (2.5 x 10^{21} m^{-3}, 40 nm) compared to equiatomic CrFeNiCo MPEA (2 x 10^{21} m^{-3}, 50 nm) during Ni ion irradiation (at 500 ^{o}C at 40 dpa, 0.002 dpa/s), which would suggest slower diffusion

in equiatomic NiCoFe compared to equiatomic CrFeNiCo [157]. Apart from equiatomic NiCoFe, equiatomic NiFe alloy also exhibited similar swelling as equiatomic CrFeNiCo MPEA during Ni ion irradiation (at 500 ^{o}C, 0.003 dpa/s) at 53 dpa, [117] and at 4 dpa [168]. However, there is no clear explanation for these observed inconsistencies.

2.4.4 RIS in MPEAs under irradiation

MPEAs under irradiation also exhibit radiation-induced segregation (RIS), which is a non-equilibrium phenomenon that occurs at defect sinks like grain boundaries, surfaces, dislocations, cavities etc. at intermediate temperatures (0.3-0.5 T_m) [185]. RIS is a direct consequence of RED, where the excessive point defects generated while irradiation are mobile and travel to defect sinks. This causes a segregation or depletion of various elements at the defect sinks depending on the coupling between alloy elements and defect fluxes [186]. The primary mechanism of RIS is modified inverse Kirkendall (MIK) model [187], where the preferential exchange of vacancy flux occurs with oversize elements due to their high vacancy diffusion coefficient, and the preferential association of interstitial flux with undersize elements due to their high interstitial diffusion coefficient [2]. Once segregation or depletion has occurred, the concentration gradient induces back diffusion of the segregating elements. A steady state is achieved when the defect driven alloying element fluxes are balanced by diffusion driven back-diffusion. RIS has been observed in $Cr_{0.6}$FeNiMn at a high angle grain boundary, where Ni enriched and Cr, Fe, and Mn depleted [188] under Ni irradiation (at 500-700 ^{o}C at 10dpa), and at dislocation loops with similar profile under Fe irradiation (at 450-550 ^{o}C at 0.2 dpa) [189]. Also in equiatomic CrFeNiCo, at dislocation loops and cavities (Figure 2.15), Ni, and Co segregation and Cr, and Fe depletion under electrons (at 400 ^{o}C, 1 dpa) [190] and under Ni ions (at 500 ^{o}C at 40 dpa, 2.10^{-3} dpa/s) [157]. In equiatomic

CrFeNiCoMn loops, enrichment of Co, and Ni and depletion of Cr, Fe, and Mn was observed after electron irradiation (at 400 ^{o}C, 1dpa) [190], under Kr ions (at 500 ^{o}C) [190,191] (Figure 2.16), In equiatomic CrFeNiCoPd loops, enrichment of Co, and Ni and depletion of Pd, and Fe was observed under electrons (at 400 ^{o}C, 1dpa) [190] (Figure 2.16). This RIS behavior via MIK mechanism was also consistent with self-diffusion radiotracer diffusion coefficient measurements, which ranked Mn and Co as the fastest and slowest diffuser, respectively in equiatomic CrFeNiCoMn.

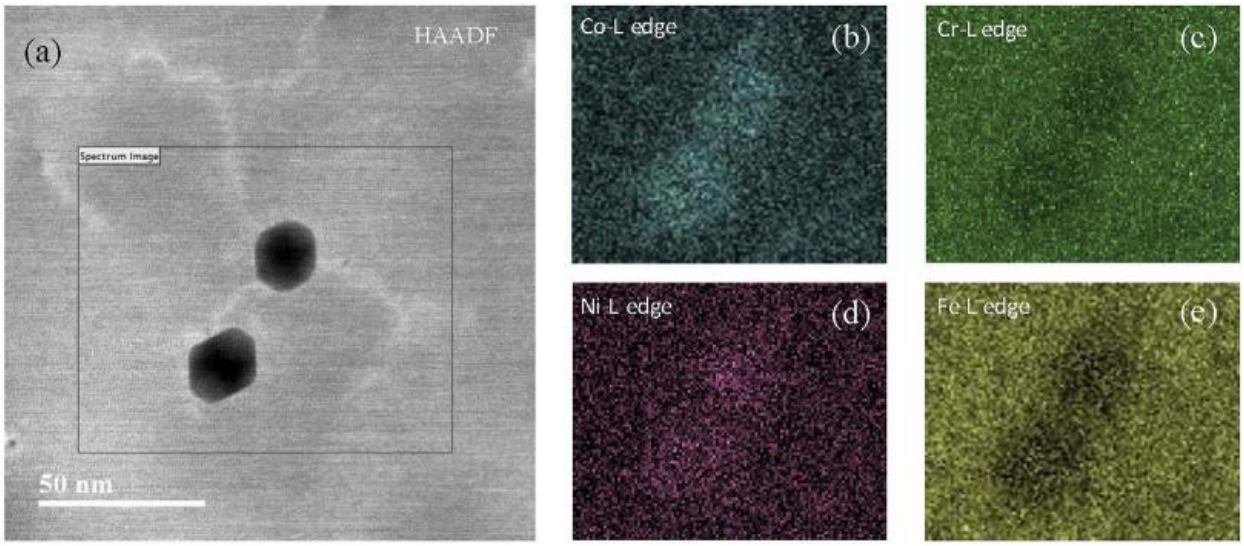

Figure 2.15: RIS at cavities in equiatomic CrFeNiCo a) HAADF image of cavities and b-e) EELS maps showing Co and Ni enrichment, and Cr and Fe depletion [157].

2.4.5 Phase stability of MPEAs under irradiation

While CrFeNi-based MPEAs such as equiatomic CrFeNiCo, $Cr_{0.6}$FeNiMn, equiatomic CrFeNiCoMn, and equiatomic CrFeNiCoPd appear stable against phase decomposition during high dose rate ion irradiation, electron irradiation studies found that these alloys are susceptible to phase decomposition. None of the ion irradiation studies on equiatomic CrFeNiCo using Ni ions

(at 500 ^{o}C, 4-53 dpa at 3 x 10^{-3} dpa/s) or on $Cr_{0.6}$FeNiMn using Ni ions (at 420-580 ^{o}C, 35-38 dpa at 2 x 10^{-3} dpa/s) [157,184,192] and Kr ions (at 25-500 ^{o}C) [191] or on equiatomic CrFeNiCoMn using Ni (at 25-700 ^{o}C, 0.03-10 dpa at 2 x 10^{-3} - 2 x 10^{-4} dpa/s) [188], Kr (at 500 ^{o}C, 2dpa) [193], and Xe and He (room temperature, 4 dpa) [194] or on equiatomic CrFeNiCoPd using Ni (at 420-580 ^{o}C, 35-40 dpa at 2 x 10^{-3} dpa/s) [184,195] reported any phase decomposition. No decomposition was found in $Cr_{0.6}$FeNiMn after neutron irradiation at relatively lower temperature (60 ^{o}C to 0.1-1 dpa at 8.9 x 10^{-7} dpa/s) [196] or in equiatomic CrFeNiCo under electron irradiation to 1 dpa at 400 ^{o}C [190]. However, NiMn ordering was noted in equiatomic CrFeNiCoMn and <001>-oriented spinodal decomposition between Co/Ni and Pd in equiatomic CrFeNiCoPd under electron irradiation to 1 dpa at 400 ^{o}C [190,197] (Figure 2.17). The different responses to electron and ion irradiations suggest that dose rate via cascade mixing may play a significant role in hindering phase decomposition in $Cr_{0.6}$FeNiMn, equiatomic CrFeNiCoMn, and equiatomic CrFeNiCoPd alloys [43].

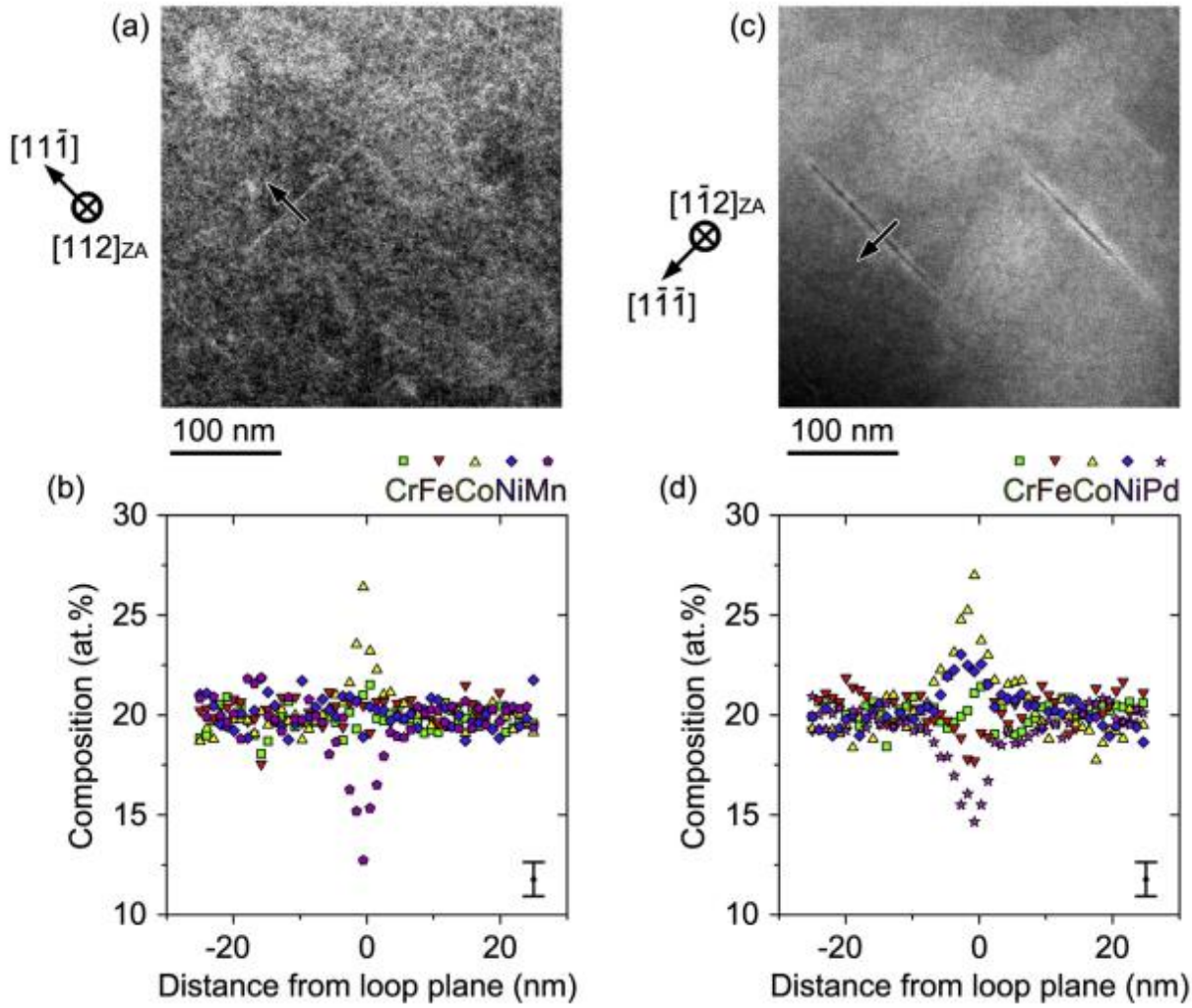

Figure 2.16: ADF-STEM edge-on views of the loops and EDS line-scans across the habit planes showing RIS in equiatomic CrFeNiCoMn (a, b) and equiatomic CrFeNiCoPd (c, d).

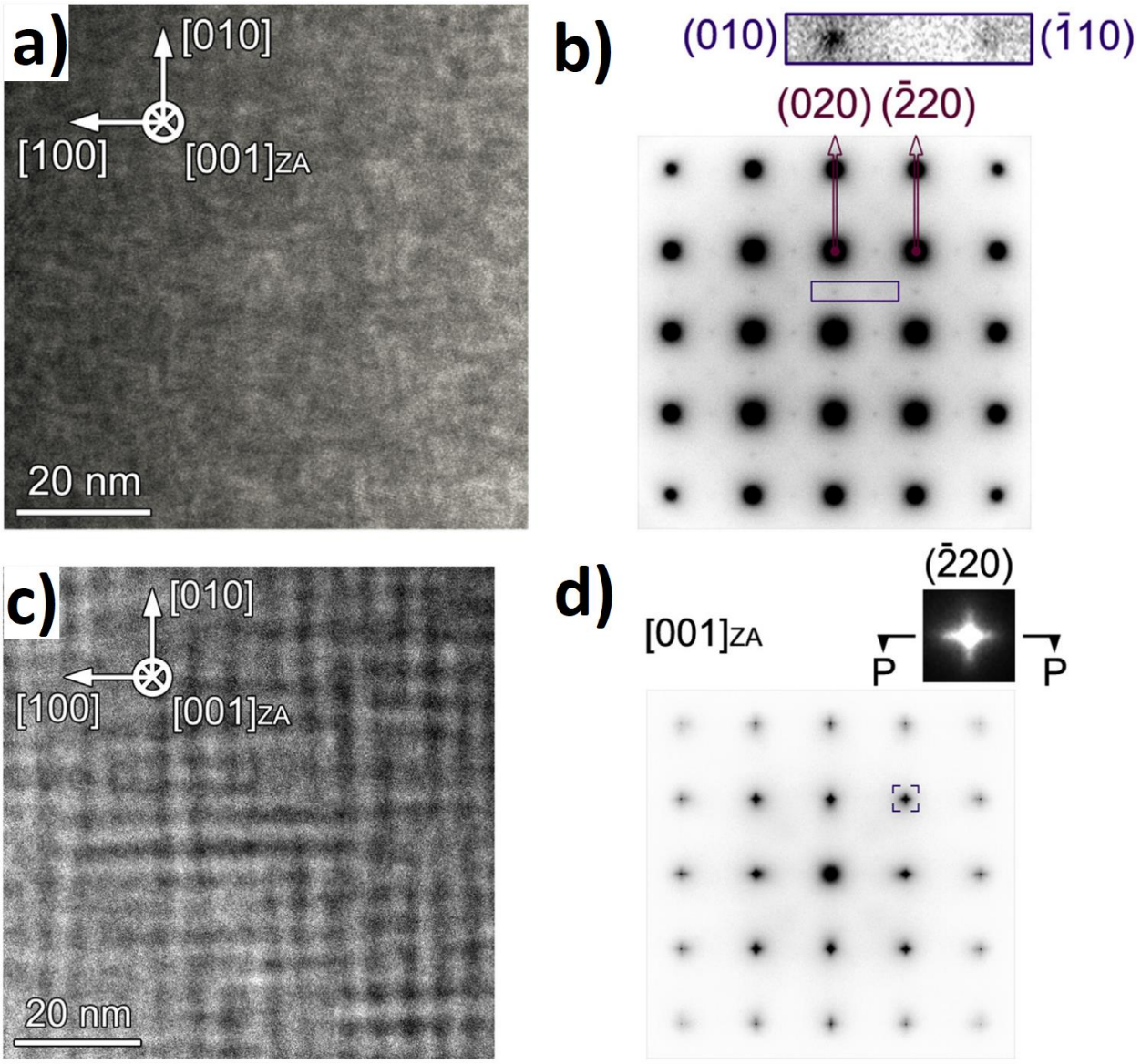

Figure 2.17: ADF-STEM image showing electron-irradiated matrix of a) equiatomic CrFeNiCoMn and c) equiatomic CrFeNiCoPd with corresponding SADP showing b) $L1_0$ NiMn superlattice spots in equiatomic CrFeNiCoMn and d) <001> oriented streaks of diffraction spots in equiatomic CrFeNiCoPd [190].

2.5 Outlook

This chapter provided an overview of the current knowledge on precipitation behavior in RPV steels and microstructure evolution in MPEAs under irradiation. Despite the considerable research conducted in this area, several knowledge gaps have been identified in the current understanding. Therefore, this thesis aims to address these gaps and contribute to the advancement of knowledge in this field.

2.5.1 RPV steels

Considerable research has been conducted on the impact of Cu and Ni concentration on the precipitation of Cu-MNS and MNS phases in RPV operating temperatures of approximately 290 ^{o}C. Although the effects of low P (<0.015 at. %) on grain boundary embrittlement are well understood, there is currently no experimental evidence to support a mechanistic understanding of the effects of P on the matrix. Additionally, much of the existing literature on RPV steels has focused on precipitation under lower dose rate neutron irradiation. Alternatively, ion irradiation can provide a faster means of studying the precipitation mechanism in RPV steels. Nonetheless, a correlation between the precipitate number density, radius, volume fraction, and composition has yet to be established between neutron and ion irradiation for any given composition of RPV steel.

2.5.2 MPEAs

Several studies have demonstrated intriguing irradiation behavior in Ni-based MPEAs with increasing composition complexity. However, most of these studies have utilized ion irradiation at high dose rates, which can significantly impact the dislocation loops and cavity microstructure

and prevent phase decomposition. Currently, no investigations have examined the dose rate effect in MPEAs or whether the interesting properties of MPEAs extend to lower dose rates. Additionally, limited thermal aging and simulation studies exist to establish equilibrium phases in CrFeNi-based MPEAs, and more thermal aging studies are necessary to confirm the anticipated equilibrium phases and mode of phase decomposition in these alloys.

Chapter 3 Effect of Phosphorus on the Precipitation in Irradiated RPV Steels

3.1 Introduction

Phosphorus is a common trace impurity element in steels. It is well established that it also plays a role in hardening and embrittlement [198,199]. Dissolved P also segregates to grain boundaries lowering its cohesive energy, which can lead to brittle intergranular fracture [200–203]. The phenomena of radiation-enhanced temper embrittlement has been extensively studied and modeled [204], but is not a significant contributor to ΔT in bainitic low alloy RPV steels [89]. However, there is limited understanding of the role of P on precipitation and the associated hardening [89,200,204]. Under irradiation, P clusters and segregates to dislocations along with Cu, Mn, Ni, and Si [200,201,205–207]. Hardening and embrittlement increase with increasing P concentrations in very low and nominally Cu-free steels (denoted as Cu-free steels from here on) but the impact generally decreases with increasing Cu [17,208]. While it is a minor constituent, the presence of P was also found to correlate with an increase in the number density of CRPs and a decrease in the average CRP radius [89].

In this chapter, we tested the hypothesis that P promotes early nucleation of MSN precipitates, much like the well-established effect of trace amounts of Cu [199–203,205–207] by characterizing six RPV split melt steels, with varying amounts of P, Ni and Cu, which were irradiated at the same condition in the UCSB Advanced Test Reactor-2 (ATR-2) experiment. We also characterized a low-Cu, medium-Ni, high-P steel irradiated to a lower fluence in the UCSB Irradiation Variables Program (IVAR) experiment, since it was not available from ATR-2 study.

While the lower fluence results cannot be directly compared to the ATR-2 results, observing the earlier morphologies of the precipitates in a low-Cu, high-P steel remains informative.

3.2 Experimental

The seven selected low alloy steels were three Cu-free medium-Ni (CM3-CM4-CM5), two Cu-free high-Ni (CM6-CM7), and two low-Cu medium-Ni (CM13-CM14) alloys with varying P. They are a subset of a systematic matrix of split melt steels acquired by UCSB from Sheffield University aimed at evaluating the effects of various combinations of Cu, Ni, Mn, P, and other selected elements on irradiation hardening. The alloys were fabricated by a remelting and hot forging sequence to form 18 mm plates. The baseline heat treatment sequence was: austenitization at 900°C for 0.5h; salt bath quench to 450°C with a 10 min hold; air cool; tempering at 660°C for 4h: air cool; stress relief anneal at 607˚C for 24 h; programmed cool at 8˚C/h to 300˚C; air cool. These steels have microstructures and unirradiated properties that are typical of commercial A533 steels [209]. Their as-received compositions obtained by optical emission spectroscopy are summarized in Table 3.1. Six alloys were irradiated at the Idaho National Laboratory in the UCSB ATR-2 experiment. The irradiation conditions are listed in Table 3.2. One alloy (CM14) was irradiated in the UCSB IVAR T16 capsule to a lower fluence. All the irradiations were at ~ 290°C. Further details of the irradiations are available in [210–212].

Atom probe tomography (APT) characterization was carried out using a Cameca LEAP 4000xHR at the Idaho Center for Advanced Energy Studies (CAES). The APT specimens were prepared from the intragranular regions, away from grain boundaries, using a standard focused ion beam milling (FIB) method. All of the tips were run in laser mode at a temperature of 55 K with a

pulse energy of 50 pJ, a pulse frequency of 200 kHz and target evaporation rate of 0.5%. Reconstructions were performed using the commercially available IVAS 3.8.6 software. The radius evolution of the reconstructed data was based on the voltage evolution by using the evaporation field of Fe. The image compression factor and field factor ranged between 1.3 and 1.6, and between 3 and 3.3, respectively. The width of the mass to charge ratio peaks were ranged using the full width at 1% of the peak maximum (FW1M) and a background correction was applied to obtain bulk compositions. To address the overlap between the Fe^{2+} and Ni^{2+} peaks at 29 m/q, the 29 peak was assigned to Ni during the cluster identification step to obtain cluster number density, size, and volume fraction as it consist of the large fraction of Ni present [213]. Next, peak deconvolution was performed using the natural abundances of non-overlapping isotopes to obtain the bulk composition and the cluster composition in each tip. After deconvolution, the bulk composition of Ni decreased by 0.2-0.3 at. %, while the Ni content in the clusters decreased by 2-4 at. %.

Table 3.1: As-received composition of irradiated RPV steel samples (% at.).

Sample ID	**Description**	**Cu**	**Ni**	**Mn**	**Si**	**P**	**Cr**	**Mo**	**C**	**Fe**
CM3	Low-P, Cu-free, Medium-Ni	0.02	0.81	1.62	0.32	0.011	0.00	0.28	0.60	96.34
CM4	Medium-P, Cu-free, Medium-Ni	0.02	0.81	1.55	0.32	0.056	0.05	0.32	0.74	96.13
CM5	High-P, Cu-free, Medium-Ni	0.02	0.81	1.63	0.32	0.090	0.04	0.31	0.69	96.09
CM6	Low-P, Cu-free, High-Ni	0.02	1.59	1.52	0.34	0.013	0.05	0.31	0.70	95.46
CM7	High-P, Cu-free, High-Ni	0.00	1.70	1.55	0.34	0.084	0.05	0.32	0.74	95.28
CM13	Low-P, Low-Cu, Medium-Ni	0.10	0.79	1.63	0.32	0.007	0.00	0.30	0.70	96.17
CM14 (IVAR)	High-P, Low-Cu, Medium-Ni	0.10	0.79	1.64	0.34	0.072	0.00	0.30	0.74	96.03

Table 3.2: Neutron irradiation conditions (Energy > 1MeV).

Irradiation	Flux (n cm^{-2} s^{-1})	Fluence (n cm^{-2})	Temperature (^oC)
ATR-2	$3.6x10^{12}$	$1.4x10^{20}$	290
IVAR T16	$3.0x10^{11}$	$1.57x10^{19}$	290

Given their relatively large size and high concentration difference between clusters and surrounding matrix, solute cluster analysis was performed using the commercially available maximum separation method (MSM) as implemented in the IVAS 3.8.6 software [110]. Mn, Ni, Si, and P were selected as core atoms in the Cu-free steels (CM3-CM7) and Cu, Mn, Ni, Si, and P were selected as core atoms in the low-Cu steels (CM13-CM14). For all alloys, the order parameter was set at 8. D_{max} was obtained from nearest neighbor distributions (NND) of the core atoms by deconvoluting the clusters NND and matrix NND from the original bi-modal distribution and selecting their intersection. N_{min} was obtained from cluster size distribution at a given D_{max} by selecting the highest cluster size in a randomized dataset. The selected D_{max} and N_{min} values ranged between 0.6 and 0.7 nm and 70 and 120 atoms, respectively. The number density (ND), mean radius (<r>), and volume fraction (f) of the clusters were calculated using equations 3.1, 3.2, and 3.3, respectively.

$$ND = \frac{No.\ of\ clusters}{Volume\ of\ reconstruction\ (V)} \text{ where, } V = \frac{(No.of\ atoms)*(Atomic\ volume\ of\ Fe)}{Detection\ efficiency\ *Packing\ fraction} \quad (3.1)$$

$$< r > = \sqrt[3]{\frac{3*(No.of\ atoms\ in\ a\ given\ cluster)*(Atomic\ volume\ of\ Fe)}{4*\pi*Detection\ efficiency}} \quad (3.2)$$

$$f = \frac{Total\ no.of\ atoms\ in\ clusters*100}{Total\ no.\ of\ atoms\ in\ the\ reconstruction} \quad (3.3)$$

The average and standard errors of these quantities were estimated by varying D_{max} by 0.1 and N_{min} by 20 atoms for each dataset. To ensure consistent cluster analysis and precipitate

composition measurements, Fe was excluded based on the understanding that trajectory aberrations and likely other artefacts contribute significantly to its presence in the clusters. Prior studies on RPV steels using APT have pointed out that the higher content in the precipitates observed in APT datasets is inconsistent with results from other techniques such as small angle neutron scattering (SANS), STEM EDS, as well as thermodynamic calculations [44,80,214–216].

Multiple APT measurements were carried out with a minimum of 2 datasets per alloy except CM4 and CM14, for which only one dataset was collected. The dense solute clusters were classified manually into two categories: precipitates associated with dislocations and precipitates in the matrix, based on their spatial arrangements. The precipitates in the matrix were further classified in two additional categories, namely Mn-Si-Ni or MSN, and P-associated Mn-Si-Ni or P-MSN precipitates, depending on the presence of P. Clusters containing more than 5 P atoms were classified as P-MSN, while the others were considered MSN. The number density, mean radius, volume fraction, and composition of the precipitates on dislocations, and MNS and P-MNS precipitates in the matrix were analyzed separately. As a note, P in medium and high-P samples was also found to be distributed along crystallographic poles as shown by the representative evaporation map of P in supplementary material (Figure B 1).

In five out of the seven steels, the irradiation hardening (Ds_y) was measured by testing two to three sub-sized 15x4x0.5 mm SS-J2 EDM fabricated tensile specimens, on a MTS-810 servo hydraulic load frame at a strain rate of ~ 10^{-3}/s. In other two cases, hardening was estimated based on multiple (10-15) Vickers Hardness (DH_v in units of kg/mm^2) measurements, at a load of 500 g, converted to as $Ds_y \sim 3.3\ DH_v$ [212].

3.3 Results

The Cu, Ni, Mn, and Si concentrations measured by APT were reasonably consistent with the as-received compositions as summarized in Table 3.3. For a given alloy, slight variations in compositions from tip to tip were noted. Therefore, the individual measured APT tip values were used when plotting the precipitate number density, radius, volume fraction.

Table 3.3: RPV steel compositions (at. %) averaged over multiple datasets where appropriate except CM4 and CM14. The errors were estimated using the equation: $\frac{Concentration\ of\ a\ given\ element}{\sqrt{Number\ of\ atoms\ of\ given\ element}}$. At a composition below 0.001 at. %, an element is considered as not detected.

Sample	**Description**	**Cu**	**Ni**	**Mn**	**Si**	**P**
CM3	Low-P, Cu-free, medium-Ni	0.01 ± 0	0.62 ± 0.02	1.43 ± 0.02	0.29 ± 0.01	Not detected
CM4	Medium-P, Cu-free, medium-Ni	0.03 ± 0	0.78 ± 0.03	1.64 ± 0.03	0.43 ± 0.03	0.006 ± 0
CM5	High-P, Cu-free, medium-Ni	Not detected	0.83 ± 0.03	1.23 ± 0.05	0.32 ± 0.01	0.010 ± 0.001
CM6	Low-P, Cu-free, high-Ni	Not detected	1.40 ± 0.03	1.41 ± 0.06	0.33 ± 0.02	0.002 ± 0
CM7	High-P, Cu-free, high-Ni	Not detected	1.30 ± 0.02	1.36 ± 0.04	0.30 ± 0.01	0.012 ± 0.001
CM13	Low-P, low-Cu, medium-Ni	0.08 ± 0.01	0.81 ± 0.03	1.49 ± 0.05	0.33 ± 0.01	Not detected
CM14	High-P, low-Cu, medium-Ni	0.08 ± 0.01	0.77 ± 0.03	1.51 ± 0.04	0.35 ± 0.02	0.011 ± 0.001

In Cu-free medium-Ni steels, our APT analyses revealed MSN and P-MSN precipitates in the matrix, and precipitates on dislocations, depending on the P content. In the low-P CM3, closely spaced precipitates decorated dislocations while a low number density of MSN precipitates were present in the surrounding matrix, as shown in Figure 3.1a. A 1-D concentration profile along one of the dislocations confirmed that distinct precipitates containing Mn, Ni, and Si formed, which were separated by about 10 ± 1 nm. In the medium-P CM4 and high-P CM5, higher number densities of both MSN and P-MSN precipitates were found in the matrix, as shown in Figure 3.1b and c**;** no dislocations were observed in the CM4 and CM5 datasets.

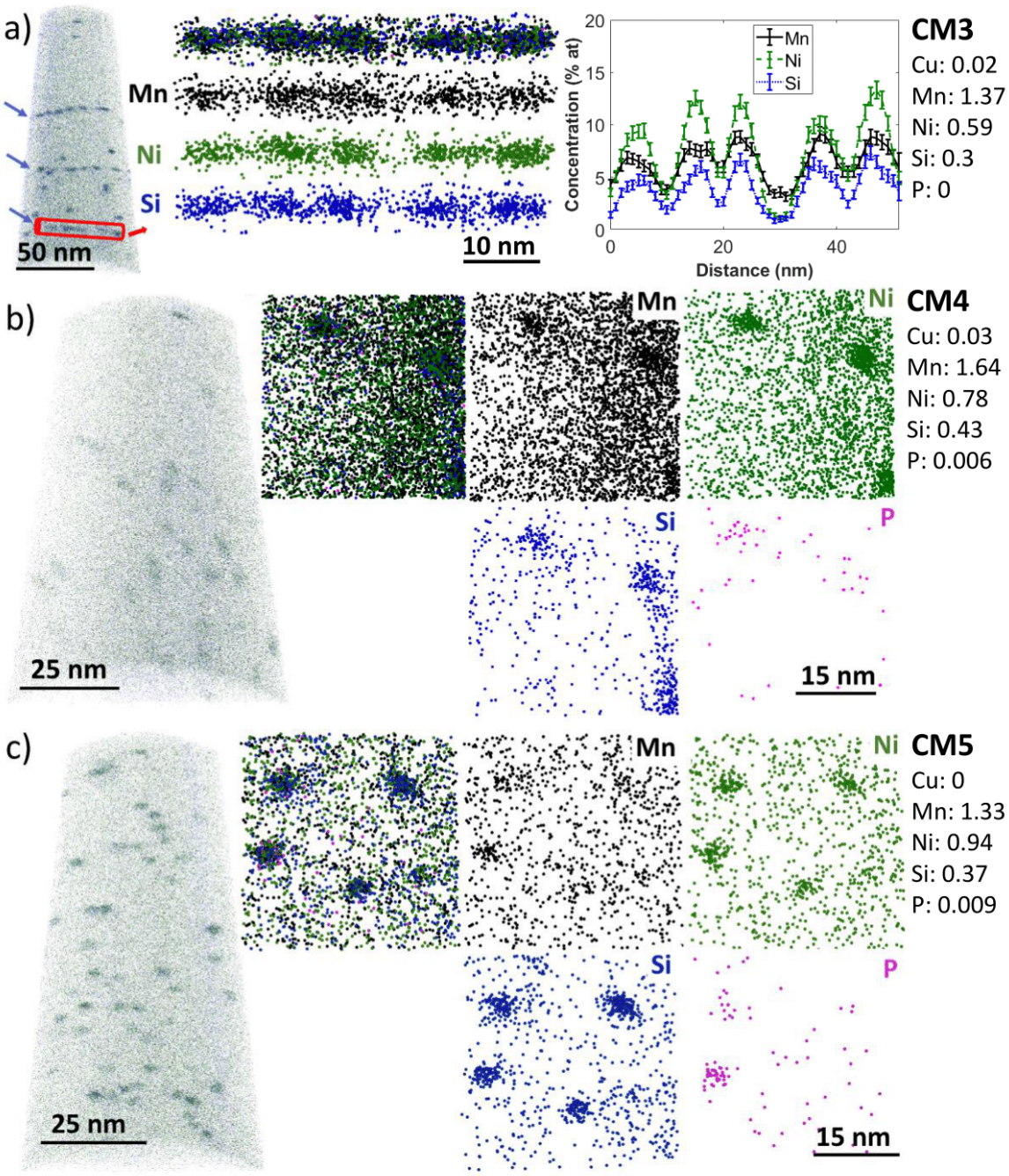

Figure 3.1: Full view of reconstructions displaying Mn, Ni, Si, and P atoms only and zoomed in 30x30x10 nm^3 thick slices of a) precipitates on dislocations in CM3; b) MSN and P-MSN precipitates in the matrix of CM4; c) MSN and P-MSN precipitates in the matrix of CM5. The solute content (in at. %) of each reconstructed volume is listed next to the corresponding slices.

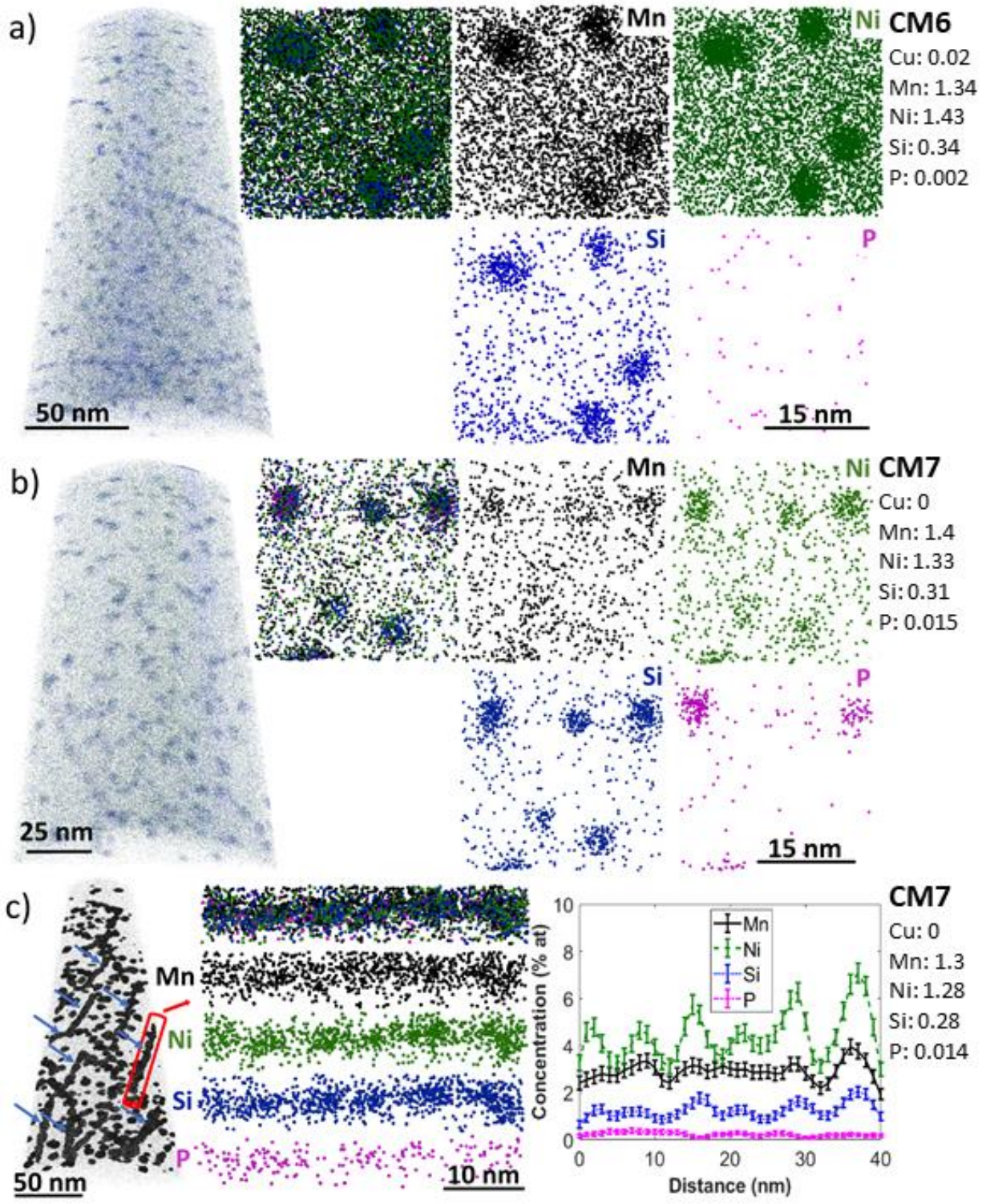

Figure 3.2: Full view of reconstruction using Mn, Ni, Si, and P atoms only and zoomed in 30x30x10 nm^3 thick slice showing the distributions and chemical structure of a) MSN precipitates in the matrix of CM6; b) MSN and P-MSN precipitates in the matrix of CM7; c) Precipitates on dislocations in CM7. The solute content (in at. %) of each reconstructed volume is listed next to the corresponding slices.

As illustrated in Figure 3.2a and b, compared to the medium-Ni steels (CM3 and 5), higher number densities of MSN and P-MSN precipitates in the matrix were found in the high-Ni steels at both low and high-P (CM6 and CM7) steels. In addition, precipitates on dislocations were also observed. In the low-P CM6, the precipitate spacing along the dislocation lines (~ 10 ± 2 nm) is the same as in the low-P Cu-free medium-Ni steel. However, as seen in Figure 3.2c**,** in the high-P CM7 steel, the precipitates on dislocations were more closely spaced at 7 ± 1 nm.

The number densities, radius, volume fractions, and chemistry of MSN and P-MSN precipitates in the matrix, and precipitates on dislocations in different alloys were analyzed in detail. The results for the Cu-free medium and high-Ni steels for all precipitate types are summarized in Table 3.4 and Table C 1, showing that the matrix MSN and P-MSN precipitate characteristics were influenced by the alloy Ni and P concentrations. In particular, the number density and volume fraction of MSN precipitates in the matrix increased with Ni content (Figure 3.3a and c**)**, while the mean radius remains roughly constant at ~ 1.65 nm (Figure 3.3b**)**. The characteristics of the MSN precipitates in the matrix did not, however, vary with the P concentration. The number density and volume fraction of P-MSN precipitates in the matrix increased with increasing P content (Figure 3.3d and f), while the mean radius decreased slightly in both the medium and high-Ni steels (CM3-CM7). The number density of P-MSN precipitates in the matrix was slightly higher while their mean radius increased by 0.3 nm in the medium-Ni steels (CM3-CM5) compared to the high-Ni steels (CM6 and CM7) (Figure 3.3e**)**, yielding similar overall P-MSN precipitates volume fractions. Comparing MSN and P-MSN precipitates in the matrix, the MSN number density and volume fraction were systematically higher than those of the P-MSN, while the P-MSN mean radii were systematically slightly larger than that of MSN precipitates. Specifically, the P-MSN mean radii were on average larger than the MSN radius by

0.3 nm in the medium-Ni steels and 0.65 nm in the high-Ni steels. In the medium-Ni steels, the MSN volume fraction was higher in C3 (nominal bulk 0.011 at. % P), equal in C4 (nominal bulk 0.056 at. % P) and lower in C5 (nominal bulk 0.09 at. % P) compared to that of P-MSN. However, in high-Ni steels, the MSN volume fraction was significantly higher than that of P-MSN. Furthermore, the total precipitate number density and volume fraction obtained by considering all types of precipitates (MSN and P-MSN in the matrix, and precipitates on dislocations) also increased with increasing Ni content (Figure 3.3g and i**)**, but the average radius remained unchanged (Figure 3.3h).

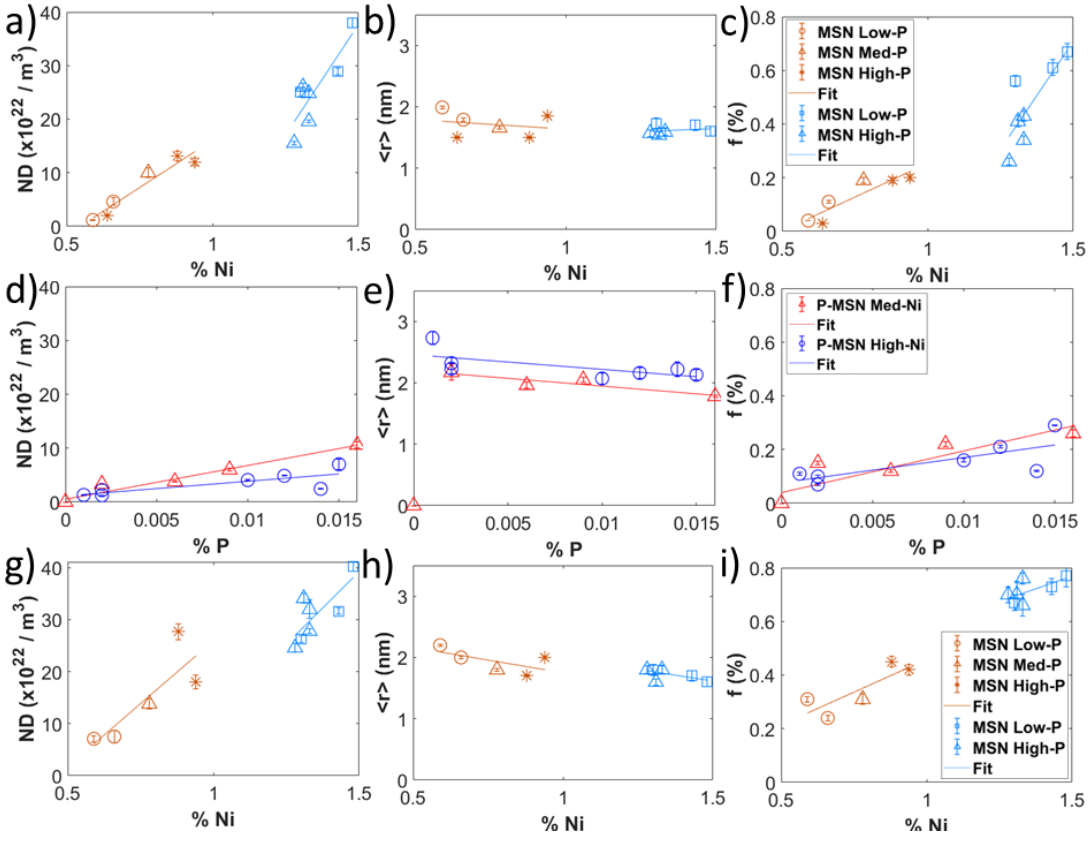

Figure 3.3: a) Number density, b) radius, and c) volume fraction of MSN precipitates in the matrix of Cu-free medium and high-Ni steels (CM3-CM7) as a function of APT measured Ni concentration (in at. %). d) Number density, e) radius, and f) volume fraction of P-MSN precipitates in the matrix of Cu-free medium and high-Ni steels (CM3-CM7) as a function of APT measured P concentration (in at. %). g) Number density, e) radius, and f) volume fraction considering all the precipitates i.e., MSN and P-MSN in the matrix, and precipitates on dislocations in Cu-free medium and high-Ni steels (CM3-CM7) as a function of APT measured Ni concentration (in at. %).

Table 3.4: Number density, average radius, and volume fraction of the MSN and P-MSN precipitates in the matrix, and precipitates on dislocation in the Cu-free medium and high-Ni steels within each APT analysis.

Sample	Bulk composition (at. %)					Precipitate type	Number density (10^{22} /m^3)	Radius (nm)	Volume fraction (%)
	Cu	Ni	Mn	Si	P				
CM3 Tip 1	0.02	0.59	1.37	0.03	0	MSN in the matrix	1.2 ± 0.1	2.0 ± 0	0.04 ± 0
						P-MSN in the matrix	0	0	0
						Precipitates on dislocation	5.9 ± 0.5	2.2 ± 0.1	0.27 ± 0.01
						Total	7.1 ± 0.6	2.2 ± 0.1	0.31 ± 0.01
CM3 Tip2	0	0.66	1.5	0.29	0	MSN in the matrix	4.6 ± 0.7	1.8 ± 0	0.11 ±0.01
						P-MSN in the matrix	0	0	0
						Precipitates on dislocation	2.9 ± 0.5	2.2 ± 0.2	0.13 ± 0
						Total	7.5 ± 1.2	2 ± 0.1	0.24 ± 0.01
CM4	0.03	0.78	1.64	0.43	0.006	MSN in the matrix	10.0 ± 0.9	1.7 ± 0	0.19 ± 0.01
						P-MSN in the matrix	3.8 ± 0.1	2.0 ±0.1	0.12 ±0.01
						Precipitates on dislocation	0	0	0
						Total	13.8 ± 1	1.8 ± 0.1	0.31 ± 0.02
CM5 Tip1	0	0.94	1.33	0.37	0.009	MSN in the matrix	12.0 ± 0.7	1.9 ± 0	0.2 ± 0.01
						P-MSN in the matrix	6.0 ± 0.6	2.1 ± 0.1	0.22 ± 0.01
						Precipitates on dislocation	0	0	0
						Total	18 ±1.3	2 ± 0.1	0.42 ± 0.02
CM5 Tip2	0	0.88	1.15	0.34	0.016	MSN in the matrix	13.1 ± 0.9	1.5 ± 0	0.19 ± 0.01
						P-MSN in the matrix	10.6 ± 0.6	1.8 ± 0	0.26 ± 0.01
						P-MSN on dislocation	0	0	0
						Total	23.7 ± 1.5	1.7 ± 0	0.45 ± 0.02
CM6 Tip1	0	1.48	1.47	0.33	0.002	MSN in the matrix	38.0 ± 0.9	1.6 ± 0.1	0.67 ± 0.03
						P-MSN in the matrix	2.2 ± 0	2.2 ± 0.1	0.1 ± 0.01
						Precipitates on dislocation	0	0	0
						Total	40.2 ± 0.9	1.6 ± 0.1	0.77 ± 0.04
CM6 Tip2	0	1.3	1.44	0.31	0.001	MSN in the matrix	25.0 ± 0.7	1.7 ± 0.1	0.56 ± 0.02
						P-MSN in the matrix	1.3 ± 0	2.7 ± 0.1	0.11 ± 0.01
						Precipitates on dislocation	0	0	0
						Total	26.3 ± 0.7	1.8 ± 0.1	0.67 ± 0.03
CM6 Tip3	0	1.43	1.34	0.34	0.002	MSN in the matrix	28.9 ± 0.6	1.7 ± 0.1	0.61 ± 0.03
						P-MSN in the matrix	1.3 ± 0	2.3 ± 0.1	0.07 ± 0
						Precipitates on dislocation	1.4 ± 0	2 ± 0.1	0.05 ± 0
						Total	31.6 ± 0.6	1.7 ± 0.1	0.73 ± 0.03
CM7 Tip1	0	1.33	1.4	0.31	0.015	MSN in the matrix	24.8 ± 0.7	1.6 ± 0.1	0.43 ± 0.02
						P-MSN in the matrix	7 ± 1.0	2.1 ± 0.1	0.29 ± 0
						Precipitates on dislocation	1.2 ± 0.1	2 ± 0.1	0.04 ± 0
						Total	32 ± 1.8	1.8 ± 0.1	0.76 ± 0.02
CM7 Tip2	0	1.33	1.33	0.27	0.012	MSN in the matrix	19.6 ± 0.3	1.6 ± 0.1	0.34 ± 0.02
						P-MSN in the matrix	4.9 ± 0.1	2.2 ± 0.1	0.21 ± 0.01
						Precipitates on dislocation	3.3 ± 0	2 ± 0	0.11 ± 0.01
						Total	27.8 ± 0.4	1.8 ± 0.1	0.66 ± 0.04
CM7 Tip3	0	1.31	1.28	0.33	0.01	MSN in the matrix	26.1 ± 0.7	1.5 ± 0.1	0.41 ± 0.02
						P-MSN in the matrix	4.1 ± 0.1	2.1 ± 0.1	0.16 ± 0.01
						Precipitates on dislocation	3.9 ± 0.1	2 ± 0.1	0.13 ± 0.02
						Total	34.1 ± 0.9	1.6 ± 0.1	0.7 ± 0.05
CM7 Tip4	0	1.28	1.3	0.28	0.014	MSN in the matrix	15.6 ± 0.3	1.6 ± 0.1	0.26 ± 0.01
						P-MSN in the matrix	2.5 ± 0.1	2.2 ± 0.1	0.12 ± 0
						Precipitates on dislocation	6.5 ± 0.5	2.3 ± 0.1	0.32 ± 0.02
						Total	24.6 ± 0.9	1.8 ± 0.1	0.7 ± 0.03

The results for low-Cu medium-Ni steels are summarized in Table 3.5. The low-Cu and P medium-Ni steels (CM13) contained a uniform distribution of Cu-MSN and MSN precipitates in the matrix (Figure 3.4a). The low-Cu, high-P CM14 steel contained smaller Cu-MSN, MSN, P-MSN, and Cu-P-MSN precipitates in the matrix (Figure 3.4b). The number densities of P-MSN and Cu-P-MSN precipitates were significantly lower than MSN and Cu-MSN precipitates. No dislocations were contained in the C13 and 14 tips. Since CM13 and CM14 represent different fluences, their precipitate number density, radius, and volume fraction cannot be directly compared. However, the precipitate morphologies can be compared to gain insights into the behavior of P in low-Cu alloys.

Table 3.5: Number density, average radius, and volume fraction analyses of MSN and Cu-MSN precipitates in the matrix of low-Cu medium-Ni steels.

Sample	**Bulk composition (at. %)**					**Precipitate type**	**Number density (10^{22} /m^3)**	**Radius (nm)**	**Volume fraction (%)**
	Cu	**Ni**	**Mn**	**Si**	**%P**				
CM13 tip1	0.07	0.7	1.45	0.32	0	MSN in the matrix	4.0 ± 0.3	1.4 ± 0.1	0.05 ± 0.01
						Cu-MSN in the matrix	10.5 ± 0.2	2.1 ± 0.2	0.39 ± 0.03
						Total	14.5 ± 0.5	1.9 ± 0.2	0.44 ± 0.04
CM13 tip2	0.08	0.85	1.57	0.38	0	MSN in the matrix	8.7 ± 0.2	1.3 ± 0.2	0.09 ± 0.01
						Cu-MSN in the matrix	14.0 ± 0.3	2.1 ± 0.2	0.48 ± 0.04
						Total	22.7 ± 0.5	1.8 ± 0.2	0.57 ± 0.05
CM14 T16 IVAR	0.07	0.68	1.48	0.35	0.014	MSN in the matrix	3.5 ± 0.4	0.9 ± 0.1	0.01 ± 0
						Cu-MSN in the matrix	5.8 ± 0.6	1.3 ±0.1	0.05 ±0.02
						P-MSN in the matrix	0.4 ± 0.1	1.0 ± 0.2	0.002 ± 0
						Cu-P-MSN in the matrix	0.7 ± 0.1	1.3 ± 0.2	0.01 ± 0
						Total	10.4 ± 1.2	1.2 ± 0.1	0.07 ± 0.02

The precipitates in the Cu-free and low-Cu steels have three distinct morphologies. One consists of P associated Mn-Ni-Si, with P uniformly distributed alongside Mn, Ni, and Si in the precipitates (Figure 3.5a). Another is a Cu-rich region with a Mn-Ni-Si appendage (Figure 3.5b**)**.

This morphology was only observed in the low-Cu steels (CM13-14). The third morphology exhibits a P and Cu-rich dual core surrounded by a Mn-Ni-Si shell (Figure 3.5c). The latter precipitates were observed only in the high-P C14 steel.

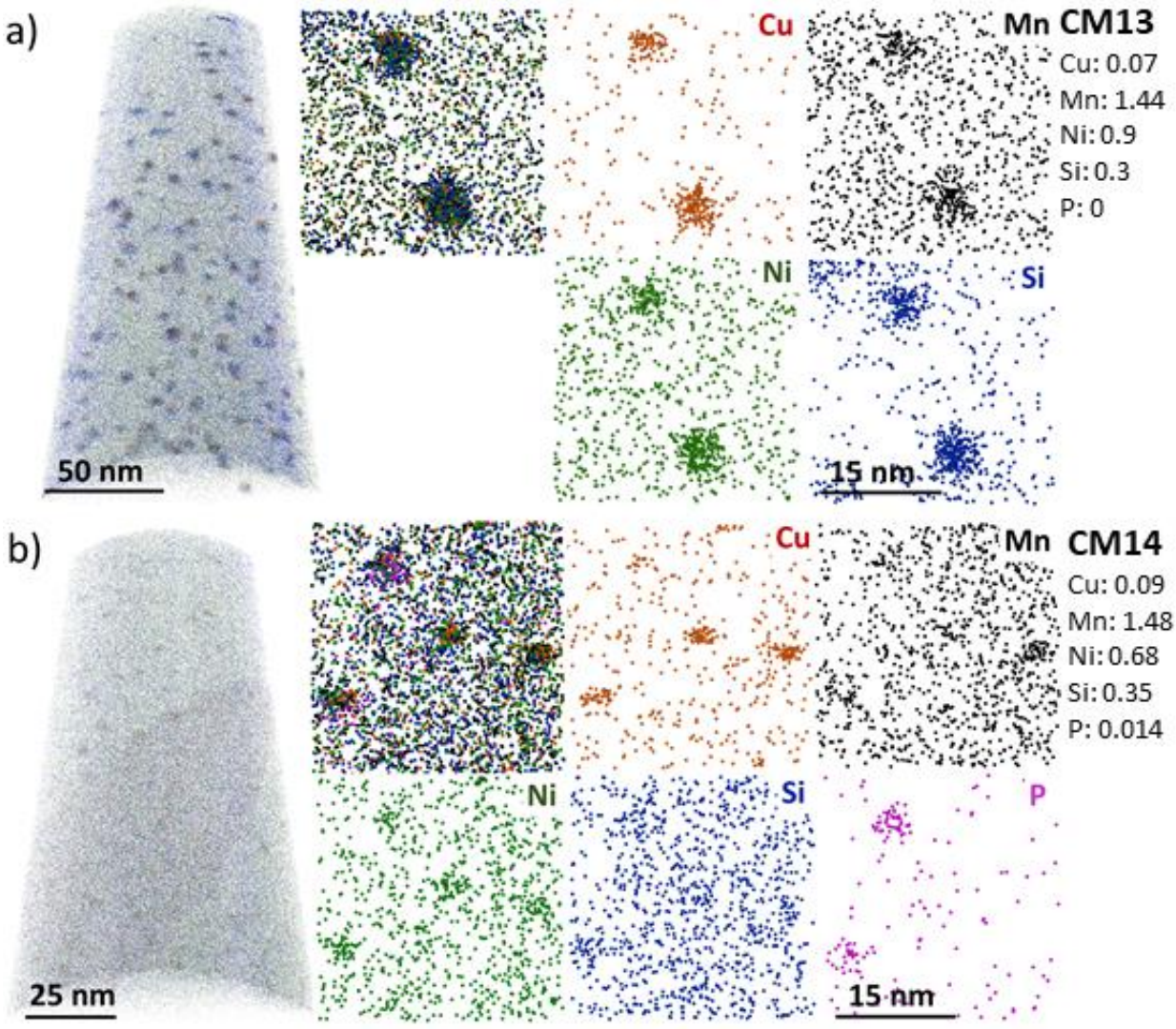

Figure 3.4: Full view of reconstruction and 30x30x10 nm^3 thick slice showing a) Cu-MSN precipitates in the matrix of CM13 and b) Cu-P-MSN, Cu-MSN, and P-MSN precipitates in the matrix of CM14. No dislocations were captured for these two alloys. Note that a grain boundary is present in the CM14 dataset, however it is not the focus of this work. The solute content (in at. %) of each reconstructed volume is listed next to the corresponding slices.

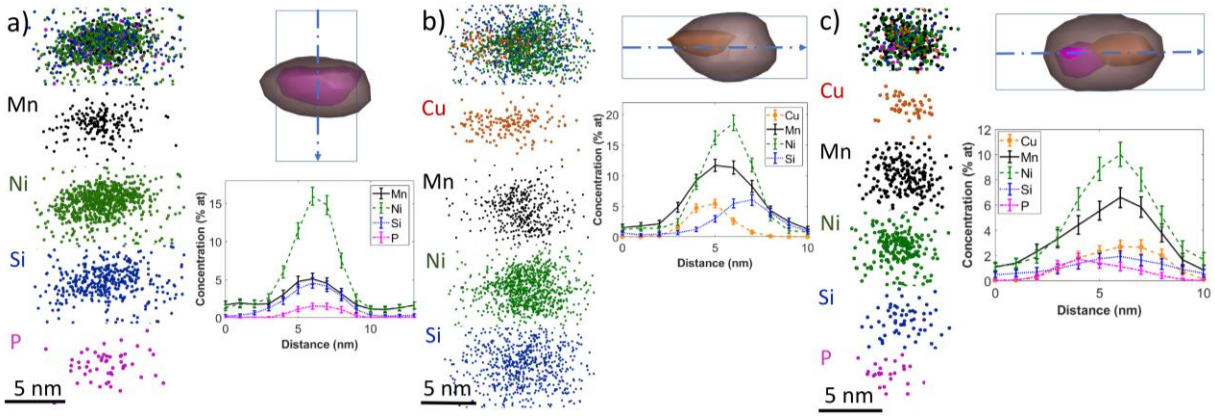

Figure 3.5: Representative spatial arrangements of elements in the observed precipitates: a) a P associated Mn-Ni-Si morphology from a P-MSN precipitate in the matrix of CM7, b) an appendage morphology as illustrated from a Cu-MSN precipitate in the matrix of CM13, and c) the multi-core shell morphology as illustrated from a Cu-P-MSN precipitate in the matrix of CM14. The distribution of the individual elements within one cluster, iso-concentration surfaces, and a 1D concentration profile taken parallel to the reconstruction axis are shown. The isoconcentration surfaces are in a) 1.1 at. % P and 13.1 at. % Mn+Si+Ni (grey), b) 3.1 at. % Cu (orange) and 9.6 at. % Mn+Si+Ni (grey), and c) 1.6 at. % (pink), 2.6 at. % Cu (orange), and 8.3 at. % Mn+Si+Ni (grey).

The precipitate compositions varied with the steel chemistry. The measured compositions of MSN, P-MSN, and Cu-MSN precipitates in the matrix are summarized in a Gibbs triangle in Figure 3.6 and Table 3.6. There is a spread in the compositions especially in the medium Ni case. The average amount of Ni in MSN and P-MSN precipitates increased from ~ 44 at. % in Cu-free medium-Ni steels to ~ 55 at. % or more in the Cu-free high-Ni steels. The higher Ni was accompanied by a corresponding roughly equal decrease in both Mn and Si. Specifically, the average amounts of Ni/Mn/Si were 44/36/19 at medium Ni and 54/30/15 at high Ni. These compositions are close to those at the end of the Γ_2 phase fields as shown by the larger blue symbol. In steels where they formed, the P-MSN precipitates exhibited either a similar or higher (average 45 at. % and 56 at. % in medium-Ni and high-Ni, respectively) Ni contents than the MSN features. Notably, the composition of the precipitates on dislocations (Table 3.6) was similar to that of the P-MSN precipitates in the matrix and therefore not plotted in Figure 3.6**.** In the low-Cu steel with low-P (C13), the precipitates compositions were very similar to those in the Cu-free steels. The

corresponding matrix Cu-MSN Ni content was also similar, at 44 at. %, to the amounts in the Cu-free steels, while the Ni was lower in the matrix MSN, at ~39 at. %, compared to the ATR-2 irradiation condition. However, in the low-Cu, high-P steel irradiated to a lower fluence in IVAR, the Mn in the precipitates was much higher, averaging ~ 45 at. %, while the Si content was lower, averaging ~ 9 at. %, than in the ATR-2 condition. Other than the difference in Ni between medium and high-Ni steels, as well as those in the lower fluence IVAR irradiation, on average the overall precipitate compositions are quite similar, and close the Γ_2 phase field composition range. Finally, Figure 3.7 shows the average overall precipiate P composition (in %), which increases with increasing P content, in both the medium and high-Ni steels.

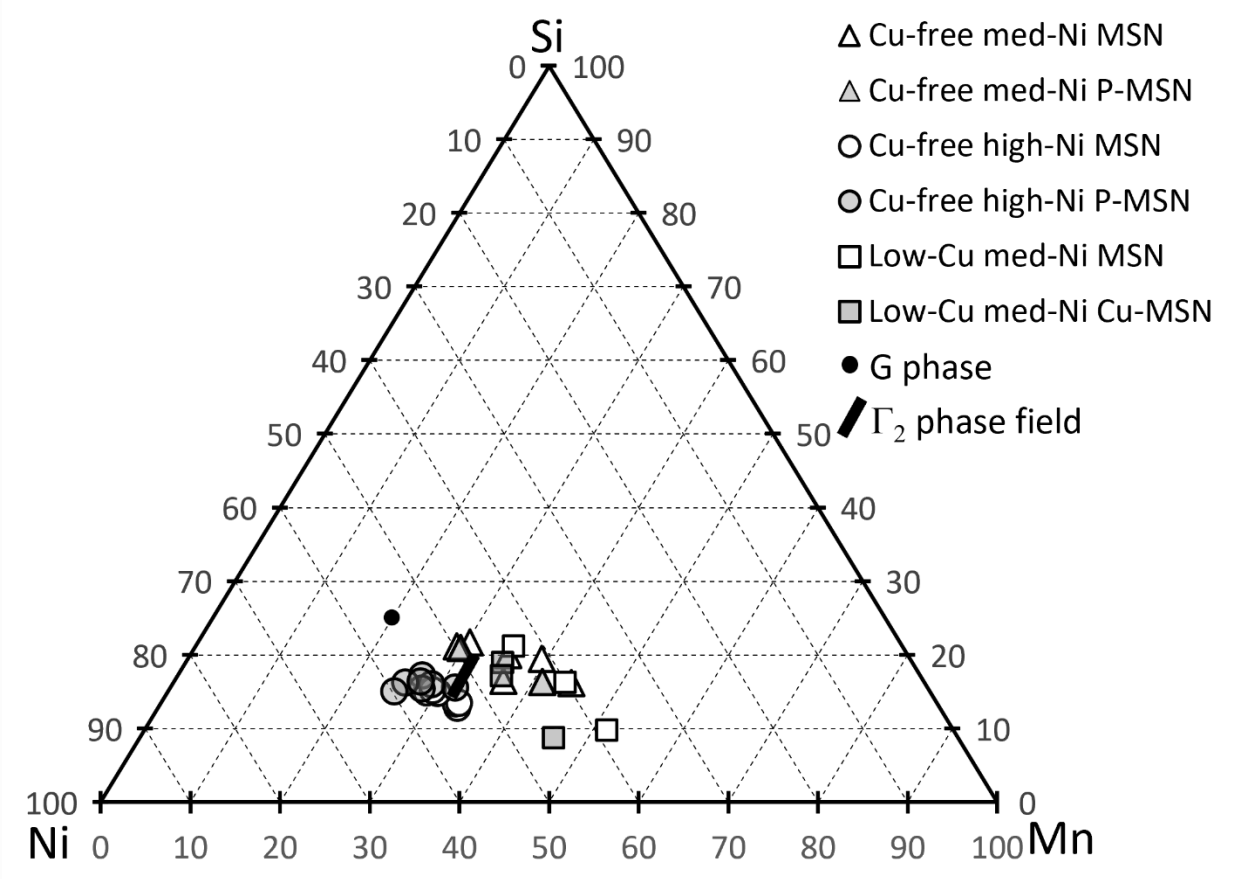

Figure 3.6: Compositions (at. %) of MSN, P-MSN, and Cu-MSN precipitates in the matrix of all the samples represented on a ternary composition diagram.

Table 3.6: Composition of the matrix MSN, P-MSN, Cu-MSN, and precipitates on dislocations in all analyzed steels.

Sample	Bulk composition (at. %)					Precipitate type	Precipitate composition (at. %)				
	Cu	Ni	Mn	Si	P		Cu	Ni	Mn	Si	P
CM3 Tip 1	0.02	0.59	1.37	0.03	0	MSN in the matrix	0	41.1	39.5	19.5	0
						P-MSN in the matrix	N/A				
						Precipitates on dislocations	0	42.1	39.2	18.7	0
CM3 Tip2	0	0.66	1.5	0.29	0	MSN in the matrix	0	48	30.3	21.7	0
						P-MSN in the matrix	N/A				
						Precipitates on dislocations	0	42.9	35.9	21.2	0
CM4	0.03	0.78	1.64	0.43	0.006	MSN in the matrix	0	39.3	44.2	16.1	0.38
						P-MSN in the matrix	0	42	40.6	16.1	1.38
						Precipitates on dislocations	N/A				
CM5 Tip1	0	0.94	1.33	0.37	0.009	MSN in the matrix	0	44.4	35.3	19.9	0.3
						P-MSN in the matrix	0	45.8	35.8	16.1	2.3
						Precipitates on dislocations	N/A				
CM5 Tip2	0	0.88	1.15	0.34	0.016	MSN in the matrix	0	49.4	28.9	21	0.7
						P-MSN in the matrix	0	48.2	29	20.4	2.4
						Precipitates on dislocations	N/A				
CM6 Tip1	0	1.48	1.47	0.33	0.002	MSN in the matrix	0	53.8	33.3	12.8	0
						P-MSN in the matrix	0	55.3	27.1	17.1	0.5
						Precipitates on dislocations	N/A				
CM6 Tip2	0	1.3	1.44	0.31	0.001	MSN in the matrix	0	53.7	32.9	13.4	0
						P-MSN in the matrix	0	52.5	31.6	15.5	0.4
						Precipitates on dislocations	N/A				
CM6 Tip3	0	1.43	1.34	0.34	0.002	MSN in the matrix	0	54.9	30.2	14.9	0
						P-MSN in the matrix	0	54.5	28.6	15.9	1
						Precipitates on dislocations	0	53.2	29.5	16.1	1.2
CM7 Tip1	0	1.33	1.4	0.31	0.015	MSN in the matrix	0	53.3	33.2	13.5	0
						P-MSN in the matrix	0	55.5	27.6	15.2	1.7
						Precipitates on dislocations	0	53.4	31.4	13	2.2
CM7 Tip2	0	1.33	1.33	0.27	0.012	MSN in the matrix	0	54.9	30.1	14.8	0.2
						P-MSN in the matrix	0	56.9	25.4	16	1.8
						Precipitates on dislocations	0	52.3	30.1	15.1	2.5
CM7 Tip3	0	1.31	1.28	0.33	0.01	MSN in the matrix	0	56	28.8	14.9	0.2
						P-MSN in the matrix	0	58.6	24.7	14.8	1.9
						Precipitates on dislocations	0	59.8	32.7	6.5	1
CM7 Tip4	0	1.28	1.3	0.28	0.014	MSN in the matrix	0	55.4	29.4	15.2	0
						P-MSN in the matrix	0	55.3	27.1	16.2	1.1
						Precipitates on dislocations	0	53.5	30	14.5	1.8
CM13 tip1	0.07	0.7	1.45	0.32	0	MSN in the matrix	2.4	42.3	34.5	20.7	0
						Cu-MSN in the matrix	7.8	42.1	32.5	17.5	0
						Precipitates on dislocations	N/A				
CM13 tip2	0.08	0.85	1.57	0.38	0	MSN in the matrix	1.9	39.3	42.7	16	0
						Cu-MSN in the matrix	4.8	44.5	34.3	16.4	0
						Precipitates on dislocations	N/A				
CM14	0.07	0.68	1.48	0.35	0.014	MSN in the matrix	6.6	36.1	48.1	9.2	0
						Cu-MSN in the matrix	16.5	37.5	38.3	7.3	0.4
						Precipitates on dislocations	N/A				

While we have focused on the effects of P and Ni on the precipitates, it is ultimately the irradiation hardening which is of primary interest. Figure 3.8a shows that yield stress ($\Delta\sigma_y$) increases with P in high, and even more so, in medium-Ni steels. It is well established that $\Delta\sigma_y$ roughly scales with the total $\sqrt{f_p}$ [11] as shown in Figure 3.8b. Here, we have included f_p obtained from ATR-2 APT data and also f_p estimates for the lower fluence IVAR irradiations based on SANS and Resistivity Seebeck Coefficient (RSC) measurements [217,218]. SANS measures the volume fraction of precipitates by analyzing the nuclear and magnetic scattering cross section curves and the RSC method relies on measuring the electrical resistivity and Seebeck coefficient changes, which depend on the amounts of Mn, Ni and Si solutes removed from solution, to determine the precipitate volume fraction [216,219]. The fitted line to the ATR-2 data has a slope that is 309 MPa/$\sqrt{f_p}$(%), which is reasonably close to widely observed results in the UCSB database, of ≈ 350±30 MPa/$\sqrt{f_p}$(%) [11]. In four of the seven IVAR cases, the lower fluence IVAR data is in good agreement with the fit line. However, two RSC and one SANS Cu-free data points are significantly lower than the fit. This is likely due to hardening by solute-defect complexes, or so-called, matrix features, which are weaker dislocation obstacles than well-developed precipitates, while they contributes to the f_p measured by RSC [218].

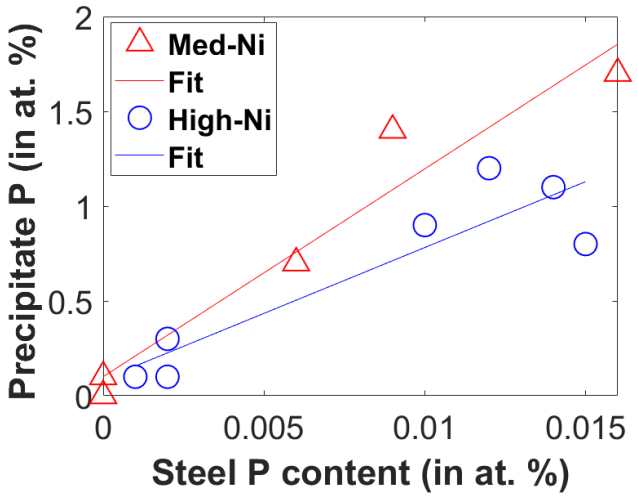

Figure 3.7: Average overall P (in at. %) in precipitates as function of APT measured P content (in at. %) in Cu-free medium and high-Ni steels (CM3-CM7).

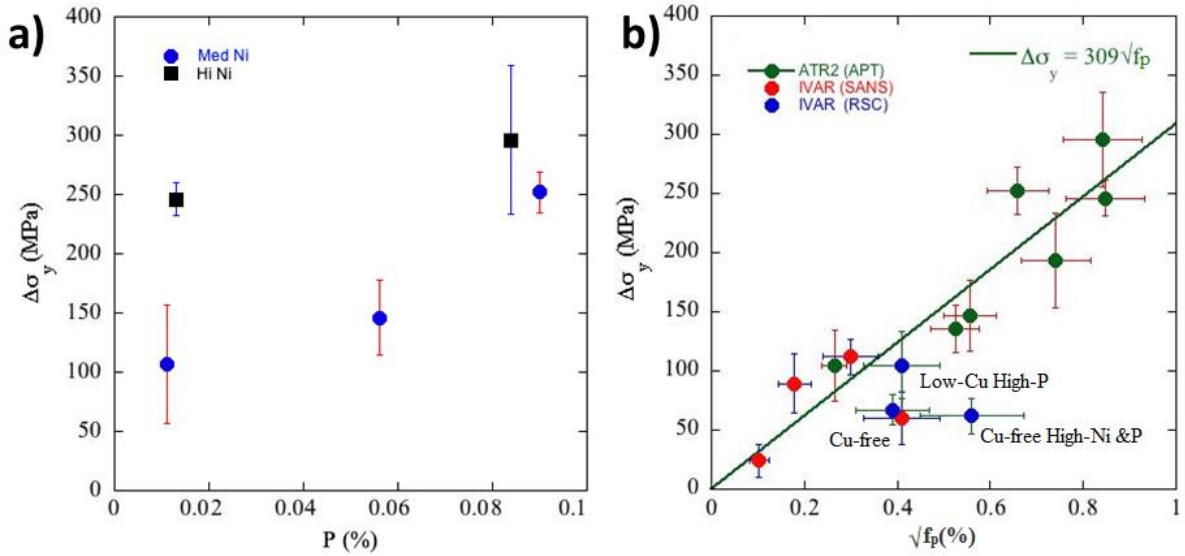

Figure 3.8: Increase in yield stress with a) P content, and b) square root of total precipitate volume fraction (f_p) in Cu-free steels.

3.4 Discussion

The APT measured Cu, Ni, and Si content in the tips exhibited small, but notable variations for a given alloy, but deviated only slightly from the nominal bulk compositions even in the case

of Mn, suggesting the absence of nearby carbides. However, the measured P was much lower than nominal bulk values likely due to the grain boundary segregation [17], and pre-pulse evaporation of this very low solubility element, analogous to the behavior of Cu [109].

MSN precipitates were observed in the matrix of all Cu-free steels (CM3-CM7), in agreement with prior studies of neutron-irradiated low-P Cu-free RPV steels [44,60,73]. In all the Cu-free, medium, and high-P steels (CM4, CM5, and CM7), P-MSN precipitates were observed in the matrix. Furthermore, a high density of precipitates also formed along dislocation lines. This is consistent with previous findings in low-Cu RPV steels [82,88]. In the low-Cu steels (CM13, CM14), both MSN precipitates and Cu-MSN precipitates were found in the matrix, again in agreement with prior studies of low-P RPV steels [10,44,82,101]. Notably, Cu-P-MSN and P-MSN precipitates were found in the matrix of high-P steel (CM14), even at a much lower fluence.

In the Cu-free steels, the number densities of P-MSN in the matrix of both medium and high-Ni steels increased with increasing P. The P enriched core and the larger average radius of the P-MSN precipitates, compared to MSN features in the matrix, suggest that they nucleated at lower doses. The P in the medium and high-P steels is near the solubility limit for the Fe_3P phase in ferrite [17]. However, alloying elements like Mo and Mn greatly lower the P solubility limit [220], promoting P precipitation, which may be further enhanced by radiation-induced segregation [10]. Thus, effective P supersaturations appear to cause early nucleation of P-rich clusters, which then act as a heterogenous nucleation site for MSN nucleation, and subsequent RED driven growth, eventually forms P-MSN precipitates [10]. The MSN precipitates in the matrix nucleate more slowly, therefore do not grow as much as the matrix P-MSN features, but at very high fluence accumulate in larger numbers, again in agreement with prior studies [44,74].

In the low-Cu steels, Cu-MSN and MSN precipitates were observed in the matrix with the average radius of Cu-MSN precipitates being significantly larger than that of the MSN precipitates. Again, these observations are consistent with prior studies [44,82,83], which hypothesized that Cu supersaturations result in early formation of Cu clusters [17,55] that then act as heterogeneous nucleation sites for MSN precipitation, eventually forming an appendage [25,35]. Therefore, Cu-MSN precipitates are larger than MSN precipitates, as observed in the low-Cu steels.

The additional observation of Cu-P-MSN and P-MSN precipitates in the matrix of high-P, low-Cu steel (C14) is unique. Separate P and Cu clusters form the Cu-P-MSN core, which is surrounded by a Mn, Ni, Si shell. The Cu-P-MSN morphology and the simultaneous presence of Cu-MSN, Cu-P-MSN, and P-MSN precipitates in CM14 suggest that both Cu and P clusters nucleate early, both providing heterogeneous nucleation sites for MSN precipitation. The larger volume fraction of Cu-MSN precipitates compared to Cu-P-MSN or P-MSN precipitates suggests that Cu is more effective than P likely due to its higher concentration.

Comparing the precipitate volume fractions of the Cu-free medium-Ni steel (CM5) to the low-Cu medium-Ni steel (CM13) suggests that a high concentration of P lead precipitation similar to low-Cu steels. The total precipitate volume fraction in CM5 is 0.44%, which is close to the corresponding ~ 0.46% in CM13. The precipitate number density is larger in the high P steel than in the low Cu steel, while their average sizes are similar. Notably, the corresponding precipitate volume fraction in the low-P (0.01 at. %) steel (CM3), of ~ 0.28%, suggests that the effect of P on precipitation is significant and is comparable to that for modest concentrations of Cu. That is, P acts much like Cu to promote MSN nucleation, at least at nominal bulk concentration of ~ 0.05 at. %. The increased volume fraction results in higher hardening, generally scaling with the $\sqrt{f_p}$.

3.5 Conclusions

We investigated the individual and synergistic effects of P, Cu, and Ni on the precipitation in neutron-irradiated RPV steels using APT. MSN, P-MSN, Cu-MSN, and Cu-P-MSN precipitates in the matrix were analyzed in seven different steels with systematic variations in Cu, Ni, and P concentrations. We reached the following conclusions:

In Cu-free steels,

- The nucleation and growth of MSN precipitates is a function of Ni as evident from an increase in number density and volume fractions with increasing Ni concentration, consistent with many previous observations [44].
- Early P clustering likely provides heterogenous nucleation sites for the formation of P-MSN precipitates with a core-shell morphology as evident from their increasing number density and volume fraction with increasing P concentration and their larger size compared to MSN precipitates.

In low-Cu steels,

- Supersaturated Cu precipitates early and provides heterogenous nucleation sites for Cu-MSN precipitates with an appendage morphology.
- In high-P steels, Cu and P nucleate early and provide heterogeneous nucleation sites, eventually forming Cu-P-MSN precipitates with multi core-shell morphology. Cu has a significantly higher impact than P due to its higher concentration.

Overall, high-P plays a role analogous to Cu in providing heterogeneous nucleation sites for MSN precipitates. The effect of P on precipitation in Cu-free medium and high-P steels is significant and is comparable to the effect of Cu in low-Cu low-P steels, thus may lead to similar

levels of embrittlement in both cases. Finally, increases in yields strength with higher P and Ni are due to corresponding increases in volume fraction of precipitates.

Chapter 4 Dose Dependence of Precipitation in RPV Steels Under Ion Irradiation

4.1 Introduction

In nuclear powered reactors, surveillance capsules containing irradiation-sensitive vessel steels are located on the inner wall of the RPV, and periodically removed and tested to monitor embrittlement [222]. However, the low dpa rates (~10^{-10} dpa/s) found in commercial reactors takes 80 years to reach the end-of-life dose of ≈ 0.2 dpa. Consequently, test reactors with higher neutron fluxes (up to ~10^{-7} dpa/s) [44,92] have been used to help develop correlations to predict end-of-life dpa of RPV steels. Despite their higher dose rates, test reactors can still take several months to years to reach the end-of-life dpa levels relevant to RPV service applications. In contrast, heavy ion irradiation, at very high dose rates (10^{-3} - 10^{-6} dpa/s), can reach the end-of-life dpa, and well beyond, in hours to days [93,94]. Therefore, ion irradiation offers a rapid alternative to study irradiation effects, including precipitation in RPV steels. However, it is important to emphasize that ion irradiations cannot be assumed to simulate neutrons but are rather more generally useful for studying mechanisms.

In this chapter, we analyzed the precipitate microstructures in eight different ion irradiated steels, with varying Cu, Ni, and Si, at two dose levels, characterized by atom probe tomography (APT). The results for four steels at the lower dpa, high dpa rate ion irradiated condition, were compared with those for lower flux neutron irradiations to observe similarities and differences. Note the ion dpa was of ≈ 0.3 dpa was 50% higher at 0.2 dpa in the neutron irradiation.

4.2 Experimental

The as-received compositions of the eight RPV steel samples obtained by optical emission spectroscopy or by electron probe microanalysis [223] are summarized in Table 4.1. Notably, 7 out of 8 of them are actual surveillance steels, while CMQ is from a widely irradiated reference RPV steel plate. These steels have also been previously characterized after neutron irradiation [223,224]. The eight steels were grouped into three categories based on their Ni contents i.e., low-Ni (< 0.3 at. %), medium-Ni (0.3-0.7 at. %), and high-Ni (> 0.7 at. %). The steels were machined into 1x2x8 mm^3 matchstick shaped specimens, which were clamped in an ≈ 9x9 array in the pocket of the high conductivity ion beam target holder. These samples were mechanically polished (down to 0.05 um colloidal silica) facing the ion beam. They were irradiated with 70 MeV Fe^{2+} ions at 290 ± 5 ^oC to the same nominal peak dose (3 dpa) at two different times and peak dose rates: $2x10^{-5}$ dpa/s and $2x10^{-6}$ dpa/sec at Center for Accelerator Mass Spectrometry (CAMS). The dpa versus depth profile was calculated for individual samples using SRIM-2013 using the Kinchin-Pease [225] mode with a displacement threshold energy of 40 eV for all elements. The position of the sample relative to the beam's Gaussian-like x-y profile was taken into consideration leading to the slight variations in the dose profiles shown in Figure 4.1.

Table 4.1**:** APT measured and as received (in parenthesis) composition (at. %) of ion irradiated CAMS RPV steel samples (balance Fe).

Steel*	**Description**	**Cu**	**Ni**	**Mn**	**Si**	**P**	**Cr**	**Mo**	**C**
SW1	Medium-Cu Low-Ni	0.14 (0.12)	0.18 (0.18)	1.04 (1.07)	0.36 (0.59)	0.01 (0.04)	0.08 (0.06)	0.21 (0.5)	0.13 (0.6)
SW2	Low-Cu Medium-Ni	0.02 (0.02)	0.62 (0.61)	1.3 (1.3)	0.62 (0.8)	0.01 (0.02)			0.08 (0.37)
SW3	Medium-Cu Medium-Ni	0.15 (0.19)	0.6 (0.57)	1.4 (1.46)	0.84 (0.99)	0.02 (0.04)	0.07 (0.1)	0.16 (0.39)	0.08 (0.37)
SP1	Medium-Cu Medium-Ni	0.07 (0.04)	0.54 (0.53)	1.08 (1.33)	0.45 (0.47)	0.01 (0.02)	0.09 (0.09)	0.20 (0.4)	0.1 (0.2)
SW4	High-Cu Medium-Ni	0.21 (0.31)	0.72 (0.74)	1.15 (1.43)	0.39 (0.4)	0.01 (0.02)	0.05 (0.04)	0.10 (0.49)	0.18 (0.83)
SW5	Low-Cu High-Ni	0.04 (0.02)	1.58 (1.49)	1.12 (1.48)	0.26 (0.73)	0.01 (0.02)			0.08 (0.37)
JRQ	Medium-Cu High-Ni	0.10 (0.12)	0.78 (0.77)	1.10 (1.41)	0.46 (0.59)	0.02 (0.04)	0.09 (0.13)	0.17 (0.5)	0.18 (0.83)
SP2	Medium-Cu High-Ni	0.16 (0.18)	0.97 (1.14)	0.99 (1.32)	0.33 (0.4)	0.02 (0.02)	0.03 (0.04)	0.17 (0.54)	0.11 (0.51)

*SW surveillance weld, SP surveillance plate, CM correlation monitor plate

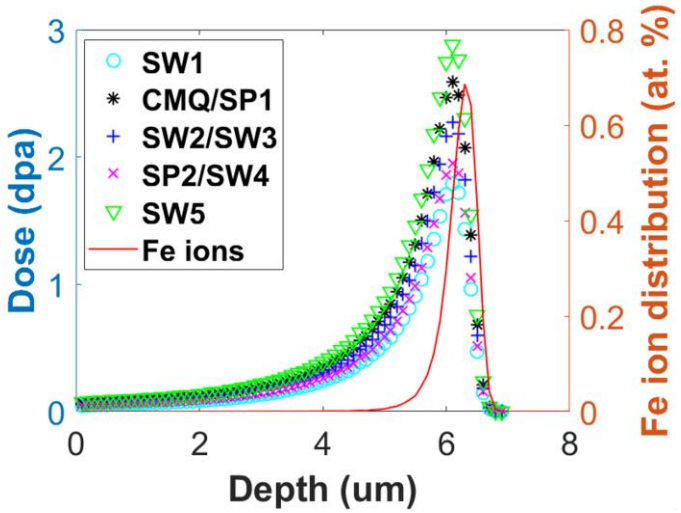

Figure 4.1: Dose (dpa) depth profiles for the analyzed steels. The variations in damage profiles among samples are attributed to their different lateral positions within the defocused ion beam, which exhibits a Gaussian-like lateral profile.

Atom probe tomography (APT) analysis was conducted at two damage depths at about 4 ± 0.3 um and 5.5 ± 0.3 um, corresponding to 0.3 ± 0.04 dpa at 2.8 x 10^{-6} dpa/s and 1.2 ± 0.1 dpa at 12 x 10^{-6} dpa/s, respectively. The lower dose and higher dose conditions will thereafter be

abbreviated as LD and HD, respectively. Furthermore, to study the effect of dose rate, ion irradiation results in SW1 (Medium-Cu low-Ni), SW2 (Low-Cu medium-Ni), SW4 (High-Cu medium-Ni), and SW5 (Low-Cu high-Ni) were compared with previous data collected and analyzed by UCSB on same alloys that had been neutron-irradiated (E > 1 MeV) at 290 ^{0}C using ≈ 5.4 x 10^{-9} dpa/s to ≈ 0.2 dpa in the Advanced Test Reactor (ATR2) [44,223,224].

APT specimens were prepared using a standard lift-out and Ga ion beam thinning process on FEI Nova 200 Nanolab dual scanning electron microscope (SEM)/focused ion beam (FIB) instruments. APT data were collected using a CAMECA LEAP 5000 XR instrument operated in laser mode using a pulse energy of 20-30 pJ, 200 kHz pulse rate, and a target detection rate of 0.5% at 40 K. APT data reconstruction was performed using IVAS 3.8.6 software. The tip radius change in the reconstructed data was based on the voltage evolution using the evaporation field of Fe. The field factor and image compression factor ranged between 3 and 3.3, and between 1.3 and 1.6, respectively. To address the overlap between the Fe^{2+} and Ni^{2+} peaks at 29 m/q, the 29 peak was assigned to Ni during the cluster identification step to obtain cluster number density, size, and volume fraction as it consist of the large fraction of Ni present [213]. Next, peak deconvolution was performed using the natural abundances of non-overlapping isotopes to obtain the bulk composition and the cluster composition in each tip.

Analysis of solute clusters in the APT datasets from the CAMS alloys was performed using the combined HDBSCAN and DeBaCl (CHD) software in MATLAB [112], choosing Cu, Mn, Ni, and Si atoms as core atoms with MinClusterSizeHDBSCAN = 35, MinSamplesHDBSCAN = 7, hdbscanProbabilityThreshold = 0.1, and hdbscanPersistencyThreshold = 0.01-0.1. MinClusterSizeHDBSCAN is the minimum number of atoms required for a cluster to be detected, while MinSamplesHDBSCAN reflects the level of stringency applied in the detection process.

hdbscanProbabilityThreshold defines a threshold probability for atoms to be considered as members of a cluster, while hdbscanPersistencyThreshold is used to distinguish actual clusters from noise clusters.

To ensure consistent cluster analysis and measured precipitate compositions across steel compositions and irradiation condition, we selected to remove Fe from the analysis based on the assumptions that its presence in the clusters is small compared to other solutes [215] and is strongly affected by APT artifacts, i.e., evaporation and trajectory aberrations [64,103,105,107], leading to unphysically high local atomic densities [44] and positioning errors that cannot currently be controlled or corrected for. Nonetheless, prior studies opted in favor of including the Fe concentration measurements as part of the cluster composition analyses [226–228]. However it is important to note that the high Fe content in the precipitates often observed in APT datasets is inconsistent with results from other experimental techniques, such as small angle neutron scattering (SANS) and STEM EDS, and thermodynamic calculations [44,80,214–216].

Analysis of solute clusters in the APT datasets from the ATR2 alloys was performed using the maximum separation method (MSM) as implemented in the IVAS 3.6.12 software. Cu, Mn, Ni, and Si were selected as core atoms used to define clusters. The order parameter was set at 5. D_{max} was obtained from nearest neighbor distributions (NND) of the core atoms by deconvoluting the clusters NND and matrix NND from the original bi-modal distribution and selecting their intersection. N_{min} was obtained from cluster size distribution at a given D_{max} by selecting the highest cluster size in a randomized dataset. The final D_{max} and N_{min} values used ranged between 0.5-0.6 nm and 15-30 atoms, respectively. To verify the cluster quantification is independent of algorithm used, four ATR2 datasets that were originally analyzed using the MSM algorithm

[44,223,224], were re-analyzed using CHD algorithm and yielded similar results with less than 10% difference.

The cluster number density (ND) was calculated using ND = $\frac{\eta C}{N V_{Fe}}$, where the detection efficiency, η, is 0.5, C is the number of detected clusters, N is the number of detected ions, and V_{Fe} is the atomic volume of Fe. The mean radius (<r>) was obtained using $< r >= \sqrt[3]{\frac{3 * N_{cluster} V_{Fe}}{4\pi\eta}}$, where $N_{cluster}$ is the number of detected atoms in a cluster. Finally, the volume fraction (f) of the clusters were calculated using f = $\frac{\sum_{all\ clusters} N_{cluster}}{C}$, which assumes that the density of the clusters and matrix are comparable. The clusters on the edge of the reconstructions were counted as half for the number density calculations. However, these edge clusters were not considered while obtaining the average size of clusters.

4.3 Results

The bulk compositions measured by APT as averages from multiple datasets are summarized in Table 4.1. The slight deviations observed in the measured and as-received composition of RPV steel samples were anticipated and are consistent with the previous observations [44]. We note that the measured C content is systematically lower than the nominal composition, consistent with carbon being largely in carbides. The higher C concentration observed for a few steels may arise for different reasons, including local concentration variations, the possible proximity of carbides to the APT analyses, and/or uncontrolled surface contamination from sample preparation. Since the measured compositions slightly varied between APT analyses, the local compositions measured within each APT dataset will be used as reference when analyzing cluster characteristics [44].

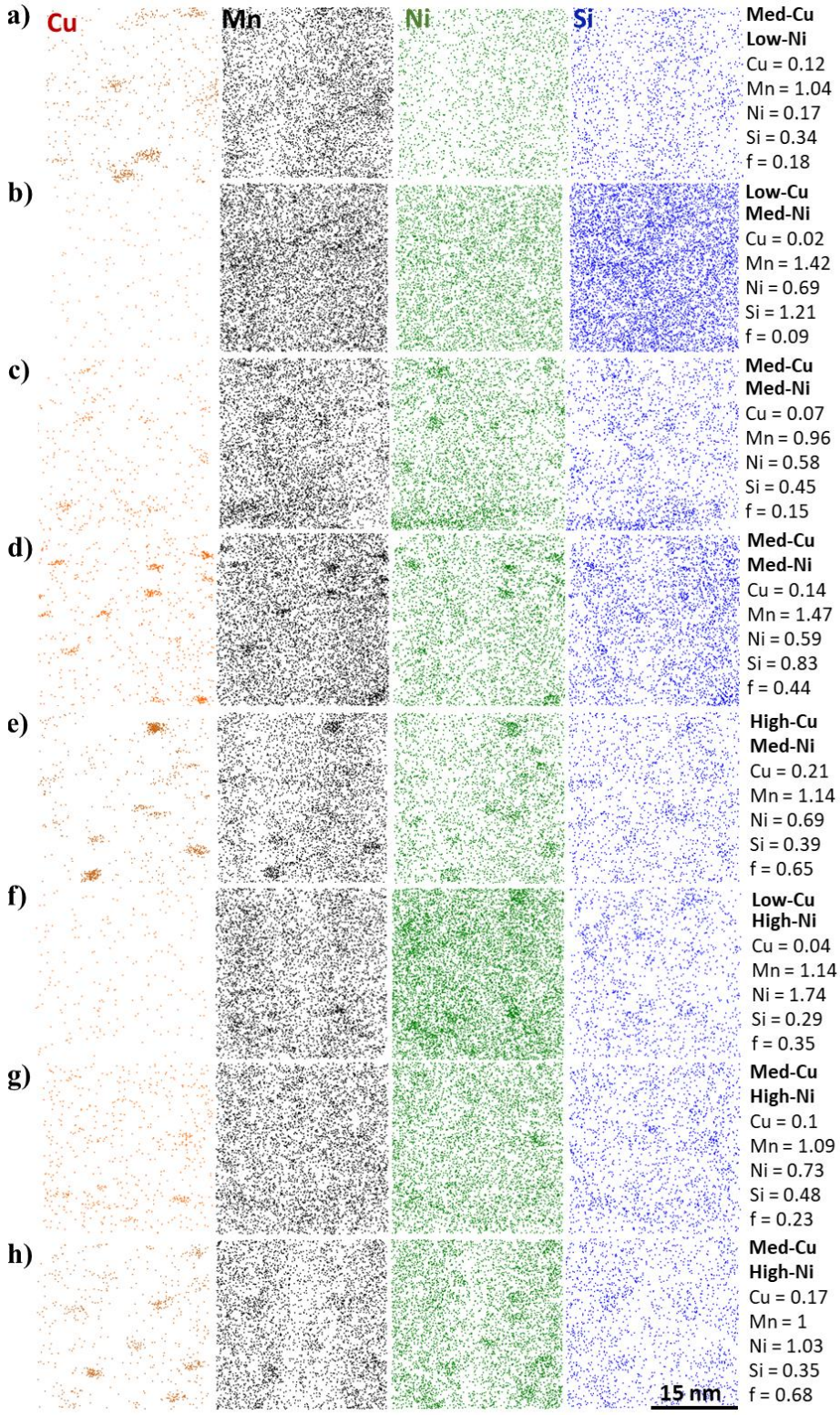

Figure 4.2: APT reconstructions 30x30x10 nm^3 showing precipitates in a) SW1, b) SW2, c) SP1, d) SW3, e) SW4, f) SW5, g) CMQ, h) SP2 at LD along with the APT measured composition (in at. %) of each steel tip and the precipitate volume fraction (f).

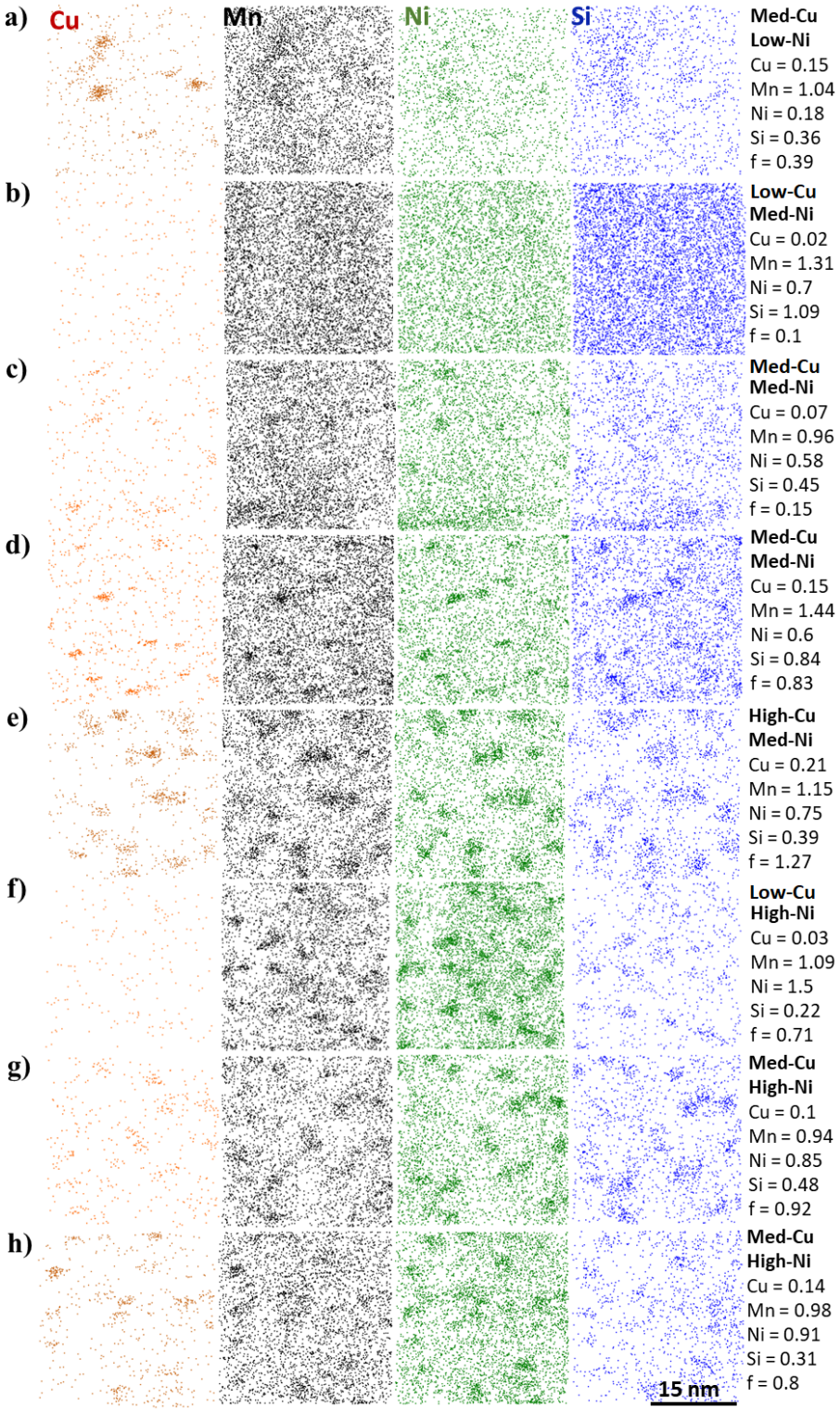

Figure 4.3: APT reconstructions 30x30x10 nm^3 showing precipitates in a) SW1, b) SW2, c) SP1, d) SW3, e) SW4, f) SW5, g) CMQ, h) SP2 at HD along with the measured composition (in at. %) of each steel tip and precipitate volume fraction (f).

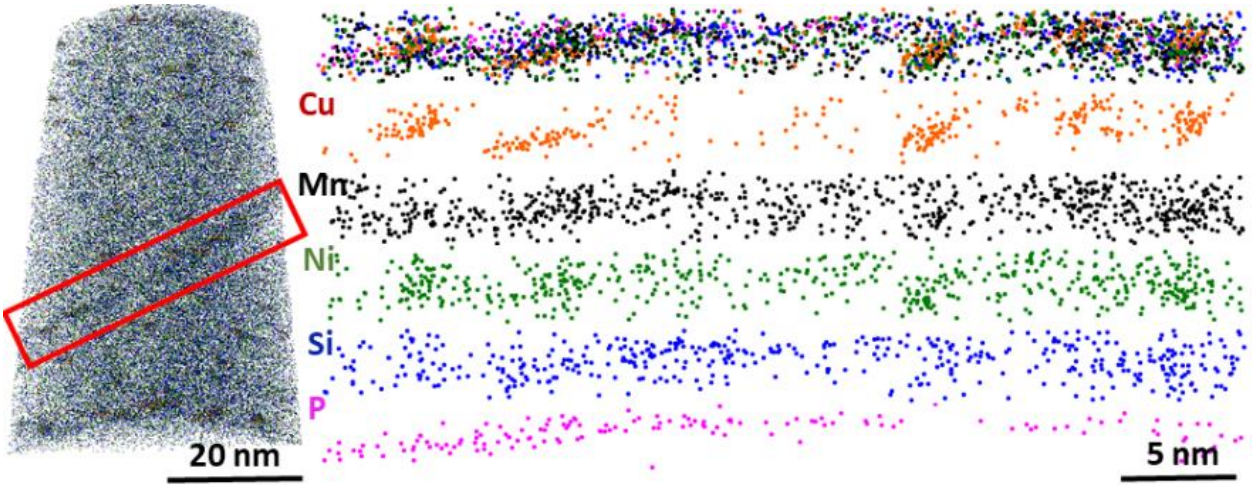

Figure 4.4: APT reconstruction and Cu, Ni, Mn, Si, and P enriched precipitates on dislocation in SW3 at LD for APT measured composition Cu-0.16, Mn-1.47, Ni-0.59, and Si-0.83 in at. %.

As shown in Figure 4.2 and 4.3, the ion-irradiated low-Cu (SW5 and SW2) steels contained Mn, Ni, and Si (MNS) matrix precipitates, which were not associated with grain boundaries or dislocations. The medium and high-Cu steels contained matrix Cu-MNS precipitates. However, as illustrated in Figure 4.4**,** some tips also contained closely spaced Cu-MNS precipitates, spaced ≈ 8 ± 4 nm apart, along segregated dislocation lines.

The precipitate number density, radius, and volume fraction at both LD and HD in all three steel categories (low, medium, and high-Ni) are summarized in Figure 4.5 and

Table 4.2. The number density and volume fraction of Cu-MNS precipitates increased with increasing Cu concentration in all cases with available data (Figure 4.5a, c, d, f). Furthermore, at a specified Cu, the precipitate number density and volume fraction also increased with increasing Ni. However, the average precipitate radius of ≈ 1±0.1 nm, did not vary significantly with Ni and Cu at either dose (Figure 4.5b, e).

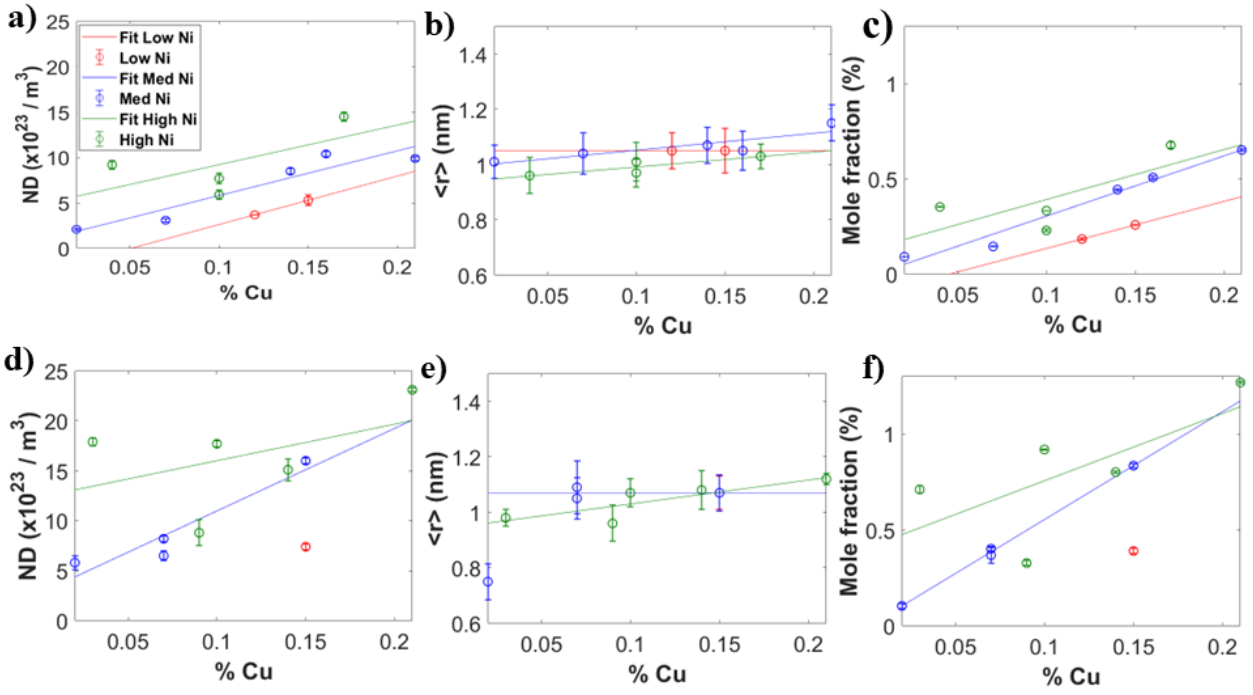

Figure 4.5: The precipitate number densities (ND), average radii (<r>), and mole fractions (f) as a function of APT measured % Cu (in at. %) at both LD (a, b, c) and HD (d, e, f).

The APT compositions of the steels and precipitates are summarized in Table 4.3. As shown by the least square fits in Figure 4.6, and as expected, the precipitate composition was systematically affected by the corresponding steel Cu, Ni, and Si contents. Figure 4.6a shows that the Cu percentage decreases between LD and HD conditions. This is due to the continued precipitation of Mn, Ni and Si after Cu has been depleted from the matrix. Note, the very high precipitate ≈ 25% Cu in Figure 4.6a is associated with the low-Ni steel SW1 and this data was not included in the fit. Figure 4.6b-d show that Ni has the strongest effect on the precipitate composition, while Si has a weaker effect and Mn has little effect. The precipitate Mn, Ni, and Si percentage (at. %) are plotted on a Gibbs triangle in Figure 4.7, along with nearby equilibrium phases. The low-Ni SW1 composition falls closer to the T8 phase, while in the medium and high-Ni samples, precipitates were closer to the Γ_2 phase.

Table 4.2: Precipitate number density, size, and volume fraction at LD and HD in all steels

			Steel Composition (at. %)						
Alloy	**Category**	**Dose**	**%Cu**	**%Mn**	**%Ni**	**%Si**	**ND (10^{23} m^{-3})**	**<r> (nm)**	**f (%)**
SW1			0.12	1.04	0.17	0.34	3.7 ± 0.1	1.1 ± 0.1	0.18 ± 0.01
SW1	Low-Ni		0.15	1.05	0.2	0.37	5.3 ± 0.2	1.1 ± 0.2	0.26 ± 0.01
SW2			0.02	1.42	0.69	1.21	2.1 ± 0.1	1 ± 0.1	0.09 ± 0.01
SP1			0.07	0.96	0.58	0.45	3.1 ± 0.2	1 ± 0.2	0.15 ± 0
SW3			0.14	1.47	0.59	0.83	8.5 ± 0.1	1.1 ± 0.1	0.44 ± 0.01
SW3			0.16	1.29	0.62	0.84	10.4 ± 0.1	1.1 ± 0.1	0.51 ± 0.01
SW4	Med-Ni		0.21	1.14	0.69	0.39	9.9 ± 0.1	1.2 ± 0.1	0.65 ± 0.01
SW5			0.04	1.14	1.74	0.29	9.2 ± 0.1	1 ± 0.1	0.35 ± 0.01
CMQ			0.1	1.09	0.73	0.48	5.9 ± 0.1	1 ± 0.1	0.23 ± 0.01
CMQ			0.1	1.09	0.8	0.45	7.7 ± 0.1	1 ± 0.1	0.33 ± 0
SP2	High-Ni	LD	0.17	1	1.03	0.35	14.5 ± 0.1	1 ± 0.1	0.68 ± 0.03
SW1	Low-Ni		0.15	1.04	0.18	0.36	7.4 ± 0.3	1.1 ± 0.1	0.39 ± 0.03
SW2			0.02	1.31	0.7	1.09	5.8 ± 0.7	0.8 ± 0.1	0.1 ± 0.03
SP1			0.07	1.01	0.44	0.47	6.5 ± 0.5	1.1 ± 0.2	0.37 ± 0.1
SP1			0.07	1.26	0.6	0.44	8.2 ± 0.3	1.1 ± 0.2	0.4 ± 0.03
SW3	Med-Ni		0.15	1.44	0.6	0.84	16 ± 0.3	1.1 ± 0.1	0.83 ± 0.02
SW5			0.03	1.07	1.62	0.23	17.9 ± 0.4	1± 0.1	0.71 ± 0.04
CMQ			0.09	1.29	0.73	0.44	8.8 ± 0.01	1 ± 0.1	0.33 ± 0.01
CMQ			0.1	0.94	0.85	0.48	17.7 ± 0.2	1.1 ± 0.1	0.92 ± 0.02
SP2			0.14	0.98	0.91	0.31	15.1 ± 0.2	1.1 ± 0.1	0.8 ± 0.05
SW4	High-Ni	HD	0.21	1.15	0.75	0.39	23.1 ± 0.3	1.1 ± 0.1	1.27 ± 0.02

Table 4.3: Solute percentage in precipitates at LD and HD in all steels

			Steel Composition (at. %)				Precipitate composition (in at. %)			
Alloy	**Category**	**Dose**	**%Cu**	**%Mn**	**%Ni**	**%Si**	**Cu**	**Mn**	**Ni**	**Si**
SW1			0.12	1.04	0.17	0.34	23 ± 4	45 ± 4	17 ± 2	15 ± 2
SW1	Low-Ni		0.15	1.05	0.2	0.37	25 ± 3	42 ± 3	18 ± 2	15 ± 2
SW2			0.02	1.42	0.69	1.21	0	37 ± 6	28 ± 5	35 ± 6
SP1			0.07	0.96	0.58	0.45	7 ± 1	37 ± 2	34 ± 2	22 ± 3
SW3			0.14	1.47	0.59	0.83	13 ± 2	37 ± 3	27 ± 1	23 ± 2
SW3			0.16	1.29	0.62	0.84	14 ± 2	34 ± 3	29 ± 1	23 ± 2
SW4	Med-Ni		0.21	1.14	0.69	0.39	20 ± 3	35 ± 2	32 ± 2	13 ± 1
SW5			0.04	1.14	1.74	0.29	0	32 ± 2	57 ± 5	10 ± 4
CMQ			0.1	1.09	0.73	0.48	8 ± 1	37 ± 3	36 ± 2	18 ± 2
CMQ			0.1	1.09	0.8	0.45	10 ± 1	34 ± 2	38 ± 2	18 ± 2
SP2	High-Ni	LD	0.17	1	1.03	0.35	13 ± 2	32 ± 2	43 ± 2	12 ± 1
SW1	Low-Ni	HD	0.15	1.04	0.18	0.36	19 ± 3	46 ± 3	19 ± 2	16 ± 2

SW2			0.02	1.31	0.7	1.09	0	39 ± 8	29 ± 7	32 ± 7
SP1			0.07	1.01	0.44	0.47	6 ± 2	38 ± 3	33 ± 3	23 ± 3
SP1			0.07	1.26	0.6	0.44	6 ± 1	43 ± 3	33 ± 2	18 ± 2
SW3	Med-Ni		0.15	1.44	0.6	0.84	10 ± 2	35 ± 2	29 ± 2	26 ± 2
SW5			0.03	1.07	1.62	0.23	0	55 ± 4	19 ± 2	11 ± 2
CMQ			0.09	1.29	0.73	0.44	7 ± 1	42 ± 3	35 ± 3	17 ± 2
CMQ			0.1	0.94	0.85	0.48	6 ± 2	31 ± 3	42 ± 2	21 ± 2
SP2			0.14	0.98	0.91	0.31	11 ± 1	32 ± 2	44 ± 2	13 ± 1
SW4	High-Ni		0.21	1.15	0.75	0.39	11 ± 1	36 ± 2	37 ± 2	15 ± 2

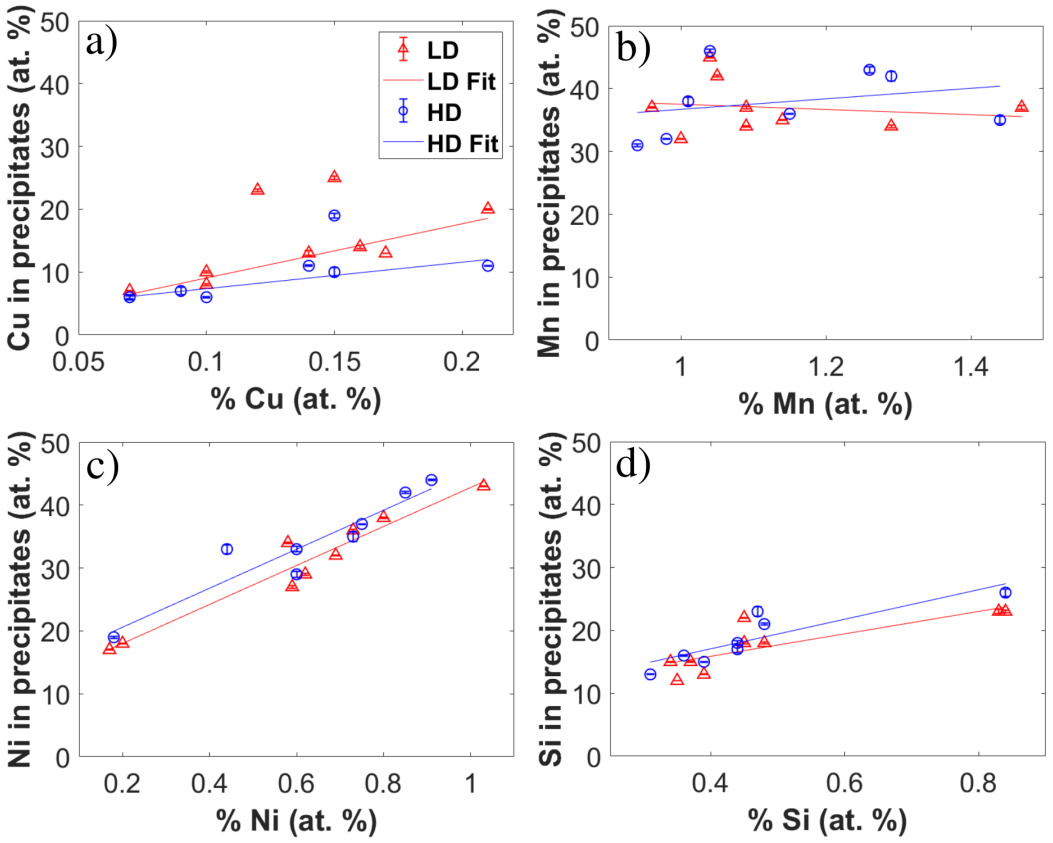

Figure 4.6: The precipitates solute percentage (at. %) as a function of the APT measured steel compositions (at. %) at both LD and HD.

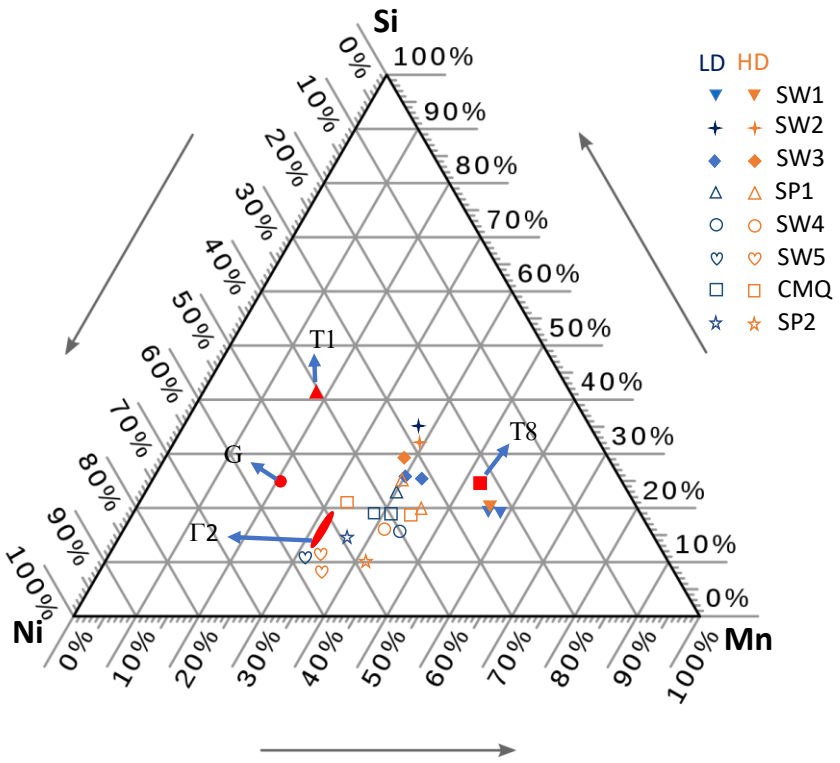

Figure 4.7: A Gibbs triangle Mn-Ni-Si projection for the FeMnNiSi system showing precipitate compositions (in at. %) for all of the steels, relative to selected equilibrium phases, at both LD and HD.

As shown in Figure 4.8 and Table 4.2**,** the precipitate number density and volume fraction increased, with increased dose from 0.3 dpa (LD) to 1.2 dpa (HD), on average by a factor of 1.8, in all three steel categories. In contrast, the average radius remained roughly constant. Due to an increase in MNS precipitation, the percentage of Cu in the precipitates slightly decreased in going from LD to HD, especially for samples with Cu > 0.1%, balanced by a corresponding increase in the Mn, Ni, and Si percentage (Figure 4.6).

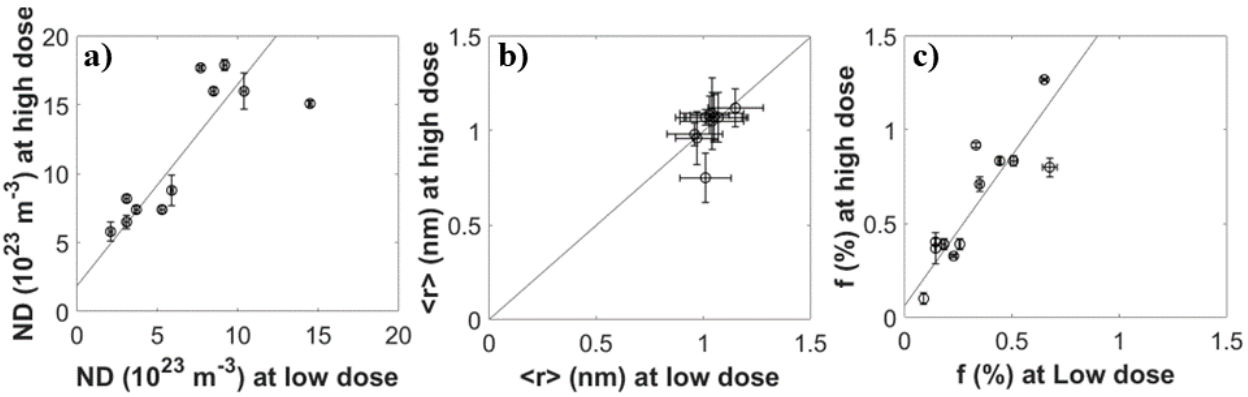

Figure 4.8: The precipitate: a) number densities (ND), average b) mean radii (<r>), and c) mole fractions (f) at LD versus HD.

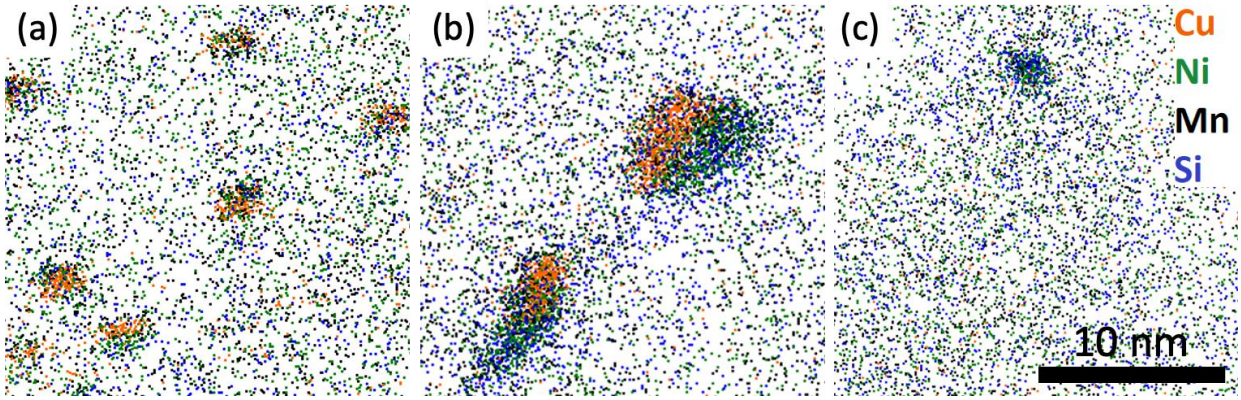

Figure 4.9: 10 nm thick slices through APT reconstructions illustrating typical differences in precipitate morphologies observed after ions (a) and neutron (b and c) irradiation of the SW4 steel.

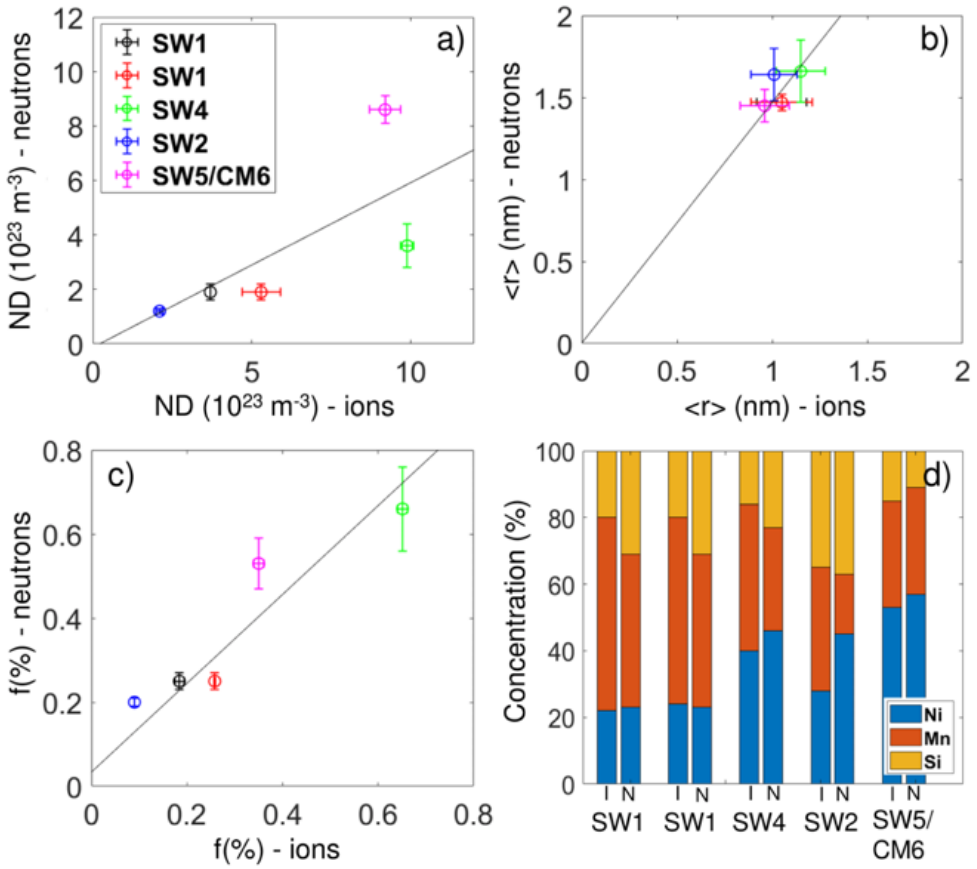

Figure 4.10: The precipitates: (a) number density (ND), (b) average radius <r>, (c) mole fraction (f), and (d) composition for ion versus neutron irradiations. Note that the precipitate compositions in the neutron case are averages of the compositions of both MSN and Cu-MSN precipitates.

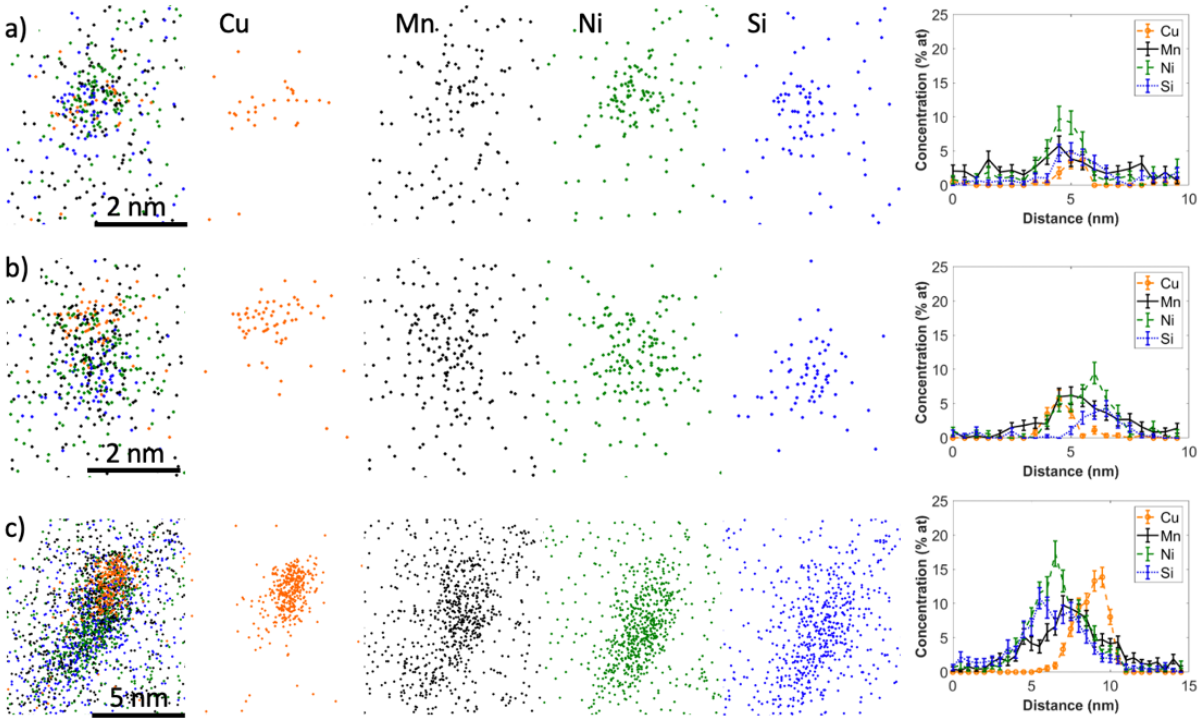

Figure 4.11: Precipitate morphologies illustrated through 4-5 nm thin slices taken from larger APT datasets and 1D concentration profiles taken parallel to the evaporation direction (also the vertical direction in the slices) a) Core shell morphology and b) appendage morphology in SW4 after LD ion irradiation; c) Appendage morphology in SW4 in the neutron irradiation condition.

To characterize the differences between ion and neutron irradiations, the LD ion irradiation results were compared with APT data previously collected from the ATR2 test reactor irradiation experiment for: SW1 (Medium-Cu, low-Ni); SW2 (Low-Cu medium-Ni); SW4 (High-Cu, medium-Ni); and two low-Cu, high-Ni steels, SW5 (CAMS) and CM6 (ATR2). While the latter are different steels than those considered presently, they have similar compositions [44]. The qualitative comparison of the microstructures is illustrated for one of the steels, i.e., SW4 in Figure 4.9 showing significantly different precipitate sizes and number densities, i.e., higher number density of smaller Cu-MNS precipitates in the ion irradiated condition compared to the neutron irradiated condition. Furthermore, the neutron irradiated steels also featured a small density of Cu free MNS precipitates (Figure 4.9c). The precipitate characteristics in both sets of steels were

quantified and are compared. The precipitate number density after ion irradiation is roughly a factor of two higher than for the neutron irradiated condition (Figure 4.10a). The corresponding average precipitate radius decreased by a factor of ≈1.5 relative to the neutron irradiation condition (Figure 4.10b). These opposing trends resulted in very similar precipitate volume fractions (Figure 4.10c). The precipitate compositions were also similar (Figure 4.10d). However, some possible differences in the precipitate morphologies were noted (Figure 4.11). In medium and high-Cu steels, ion irradiation resulted in a mixture of two morphologies: a Cu core surrounded by MNS shell (Figure 4.11a) or a slightly off-set MNS appendage attached to a Cu core (Figure 4.11b). Only the appendage morphology was observed following neutron irradiation (Figure 4.11c).

4.4 Discussion

Notably, similar precipitate microstructures are observed after ion and neutron irradiation. The microstructures of the ion-irradiated low-Cu steels consisted of matrix MNS precipitates in the low-Cu steels while Cu-MNS precipitates formed in the medium and high-Cu steels, which is globally consistent with previously reported microstructures after neutron irradiations of similar RPV steels [10,44,82,101]. The neutron-irradiated medium and high-Cu steels also contained few small Cu-free MNS precipitates in lower number density than the Cu-MNS precipitates [44,223,224], which were absent in the ion-irradiated steels. In the ion irradiated low-Cu steels, the number density and volume fraction of MSN precipitates increased with increasing Ni content at both low and high dose, as observed in prior studies of neutron-irradiated low-P low-Cu RPV steels [44,60,73]. The number density and volume fraction of Cu-MNS precipitates also increased with increasing Cu and Ni content at both low and high dose in medium and high-Cu steels, again in agreement with prior neutron studies [44,82,83].

The mechanism of formation of precipitates in RPV steels is still the object of debate, and is divided between a radiation-induced segregation mechanism [229–235] and a thermodynamically driven process. However, we believe that in these Cu, Ni, Si, Mn containing steels, precipitation under irradiation is primarily driven by the supersaturation of solutes in a thermodynamically driven process similar to that taking place under long time thermal aging conditions [44,73]. While Ni, Mn and Si are individually undersaturated, they are not jointly undersaturated with respect to formation of various intermetallic Ni-Mn-Si precipitates like G and Γ_2 phases. The formation of these, and other precipitates, in the Fe-Ni-Mn-Si system with RPV steel compositions, is predicted by Calphad [60], as well as by first principles calculations[236–243]. In addition, there is a large body of experimental evidence that supports thermodynamically driven precipitation for typical RPV steel compositions. For example, long term thermal aging results in the formation of the same type of precipitates [39,244]. Annealing experiments have demonstrated the thermal stability of NMS precipitates in low Cu steels with radii larger than the thermodynamically calculated critical radius at temperatures far above the irradiation temperature [58]. The Fe-Ni-Mn-Si system thermodynamics has been confirmed by high dpa neutron irradiations, leading to nearly fully phase separated precipitate volume fractions (f_p), which are consistent with thermodynamic solute product equilibria [61,74,205]. Further, the compositional dependence with steel composition may not be surprising and is not inconsistent with a thermodynamically driven process. Many alloys, including RPV steels [245], decompose under thermal equilibrium through the formation of metastable nanoscale solute clusters with compositions differing from the equilibrium stoichiometry. That a similar decomposition process is observed under irradiation need not be surprising. We also however do not exclude possible resolution limitation of APT that may systematically affect the compositional accuracy of these

nanoscale precipitates, as previously observed in other systems [246]. In the present case, the main contributions of irradiation are to greatly accelerate the kinetics of precipitation, as compared to thermal annealing conditions, by radiation-enhanced diffusion (RED) of solutes, which occurs due to excess concentrations of vacancies and interstitials, and at high dose rate to increase the possible impact of cascade mixing with possible consequences on precipitate compositions and number density.

The Cu-precipitates are believed to form first and act as heterogeneous nucleation sites for the MNS precipitates [247]. The precipitate number density and volume fraction also increased from low to high dose, consistent with prior studies of neutron-irradiated RPV steels [44,223]. The average radius of the Cu-MNS precipitates was constant with increasing Cu and Ni, at roughly 1±0.1 nm, which differs from prior neutron irradiation observations where precipitate sizes increased along with their number density and volume fraction [44]. The constant precipitate size with dose under ion irradiation could be a consequence of an increase in number density and/or cascade mixing. At high dose rates, the evolution of precipitates under ion-irradiation is determined by the competition between radiation-enhanced diffusion and irradiation-induced chemical mixing, which can lead to the partial dissolution of precipitates and could result in a smaller precipitate size [95,96,248].

The ion-irradiated RPV steels exhibited higher number density and lower size of precipitates compared to their neutron-irradiated counterparts. This is generally consistent with prior studies reporting a similar trend in RPV steels with increasing dose rates, under both ion and neutron irradiations [43,247,249]. The reasons for this trend likely include contributions from ballistic dissolution and reprecipitation. Most notably, however, the volume fraction and the composition of precipitates were roughly similar for both ion and neutron irradiations, though a

different mechanical response could be expected from the difference in number density and size. The similarities in observed precipitate volume fraction further supports a thermodynamically driven precipitation process. Indeed, if precipitation was governed by radiation-induced segregation, a dependence on dose rate would be expected due to the imbalance of forward and back solute fluxes, with a higher volume fraction expected after ion irradiation compared to neutron irradiation, which is not observed. It is also noted that the dose in the LD condition (≈ 0.3 dpa) is about 50% higher than that in the neutron irradiations (≈ 0.2 dpa). Thus, at the same dose of ≈ 0.2 dpa the volume fraction for neutron irradiations is estimated to be about 50% higher than for ions. This is generally consistent with prior observations requiring high dose in ion irradiations to reach the same precipitate volume fractions as in neutron irradiations, an explanation being enhanced recombination at higher dose rates and the dependence of radiation-enhanced diffusion with dose rate [92].

As expected, the precipitate compositions under ion irradiation varied with the steel composition at both low and high dose, in a way that is broadly consistent with neutron studies [44,82], showing a roughly proportional correlation with the alloy Cu, Ni and Si content. Notably, in the ion irradiated condition, differences in the precipitate Mn content were minimal, reflecting the small variation in the alloy Mn content (ranging from 0.9-1.3 at. %). We note here that the observed variations in precipitate composition with steel composition are not inconsistent with a precipitation process driven by supersaturation. Indeed, the formation of non-stoichiometric precipitates, especially at nm size scales where the composition dependent interface energy is significant, lowers the free energy of the system and nm-scale transition phases is common occurrence.

Finally, in terms of precipitate morphology, MNS appendages were observed after neutron irradiation versus a mixture of core-shell and appendage morphologies under ions. The appendage morphology was previously observed in larger precipitates, that evolved from the core-shell morphology in smaller precipitates, with increasing dose during neutron irradiation [84]. Thus, the absence of appendage morphology in all precipitates after ion irradiation is likely due to the precipitates being smaller and perhaps not as advanced in their evolution.

4.5 Conclusions

We investigated the effect of alloy composition and dose (dpa) on the characteristics of MNS and Cu-MNS precipitates formed in eight RPV steels with varying Cu, and Ni compositions that were ion irradiated to two dose levels at 290 °C. Notably, the alloys were surveillance steels with a wide range of compositions. Where possible, the low dose ion irradiated precipitate microstructures were compared to neutron irradiated microstructures of the same RPV steels, or in one case, two steels with very similar compositions, providing insights into effects of vastly different dose rates. A major difference between neutron and ion irradiations is the dose rate. The results in this study support the following key conclusions.

- Higher precipitate number densities and smaller sizes were the major differences between high dose rate ion irradiations and neutron irradiations at a much lower dose rate.
- Other precipitate characteristics are very similar in the two cases, including their volume fractions and compositions.
- Another difference is that the larger Cu-MNS precipitates in the neutron irradiated Cu bearing alloys have a MNS appendage morphology, while the smaller precipitates, formed under ion irradiations, have a mix of Cu core-MNS shell and appendage characteristics.

This is likely due to the different precipitate sizes, rather than some other effect of differing irradiation conditions.

- Despite the variation in the dose – about 50% higher in the ion-irradiated case, the differences and similarities of the precipitates with dose rate are not unexpected, since higher dose rates delay precipitation due in part to enhanced recombination.

Chapter 5 Microstructure Evolution in $Cr_{0.6}FeNiMn$ and $CrFeNiCoPd_{0.7}$ Alloys Under Ion Irradiation

5.1 Introduction

Relatively limited data on the phase stability of CrFeNi-based MPEAs is available. Atomistic simulations predicted the formation of the $L1_0$ Ni-Mn phase in $Cr_{0.6}FeNiMn$ [123] and experimentally, a Cr-rich bcc phase was observed after long term aging at 700 ^oC [124,125]. The most recent CALPHAD database includes a Ni and Mn rich $L1_0$ ordered phase below 450 ^oC and a Cr, Fe, and Mn rich sigma phase below 1000 ^oC. In a similar equiatomic CrFeNiCoMn alloy, ordered $L1_0$-NiMn, Cr-rich bcc, and ordered B2-FeCo phases were observed in the matrix and at grain boundaries after annealing between 450 and 500 ^oC [126–129], while at 700 ^oC, only the Cr-rich sigma phase was found at grain boundaries and no phase decomposition was noted upon further increasing temperature to 900 ^oC [127,129]. In equiatomic CrFeNiCoPd alloy, heat treatments at 700 ^oC and 1100 ^oC resulted in multiple FCC phases with slightly different lattice parameters [250]. However, their composition is yet to be established experimentally.

While not yet reported after thermal aging, nanoscale $L1_0$ Ni-Mn precipitates were observed after heavy ion irradiation at 500 ^oC in $Cr_{0.6}FeNiMn$ [251] along with the formation of the Cr-rich bcc phase at grain boundaries [251,252]. In equiatomic CrFeNiCoMn, electron irradiation at 400 ^oC led to the formation of $L1_0$ Ni-Mn ordered precipitates and NiFe and FeCo rich regions [190,197]. However, heavy ion irradiation of equiatomic CrFeNiCoMn [157,184,192] and CrFeNiCo [117,168] did not reveal any phase decomposition. For equiatomic CrFeNiCoPd,

the alloy decomposed into Co-Ni rich and Pd rich regions under electron irradiation at 400 ^{o}C [190], whereas, it exhibited phase stability under heavy ion irradiation [184,195]. Given the discrepancies observed during aging under thermal and irradiation conditions, additional work is needed to establish the equilibrium phases and kinetics of phase decomposition in these alloys at intermediate to high temperatures and to understand the impact of phase decomposition on the development of irradiation damage.

To address the identified knowledge gaps, the microstructures of $Cr_{0.6}FeNiMn$ and $CrFeNiCoPd_{0.7}$ alloys at 500 ^{o}C were characterized after ion irradiation. Multiple damage levels and two dose rates were used to understand the evolution of microstructure as well as the impact of cascade mixing. The mechanisms of phase decomposition under long term thermal aging of $Cr_{0.6}FeNiMn$ and $CrFeNiCoPd_{0.7}$ at 500 ^{o}C will be reported separately.

5.2 Experimental

Two alloys ($Cr_{0.6}FeNiMn$ and $CrFeNiCoPd_{0.7}$) were prepared by arc melting a mixture of pure constituent metals Cr, Fe, Ni, Co, Mn, and Pd (>99,9% purity). The cast bars were flipped and melted five times and then homogenized for 24 hrs. at 1100 ^{o}C in Argon followed by water quenching to ensure an equiaxed grain structure and a homogeneous chemistry. X-ray diffraction (XRD) was performed on both alloys to confirm a single-phase FCC solid solution. The alloy compositions measured by atom probe tomography (APT) are listed in Table 5.1.

Three irradiation experiments were performed at the Michigan Ion Beam Laboratory (MIBL). Prior to irradiation, samples were electropolished using 7 % perchloric acid in 93% methanol at -50 ^{o}C and 50 V for 10 sec to ensure a mirror finish. Two sets of $Cr_{0.6}FeNiMn$ and

$CrFeNiCoPd_{0.7}$ samples were irradiated with 6 MeV Fe^{3+} using an estimated dose rate of 10^{-4} dpa/s at 500 ^{o}C to 2 dpa and 10 dpa, respectively. A third $Cr_{0.6}FeNiMn$ sample was irradiated using an estimated dose rate of 10^{-5} dpa/s at 500 ^{o}C to 2 dpa. The irradiation times were 6, 30, and 60 hours respectively. All irradiation experiments were performed under a pressure below 10^{-7} torr using a raster-scanning beam with frequencies of 220 Hz and 2000 Hz in the x and y directions, respectively, to fully cover the sample surfaces. Ion irradiation doses were computed by SRIM-2013 using the Kinchin-Pease [225] mode with a displacement threshold energy of 40 eV [253] for all elements (Figure 5.2a). The depth of 700 nm where the nominal irradiation dose was defined was chosen for microstructural characterization to avoid the ion implantation region and possible surface effects [254].

Table 5.1: Average composition (at %) and standard error measured by APT using at least five datasets for each alloy.

Sample	**Cr**	**Fe**	**Ni**	**Mn**	**Co**	**Pd**	**C**
$Cr_{0.6}FeNiMn$	15.6 ± 0.7	28.6 ± 0.4	29.1 ± 0.4	26.3 ± 1.2	NA	NA	0.1 ± 0
$CrFeNiCoPd_{0.7}$	20.4 ± 0.5	22.0 ± 0.4	20.0 ± 0.4	NA	23 ± 1	14 ± 1	0.03 ± 0

The irradiated samples were characterized using APT and transmission electron microscopy (TEM), with electron backscatter diffraction (EBSD) employed to determine grain orientations. Specimens were prepared using a standard lift-out and Ga ion beam thinning process on FEI Helios 200 Nanolab dual scanning electron microscope (SEM)/focused ion beam (FIB) instruments. TEM and APT specimens were prepared specifically away from the grain boundaries on [001] oriented grains. The TEM lamellas, 200-250 nm in thickness, were flash electropolished using 4% perchloric acid in 96% ethanol at -50 ^{o}C and 12 V [255]. TEM specimens were

characterized using a FEI Talos and JEOL 3100 using TEM and STEM modes, including <001> on zone STEM BF imaging to obtain dislocation images [256] and phase contrast, and off-zone STEM HAADF imaging to image cavities. Cavity distribution was found to be comparable across different [001] oriented grains, therefore swelling was quantified using one liftout sample per alloy condition. For each lift out, a 1500 x 2200 nm^2 area was used to generate cavity number density, size, and swelling profiles with depth where relevant. Furthermore, EDS maps were image processed to quantify phase decomposition in $CrFeNiCoPd_{0.7}$. The Ni signal was subtracted from Pd signal, and the average filter was applied to the resulting image to enhance the contrast between the two phases and identify the interfaces. Using the interfaces, a binary image was produced, and a total of 16 vertical and horizontal 1-D line profiles were used to calculate the average phase diameter.

APT data were collected using a CAMECA LEAP 5000 XR instrument operated in laser mode using a pulse energy of 40-60 pJ, 200 kHz pulse rate, and a target detection rate of 0.5-1% at 50 K. APT data reconstruction and analysis was performed using the Cameca software package AP Suite 6. For each alloy, at least two datasets were acquired for each irradiation and thermal aging conditions. Proxigram analyses based on iso-concentration surfaces were used to quantify the composition of phases and to obtain the dislocation density, size, and chemistry. Phase compositions were calculated by averaging portions of the proxigrams where the solute concentrations were uniform. The interface width was defined as the distance over which the Ni and Mn concentration vary within the proxigrams.

5.3 Results

5.3.1 $Cr_{0.6}FeNiMn$ alloy

The non-irradiated regions showed no phase decomposition after 6 hours and 30 hours at 500 °C. TEM diffraction was consistent with a disordered FCC structure and APT exhibited a random distribution of all principal elements (Figure 5.1a, b). However, phase decomposition became evident with a longer annealing time of 60 hours (Figure 5.1c). Electron diffraction revealed superlattice spots and APT showed the formation of a high number density of nanoscale Ni-Mn rich precipitates (Figure 5.1c). A few closely spaced precipitates aligned on what appears like pre-existing dislocations (Figure B 2) were also observed.

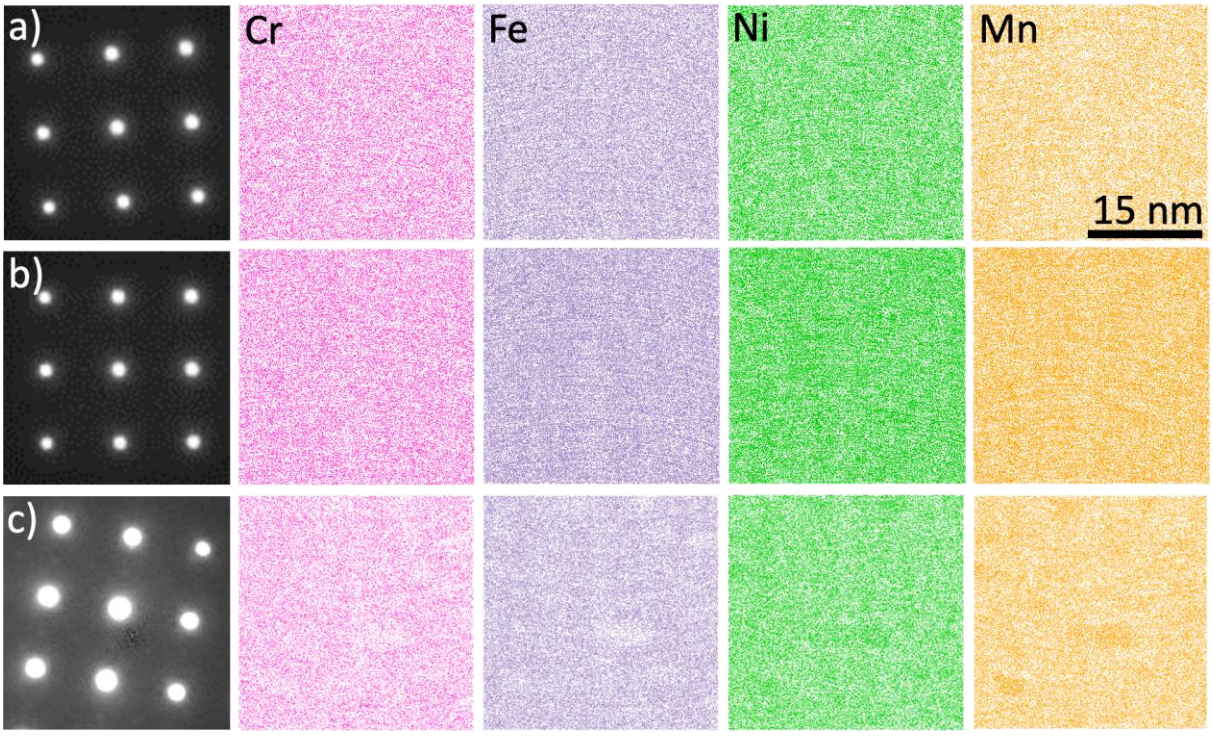

Figure 5.1: TEM diffraction patterns and 30x30x6 nm^3 APT element maps from the non-irradiated region of $Cr_{0.6}FeNiMn$ at a depth of 5-6 mm from surface showing no phase decomposition after a) 6 hrs. and b) 30 hrs. at 500 °C; Ni-Mn rich precipitates after c) 60 hrs. at 500 °C.

Using STEM imaging, the irradiated microstructures were characterized by high contrast throughout the irradiation region, which is illustrated with sample prepared after 2 dpa at 10^{-4} dpa/s (Figure 5.2a). Small features consistent with dislocation loops, with diameters ranging from 10-20 nm, were observed in the high magnification STEM BF images taken at 700 nm depth from surface (Figure 5.2b).

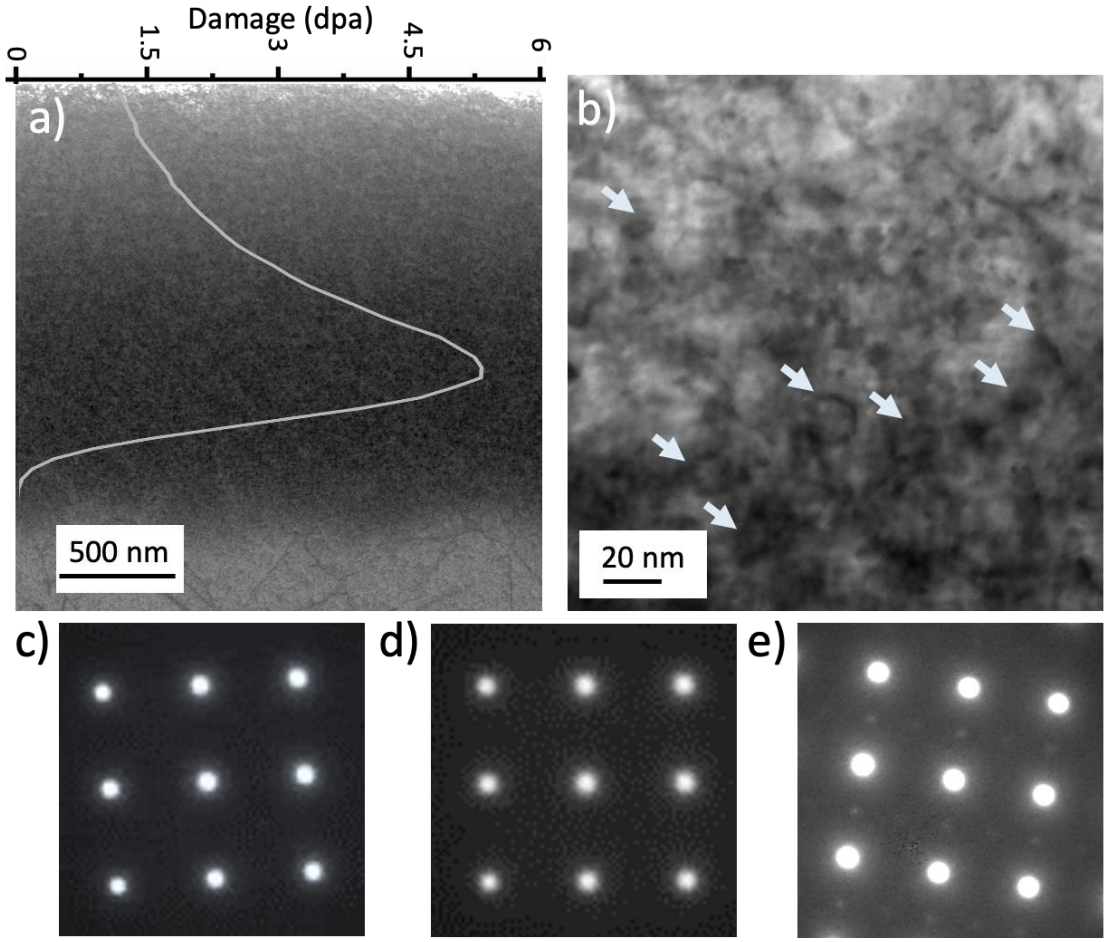

Figure 5.2: Microstructure of $Cr_{0.6}FeNiMn$ after 2 dpa at 10^{-4} dpa/s, a) Damage profile superimposed on a STEM-BF image at <001> zone axis showing a high contrast in irradiated region, pre-existing dislocations in the non-irradiated region after, b) high magnification images taken at 700 nm depth showing dislocation loops (white arrows), and c) diffraction pattern from irradiated region. Diffraction pattern from irradiated region at d) 10 dpa using 10^{-4} dpa/s and e) 2 dpa using 10^{-5} dpa/s.

While electron diffraction revealed only a disordered FCC structure after irradiation at 10^{-4} dpa/s, APT revealed phase decomposition. Specifically, a high number density of Ni-Mn rich precipitates and a small number of Cr-rich precipitates were observed (Figure 5.3). The NiMn precipitates were oblong in shape and oriented along <001> directions. The number density, size, and volume fraction of Ni-Mn and Cr precipitates are listed in Table 5.2. At the higher dose (10 dpa), a lower density of larger Ni-Mn precipitates was noted, while Cr-rich precipitates were not observed within the APT datasets, presumably due to a lower number density than at 2 dpa.

After irradiation at the lower dose rate (10^{-5} dpa/s), electron diffraction revealed superlattice spots with significantly higher intensity than in the non-irradiated region of the sample. Higher volume fractions of interconnected NiMn rich precipitates and Cr-rich precipitates were also observed by APT. Proxigram analyses revealed comparable precipitate compositions after thermal ageing and irradiation (Table 5.3). However, the width of the precipitate interface increased from 2.6 nm after thermal ageing to about 4.3 nm under 10^{-4} dpa/s and 3.5 nm under 10^{-5} dpa/s (Figure 5.4). Due to the larger volume fraction of NiMn rich precipitates after irradiation at the lower dose rate, the matrix concomitantly showed significant enrichment of Cr and Fe (Table 5.3). In addition to precipitate phases, Ni enrichment was observed in the shape of partial and complete loops (brown isosurfaces) assumed to be dislocation (Figure 5.3) and proxigram analyses revealed concomitant depletion of Cr, Fe, and Mn along the same dislocation lines (Figure B 3). Finally, the dislocation number density and average diameter, estimated using APT, were consistent with STEM observations (Table 5.4).

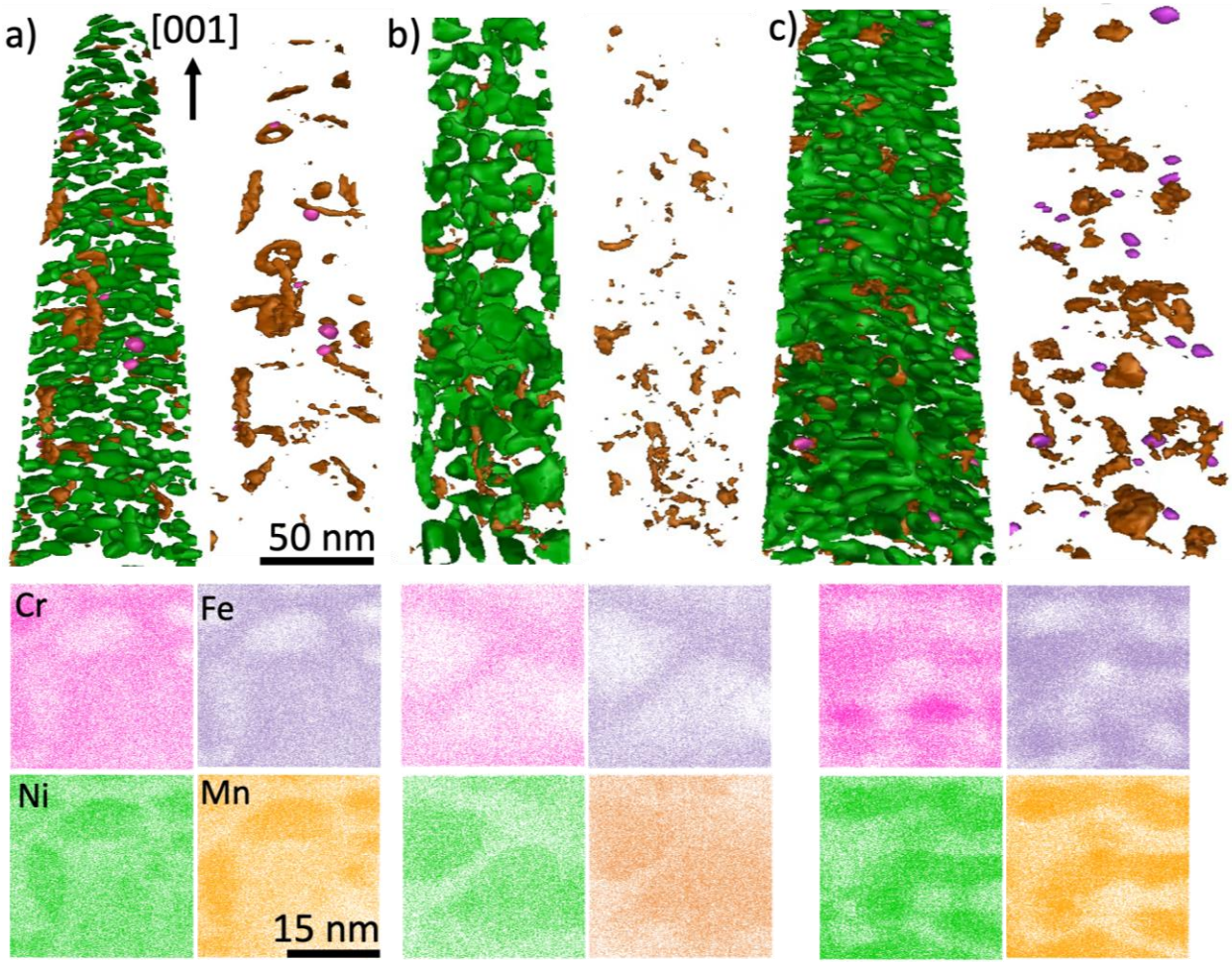

Figure 5.3: APT reconstruction and 30x30x10 nm^3 element maps from the irradiated regions of $Cr_{0.6}FeNiMn$ at a depth of 700 nm showing <001> oriented Ni-Mn rich phase (green isosurface 70 at. % Ni+Mn), Cr-rich phase (pink isosurfaces 30 at. % Cr), and Fe-Cr rich matrix and dislocation loops (brown isosurfaces 70 at. % Ni+Fe) in a) 2 dpa using 10^{-4} dpa/s, b) 10 dpa using 10^{-4} dpa/s, and c) 2 dpa using 10^{-5} dpa/s.

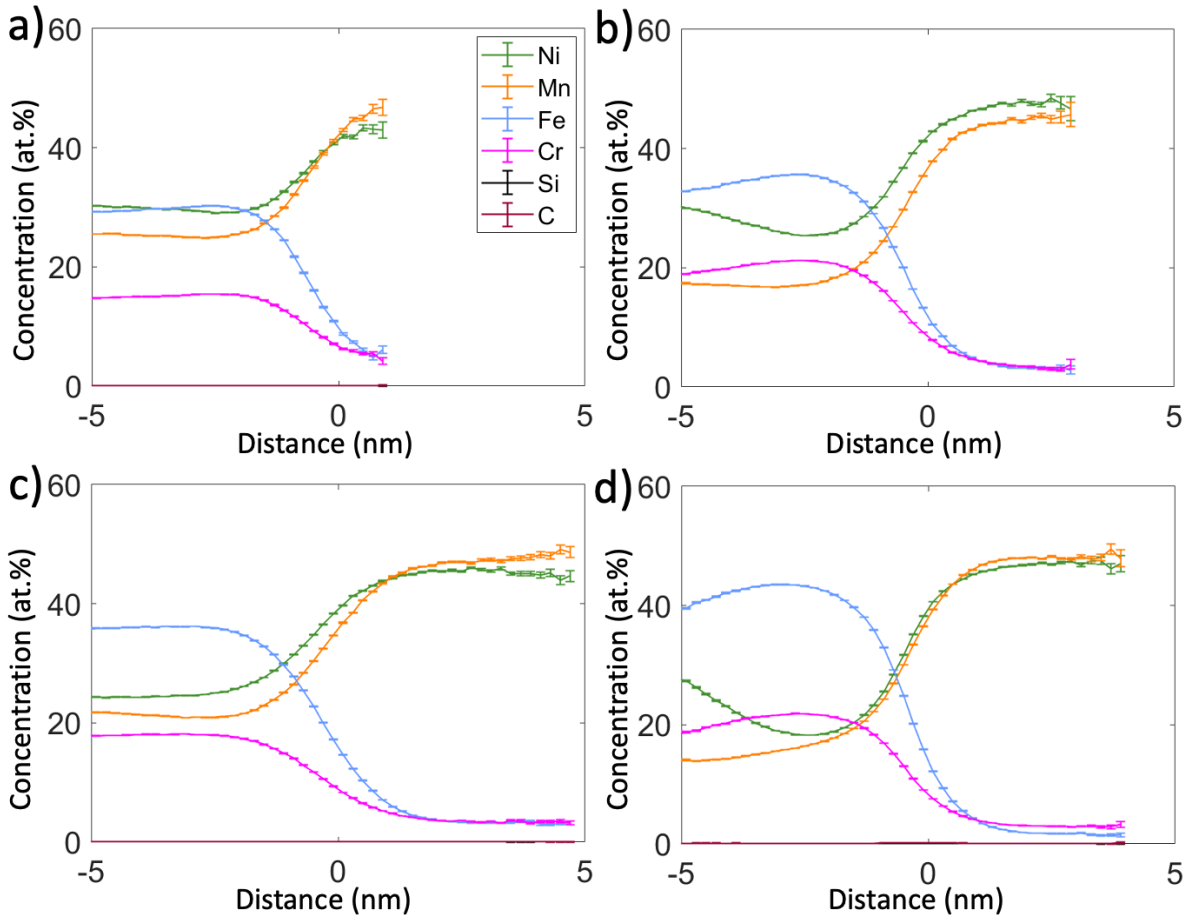

Figure 5.4: Proxigram analysis (isosurface 70 at. % Ni+Mn) showing the distribution of elements in the precipitates and the matrix in $Cr_{0.6}FeNiMn$ after a) 60 hrs. at 500^0 C, b) 2 dpa using 10^{-4} dpa/s, c) 10 dpa using 10^{-4} dpa/s, and d) 2 dpa using 10^{-5} dpa/s.

Table 5.2: The number density, size, and volume fraction of Ni-Mn rich precipitates and Cr-rich precipitates in $Cr_{0.6}FeNiMn$ after irradiation and thermal ageing. Average and standard errors were estimated using at least two datasets at each condition.

	60 hrs. at 500 °C	**2 dpa; 10^{-4} dpa/s**		**10 dpa; 10^{-4} dpa/s**		**2 dpa; 10^{-5} dpa/s**	
	Ni-Mn rich	Ni-Mn rich	Cr-rich	Ni-Mn rich	Cr-rich	Ni-Mn rich	Cr-rich
Number density (x 10^{23} m^{-3})	8.9 ± 0.7	8.2 ± 1.1	0.1 ± 0.1	3.1 ± 0.6	N/A	N/A	0.3 ± 0.1
Radius (nm)	0.5 ± 0.3	3 ± 0.4	0.6 ± 0.3	4.7 ± 0.5		4 ± 0.2	1 ± 0.2
Volume fraction (%)	0.6 ± 0	9.3 ± 1.4	0.1 ± 0.1	12.4 ± 1.7		26	0.2 ± 0.1

Table 5.3: Average compositions and associated standard errors of phases found in $Cr_{0.6}FeNiMn$. Data was averaged from at least two APT datasets per condition. The compositions of Ni-Mn precipitates and the matrix were determined using on 67-70 at. % (Ni+Mn) iso-concentration surfaces, while 35 at. % Cr iso-concentration surfaces were used for Cr-rich precipitates.

Condition	**Phase**	**Cr**	**Fe**	**Ni**	**Mn**	**C**
Annealing for 60 hours	Overall sample	14.2 ± 0.9	27.9 ± 1.3	29.6 ± 1.7	28.1 ± 1.6	0.1 ± 0
	Ni-Mn precipitates	5.4 ± 0.4	5.7 ± 0.6	43.2 ± 1.4	45.6 ± 2.1	0.1 ± 0
	matrix	15.1 ± 0.5	29.9 ± 1.2	29 ± 1	25.9 ± 1.7	0.1 ± 0
10^{-4} dpa/s 2 dpa	Overall sample	17.8 ± 1.3	28.5 ± 1.2	29.9 ± 1.6	23.1 ± 1.7	0.2 ± 0
	Cr-rich precipitates	70 ± 2.9	14.1 ± 1.6	4.4 ± 1.3	5.6 ± 1.1	5.9 ± 1.3
	Ni-Mn precipitates	4.5 ± 0.5	3.9 ± 0.9	45.7 ± 2.3	45.3 ± 2.2	0.1 ± 0
	matrix	21.5 ± 0.5	36 ± 1.8	25 ± 1.3	16.8 ± 1	0.2 ± 0
10^{-4} dpa/s 10 dpa	Overall sample	15.3 ± 0.7	29.9 ± 1.3	28.6 ± 1.6	25.9 ± 1.5	0.1 ± 0
	Ni-Mn precipitates	3.6 ± 0.4	3.3 ± 0.4	45.1 ± 1.9	47.5 ± 1.8	0.1 ± 0
	Matrix	18.8 ± 0.4	37.3 ± 1.3	22.4 ± 1	21.3 ± 0.9	0 ± 0
10^{-5} dpa/s 2 dpa	Overall sample	15.1 ± 0.6	28.2 ± 1.3	28.2 ± 1.3	28.3 ± 1.8	0.1 ± 0
	Cr-rich precipitates	70.2 ± 2	12.4 ± 0.6	3.5 ± 0.4	7.6 ± 0.2	6.3 ± 0.3
	Ni-Mn precipitates	3.2 ± 0.3	1.6 ± 0.4	45.1 ± 2.4	49.8 ± 2.2	0.1 ± 0
	Matrix	21.7 ± 0.7	42.9 ± 2.1	18.2 ± 1.6	16.9 ± 1.1	0.1 ± 0

Table 5.4: Average dislocation number density and diameter and associated standard errors in irradiated $Cr_{0.6}FeNiMn$. Data was averaged from at least two APT datasets per condition.

Parameters	**2 dpa using 10^{-4} dpa/s**	**10 dpa using 10^{-4} dpa/s**	**2 dpa using 10^{-5} dpa/s**
Number density (m^{-3})	$4.5 \pm 0.5 \times 10^{22}$	$3.2 \pm 1.1 \times 10^{22}$	$3.7 \pm 0.8 \times 10^{22}$
Diameter (nm)	21.1 ± 3	17.3 ± 2.7	18.6 ± 4

After 2 dpa at 10^{-4} dpa/s, a very low density of small cavities was observed near the surface and the damage peak (Figure 5.5), with slightly larger sizes for those forming around the damage peak, resulting in very minimal swelling of 0.005% (total 12 cavities). At 10 dpa, larger cavities uniformly distributed from the sample surface to a depth of about 800 nm were observed, yielding a total swelling of 0.25% (total 24 cavities). After 2 dpa at the lower dose rate of 10^{-5} dpa/s, a very low density of small cavities was again observed in the non-irradiated region, causing a total swelling of 0.006% (a total of 4 cavities).

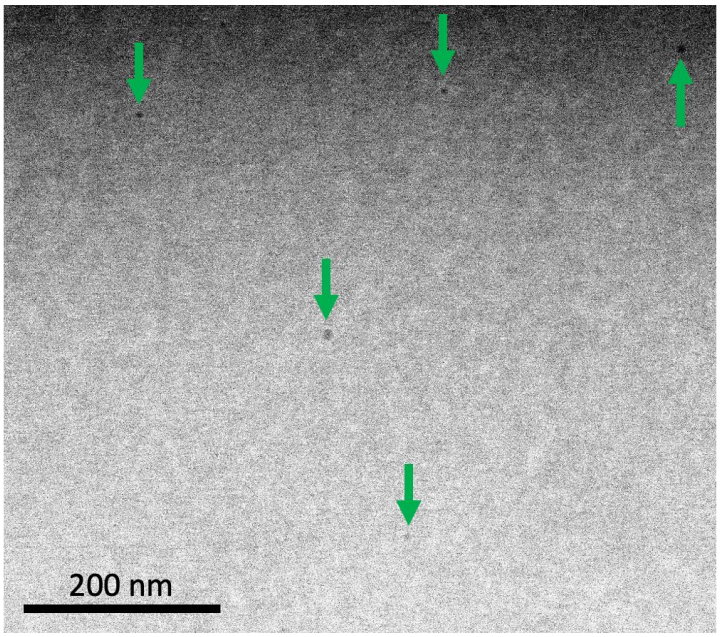

Figure 5.5: Off-zone STEM HAADF image of the distribution of cavities (green arrows) in the irradiated region of $Cr_{0.6}FeNiMn$ after 2 dpa using 10^{-4} dpa/s. The image is centered about 600 nm from the irradiated surface.

5.3.2 $CrFeNiCoPd_{0.7}$ alloy

After 6 hours and 30 hours at 500 °C, no phase decomposition was observed in the non-irradiated region. The TEM diffraction patterns were consistent with a disordered FCC structure, which is illustrated with the condition 10 dpa at 10^{-4} dpa/s (Figure 5.6), and EDS and APT exhibited a random distribution of all elements (Figure 5.7a, c and Figure B 4).

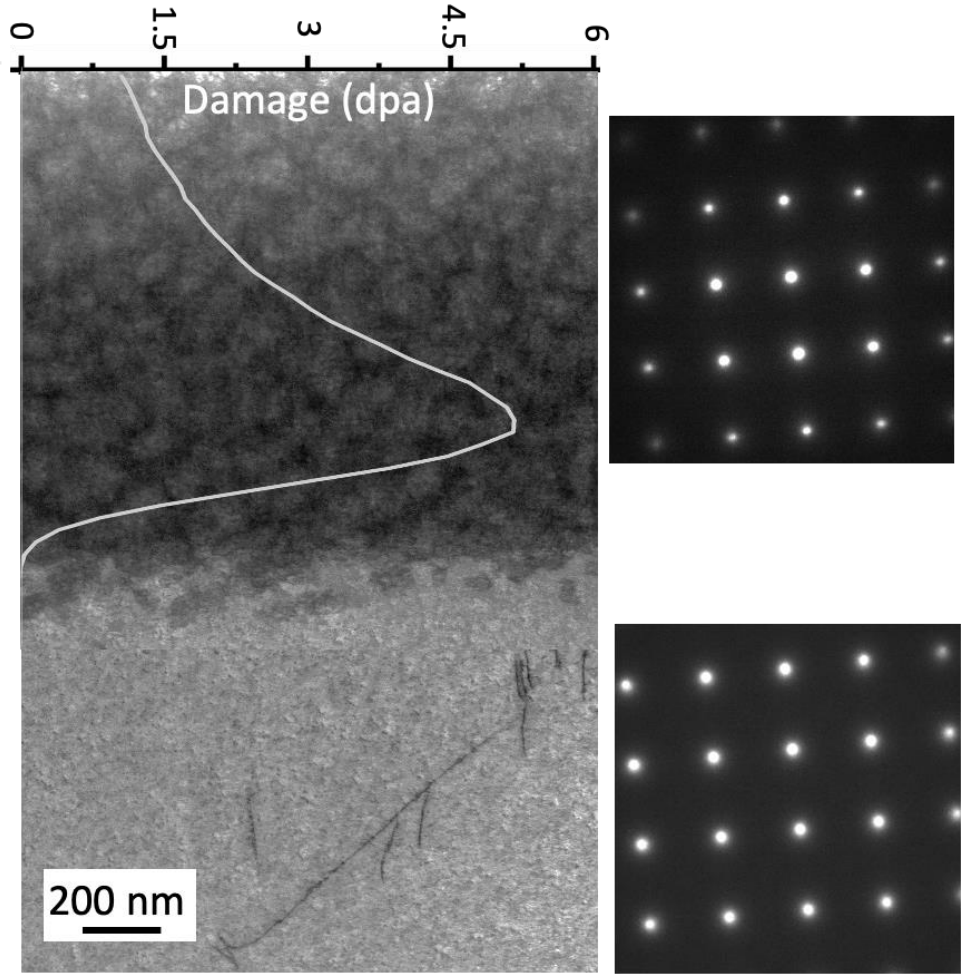

Figure 5.6: Damage profile superimposed on a STEM-BF image at <001> zone axis showing a high contrast in the irradiated region, pre-existing dislocations in the non-irradiated region, and diffraction patterns from marked locations in of $CrFeNiCoPd_{0.7}$ after 10 dpa using 10^{-4} dpa/s.

Phase separation into Co-Ni rich and Pd-Fe rich regions was observed after 2 dpa and 10 dpa at 10^{-4} dpa/s by STEM EDS and APT analyses (Figure 5.7 and Figure 5.8). While Cr did not appear to partition strongly after 2 dpa, it did so after 10 dpa leading to a separation into interconnected Co-Ni-Cr rich and Pd-Fe rich regions. The width of the Co-Ni-Cr rich and Pd-Fe rich regions increased from 49 ± 19 nm at 2 dpa to 71 ± 21 nm at 10 dpa. The reported errors reflect the standard deviation. EDS maps suggested no sharp interface separating the two regions and small compositional fluctuations within the Co-Ni rich and Pd-Fe rich regions. APT data confirmed the composition fluctuations were coming from further chemical partitioning within the Co-Ni rich and Pd-Fe rich regions (Figure 5.8). At 2 dpa, the Pd-Fe rich region was homogeneous while the Co-Ni rich region decomposed into two sub regions, one further enriched with Co and more slightly in Ni, termed high Co-Ni, and another with lower Co concentration labelled low Co-Ni. At 10 dpa, similar sub regions i.e., low Co-Ni and high Co-Ni were observed within the Co-Ni-Cr rich regions. The Pd-Fe rich region similarly decomposed into a further enriched Pd region with a slight increase in Fe concentration (high Pd-Fe) and a region with comparatively lower Pd concentration (low Pd-Fe) (Figure 5.9). The compositions of the four different regions are summarized in Table 5.5.

After irradiation, cavities were observed through the irradiation region and in the first 600-800 nm of the non-irradiated region (Figure 5.10**)**. At 2 dpa, the cavity number density was nearly uniform from 200 nm from the surface to a depth of 2200 nm. Even though the average diameter of the cavities was slightly higher near the surface, the calculated swelling was uniform through the irradiated region and the observed total swelling at 2 dpa was 0.33% (from a total of 133 analyzed cavities). At 10 dpa, the cavity number density, diameter, and swelling remained uniform through the irradiated region before eventually becoming zero beyond 1400 nm in depth. The

cavity number density decreased from 2 dpa but their size and the overall swelling increased. The observed total swelling at 10 dpa was 0.75% (from a total of 81 analyzed cavities). Finally, we note that the Z contrast in the STEM HAADF images is consistent with the chemical partitioning and length scales of the phases described above.

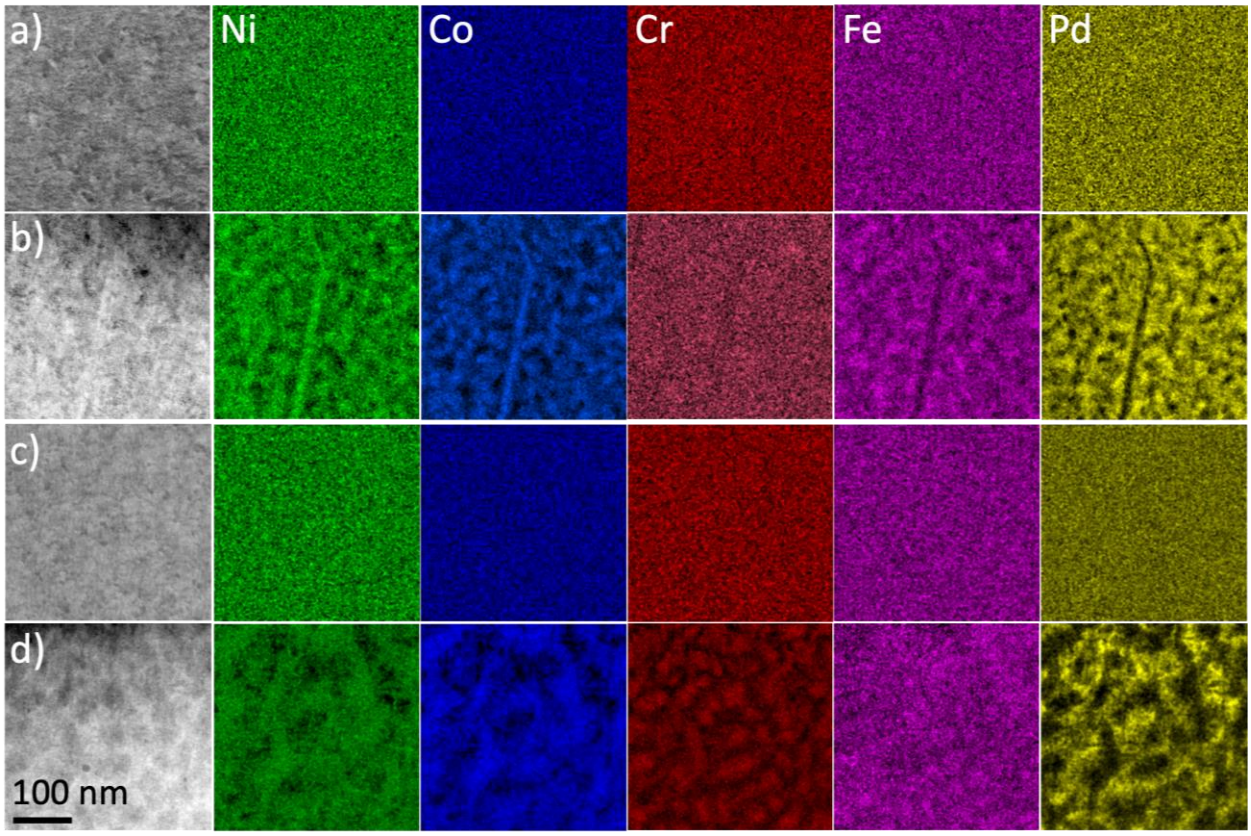

Figure 5.7: STEM-EDS maps of non-irradiated and irradiated regions in $CrFeNiCoPd_{0.7}$ after 2 dpa (a, and b) and 10 dpa (c, and d) at 10^{-4} dpa/s.

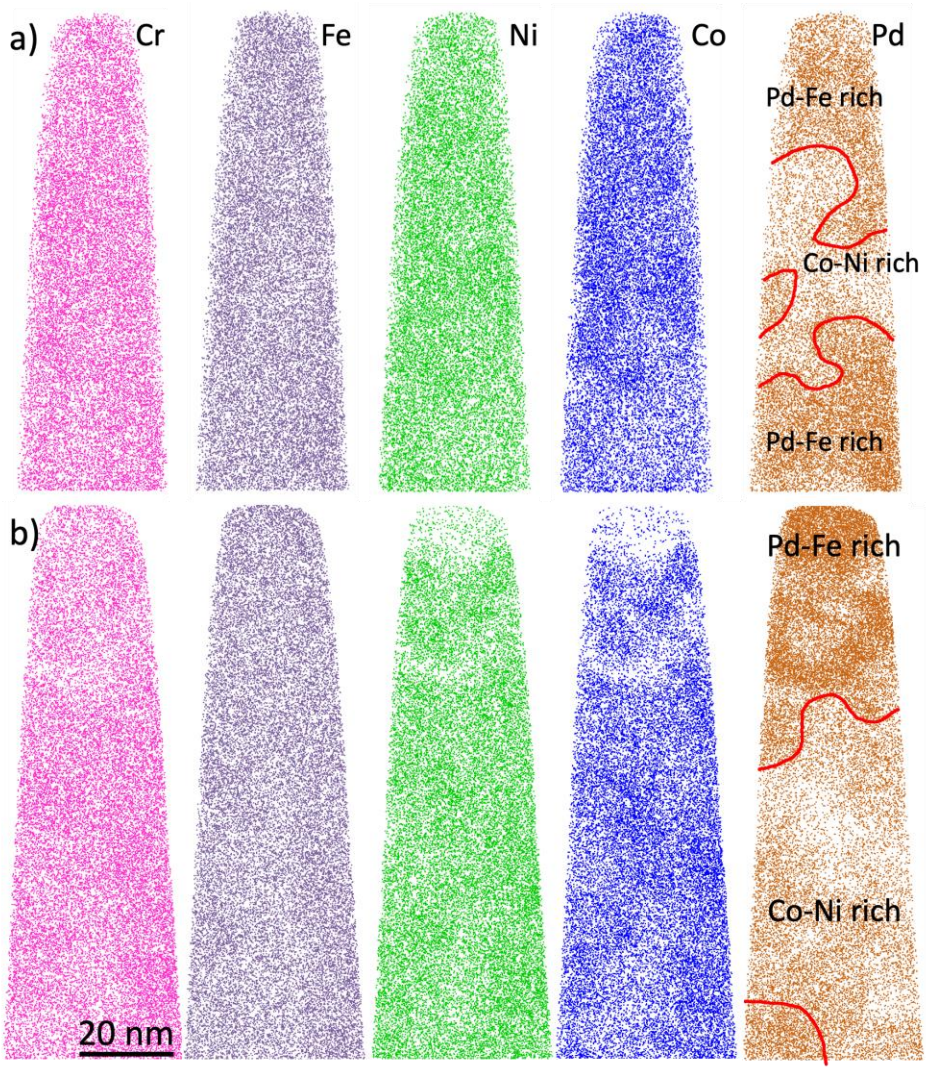

Figure 5.8: APT element maps from $CrFeNiCoPd_{0.7}$ after irradiation to a) 2 dpa and b) 10 dpa using 10^{-4} dpa/s showing phase decomposition into a Pd-Fe rich and Ni-Co rich regions. The thickness of the slices is 5 nm.

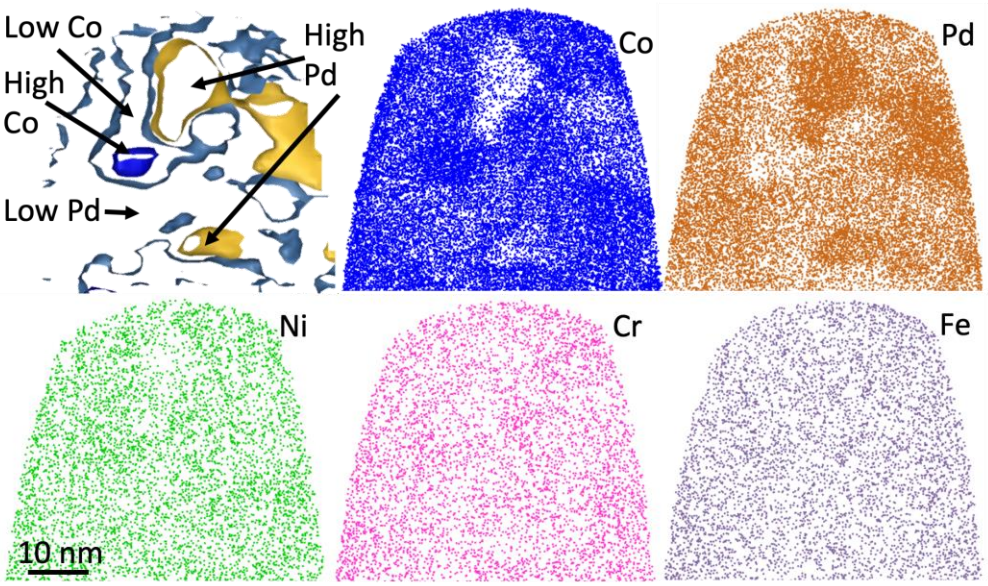

Figure 5.9**:** Iso-concentration surfaces and APT element maps in $CrFeNiCoPd_{0.7}$ after 10 dpa using 10^{-4} dpa/s. Thickness of the slice is 2 nm. The iso-concentration surfaces of 20 at. % Co (sky blue), 30 at. % Co (navy blue), and 35 at. % Pd (yellow) were used to illustrate the low Co-Ni and high Co-Ni, and the high Pd-Fe regions, respectively.

Table 5.5: Average compositions and associated standard errors of the different regions identified in $CrFeNiCoPd_{0.7}$. Data was averaged from least three APT datasets per condition. The iso-concentration surfaces of 20 at. % Co, 30 at. % Co, 20 at. % Pd, and 35 at. % Pd were used to define the low Pd-Fe, high Pd-Fe, low Co-Ni, and high Co-Ni regions, respectively.

Condition	**Phase**	**Cr**	**Fe**	**Ni**	**Co**	**Pd**
2 dpa 10^{-4} dpa/s	Overall Sample	20.8 ± 0.4	22.6 ± 0.3	19.4 ± 0.2	23 ± 1.3	13.8 ± 1.6
	Pd-Fe	19 ± 2.1	26.3 ± 0.2	14.5 ± 0.6	15.3 ± 1.3	25 ± 2
	Low Co-Ni	20.8 ± 0.5	20.3 ± 0.2	21.5 ± 0.6	28.3 ± 1	9.3 ± 1
	High Co-Ni	20.3 ±0.7	16.3 ± 0.5	22.3 ± 0.6	37.5 ± 0.8	4.5 ± 0.8
10 dpa 10^{-4} dpa/s	Overall Sample	20.1 ± 0.9	21.8 ± 0.6	20.2 ± 0.7	22 ± 1.4	15.6 ± 2.3
	Low Pd-Fe	16.7 ± 0.5	22.7 ± 0.3	18.3 ± 1.4	15.7 ± 1.5	26.3 ± 2.8
	High Pd-Fe	15.7 ± 1.9	26.3 ± 1.5	9 ± 1.4	6 ± 1.2	43 ± 1.7
	Low Co-Ni	22 ± 0.9	20.7 ± 0.3	22.3 ± 0.5	25.7 ± 0.5	9.3 ± 0.3
	High Co-Ni	19.3 ± 0.5	16.3 ± 0.7	24 ± 0.9	37 ± 0.5	3 ± 0

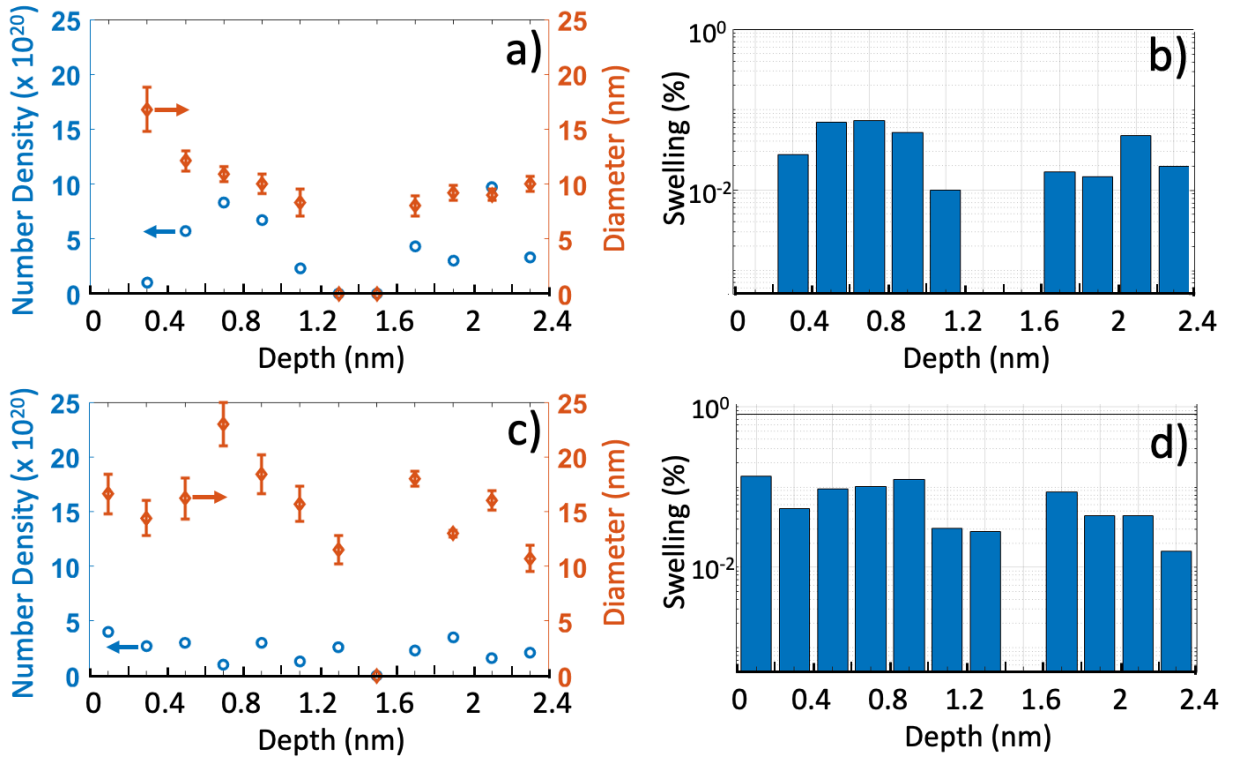

Figure 5.10: Cavity number density, size, and swelling distribution with depth in $CrFeNiCoPd_{0.7}$ after 2 dpa at 10^{-4} dpa/s (b, c) and after 10 dpa at 10^{-4} dpa/s (e, f).

5.4 Discussion

The microstructures developing in two MPEAs, $Cr_{0.6}FeNiMn$ and $CrFeNiCoPd_{0.7}$, during ion irradiation at 500 °C were characterized. The selected dose rates (10^{-4} dpa/s and 10^{-5} dpa/s) were lower than used in prior published work, providing insights into phase decomposition pathways and the development of cavities and dislocation loops.

In $Cr_{0.6}FeNiMn$ under thermal annealing at the irradiation temperature (500 °C), a high density of $L1_0$ ordered Ni-Mn rich precipitates nucleated homogeneous and heterogeneously on dislocations by 60 hrs. (per the analysis of the non-irradiated region Figure 5.1 and Figure B 2). This is the first indication that this alloy is not thermally stable at 500 °C and this observation

supports the predictions from a first principles modelling study that predicted the formation of the $L1_0$ Ni-Mn phase [123].

In comparison, analyses of the irradiated regions revealed irradiation-accelerated phase decomposition. During irradiation at 10^{-4} dpa/s, <001> oriented Ni-Mn rich precipitates nucleated more rapidly than under thermal conditions and grew and coarsened with dose as suggested by the slight increase in volume fraction, their decrease in number density and increase in size from 2 to 10 dpa. However, the precipitates remained disordered during irradiation at 10^{-4} dpa while they regained an ordered structure at the lower dose rate (10^{-5} dpa/s) where a significantly larger volume fraction of Ni-Mn precipitates with $L1_0$ ordering was also noted. We also note an increase in the volume fraction of Cr-rich precipitates after irradiation at 10^{-5} dpa/s. This behavior under irradiation is consistent with cascade mixing effects contributing to disordering, partial dissolution, and broader precipitate interfaces [251]. At the lower dose rate, the smaller contribution of cascade mixing enabled the precipitates to adopt the ordered structure, limited the broadening of their interfaces while also limiting re-dissolution and therefore enabling a larger volume fraction of precipitates to form [43,95–98,248]. The measured composition of Ni-Mn rich precipitates was comparable under thermal aging and all irradiation conditions. These findings extend prior thermal ageing studies conducted at 700 ^{o}C and above [124,125,252], which only identified a Cr-rich BCC phase in the matrix and grain boundaries. Finally, these results are also consistent with phase decomposition observed in a similar alloy equiatomic CrFeNiCoMn after thermal aging [126–129] and electron irradiation [190,197].

While $CrFeNiCoPd_{0.7}$ did not phase decompose under the thermal annealing conditions studied here, the alloy exhibited phase separation into Co-Ni rich and Pd-Fe rich regions after irradiation at 10^{-4} dpa/s. Prior electron-irradiation (1 dpa at 400 ^{o}C) [52] and thermal aging studies

(at 400-1100 ^{o}C) [250,257–260] had revealed phase decomposition into Pd and Co-Ni rich regions, both exhibiting a disordered FCC structure with slightly different lattice parameters [250]. Notably, ion irradiation led to significantly coarser microstructures than electron irradiation, possibly due to a combination of higher temperature, higher dose, and contributions of cascade mixing not present during electron irradiation. Here, phase decomposition under ion irradiation appeared to take place progressively, with the formation of regions with higher Co and Pd concentrations within the already Co-Ni rich and Pd-Fe rich regions, respectively. These findings are generally consistent with a prior neutron and x-ray diffraction study [250].

In terms of radiation damage, both alloys exhibited cavity swelling. In $Cr_{0.6}$FeNiMn, 2 dpa at both 10^{-4} and 10^{-5} dpa/s appears to be within the incubation period since a handful of cavities contributed to a very low swelling of about 0.005%. The increase in cavity swelling to 0.25 % at 10 dpa is consistent with cavity nucleation and growth regime, where sufficient vacancy flux is available to overcome the minimum number of vacancies required to cause cavity nucleation and to contribute towards the growth of existing cavities [261,262]. However, in CrFeNiCoPd$_{0.7}$, the higher swelling values and the decrease in the cavity number density concomitant with increases in the cavity size with dose are consistent with cavity growth and coalescence [262–264], where void growth is likely controlled by the diffusion of radiation-produced vacancies and void coalescence. Furthermore, swelling was also observed in the un-irradiated region, which is consistent with prior swelling studies on Ni-based MPEAs such as equiatomic NiCoFe, equiatomic CrFeNiCo, and equiatomic CrFeNCoMn [35,36,168]. The higher swelling observed in CrFeNiCoPd$_{0.7}$ as compared to $Cr_{0.6}$FeNiMn at both 2dpa and 10 dpa is likely due to their different dislocation microstructures. In $Cr_{0.6}$FeNiMn, the high number density of dislocation loops can act as defect sinks [265,266], annihilating newly produced interstitials and vacancies and preventing

vacancy supersaturation. However, in $CrFeNiCoPd_{0.7}$, no clear evidence of dislocation loops was found. We note that the swelling levels observed here in both the $Cr_{0.6}FeNiMn$ and $CrFeNiCoPd_{0.7}$ alloys were higher than those previously reported after irradiations at higher dose rates. For example, no swelling was reported in $Cr_{0.6}FeNiMn$ and equiatomic CrFeNiCoPd after ion irradiations up to 10 dpa and 38 dpa respectively at 2×10^{-3} dpa/s [184,188,193]. Higher dose rates enhance recombination leading to lower vacancy supersaturation causing a shift in the swelling bell curve to higher temperature with increasing dose rates [262].

In terms of dislocation loops, the present study found an order of magnitude higher number density and similar loop size in $Cr_{0.6}FeNiMn$ than a prior irradiation study (using Kr ions at 500 ^{o}C, 2 dpa using $>10^{-3}$ dpa/s) [193]. Despite the higher dose rate used in the prior study, which typically would lead to a lower number density and larger size of dislocation loops [267–269], the opposite trend is observed suggesting a significant role of precipitates in the evolution of dislocation loops. At early dose levels, the interfaces of the coherent $L1_0$ precipitates may act as sinks for faster-diffusing interstitials and provide nucleation sites for interstitial clusters, eventually transforming into dislocation loops. This higher density of loops may also act as sinks for the newly generated interstitials and vacancies, resulting in a steady loop number density and size [265,266]. This synergy between dislocation loops and precipitates may explain why the dislocation loop number density and size did not vary with changes in dose or dose rate in $Cr_{0.6}FeNiMn$, contrary to the general trend observed in Ni-based alloys [270,271]. The dislocations in $Cr_{0.6}FeNiMn$ exhibited elemental enrichment and depletion. The trends are generally consistent with prior studies, and may be the result of radiation-induced segregation (RIS) [52,84–86]. This RIS behavior may originate from an inverse Kirkendall mechanism, where the fastest diffusing species like Mn [273] depletes at the sink resulting in the enrichment of slower diffusing species

like Ni [272] and Co [163]. DFT calculations in Ni-X (X = Co, Ni, Fe, Mn, and Pd) binary alloys ranked the vacancy migration energy of various elements in the order Co>Ni>Fe ≈ Pd >Cr>Mn [163]. In $CrFeNiCoPd_{0.7}$, no conclusive evidence of dislocations was obtained. Although, the composition of the high Co-Ni regions was close to the chemistry of dislocations reported under electron irradiation in equiatomic CrFeNiCoPd [52], the APT data could not conclusively confirm whether these regions were formed along dislocations.

5.5 Conclusions

Phase decomposition and defect evolution were characterized in $Cr_{0.6}FeNiMn$ and $CrFeNiCoPd_{0.7}$ alloys after ion irradiations at dose rates of 10^{-4} dpa/s and 10^{-5} dpa/s. Contrary to prior ion irradiation studies performed at higher dose rates, both alloys exhibited irradiation-accelerated phase decomposition. In $Cr_{0.6}FeNiMn$, a high number density of homogeneously distributed nanometer scale $L1_0$ Ni and Mn rich precipitates along with fewer Cr rich precipitates formed in the matrix. Additionally, the high density of NiMn precipitates likely contributed towards a higher-than-expected density of dislocation loops, which further slowed cavity swelling. In $CrFeNiCoPd_{0.7}$, phase decomposition into Pd-Fe rich and Co-Ni rich regions was observed.

Chapter 6 Phase Decomposition in $Cr_{0.6}FeNiMn$ Alloy Under Thermal Aging

6.1 Introduction

In the previous chapter, ion irradiation of $Cr_{0.6}FeNiMn$ revealed phase decomposition in the form of nanoscale Ni-Mn rich, and Cr-rich precipitates. The observed phases are in agreement with previous studies. Atomistic simulations predicted the presence of $L1_0$ NiMn phase [123], and studies using CALPHAD and experimental observations after thermal aging suggested the formation of $L1_0$ NiMn and Cr-rich BCC phase [124,125]. However, the volume fraction of the Cr-rich precipitates compared to that of the Ni-Mn rich precipitates observed after irradiation is significantly lower than predicted and previously reported [125]. Under relatively high dose rate ion irradiation, cascade mixing can lead to the partial or full dissolution of expected equilibrium phases [95,96,274,275], preventing the system from reaching thermodynamic equilibrium. Therefore, the observed inconsistencies highlight the need to further understand the nature of equilibrium phases and the kinetics of phase decomposition in $Cr_{0.6}FeNiMn$ under thermal condition, i.e., without irradiation.

6.2 Experimental

6.2.1 Arc-melting and experimental preparation

$Cr_{0.6}FeNiMn$ alloy was prepared by arc melting a mixture of pure constituent metals Cr, Fe, Ni, and Mn (>99,9% purity). The cast bars were flipped and melted five times and then

homogenized for 24 hrs. at 1100 ^{o}C in argon followed by water quenching to ensure an equiaxed grain structure and a homogeneous chemistry. The samples were encapsulated in tubes and aged at 500 ℃ for 0, 40, 144, 240, 336, 504, 1008, and 1512 hrs. A thermocouple was placed close to the samples in the furnace to monitor their temperature throughout the aging process and maintained at 500 ± 3℃. After each annealing time, samples were quenched, and the microstructures were characterized using SEM and XRD. In addition, TEM characterization was performed in samples annealed for 336 hrs. and 1512 hrs., and APT characterization was performed in samples annealed for 0 hrs., 40 hrs., 144 hrs., 336 hrs., 504 hrs., and 1008 hrs.

6.2.2 Scanning Electron Microscope (SEM)

The samples were first prepared by grinding on mechanical polisher in the sequence of 320, 600, 800, and 1200 SiC papers for 3 minutes each at 100 rpm. The samples were then polished using diamond suspension of 9 um and 1 um for 3 minutes each. Finally, the samples were polished using 50 nm alumina suspension. The microstructure of polished samples was analyzed in a Thermo Fisher Scientific Helios 650 Nanolab FIB-SEM. The imaging of the sample surface was performed using the circular backscatter detector (CBS) using 5kV and a current of 0.40 nA. The images obtained at 300x magnification were used to quantify the fraction of phase decomposed areas. At least three images were used at each annealing condition for quantification. Electron backscatter diffraction (EBSD) detector in a Tescan RISE SEM was employed to study the correlation between the phase decomposed grain boundaries and their misorientation angles.

6.2.3 X-Ray Diffraction (XRD)

X-Ray Diffraction data was collected to identify the phases observed through the SEM. XRD graphs were collected using the Rigaku Miniflex 600 and were analyzed using the integrated x-ray powder diffraction software PDXL. The peaks were identified by matching known phases consisting of Cr, Fe, Ni, and Mn available in the crystallography open database (COD).

6.2.4 Transmission Electron Microscope (TEM)

TEM was used to characterize the interface between the phase decomposed region and the matrix in 336 hrs. and 1512 hrs. aged samples. Specimens were prepared using a standard lift-out and Ga ion beam thinning process on FEI Helios 200 Nanolab dual SEM/FIB instruments. TEM specimens were characterized using a FEI Talos and JEOL 3100 using TEM and STEM modes. STEM EDS was performed to visualize different phases in the phase decomposed region and their position relative to interface.

6.2.5 Atom Probe Tomography (APT)

APT was used to study the chemistry of matrix, different phases in phase decomposed regions, and their interfaces in 40 hrs., 144 hrs., 336 hrs., 504 hrs., and 1008 hrs. aged samples. APT tips were performed using a standard lift-out and Ga ion beam sharpening on FEI Helios 200 Nanolab dual SEM/FIB instruments. APT data were collected using a CAMECA LEAP 5000 XR instrument operated in laser mode using a pulse energy of 50 pJ, 200 kHz pulse rate, and a target detection rate of 0.5-1% at 50 K. APT data reconstruction and analysis was performed using the Cameca software package AP Suite 6. The tip radius change in the reconstructed data was based

on the voltage evolution using the compositionally averaged evaporation field of Cr, Fe, Ni, and Mn. The field factor (k) and image compression factor (ICF) were adjusted within the range of 3 to 3.3 and 1.3 to 1.6, respectively, to ensure that precipitates or interfaces appear linear instead of curved. At least four datasets were acquired for the listed thermal aged samples. Iso-surface analysis was used to quantify the composition of phases in the phase decomposed region and matrix. The precipitates within the matrix were identified using 70 at. % (Ni+Mn) isosurfaces, and their number density was calculated by dividing the total number of detected precipitates by the volume of the reconstruction. The volume of reconstruction (V) is given by the following equation:

$$V = \frac{(No.of\ atoms)*(0.16*V_{Cr}+0.29*V_{Fe}+0.26*V_{Ni}+0.29*V_{Mn})}{Detection\ efficiency*Packing\ fraction\ of\ FCC},$$

where V_{Cr}, V_{Fe}, V_{Ni}, and V_{Mn} represent the atomic volume of respective elements.

The mean radius of the precipitates was estimated assuming a spherical shape based on the volume of the isosurfaces. Finally, the volume fraction of precipitates was calculated by dividing the total number of atoms within the precipitates by the total number of atoms within the reconstruction. Heatmaps of thin slices at the interface between phase decomposed region and matrix were used to speculate the mechanism of phase decomposition. The bulk composition of samples was calculated using APT and summarized in Table 6.1 for different annealing conditions. Finally, to address the peak overlap in the mass spectrum between the Cr^{2+} and Fe^{2+} peaks at 27 m/q, Fe^{2+} and Ni^{2+} peaks at 29 m/q, Cr^{+} and Fe^{+} peaks at 53.9 m/q, and Fe^{+} and Ni^{+} peaks at 57.9 m/q, deconvolution was performed using the in-build function in AP Suite 6, which utilizes natural abundances of non-overlapping isotopes for composition analysis. The change in composition was less than 0.5 at. % for all elements after deconvolution.

Table 6.1: Average composition (at %) and standard deviation measured by APT using fourteen datasets from all aging conditions.

Sample	**Cr**	**Fe**	**Ni**	**Mn**	**C**
$Cr_{0.6}FeNiMn$	15.4 ± 0.5	29.3 ± 1.1	25.9 ± 2.3	29.2 ± 1	0.02 ± 0.01

6.3 Results

SEM observations of the samples after increasingly long aging times showed phase decomposition into three distinct phases (Figure 6.1). Following homogenization, a uniform microstructure with large equiaxed grains was first observed. The matrix and grain boundaries showed no signs of phase decomposition, although some porosity and Cr_2O_3 inclusions were present from the arc melting process, which were deemed insignificant for subsequent microstructure evolution. After 40 hours, phase decomposition appeared at several grain boundaries, which increased as time progressed. At 144 hrs., the phase decomposition became evident at several grain boundaries. After 240 hrs., the fraction of decomposed regions increased significantly, and most grain boundaries exhibited phase decomposition. At 336 and 504 hrs., the fraction of phase-decomposed regions increased substantially, expanding into the grain interiors. After 1008 hrs., only a small fraction of matrix remained, and after 1512 hrs., the sample was completely phase decomposed. Although only shown here for 1512 hrs., the higher magnification images revealed three types of contrast consistent in all samples.

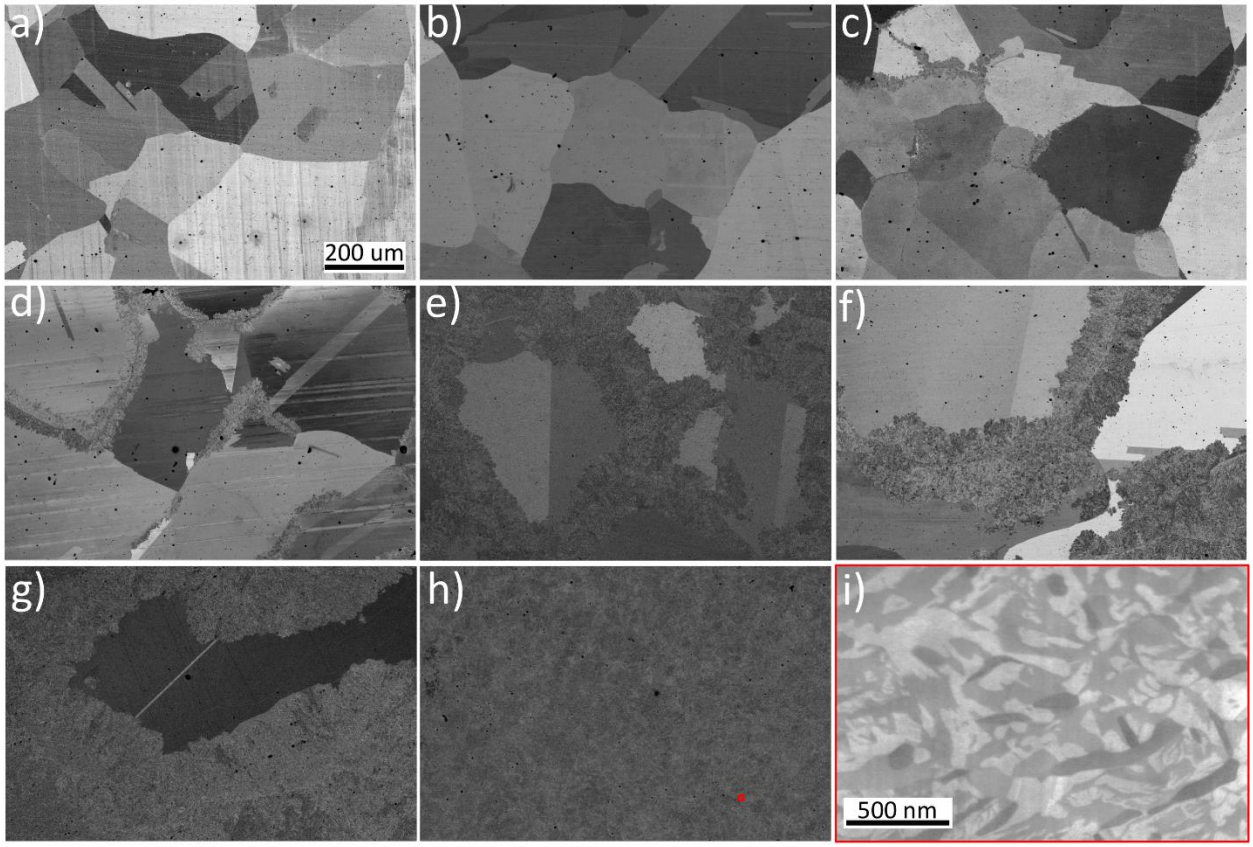

Figure 6.1: SEM images showing evolution of phase decomposition at 500 °C after a) 0 hr., b) 40 hrs., c) 144 hrs., d) 240 hrs., e) 336 hrs., f) 504 hrs., g) 1008 hrs., h) 1512 hrs., and i) higher magnification cross-section image taken from region marked in red in 1512 hrs. sample.

The evolution of the fraction of the phase-decomposed region was estimated by analyzing the collected SEM images and is shown in Figure 6.2. The kinetics of phase decomposition were modeled using the Johnson-Mehl-Avrami-Kolmogorov (JMAK) equation 6.1:

$$y = 1 - exp^{-Kt^n} \tag{6.1}$$

where y = fraction of phase decomposed region, K = rate constant, and n = Avrami constant. The fitting equation revealed a rate constant of 1.5 x 10^{-6} and Avrami constant of 2.03.

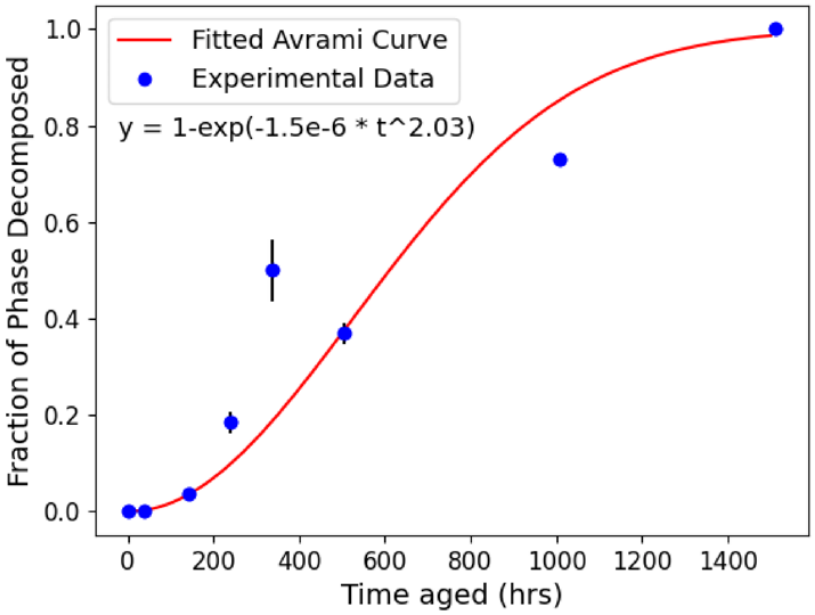

Figure 6.2: Area fraction of the phase-decomposed region with annealing time in all samples. The fitting was generated using JMAK equation. Error bars represent standard error calculated from three SEM images taken from different parts of a given sample.

EBSD analysis after 40 hrs. revealed the initiation of phase decomposition only at HAGB (with misorientation > 15^0), while low-angle grain boundaries (LAGB) and $\sum 3$ twin-boundaries showed no signs of phase decompositions (Figure 6.3). The boundaries that phase decomposed were characterized by a darker contrast. After 2 weeks, when roughly half of the sample has phase decomposed, the remaining untransformed grain boundaries were found to be either LAGB or $\sum 3$ twin-boundaries.

Phase decomposition was confirmed by XRD, and analysis revealed three distinct phases (Figure 6.4). After homogenization, the observed XRD peaks were consistent with a single FCC solid solution. The exclusive FCC crystal structure was maintained until 240 hrs. of aging. Additional peaks appeared with further increase in aging time. From 336 hrs. to 1512 hrs., a BCC phase and a tetragonal phase were noted in addition to the FCC phase. The BCC and tetragonal peak intensity increased with aging time. The tetragonal peak matched with the $L1_0$ NiMn phase.

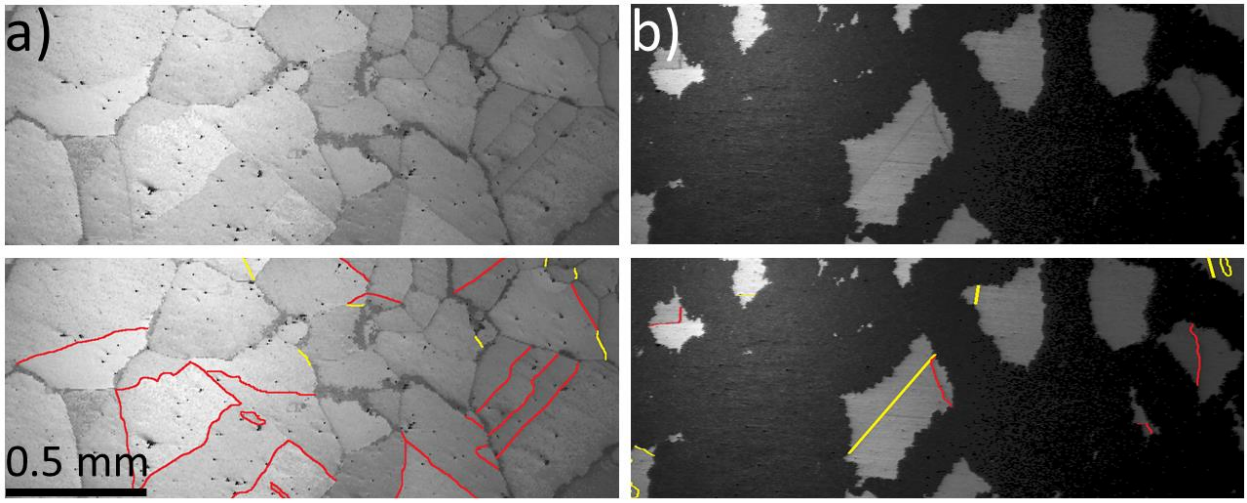

Figure 6.3: EBSD showing the initiation of phase decomposition at HAGBs with darker contrast, while no phase decomposition at LAGBs (yellow) or $\sum 3$ twin-boundaries (red) after a) 40 hrs., and b) 336 hrs.

STEM and EDS analyses were conducted at the reaction front, which is the interface between the phase decomposed region and the matrix in the 336 hrs. sample, as shown in Figure 6.5. In the untransformed region, the EDS maps indicated a uniform distribution of Cr, Fe, Ni, and Mn. No preferential segregation or depletion of elements was observed in the matrix region adjacent to the reaction front. In the phase decomposed region, three distinct phases that were Cr-rich, Fe-rich, and NiMn-rich respectively with a plate-like morphology were confirmed. The Cr-rich phase also contained some Fe, while the NiMn-rich phase consisted only of Ni and Mn. The Fe-rich phase contained some amount of Cr, Ni, and Mn. The interface between the Cr-rich phase and the other phases appeared to be sharp and smooth, whereas the interface between the NiMn-rich phase and Fe-rich phase looked ragged. Fe-rich needles or plates (highlighted in Figure 6.5 by the white arrows) appeared to penetrate the NiMn-rich phase along directions away from the reaction front.

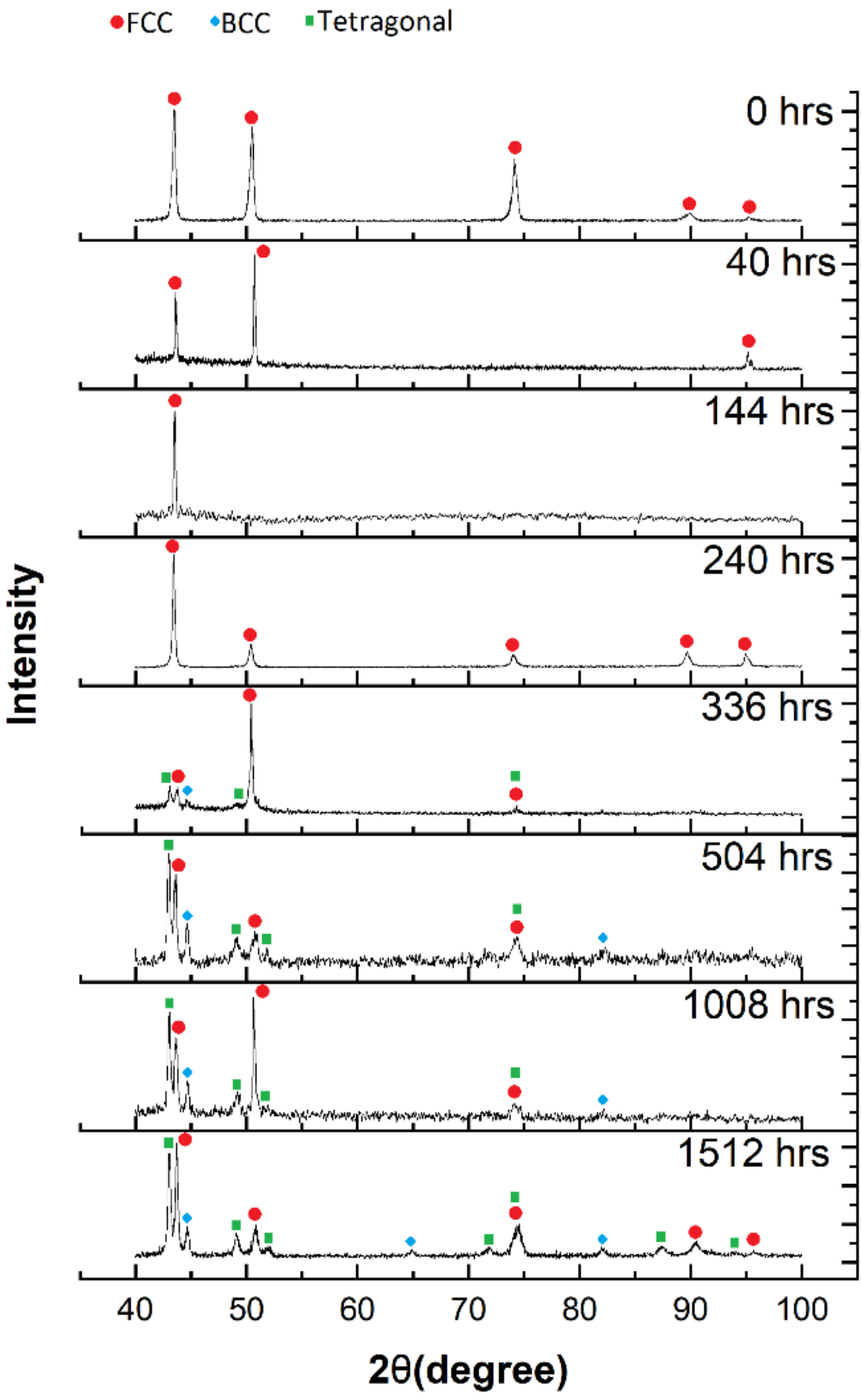

Figure 6.4: XRD peaks evolution with aging time

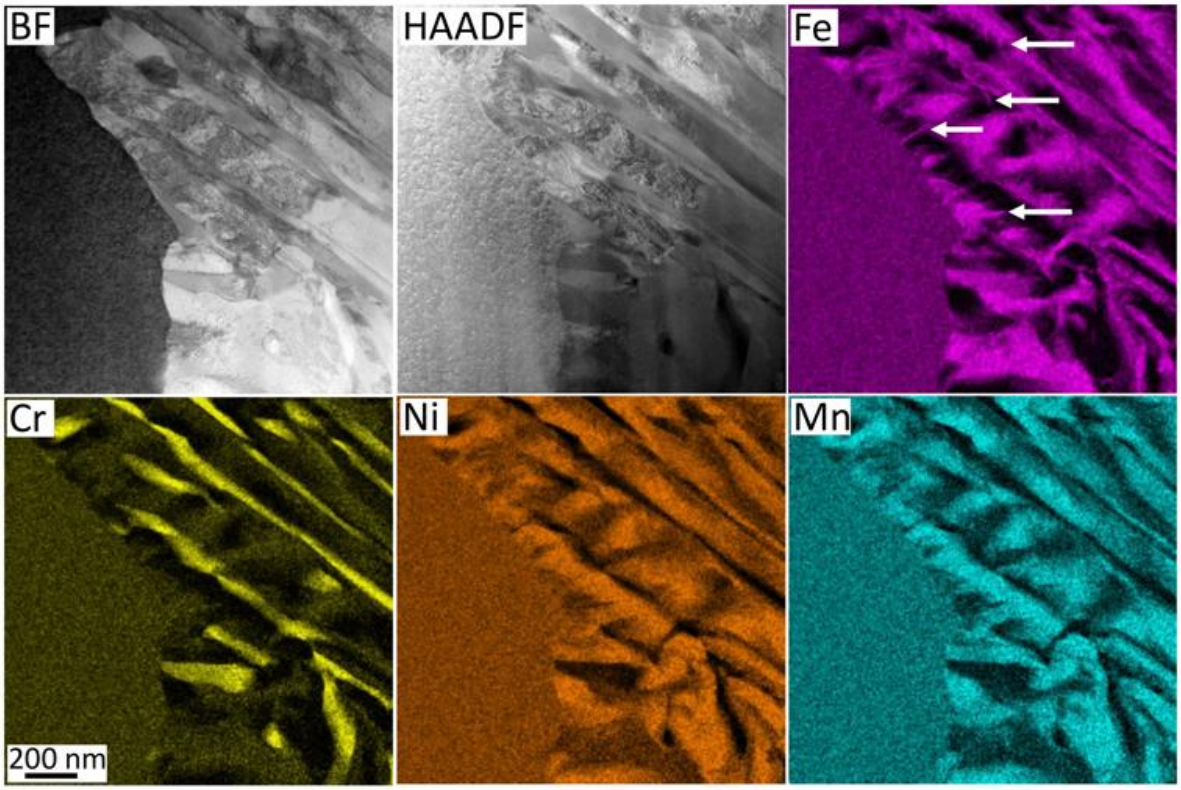

Figure 6.5: STEM images and EDS maps near the reaction front in 336 hrs. annealed sample.

The diffraction patterns collected using nanobeam diffraction confirmed the structure of each phase (Figure 6.6). The diffraction patterns after 1008 hrs. are consistent with the XRD observations. The matrix and Fe-rich phase exhibited FCC structure. The NiMn-rich phase is consistent with tetragonal structure whereas, the Cr-rich phase possesses BCC structure.

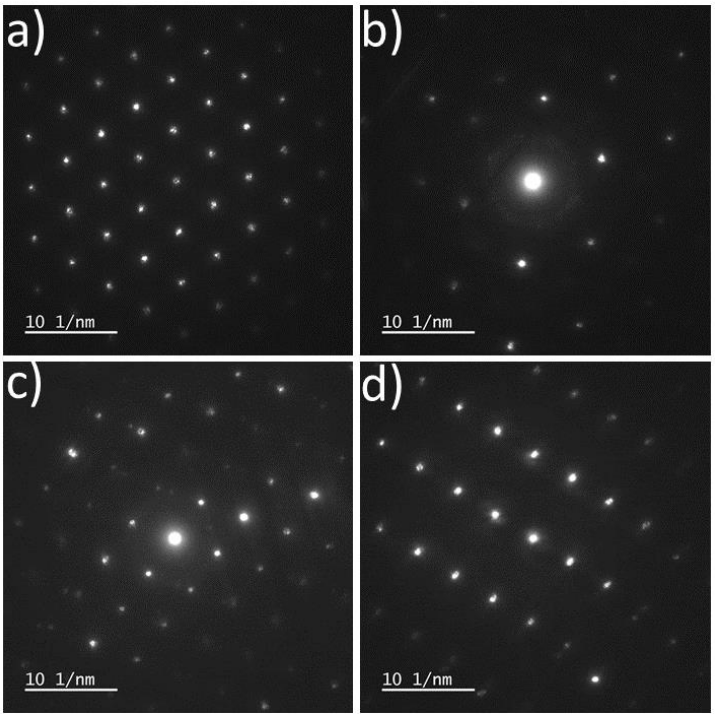

Figure 6.6: Nanobeam diffraction at [011] zone axis in a) matrix, b) NiMn phase, c) Fe-rich phase, and d) Cr-rich phase in 1008 hrs. aged sample.

APT analysis revealed the presence of NiMn rich precipitates in the un-transformed regions of the samples. Upon homogenization and annealing for 40 hours, a random distribution of alloying elements was observed in the matrix (Figure 6.7). However, after 144 hrs., small NiMn-rich precipitates were detected, which became larger with increasing times to 336, 504, and 1008 hrs. Quantification of these precipitates in terms of their number density, size, and volume fraction is provided in Figure 6.8. The number density of precipitates increased with time and reached saturation after 504 hrs., whereas size and volume fraction continued to increase with aging time. The composition of the precipitates is presented in Table 6.2 and predominantly consisted of Ni and Mn.

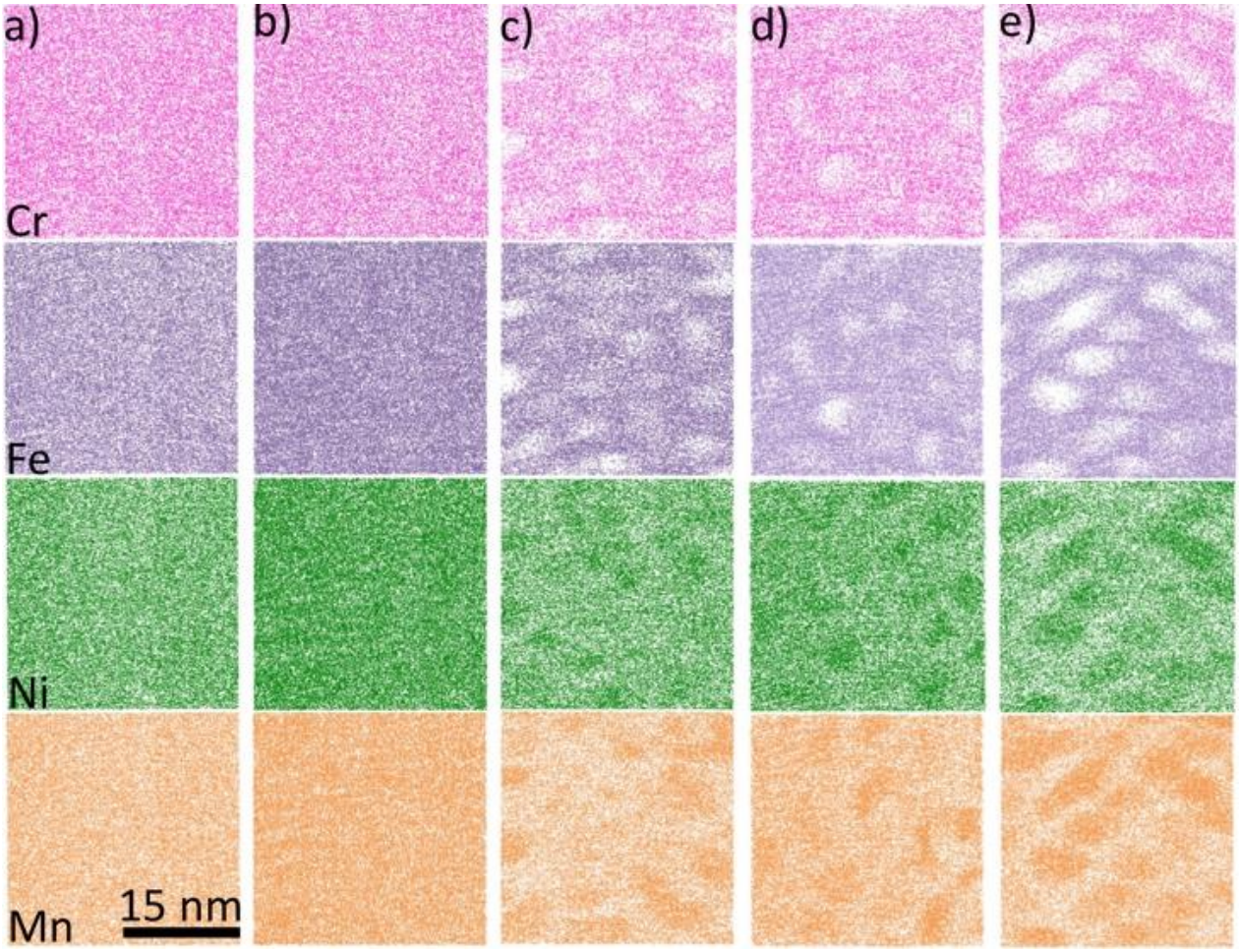

Figure 6.7: APT element maps (30x30x5 nm^3) showing the evolution of NiMn rich precipitates in the matrix at 500 ^oC after a) 40 hrs., b) 144 hrs., c) 336 hrs., d) 504 hrs., and e) 1008 hrs.

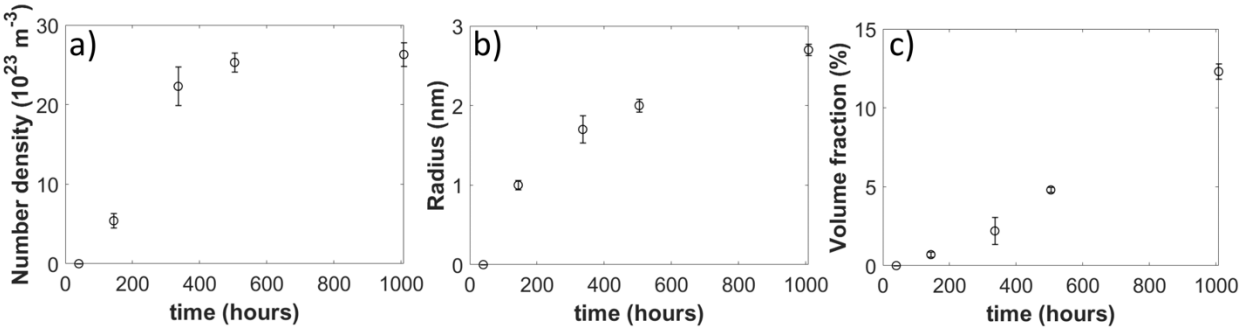

Figure 6.8: a) Number density, b) radius, and c) volume fraction evolution of NiMn rich precipitate in the matrix with annealing time.

Table 6.2: Average phase compositions and associated standard deviation measured from at least three APT datasets per condition. NiMn precipitates were defined using iso-surface analysis with iso-concentration range from 67-70 at. % (Ni+Mn). Precipitate compositions were calculated by averaging portions of the proxigrams where the solute concentrations were uniform.

Annealing time (hrs.)		**Cr (at. %)**	**Fe (at. %)**	**Ni (at. %)**	**Mn (at. %)**
144	Sample	15 ± 0	28.1 ± 0.3	28.4 0.7	28.4 ± 0.3
	Precipitates	8.2 ± 0.5	11.4 ± 1.6	37.8 ± 0.9	42.6 ± 1.2
	Matrix	15.2 ± 0.1	28.8 ± 0.2	28.2 ± 0.6	27.6 ± 0.4
336	Sample	15.5 ± 0.9	29.2 ± 1.3	25.2 ± 2.7	29.6 ± 1.4
	Precipitates	4.9 ± 0.1	3.6 ± 0.8	40 ± 2.5	51.4 ± 3.5
	Matrix	17.1 ± 0.1	33 ± 0.7	23.6 ± 2.3	25.8 ± 1.4
504	Sample	15.6 ± 0.1	29.7 ± 0.3	25.6 ± 0.9	28.9 ± 0.4
	Precipitates	4.3 ± 0.3	1.8 ± 0.4	41.5 ± 0.6	52.4 ± 1
	Matrix	17.7 ± 0.3	34.4 ± 0.6	23.2 ± 0.9	24.7 ± 0.2
1008	Sample	15.6 ± 0.1	30.5 ± 0.7	23.5 ± 1	30.2 ± 0.4
	Precipitates	3.7 ± 0.6	1.6 ± 0.4	39.2 ± 1.5	51.9 ± 1.4
	Matrix	20.1 ± 0.1	41.1 ± 0.5	17.8 ± 0.6	20.6 ± 0.4

At the reaction front, the NiMn precipitates in the matrix were found to be connected to the interface of NiMn-rich phase (Figure 6.9 and Figure B 5). The Cr rich and Fe-rich front showed roughness in the form of concave regions present throughout the interface corresponding to the location of NiMn precipitates in the untransformed matrix (Figure 6.10**)**. Some Fe buildup was sometimes observed at the reaction front of the Cr-rich phase whereas no noticeable element buildup was observed at the reaction front of either NiMn-rich or Fe-rich phases (Figure 6.11**)**. In addition, the APT reconstruction confirmed the presence of Fe-rich needles into the NiMn-rich phase (Figure 6.12). The Fe rich needles pointed towards the opposite direction as the progression of interface as illustrated in Figure B 6. These Fe-rich needles exhibited similar composition as the Fe-rich phase and therefore were combined to obtain the composition of Fe-rich phase (Table 6.3). Finally, the interfaces between the NiMn-rich phase and the Fe-rich phase were either flat or with needles or more complex asperities, as illustrated in Figure 6.13 and Figure 6.14. In Figure 6.13a, we can observe that the Fe needles stem from a thin layer of the Fe-rich phase situated between

the Cr-rich and NiMn phases. However, it is worth noting that the needles can also emerge in the absence of this layer (Figure 6.13b).

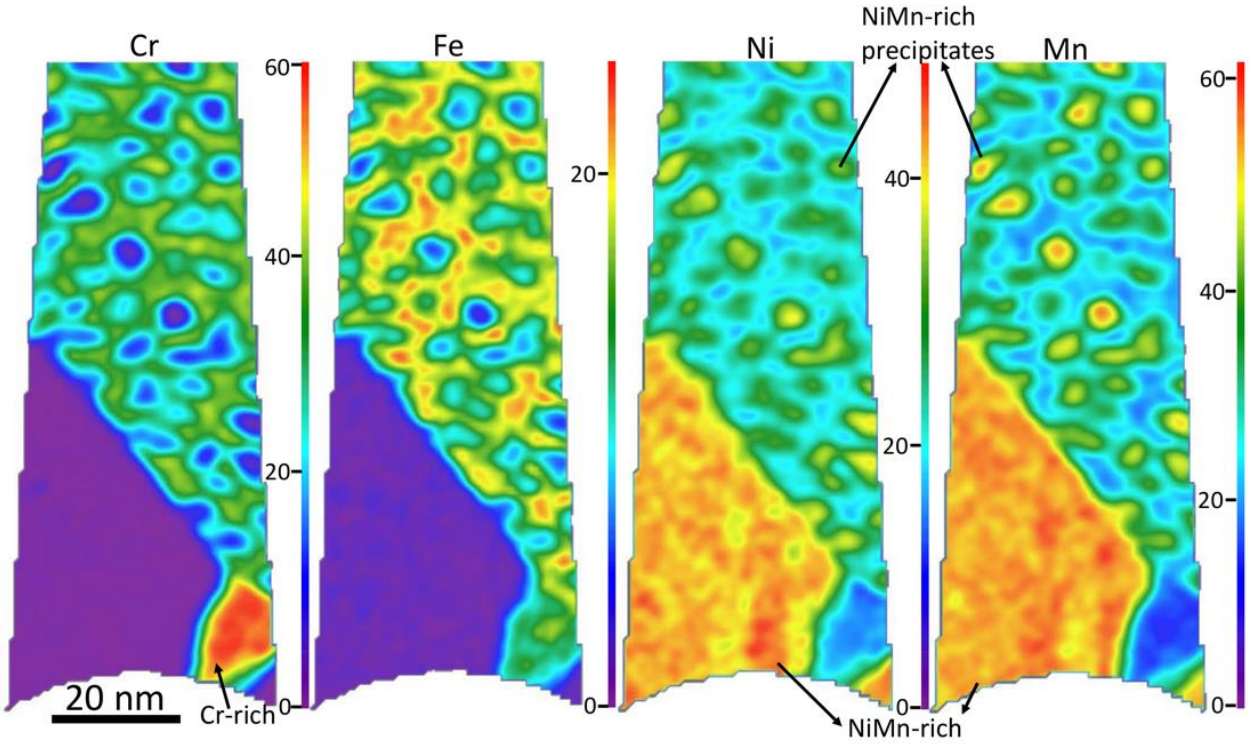

Figure 6.9: Element heatmaps of thickness 4 nm showing NiMn-rich precipitates attached to the NiMn-rich phase at the reaction front after 1008 hrs. The scale represents respective solute content in at. %.

APT analysis in the phase decomposed region far away from reaction front in a 336 hrs. sample revealed additional phase decomposition. While the Fe-rich and NiMn-rich phases displayed uniform compositions, the Cr-rich regions exhibited nanoscale Fe-rich precipitates in their centers (Figure 6.12). These Fe-rich precipitates within the Cr-rich phase exhibited higher Cr and Fe content at the expense of Ni and Mn as compared to the Fe-rich phase.

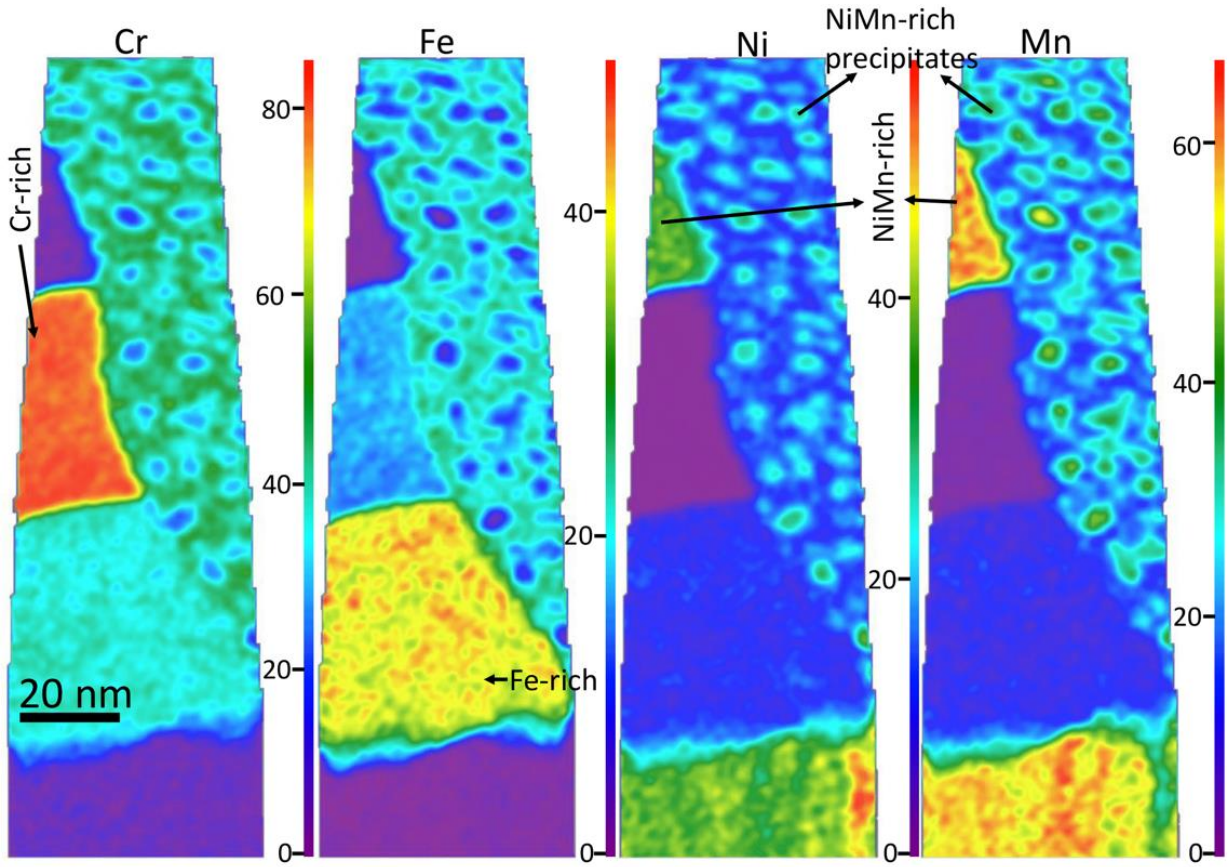

Figure 6.10: Element heatmaps of thickness 4 nm showing concave nature of interfaces of Cr-rich and Fe-rich phases at the reaction front after 1008 hrs.

Phase compositions are summarized in Table 6.3. As compared to the phases in the phase decomposed region far away from reaction front, the NiMn rich and Fe-rich phases exhibited similar composition. However, the Cr-rich matrix and the Fe-rich precipitates in Cr-rich phase were less concentrated at the reaction front.

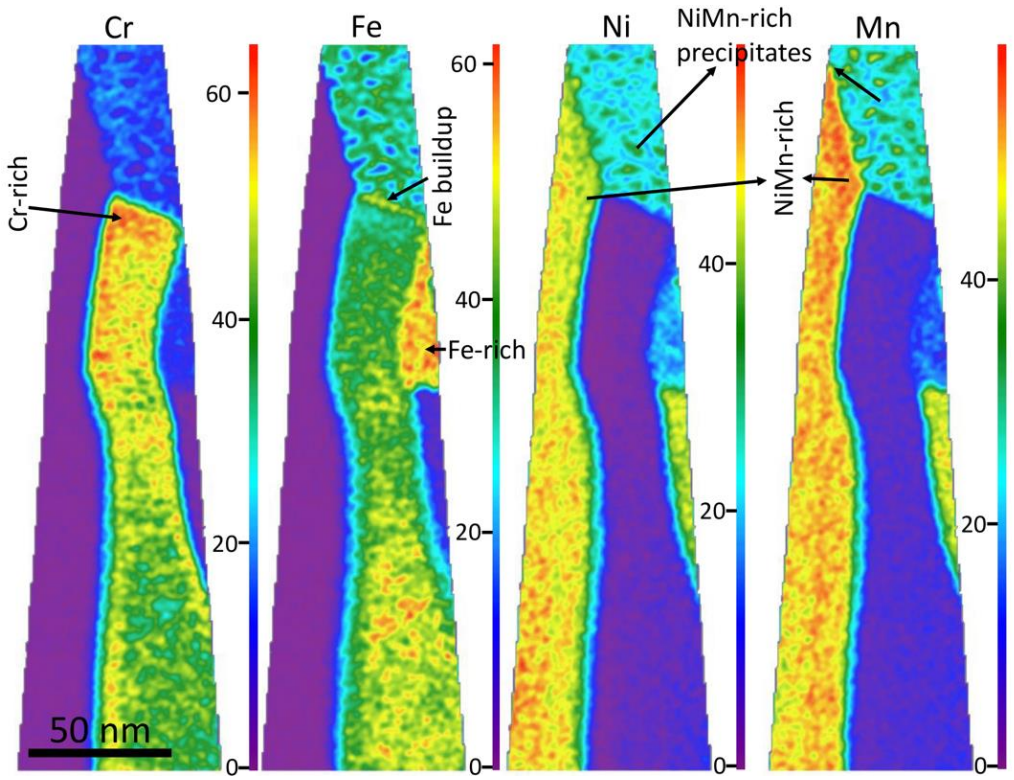

Figure 6.11: Element heatmaps of thickness 4 nm showing the Fe buildup at the reaction front of Cr-rich phase after 336 hrs.

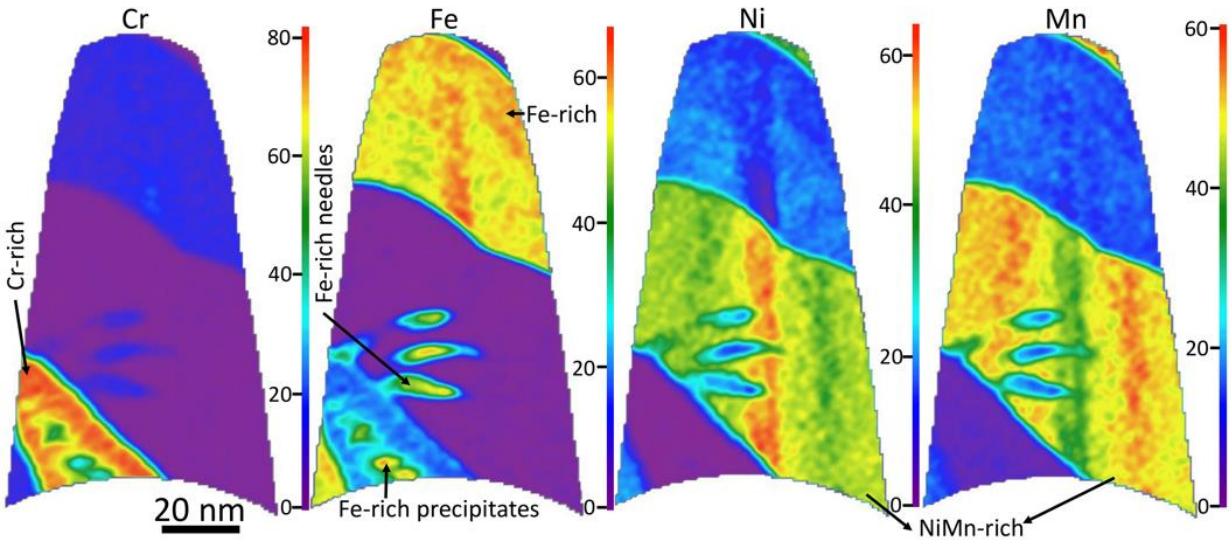

Figure 6.12: Element heatmaps of thickness 4 nm showing Fe-rich phase, NiMn-rich phase, Fe-rich precipitates in Cr-rich phase, and fingers of the Fe phase in the NiMn phase after aging for 336 hrs. The dataset was acquired far away from the reaction front (> 100 µm)

Table 6.3: Average phase compositions and associated standard errors in phase decomposed region measured from five APT datasets taken near reaction front in 336 hrs., 504 hrs., and 1008 hrs. annealed samples and from four APT datasets collected at far away from the reaction front in 336 hrs. annealed sample. Phases were defined using iso-surface analysis using iso-concentration surfaces of 70 at. % (Ni+Mn) for NiMn rich phase, 50 at. % Cr for Cr-rich phase, and 45 at. % for Fe-rich phase. The composition of Cr-rich, NiMn-rich and Fe-rich phases were calculated by isolating the phases using ROIs and estimating their bulk composition. The composition of further decomposed Cr-rich phase with Fe-rich precipitates were obtained by averaging the portions of the proxigrams where the solute concentrations were uniform.

Phases	**Cr (at. %)**	**Fe (at. %)**	**Ni (at. %)**	**Mn (at. %)**
Near reaction front (< 500 nm)				
NiMn-rich	2.6 ± 0.3	4 ± 0.7	44.8 ± 0.6	48.4 ± 0.3
Fe-rich	14.5 ± 0.5	52.5 ± 0.5	17.7 ± 0.4	15 ± 0.6
Cr-rich	63 ± 1.1	29.9 ± 0.7	1.7 ± 0.5	5.5 ± 0.3
Cr-rich matrix	72 ± 0.5	23 ± 0.5	1 ± 0.4	4.1 ± 0.4
Fe-rich precipitates in Cr-rich matrix	19.8 ± 1.6	74.3 ± 0.9	3 ± 0.4	4.3 ± 0.4
Far away from reaction front (> 100 µm)				
NiMn-rich	1.9 ± 0	2.5 ± 0.2	46.5 ± 0.2	49.1 ± 0.4
Fe-rich	13.7 ± 0.4	51.7 ± 1.5	18.4 ± 1.1	14.9 ± 0.2
Cr-rich	57.2 ± 1.6	35.3 ± 1.6	1.9 ± 0.3	5.6 ± 0.2
Cr-rich matrix	57.6 ± 1.4	35 ± 1.5	1.8 ± 0.2	5.6 ± 0.2
Fe-rich precipitates in Cr-rich matrix	40.7 ± 2.3	50 ± 1.2	3 ± 0.8	6.3 ± 0.3

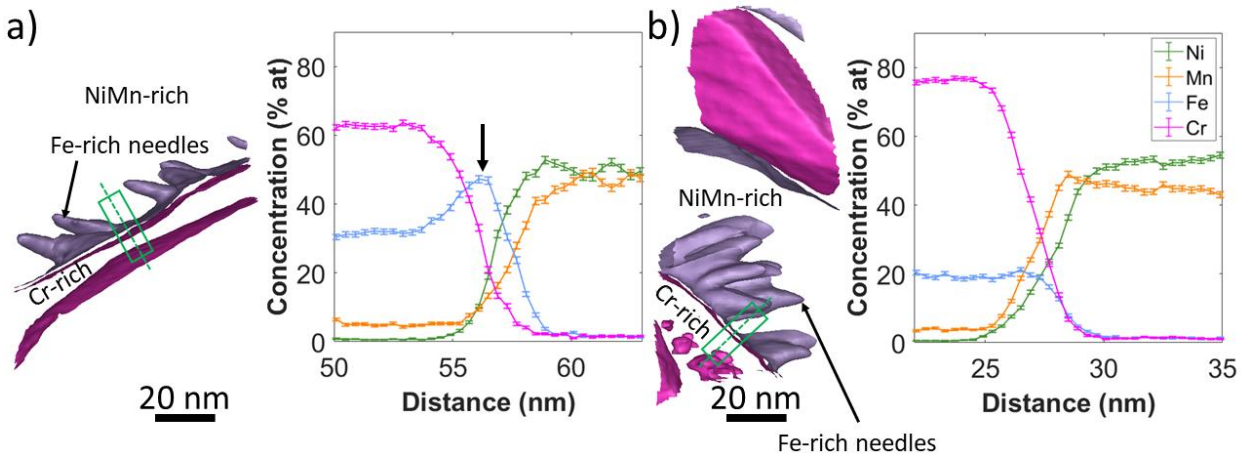

Figure 6.13: Isosurfaces and 1-D concentration profile (taken from region highlighted using green box) showing a) Fe-rich phase (arrow in 1-D profile) sandwiched between the Cr-rich phase and the Fe-rich needles penetrating into NiMn-rich phase after 1008 hrs., and b) no Fe-rich phase between the Fe-rich needles and Cr-rich phase after 336 hrs. The purple and pink isosurfaces were drawn using 40 at. % Fe, 40 at. % Cr, respectively.

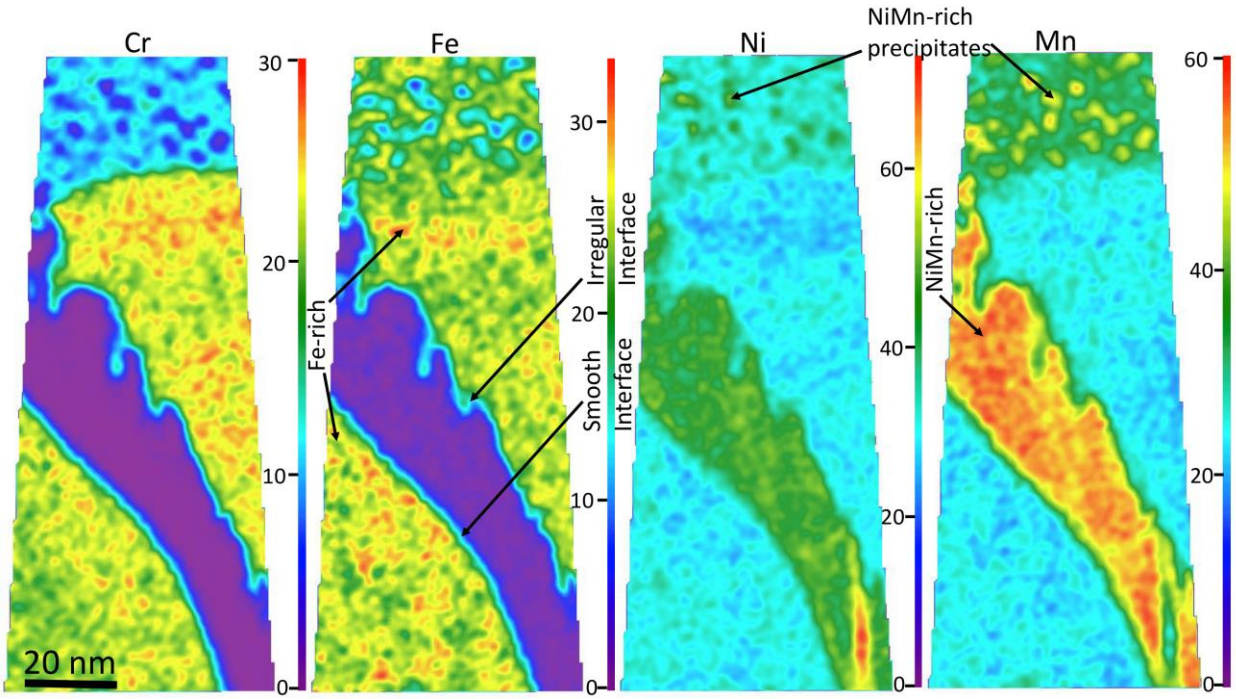

Figure 6.14: Element heatmaps of thickness 4 nm showing both smooth and ragged interface between the NiMn-rich and Fe-rich phases after aging for 1008 hrs.

6.4 Discussion

Decomposition in $Cr_{0.6}FeNiMn$ involves two independent and parallel processes: continuous precipitation via homogeneous nucleation and growth of $L1_0$ NiMn precipitates in the matrix and cellular precipitation initiating from grain boundaries.

The NiMn-rich precipitates nucleated in the matrix between 40-144 hrs. at 500 ^{o}C. Their number density increased with time and became saturated after 504 hrs., whereas their size and volume fraction continued to increase with time consistent with nucleation and growth stages. The evolution of the mean precipitate radius with time was used to estimate the bulk diffusion coefficient. According to the nucleation and growth mechanism, the formation of nanoscale precipitates occurs when nuclei reach a critical radius, beyond which precipitate growth commences. The growth regime was observed during precipitate evolution between 336-1008 hrs.,

where the number density of the precipitates remained roughly similar. Therefore, growth can be mathematically expressed over time using equation 6.2 [276].

$$R^2 = R_0^2 + 2D_{bulk}\frac{X^{matrix} - X^i}{\frac{V_{matrix}}{V_{precipitate}} - X^i}t \quad (6.2)$$

where R = radius of precipitate, R_0 = critical radius of precipitate nuclei, D_{bulk} = bulk diffusion coefficient, here taken as that of the slowest diffusing element, X^{matrix} = fraction of that element away from the interface in the matrix, X^i = fraction in the matrix at the interface with precipitates, V_{matrix} = molar volume of matrix, and $V_{precipitate}$ = molar volume of precipitate. The molar volume of precipitate ($V_{precipitate} = 7.4\,mL$) was estimated using lattice parameters of $L1_0$ NiMn phase (a = b =3.74 A and c = 3.52 A). The molar volume of matrix ($V_{matrix} = 7\,mL$) was approximated using the lattice parameter of a similar alloy equiatomic CrFeNiCoMn (a = b = c = 3.6 A) [277]. We will consider Ni since it is the slowest diffusing species [272]. The Ni fraction in the matrix (X_{Ni}^{matrix}) was calculated using the programs in each sample. X_{Ni}^{matrix} decreased from 0.23 at 336 hrs. to 0.18 at 1008 hrs. Note that we are only considering the three times between 336 hrs. and 1008 hrs. that are most consistent with the growth regime. The concentration of Ni at the interface could not be measured due to limited spatial resolution of APT for nanometer scale spherical precipitates. Instead, we consider a range from $0.5 \times X_{Ni}^{matrix}$ (relatively slow diffusion of Ni) to $0.95 \times X_{Ni}^{matrix}$ (faster diffusion of Ni). The experimental data was fit using equation 6.2 as shown in Figure 6.15 and D_{bulk} was estimated to be in the range of 9.1 x 10^{-24} – 8.2 x 10^{-23} m^2/s. The estimated value of D_{bulk} falls within the range of diffusion coefficients measured experimentally i.e., 3.3 x 10^{-23} – 5 x 10^{-22} m^2/s for Ni in 316 austenitic steels [278], the self-diffusion coefficient in Ni [134], and for Cr in pure Ni [279] at 500 ^oC. The similarity in diffusion

coefficients observed in $Cr_{0.6}FeNiMn$ alloys at 500 °C as compared to other Ni-based alloys suggest no sluggish diffusion as claimed in prior irradiation studies in CrFeNi-based MPEAs [116] and is qualitatively consistent with tracer diffusion and interdiffusion experiments, which did not provide evidence to support sluggish diffusion in MPEAs [116,170–179].

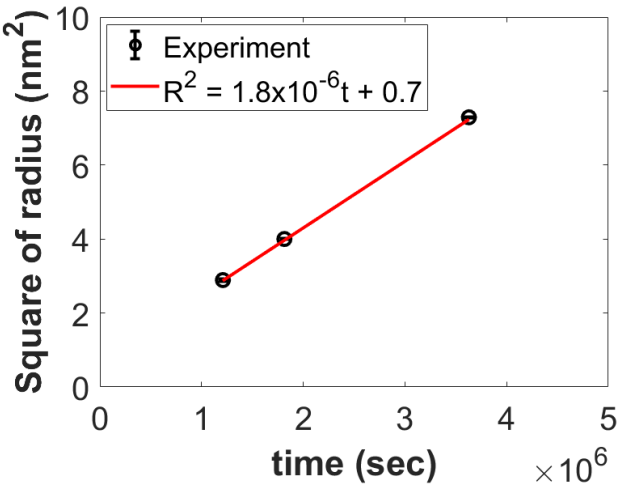

Figure 6.15: Precipitate radius evolution data fitted with precipitate growth equation.

Parallel to the continuous precipitation in the matrix, phase decomposition into three distinct phases initiated at the HAGBs after 40 hrs. and progressed into the grains with increase in aging time. The characteristics of the phase decomposition are consistent with cellular precipitation from grain boundaries. The initiation of phase decomposition at HAGB and not at LAGB and twin boundaries is consistent with prior studies on cellular precipitation [150,154,280], where the high energy HAGB provide heterogeneous nucleation sites for the nucleation of phases and also provide faster diffusion paths. The alloy fully phase decomposed into four distinct phases namely NiMn-rich, Cr-rich, Fe-rich, and Fe-rich precipitates in Cr-rich matrix. The observation of the NiMn-rich and Cr-rich phases were consistent with prior thermal ageing [124,125,252]

modelling [123], and post-irradiation studies [251]. The other phases had not yet been reported in this system.

The fraction of phase decomposed region with time was consistent with the JMAK model [281–283], which describe the kinetics of isothermal phase transformation in metals. The measured exponent of 2 is consistent with limited nucleation sites for the phase decomposition that were solely provided by HAGBs, and would eventually deplete after some time and with 2D growth of into untransformed grains [284].

Transformation took place with the cooperative formation of the three phases with no diffusional gradients noted within the APT data ahead of the transformation front. This is consistent with the extremely low solute diffusivities at 500 ^{o}C. Instead, all transport is conducted within the transformation front at rates that are multiple orders of magnitude faster than bulk diffusion. For reference, the estimated diffusion coefficient above ($D \sim 10^{-23}$ m^2/s) and an aging time of 1000 hrs., yield a diffusion distance of ~6 nm, which is vastly insufficient to explain the complete transformation of this alloy over several hundred of micrometers.

The APT reconstructions suggest that the NiMn-rich phase readily absorbed the NiMn-rich precipitates at the transformation front while rejecting Fe and Cr. Assuming that the phases grew with no particular crystallographic orientations with respect to the matrix, grain boundaries would locally have formed as the NiMn precipitates coalesced with the growing NiMn plates. Furthermore, this “easy” growth of NiMn by coalescence with existing precipitates may be the reason behind the formation of needles and complex interfaces sometimes observed between the NiMn and Fe -rich plates. The rejection of Fe and Cr as the NiMn moves forward by coalescence with NiMn precipitates ahead of the moving front can lead to Fe and Cr rich fingers. Why this

results in the formation of fingers of the Fe-rich phase and not the Cr-rich phase remains unexplained as some excess Cr (half of the rejected Cr to be exact) still needs to diffuse away.

The Cr-rich phase formed at the reaction front is a metastable phase at 500^0 C. Indeed, away from the reaction front, i.e., under prolonged aging, it eventually decomposes into Fe-rich precipitates confined within the core of the Cr-rich plates. This phase decomposition is consistent with the Fe-Cr phase diagram where the Cr-rich phase at 500 ^{o}C is within the spinodal region of the miscibility gap. The development of compositional fluctuations away from the reaction front as shown in Figure 6.11 are also consistent with spinodal decomposition. Furthermore, the kinetics of decomposition over the course of hundreds of hours are consistent with prior aging studies on Fe-Cr alloys at the same temperature of 500 ^{o}C [285].

6.5 Conclusions

Phase decomposition in $Cr_{0.6}FeNiMn$ during aging at 500 ^{o}C is characterized by two competing and parallel mechanisms. The first mechanism involves continuous precipitation through homogeneous nucleation and growth of ordered $L1_0$ NiMn precipitates. The second mechanism involves cellular decomposition initiating from grain boundaries. This complete decomposition within nine weeks of aging involves the cooperative growth of three distinct phases: the $L1_0$ NiMn phase, an FCC Fe-rich phase, and a BCC Cr-rich phase. The $L1_0$ NiMn phase grows by coalescence with NiMn precipitates ahead of the reaction front and rejection of Fe and Cr along the reaction front that enables the growth of the FCC and BCC Fe and Cr rich phases whose growth also requires dissolution of NiMn precipitates. The Cr-rich phase as formed is metastable and further decomposes into Fe-rich precipitates in a Cr-rich matrix. All estimation of kinetics of transformation were consistent with established diffusivities in Fe-Cr and more complex Fe-Cr-Ni

based MPEAs. Unlike previous work on more complex MPEAs that demonstrated discontinuous precipitation into two phases, the decomposition of $Cr_{0.6}FeNiMn$ is consistent with eutectoid reaction during aging in a three-phase region of the phase diagram – unfortunately the CALPHAD database does not currently predict the phases observed here. The mechanisms of decomposition and resulting microstructures are likely to be common to other MPEAs after low temperature aging.

Chapter 7 Effect of Chemistry and Dose Rate on the Irradiation Behavior of Multi-Principal Element Alloys

7.1 Introduction

Ion irradiation studies suggested that MPEAs tend to exhibit a high resistance to swelling [117], delayed energy dissipation [33,118], and reduced damage accumulation [119] in comparison to stainless steels [120–122] and simpler Ni-based concentrated alloys [33–36]. Ion irradiation study conducted at high dose rates (> 10^3 dpa/s) found higher number densities of smaller irradiation-induced dislocation loops in equiatomic CrFeNiCo (2 x 10^{21} m^{-3}, 50nm) and equiatomic CrFeNiCoMn (1 x 10^{22} m^{-3}, 25 nm) as compared to equiatomic NiFe (1.2 x 10^{-21} m^{-3}, 75 nm) under Ni ions (at 500 ^oC at 40 dpa, 2 x 10^{-3} dpa/s) [157]. Rutherford backscattering spectroscopy revealed a lower level of damage in equiatomic CrFeNiCo alloy as compared to pure Ni and equiatomic NiFe under Ar ion (at -257 ^oC at 0.2-0.8 dpa). Equiatomic CrFeNiCo and equiatomic CrFeNiCoMn MPEAs exhibited lower swelling (0.2% and 0.3%, respectively) as compared to equiatomic NiCoCr (1.1%), equiatomic NiFe (0.3%), equiatomic NiCo (3.5%), and pure Ni (6.7%) during Ni ion irradiation (at 500 ^oC at 53 dpa, 0.003 dpa/s) [117]. A similar trend in the swelling behavior was observed by another study using Ni ions at 500 ^oC at 60 dpa [168]. The superior irradiation behavior of MPEAs as compared to the simpler concentrated alloys was hypothesized to originate from the combined effects of reduced thermal conductivity and orders of magnitude reduction in the mean free path of electrons lead to less efficient heat conduction in MPEAs, which in turn results in prolonged thermal spikes, increased vacancy-interstitial

recombination rates, and decreased defect densities [33,118]. In addition, reduced interstitial mobility compared to that of vacancies and the 3-D motion of interstitial-clusters can further promote higher rates of recombination in MPEAs [163–165]. Notably, the superior irradiation properties of MPEAs have only been reported under ion irradiation performed at very high dose rates ($>10^{-3}$ dpa/s) and no literature is available on the behavior of the same alloys at lower dose rates.

Dose rate can significantly influence the dislocation microstructure and cavity swelling. Multiple irradiation studies on various metallic systems such as austenitic stainless steels [269,286,287], F/M steels, Fe-C alloy [288], Fe-Cr alloy [289–292], Pd [267], W [293], Ni [294], and Fe [292], etc. found a decrease in dislocation loop number density and increase in size with decrease in dose rates. These studies hypothesized that at higher dose rates, the cascades and defect production rates are higher as compared to lower dose rates. Consequently, the defect clusters produced in cascades have more chances of interaction with newly created point defects causing their higher number density at the cost of smaller size [267–269]. In addition, a recent study on ion irradiated F/M steel suggested a strong effect of dose rate on the 1-D migration of small dislocation loops [295]. The study found a significant decrease in 1-D migration of dislocation loops of similar size with decrease in dose rates. Apart from dislocation loops, dose rate also has a significant effect on the cavity swelling. Studies on pure Ni [294,296] and austenitic stainless steels [287,297,298] showed a shift in maximum swelling temperature to higher temperatures with increase in dose rate. In addition, the incubation dose, which represent the onset of cavity swelling decreased with decrease in dose rates [287,297]. To explain this behavior, it was hypothesized that increase in dose rates at a given temperature enhanced recombination and lowered vacancy

supersaturation, thereby, decreasing the cavity formation [262,296]. Therefore, it is important to explore the effect of dose rate on the dislocation loops and cavity swelling in MPEAs.

Since MPEAs exhibit unusual behavior at high dose rates, it is of interest to understand the evolution of the microstructure at lower dose rate. Therefore, in an effort to clarify chemical effects and dose rate effects, we characterized the irradiation behavior of Ni-based alloys of increasing chemical complexity under Fe ion irradiation using lower dose rates < 10^{-4} dpa/s.

7.2 Experimental

Eight different Ni based alloys with increasing complexity such as Pure Ni, $NiCr_{0.25}$, $NiMn_{0.25}$, $Cr_{0.5}FeNi$, $Cr_{0.5}FeNiMn_{0.1}$, $Cr_{0.5}FeNiMn_{0.3}$, equiatomic CrFeNiCo, and equiatomic CrFeNiCoMn were synthesized with elemental pure metals Cr, Fe, Ni, Mn, Co, and Pd (>99.9% purity) using arc melting. The arc-melted buttons were flipped and melted five times to ensure a homogeneous mixing. The arc-melted samples were then homogenized for 24 hrs. at 1100 ^{o}C followed by water quenching to ensure an equiaxed grain structure and compositional homogeneity. X-ray diffraction (XRD) was performed on selected alloys such as $Cr_{0.5}FeNi$, $Cr_{0.6}FeNiMn$, and equiatomic CrFeNiCoMn to confirm a single-phase FCC solid solution. The alloy compositions measured by atom probe tomography (APT) are listed in Table 7.1.

Three irradiation experiments were performed at the Michigan Ion Beam Laboratory (MIBL). Prior to irradiation, samples were electropolished using 7% perchloric acid in 93% methanol at -50 ^{o}C and 50 V for 10 sec to ensure a mirror finish. A set of samples from each alloy and pure Ni was irradiated by 6 MeV Fe^{3+} using an estimated dose rate of 10^{-4} dpa/s at 500 ^{o}C to 2 dpa. Additional sets of samples from the $Cr_{0.5}FeNi$, $Cr_{0.5}FeNiMn_{0.3}$, and equiatomic CrFeNiCoMn alloys were irradiated at 500 ^{o}C using an estimated dose rate of 10^{-4} dpa/s to 10 dpa

and 10^{-5} dpa/s to 2 dpa, respectively. All irradiation experiments were performed under a pressure below 10^{-7} torr using a raster-scanning beam with frequencies of 220 Hz and 2000 Hz in the x and y directions, respectively, to fully cover the sample surfaces. Ion irradiation doses were computed by SRIM-2013 using the Kinchin-Pease [225] mode with a displacement threshold energy of 40 eV [253] for all elements (Figure 7.2a**)**. The depth of 700 nm where the nominal irradiation dose was defined was chosen for microstructural characterization to avoid the ion implantation region and any surface effects [254].

Table 7.1**:** Average composition (at. %) and standard error measured by APT using at least three datasets for each alloy.

Sample	**Cr**	**Ni**	**Fe**	**Mn**	**Co**	**C**	**Si**
$NiCr_{0.25}$	21.7 ± 0.2	78.4 ± 0.2					
$NiMn_{0.25}$		75.7 ± 0.1		24.2 ± 0.1			
$Cr_{0.5}FeNi$	19.3 ± 0.1	39.6 ± 0.3	40.8 ± 0.2				0.1
$Cr_{0.5}FeNiMn_{0.1}$	19.7 ± 0.1	36.9 ± 0.5	37.3 ± 0.1	5.1 ± 0.2		0.1	0.1
$Cr_{0.5}FeNiMn_{0.3}$	18 ± 0.2	32.9 ± 0.6	35.4 ± 0.5	13.6 ± 0.3		0.1	0.1
Equiatomic CrFeNiCo	25.5 ± 0.1	23.7 ± 0.2	24.5 ± 0.2		26 ± 0.2	0.1	
Equiatomic CrFeNiCoMn	18.8 ± 0.2	18.2 ± 0.4	21.3 ± 0.2	20.7 ± 0.6	20.6 ± 0.2		

The irradiated samples were characterized using APT and TEM, with EBSD employed to determine grain orientations. Specimens were prepared using a standard lift-out and Ga ion beam thinning process on FEI Helios 200 Nanolab dual SEM/FIB instruments. TEM and APT specimens were prepared specifically away from the grain boundaries on [001] oriented grains. The TEM lamellas, 200-250 nm in thickness, were flash electropolished using 4% perchloric acid in 96% ethanol at -50 ^{o}C and 12 V [255]. TEM specimens were characterized using a FEI Talos and JEOL

3100 in TEM or STEM mode. Dislocation images were obtained with <001> on zone STEM BF imaging [256], and cavities were imaged using off-zone STEM HAADF imaging. Dislocation number density and size were quantified using STEM BF images of area 533 x 533 nm^2 for 10^{-4} dpa/s, and 760 x 760 nm^2 for 10^{-5} dpa/s conditions, whose center is positioned about 700 nm depth from surface. All dislocation loops and lines were counted manually, and their sizes were estimated using ImageJ software. An example is illustrated for $NiCr_{0.25}$ sample at 2 dpa using 10^{-4} dpa/s in Figure 7.1. The faulted loops were distinguished from the perfect loops based on their contrast in the STEM BF images. Dislocation density was estimated after multiplying the imaged area by the thickness of the TEM sample obtained using EELS. To quantify cavity swelling, one lift out was made for all sample conditions. For each lift out, a 1500 x 2200 nm^2 area was used to quantify cavity swelling and generate cavity number density, size, and swelling profiles with depth where relevant.

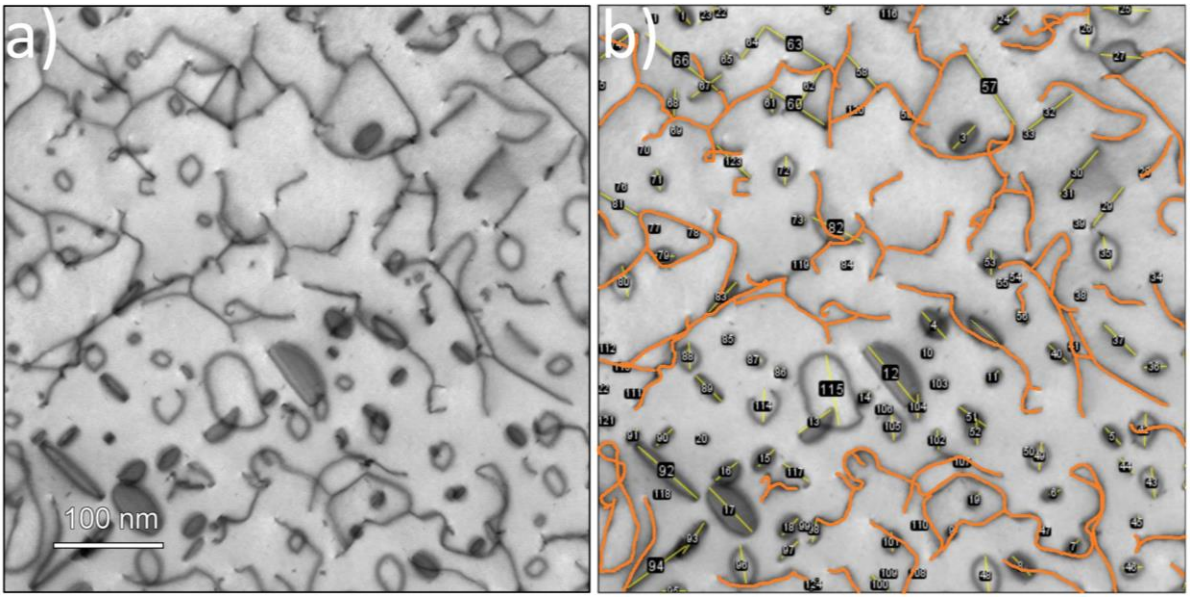

Figure 7.1: a) STEM-BF image at <001> zone axis showing irradiation induced dislocation loops and lines in the irradiated region at a depth of 700 nm from surface in $NiCr_{0.25}$ after 2 dpa at 10^{-4} dpa/s, and b) quantification of faulted (labelled in sequence from 1-20) and perfect (21-124) dislocation loops. The loop diameter is marked with yellow lines, and dislocation lines marked in orange.

APT data were collected using a CAMECA LEAP 5000 XR instrument operated in laser mode using a pulse energy of 40-60 pJ, 200 kHz pulse rate, and a target detection rate of 0.5-1% at 50 K. APT data reconstruction and analysis were performed using the Cameca software package AP Suite 6. The reconstruction image compression factor (ICF) and k-factor were in the range 1.4-1.65, and 3-3.3, respectively. Both ICF and k-factor were chosen to avoid any curvature of the dislocation loops, which are known to be linear features. For each alloy, at least three datasets were acquired for each irradiation. Iso-surface analysis and proxigrams were used to obtain the dislocation chemistry.

7.3 Results

In pure Ni and all seven alloys, the microstructural response to irradiation was observed in the form of extended defect structures. Although only illustrated for $Cr_{0.5}FeNi$ after 2 dpa at 10^{-5} dpa/s (Figure 7.2), similar features were observed in all alloys at all irradiation conditions. In the non-irradiated region, cavities were observed in addition to a low density of pre-existing dislocations. In the irradiated region, cavities, dislocation loops consisting of {110} perfect loops and {111} faulted loops, and dislocation lines were noted. Both faulted and perfect loops were quantified jointly, and their number density and size were reported together, while the dislocation lines were reported separately. The dislocation loops density increased with depth, following the damage level. Apart from the seven alloys, in pure Ni, a different distribution of defect structures was observed. In the non-irradiated region, {110} perfect loops and dislocation lines were observed. In the irradiated region, similar features along with a high density of cavities were observed.

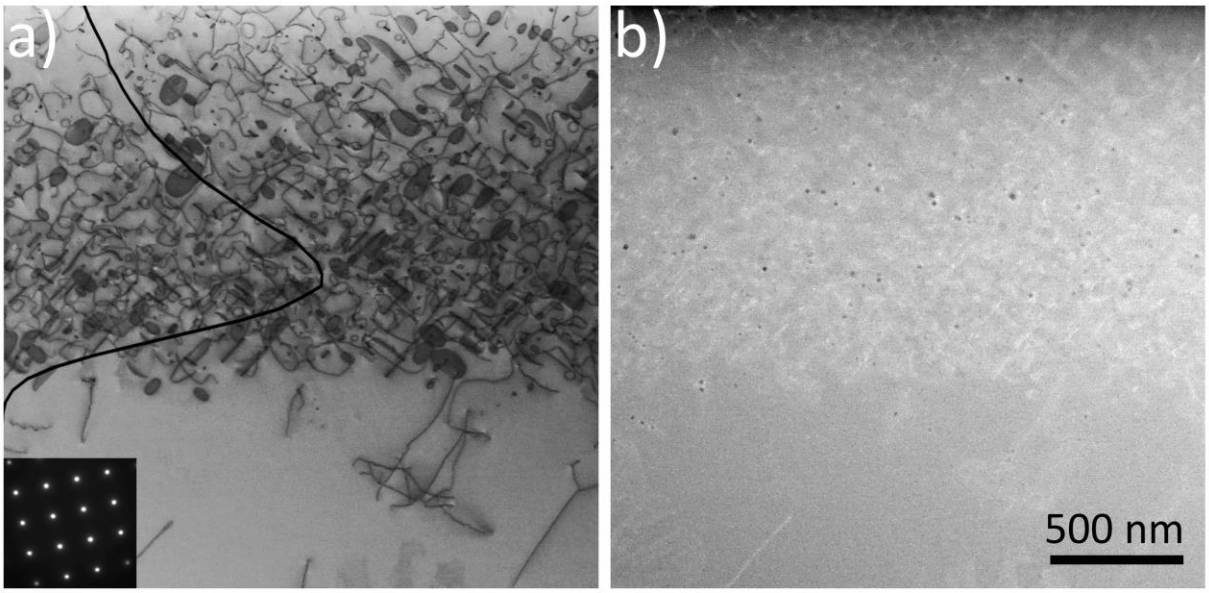

Figure 7.2: After 2 dpa at 10^{-5} dpa/s, a) damage profile superimposed on a STEM-BF image at <001> zone axis showing irradiation induced dislocation loops in the irradiated region and pre-existing dislocations in the non-irradiated region after, and b) Off-zone STEM HAADF image of the distribution of cavities (black dots) in irradiated region in $Cr_{0.5}FeNi$.

The alloys exhibited very different total dislocation loop (combined faulted and perfect) number densities and sizes after the irradiation to 2 dpa at 10^{-4} dpa/s, as illustrated in Figure 7.3, with no clear direct correlation with compositional complexity, e.g., number of elements. Quantification of the total loop number densities, average sizes, fraction of faulted loops, and dislocation line density is summarized in Figure 7.4. The lowest loop density and largest loop size was observed for pure Ni. Comparisons within the alloys revealed lower densities for the two binary alloys, $NiCr_{0.25}$ and $NiMn_{0.25}$. However, a similarly low density of loops was noted for equiatomic CrFeNiCo. The highest number density and smallest size was observed for $Cr_{0.5}FeNi$ and equiatomic CrFeNiCoMn whereas, the smallest number density and highest size was observed for $NiMn_{0.25}$ and $Cr_{0.5}FeNiMn_{0.3}$.

The size distribution of dislocation loops is illustrated in Figure 7.5. The distribution was unimodal for pure Ni with peak around 40-50 nm loop diameter. However, all other alloys

exhibited bimodal distribution with the first peak coming from smaller loops with a diameter less than 50 nm and the second peak from larger loops with diameter greater than 50 nm in all samples. Notably, the extent of both smaller and larger loops varied in each sample at all conditions. The addition of Mn or Co decreased the percentage of smaller loops and increased the percentage of larger loops. In $NiCr_{0.25}$, the smaller loops accounted for approximately 78% of total loops. Replacing Cr with Mn decreased the percentage of smaller loops to 58%. In $Cr_{0.5}FeNi$, 96% were smaller loops. With the addition of Mn, the percentage of smaller loops decreased to 90% in $Cr_{0.5}FeNiMn_{0.1}$. With further addition of Mn, the smaller loops further decreased to 73% in $Cr_{0.5}FeNiMn_{0.3}$. Replacing Mn with Co, the smaller loops further decreased to 63% in equiatomic CrFeNiCo. However, the addition of both Co and Mn increased their percentage to 95% in CrFeNiCoMn. Furthermore, the fraction of faulted loops is plotted in Figure 7.4, showing roughly 10-30% of faulted loops out of total loops in all samples except $NiMn_{0.25}$ and pure Ni, which showed negligible number of faulted loops. The higher fraction of roughly 20-28% was observed in $NiCr_{0.25}$, $Cr_{0.5}FeNi$, $Cr_{0.5}FeNiMn_{0.3}$, and equiatomic CrFeNiCo, while 10-13% observed in $Cr_{0.5}FeNiMn_{0.1}$, and equiatomic CrFeNiCoMn. Furthermore, the dislocation line density in $NiCr_{0.25}$, $NiMn_{0.25}$, $Cr_{0.5}FeNiMn_{0.1}$, equiatomic CrFeNiCo, and equiatomic CrFeNiCoMn were similar and roughly twice as compared to pure Ni, $Cr_{0.5}FeNi$, and $Cr_{0.5}FeNiMn_{0.3}$.

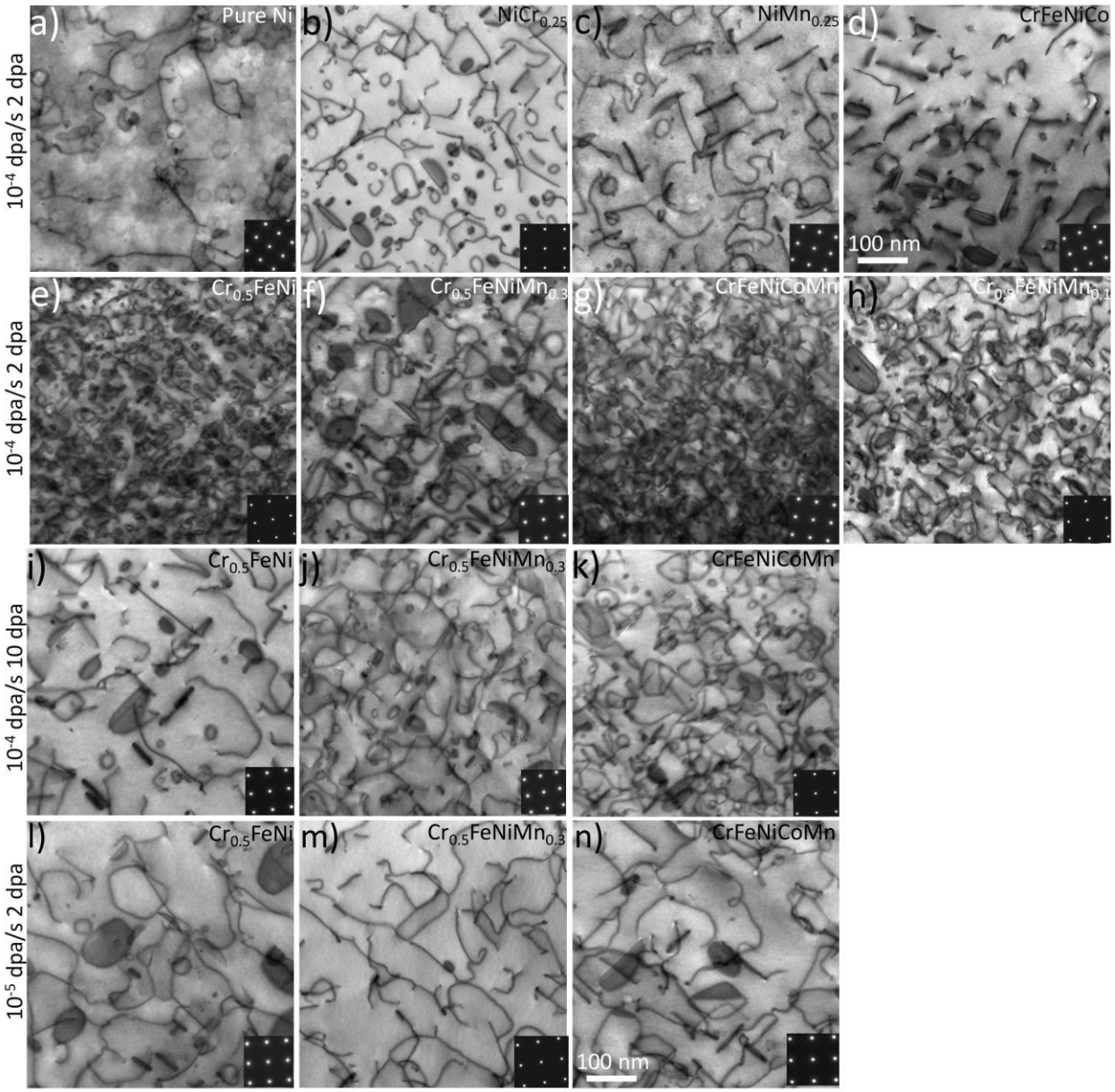

Figure 7.3: STEM-BF image at <001> zone axis showing irradiation induced dislocation loops in the irradiated region at a depth of 700 nm from surface in all samples after 2 dpa at 10^{-4} dpa/s (a-g), 10 dpa using 10^{-4} dpa/s (h-j), and 2 dpa at 10^{-5} dpa/s (k-m) with their diffraction pattern enclosed.

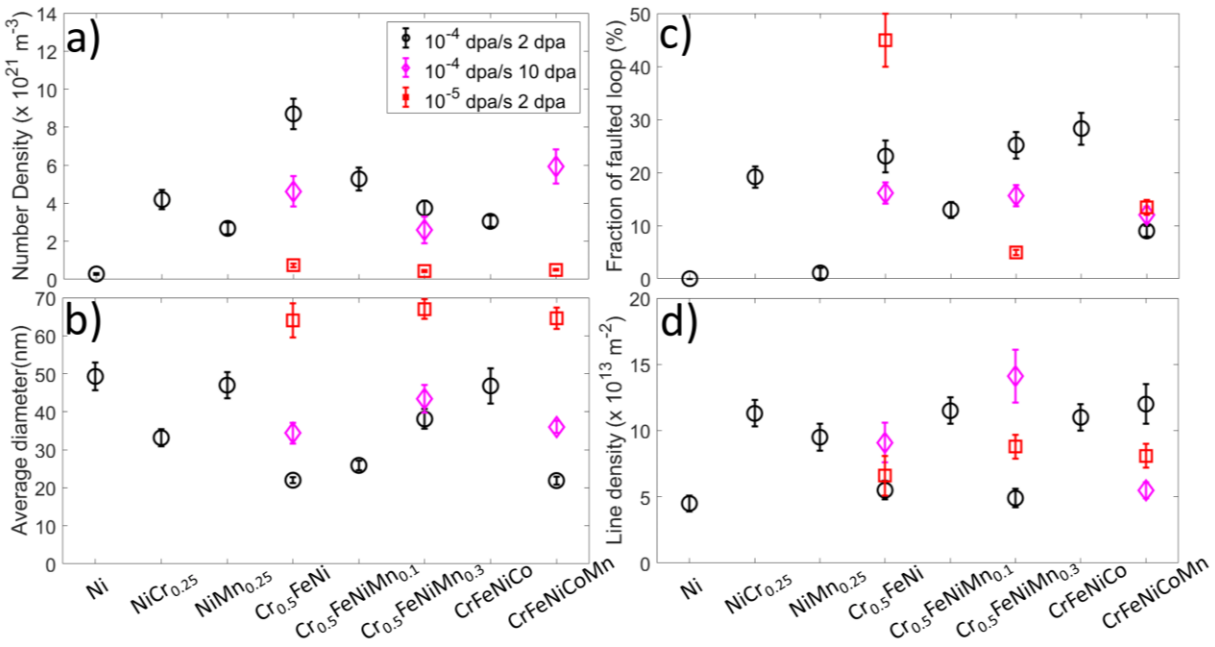

Figure 7.4: Total dislocation loop number density, diameter, fraction of faulted loops, and line density in all alloys at all conditions. Error bars represent standard error accumulated from the error in the thickness of TEM sample.

A small number of small cavities were observed in all alloys after 2 dpa at 10^{-4} dpa/s. Representative images are shown in Figure B 7. These images were used to obtain swelling distribution profiles with depth (Figure 7.6). and calculate total swelling (Figure 7.7). $NiMn_{0.25}$ displayed the highest cavity swelling of roughly 0.05%, with 12 cavities distributed in the irradiated region. $Cr_{0.5}FeNiMn_{0.3}$ and CrFeNiCoMn exhibited roughly 0.02% swelling, with 12 and 20 cavities, respectively. $Cr_{0.5}FeNiMn_{0.3}$ only had cavities in the irradiated region, while the cavities in CrFeNiCoMn were found in the irradiated and non-irradiated regions. The other alloys exhibited even smaller swelling values (<0.01%). Only 2 cavities, one in the irradiated region and the other in the non-irradiated region, were noted for $Cr_{0.5}FeNi$. equiatomic CrFeNiCo had 6 cavities, all in the non-irradiated region. No cavities were observed for $NiCr_{0.25}$ and $Cr_{0.5}FeNiMn_{0.1}$.

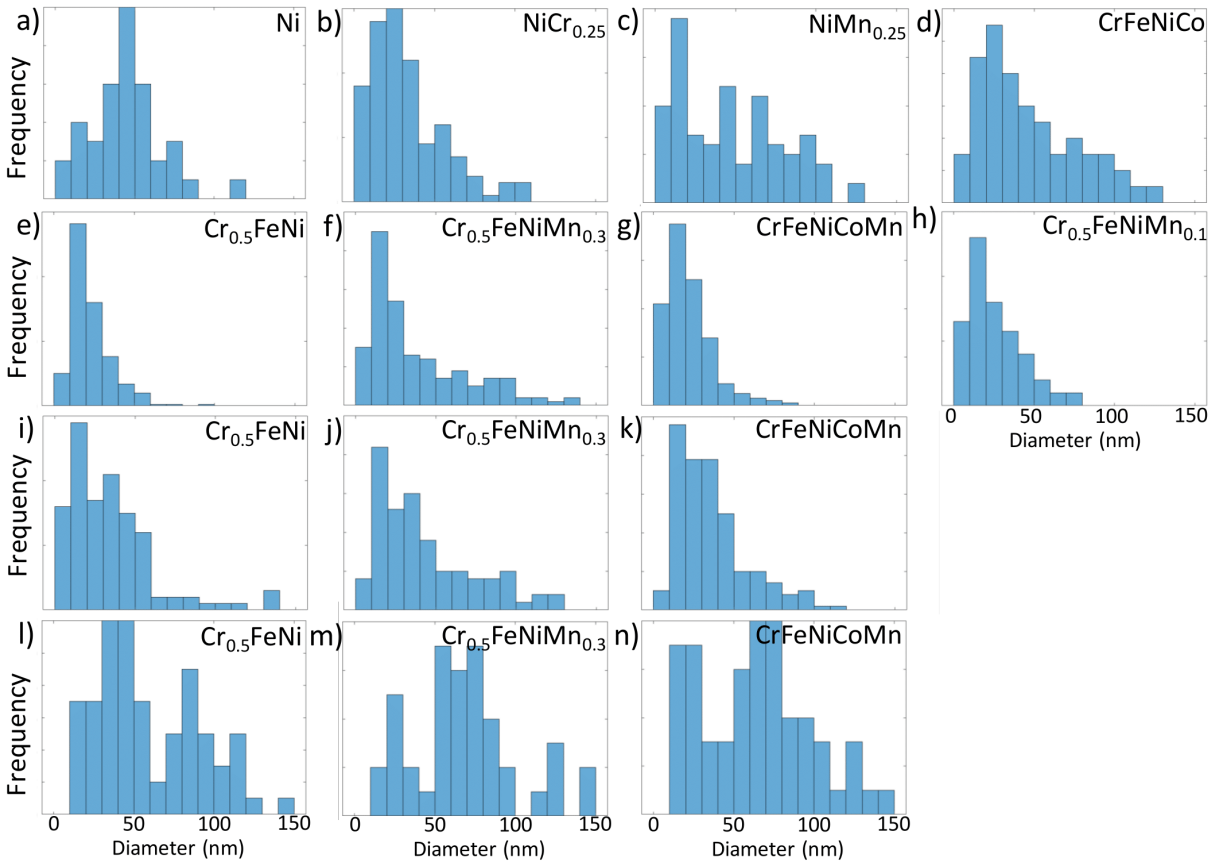

Figure 7.5: Dislocation loops size distribution in all samples at all irradiation conditions i.e., 2 dpa at 10^{-4} dpa/s (a-g), 10 dpa using 10^{-4} dpa/s (h-j), and 2 dpa at 10^{-5} dpa/s (k-m).

After 10 dpa, the extent of cavity swelling increased for $Cr_{0.5}FeNiMn_{0.3}$ by a factor of 3 and equiatomic CrFeNiCoMn by a factor of 7, while no change was observed in $Cr_{0.5}FeNi$. Specifically, $Cr_{0.5}FeNi$ exhibited two cavities with one in the irradiated region and the other in the non-irradiated region. In contrast, $Cr_{0.5}FeNiMn_{0.3}$ displayed 42 cavities in the irradiated region, and equiatomic CrFeNiCoMn exhibited 25 cavities, with only four in the irradiated region and the rest in the non-irradiated regions.

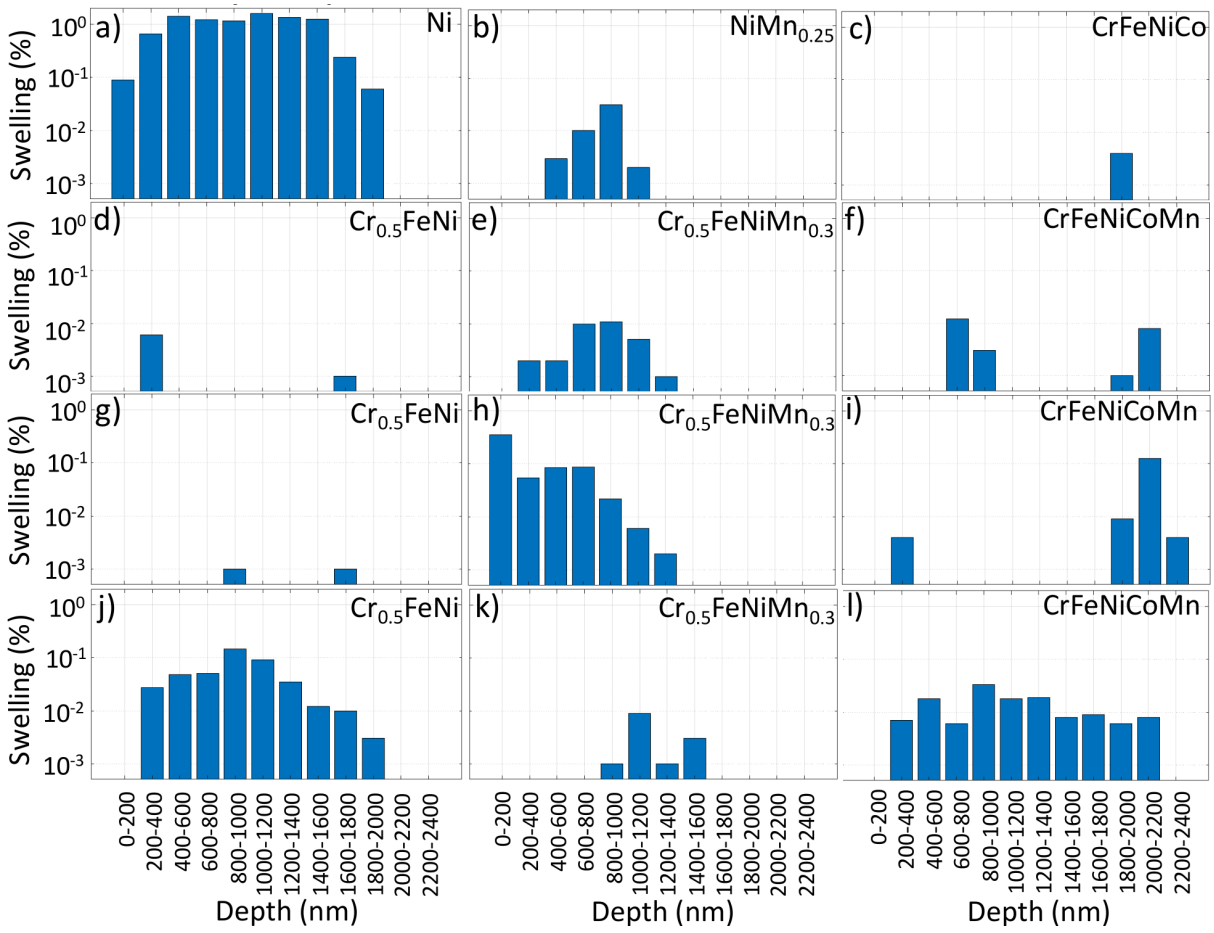

Figure 7.6: Cavity swelling distribution with depth in all samples at all irradiation conditions i.e., 2 dpa at 10^{-4} dpa/s (a-f), 10 dpa using 10^{-4} dpa/s (g-i), and 2 dpa at 10^{-5} dpa/s (j-l).

After 2 dpa at the lower dose rate of 10^{-5} dpa/s, swelling in $Cr_{0.5}FeNi$ and equiatomic CrFeNiCoMn increased significantly. However, $Cr_{0.5}FeNiMn_{0.3}$ showed similar low swelling. In the case of $Cr_{0.5}FeNi$, 105 cavities were found to be uniformly distributed in the irradiated region and extended in the non-irradiated area within a depth of 300 nm below the irradiated region. In equiatomic CrFeNiCoMn, 81 cavities were found uniformly distributed with a similar spatial distribution. In contrast, $Cr_{0.5}FeNiMn_{0.3}$ showed only six cavities in the irradiated region.

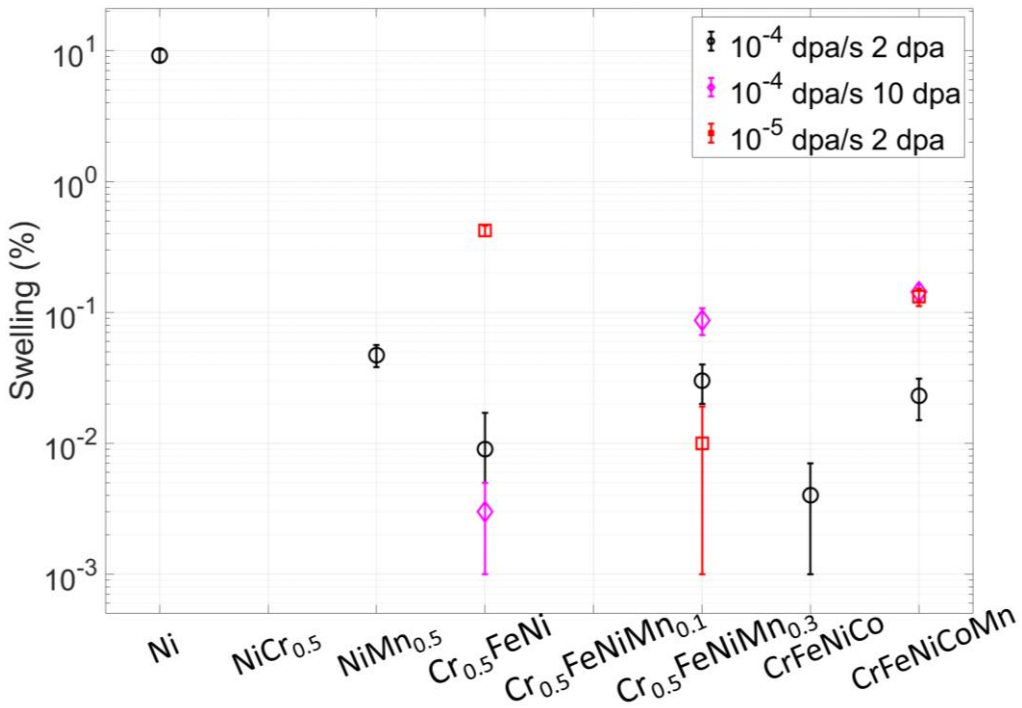

Figure 7.7: Total swelling in all samples at all irradiation conditions. Error bars represent standard error accumulated from the error in the thickness of TEM sample. In cases where less than ten cavities were observed (i.e., $Cr_{0.5}FeNi$ 10 dpa 10^{-4} dpa/s, $Cr_{0.5}FeNiMn_{0.3}$ 2 dpa 10^{-5} dpa/s, and CrFeNiCo 2 dpa 10^{-4} dpa/s), the standard error reflects the error in swelling measured from two distinct areas of 1500 x 2200 nm^2.

No features other than dislocations and cavities were observed in any of the samples under all irradiation conditions. All diffraction patterns were consistent with the FCC matrix and no superlattice spots were observed (Figure 7.3). APT was conducted to determine the chemistry of dislocation loops and confirm the absence of phase decomposition. All samples showed a random distribution of elements in the irradiated region, confirming the absence of phase decomposition under all irradiation conditions (Figure B 9 and Figure B 10). Furthermore, APT reconstructions revealed curved linear features in all samples at all irradiation conditions that were likely solute-decorated dislocation loops as shown in Figure B 8 for $Cr_{0.5}FeNi$ after 10 dpa at 10^{-4} dpa/s. Compositional analysis indicated a strong enrichment of Ni and depletion of Cr in $NiCr_{0.25}$, enrichment of Ni and depletion of Mn in $NiMn_{0.25}$, enrichment of Ni and depletion of Cr and Fe in

$Cr_{0.5}FeNi$, enrichment of Ni and depletion of Cr, Fe, and Mn in $Cr_{0.5}FeNiMn_{0.1}$, and in $Cr_{0.5}FeNiMn_{0.3}$, enrichment of Co and Ni and depletion of Cr, Fe, and Mn in equiatomic CrFeNiCoMn. The extent of enrichment and depletion was roughly similar with change in dose and dose rate as shown in Figure 7.8.

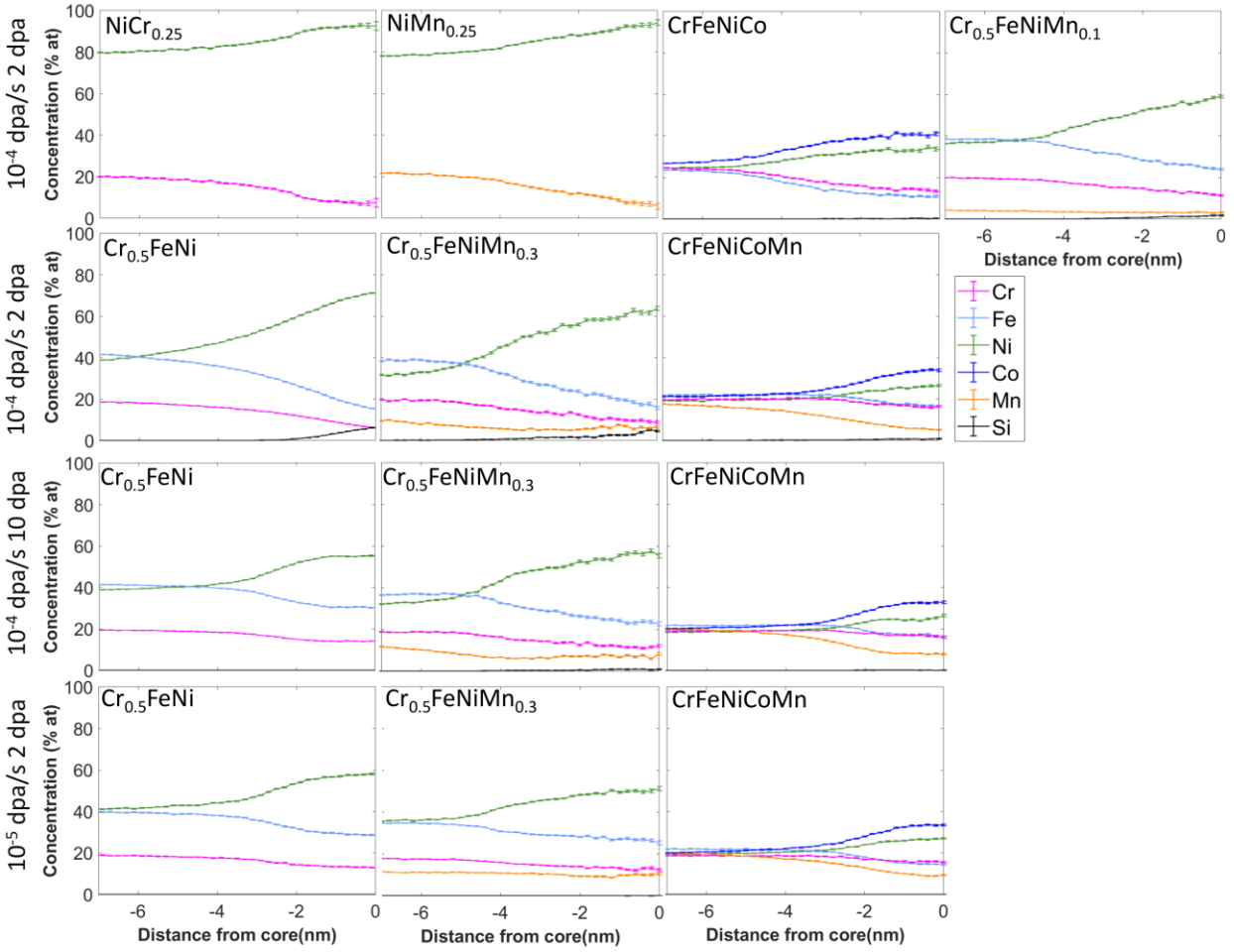

Figure 7.8: Proxigram analysis showing concentration profile across dislocations in all samples at all irradiation conditions.

7.4 Discussion

The study characterized the effect of dose rate and chemistry on the development of cavities and dislocation loops in seven Ni-based alloys of increasing compositional complexity during ion irradiation at 500 °C. The selected dose rates (10^{-4} dpa/s and 10^{-5} dpa/s) were lower than those used in prior published work, typically >10^{-3} dpa/s [33,35,36,183].

At higher dose rate (10^{-4} dpa/s), no simple relationship between alloy chemistry and the dislocation number density and size was observed. After 2 dpa, the simpler alloys ($NiCr_{0.25}$, $NiMn_{0.25}$) as well as $Cr_{0.5}FeNiMn_{0.3}$, and CrFeNiCo displayed lower loop number densities and higher sizes, while $Cr_{0.5}FeNi$ and equiatomic CrFeNiCoMn showed highest loop number densities and smallest sizes. The measured density and sizes and trends are in agreement with previous ion irradiation studies to higher dose (> 40 dpa) at higher dose rates (> 10^{-3} dpa/s), which also suggested that additions of Co or Mn tends to yield higher densities of smaller loops [157,183,299,300]. However, compared to $NiCr_{0.25}$, $NiMn_{0.25}$ exhibited smaller density of larger loops, contrary to the results of a prior higher dose rate irradiation [299]. Similarly, addition of Mn to $Cr_{0.5}FeNi$ is associated with lower densities of larger loops. On the contrary, in the presence of Co, Mn appears to significantly increase loop number density and decrease their size as shown with the behavior of the equiatomic CrFeNiCoMn alloy.

These initial differences in dislocation loop densities and sizes observed after 2 dpa became less pronounced after 10 dpa. For the three studied alloys, the number density of loops decreased while their size increased. This is generally consistent with the effect of dose reported in many metallic systems [268]. A possible explanation is that the nucleation rate of new dislocation loops becomes very small as dose increases, causing the continuously produced freely migrating interstitials to go to existing dislocation loops. In addition, at very high dislocation loop densities,

neighboring small dislocation loops can coalesce to form more stable dislocation loops [268,301,302], leading to a decrease in loop number density and increase in size.

At lower dose rates, the three studied alloys revealed a significant decrease in the loop number densities and increase in their size. This is consistent with prior literature on Ni-based alloys, which hypothesized that a decrease in the rate of defect production with dose rate results in fewer nucleation sites and leads to a lower density of larger dislocation loops [268,269,303]. In addition, alloy chemistry appears to have little effect on loop microstructure at lower dose rates as all three alloys exhibited roughly similar loop number density and size in all three alloys. This finding contrasts with previous studies [33,35,36,183], which suggested a strong correlation between chemistry and loop microstructure at very high dose rates. It is possible that the significant effect of chemistry on loop microstructure at very high dose rates is a dose rate effect. Under higher dose rates, at early dose levels, a higher number density of interstitial clusters are formed, which are potential nucleation sites for dislocation loops as compared to lower dose rates [268]. In less concentrated alloys, the presence of 1-D diffusion paths for interstitial clusters would result in long-range migration of interstitial clusters and interaction with other interstitial clusters causing them to coalesce and form dislocation loops [183]. This may result in the faster growth of dislocation loops at the expense of their number density. Other interstitial clusters, which do not experience coalescence grow via the continuous flux of freely migrating interstitials in their surrounding and form dislocation loops [267]. Therefore, at higher dose rates and early dose levels, in less concentrated alloys, the loop number density and size are controlled by two factors i.e., the coalescence of interstitial clusters via long-range migration and the flux of freely migrating interstitials around interstitial clusters. Notably, with increase in dose, the number density of these loops saturates as the newly created interstitial clusters are more likely to be captured by existing

loops, which acts as sinks before it meets other interstitials to form a new loop nucleus [266]. However, in MPEAs, the interstitial clusters migration is shown to be more localized in 3-D instead of long range 1-D using MD simulations [183], which suggest that the loops number density and size would be controlled by the flux of freely migrating interstitials around interstitial clusters. Perhaps, that's why a lower number density and higher size of dislocation loops is reported in less concentrated alloys as compared to MPEAs under high dose rate heavy ion irradiation [33,35,36,183]. However, at lower dose rates, the lower number density of interstitial clusters may reduce the probability of interaction of interstitial clusters via long range 1-D migration. Consequently, the loop number density and size would only be controlled by the flux of freely migrating interstitials around interstitial clusters and the effect of chemistry would be insignificant on the dislocation loops. Therefore, this may be the reason why the effect of chemistry was insignificant at lower dose rates.

Regarding cavity swelling, while pure Ni exhibited the highest extent of swelling at about 10% after 2 dpa at 10^{-4} dpa/s, swelling was reduced to less than 0.05% in all the alloys. One possible explanation is in the switch from long range 1-D migration of interstitial clusters in pure Ni to the trapping of defects in the alloys leading to a higher number density of dislocations, acting as sinks for vacancies and contributing towards decreasing the vacancy supersaturation [117,168,184]. At higher dose (10 dpa), the overall swelling increased in $Cr_{0.5}FeNiMn_{0.3}$ and equiatomic CrFeNiCoMn, while it remained unchanged in $Cr_{0.5}FeNi$. The increase in swelling with dose is consistent with cavity nucleation and growth regime, where sufficient vacancy flux is available to overcome the minimum number of vacancies required to cause cavity nucleation and to contribute towards the growth of existing cavities [261,262]. The addition of Mn leading to

earlier swelling may be linked to its fast diffusivity as compared to Ni, Fe, Cr, and Co, enhancing the mobility of vacancies, and reducing recombination [183,273].

At a dose rate of 10^{-4} dpa/s, $Cr_{0.5}FeNi$ and equiatomic CrFeNiCoMn showed significant cavities in the non-irradiated regions, whereas in $Cr_{0.5}FeNiMn_{0.3}$, cavities were only observed in the irradiated region. This can be correlated with the loop density in all three alloys where $Cr_{0.5}FeNi$ and equiatomic CrFeNiCoMn exhibit higher loop density. The higher dislocation density in the irradiated region acts as sinks for vacancies and prevents vacancy supersaturation and therefore slows down the void growth rate leading to lower swelling in the irradiated region [265]. Instead, the vacancies that escaped the irradiated region contribute to swelling. The presence of cavities in the non-irradiated region in some MPEAs is consistent with prior studies under high dose rate ion irradiation (Ni ions, $>10^{-3}$ dpa/s, 40-60dpa, 500 ^{o}C) [35,36,183], which is hypothesized to be caused by the increased vacancy mobility in MPEAs compared to less concentrated alloys. However, at 500 ^{o}C, the interstitial mobility is far greater than the vacancy mobility, which should also cause interstitial clusters/loops to form in the non-irradiated region, but this has not been observed experimentally. Therefore, this hypothesis is questionable and also does not account for the effect of dislocation density on swelling. Our results indicate that the effect of chemistry on dislocation loops, which are present at high dose rates, significantly affects the distribution of cavities in concentrated alloys.

With decreasing dose rate to 10^{-5} dpa/s, an increase in cavity swelling was observed in $Cr_{0.5}FeNi$ and equiatomic CrFeNiCoMn, which is expected due to lower recombination rate and a lower dislocation loop density, leading to higher vacancy supersaturation under lower dose rates [262]. However, no change in swelling was observed in $Cr_{0.5}FeNiMn_{0.3}$ likely due to a similar dislocation density. The swelling of 0.15% in equiatomic CrFeNiCoMn at 2 dpa using 10^{-5} dpa/s

in this study is compared to 0.1-0.2% reported in literature in the same alloy (using Ni ions, at 500 ^{o}C using 0.003 dpa/s at 50-60 dpa) [117,168,184]. This is a dose rate effect where the swelling curve with dose shifts towards lower dose levels at lower dose rates. In addition, cavity distribution became uniform throughout the irradiated region and non-irradiated region in $Cr_{0.5}FeNi$ and equiatomic CrFeNiCoMn, and only in the irradiated region in $Cr_{0.5}FeNiMn_{0.3}$ possibly due to a lower loop density in all alloys.

The dislocation loops exhibited enrichment of Co and Ni, and a depletion of Cr, Fe, and Mn wherever applicable. These findings are in line with prior irradiation studies on Ni-based concentrated alloys [157,188–191], and is consistent with radiation induced segregation (RIS) via modified inverse Kirkendall (MIK) mechanism, where the fastest diffusing species like Mn and Cr depletes and slower diffusing species like Co and Ni enriches [179,183,272,273]. The extent of element enrichment/depletion did not change with dose or dose rate despite variations in the number density and size of the loops. This suggests that the effect of dislocation chemistry on loop migration or growth is insignificant.

7.5 Conclusions

The study examined the impact of dose rate and chemistry on the formation of dislocation loops and cavities in seven Ni-based alloys with increasing compositional complexity, subjected to ion irradiation at 500 °C. Results showed that the effect of chemistry on the density and size of dislocation loops in concentrated Ni-based alloys is more prominent at high dose rates ($>10^{-4}$ dpa/s), but becomes insignificant at 10^{-5} dpa/s possibly due to the significant decrease in the defect production rate at lower dose rates causing the localized 3-D interstitial migration in MPEAs to not contribute towards the nucleation of dislocation loops. The lack of cavity swelling in the

irradiated region is only observed at high dose rates (>10^{-4} dpa/s) likely due to the high dislocation densities in the irradiated region, which can act as sinks whereas, at 10^{-5} dpa/s, the density of cavities becomes uniform in the irradiated region due to the significantly lower dislocation densities.

Chapter 8 Summary and Future Work

In this thesis, we delved into critical unanswered questions related to precipitation behavior in reactor pressure vessel (RPV) steels during irradiation, as well as the evolution of the microstructure in Ni-based multi-principal element alloys (MPEAs) under irradiation and thermal aging. RPV steels are low-alloy ferritic steels that are currently employed in light-water reactors due to their good mechanical and chemical properties while MPEAs are promising materials for nuclear energy applications due to their superior mechanical properties and possible increased resistance to irradiation damage compared to traditional alloys. This research yielded important findings, which we summarize below before offering insights into future research directions that will further advance the field of materials research.

8.1 Effect of phosphorus on the precipitation in RPV steels

Phosphorus is a common trace impurity element in steel that can lead to hardening and embrittlement. Dissolved phosphorus also segregates to grain boundaries, reducing their cohesive energy and resulting in brittle intergranular fracture. When exposed to irradiation, phosphorus clusters and segregates to dislocations alongside Cu, Mn, Ni, and Si. Hardening and embrittlement increase with rising phosphorus concentrations in low-Cu steels. However, the role of phosphorus in precipitation and associated hardening remains inadequately understood. To address this knowledge gap, we used atom probe tomography to investigate the individual and synergistic effects of P, Cu, and Ni on precipitation in seven different neutron-irradiated reactor pressure

vessel (RPV) steels with varying Cu, Ni, and P content at 290 ^{o}C (**Chapter 3**). Our analysis of different types of precipitates, including Mn-Si-Ni, P-Mn-Ni-Si, Cu-Mn-Si-Ni, and Cu-P-Mn-Si-Ni precipitates, suggests that early P clustering provides heterogeneous nucleation sites for the formation of P-Mn-Si-Ni precipitates, as evidenced by the increasing number density and volume fraction with rising P concentration and larger size compared to Mn-Si-Ni precipitates in Cu-free steels. The increase in precipitate volume fraction with increasing P and Ni concentration correlates with increased yield strength. In high-P steels, both Cu and P nucleate early and provide heterogeneous nucleation sites, eventually forming Cu-P-MSN precipitates with multi-core-shell morphology. This role of P is similar to that of Cu; both provide heterogeneous nucleation sites for Mn-Si-Ni precipitates. In high-P steels, the effect of P on precipitation is significant and is comparable to the effect of Cu in low-Cu low-P steels, leading to similar levels of embrittlement in both cases.

This work has significant implications for predictive embrittlement models. Accurate microstructural information is essential to predicting changes in mechanical properties during service. Although several programs have developed predictive embrittlement models and a quantitative understanding of radiation damage, these models rely on accurate microstructural information. However, current research on the effects of phosphorus has largely focused on nanoscale precipitation within grain interiors, with little attention paid to the evolution of precipitation on grain boundaries despite their role in hardening and embrittlement. Therefore, to fully comprehend the role of phosphorus, it is essential to investigate its effects on grain boundaries. Future work could extend the findings presented here by examining the effect of phosphorus on grain boundaries and incorporating these findings into predictive models of embrittlement.

8.2 Precipitate evolution in RPV steels under high dose rate ion irradiation

Surveillance capsules containing irradiation-sensitive vessel steels are used in nuclear reactors to monitor embrittlement. These capsules are placed on the inner wall of the RPV and periodically removed for testing. However, the low dpa rates (< 10^{-7} dpa/s) found in both test and commercial reactors mean that it can take years to reach the end-of-life dose of ≈ 0.2 dpa. Alternatively, heavy ion irradiation is used to produce very high dose rates (10^{-3} - 10^{-6} dpa/s) that can reach the end-of-life dose and beyond in a matter of hours or days. Although ion irradiation is a rapid alternative for studying the precipitation in RPV steels, there is limited understanding of the similarities and differences in the precipitation evolution between ions and neutrons. To bridge this knowledge gap, we conducted a systematic study of the microstructure evolution of eight different surveillance RPV steels with varying Cu, Ni, and Si. The steels were irradiated to two dose levels (0.3 and 1.2 dpa) under ion irradiation using 10^{-5}-10^{-6} dpa/s at 290 ^{o}C (**Chapter 4**). We also compared the low-dose ion irradiated precipitate microstructures to those in the same neutron-irradiated RPV steels. Our findings suggest that there is a similar qualitative precipitate evolution under high dose rate ions as reported under lower dose rate neutrons in the literature where, the precipitate number density and volume fraction increased with dose, and the precipitate compositions followed the steel composition at both low and high doses. Furthermore, we compared ion-irradiated and neutron-irradiated steels with similar compositions after 0.2-0.3 dpa. Our results revealed higher precipitate number densities and smaller sizes under high dose rate ion irradiations, while the precipitate volume fractions and compositions were very similar. The larger Cu-Mn-Ni-Si precipitates in the neutron-irradiated Cu bearing alloys exhibited a Mn-Ni-Si appendage morphology, while the smaller precipitates formed under ion irradiations had a mix of Cu core Mn-Ni-Si shell and appendage characteristics likely due to the different precipitate sizes.

This work has the potential to be extended in the future to develop models that can extrapolate ion irradiation data to understand damage development under low neutron flux conditions in RPV steels. However, to build robust models, more precipitation and hardening data in a series of RPV steels with varying solute contents at different dose levels are needed. While this current research provides a correlation between ion and neutron irradiation in only three steels, similar atom probe tomography characterization can be applied to samples of the same eight RPV steels that were neutron-irradiated (E > 1 MeV) at 290 ^{o}C at 0.2 dpa and 1.2 dpa using 5.4 x 10^{-9} dpa/s in the Advanced Test Reactor. Such a systematic comparison can generate insights into dose rate effects for a range of alloy chemistries. This will be a valuable addition to the current understanding of the effects of ion irradiation on RPV steels and will provide valuable data for the development of models that can better predict the behavior of RPV steels under neutron irradiation.

8.3 Phase stability of CrFeNi-based MPEAs under irradiation

Prior studies have shown the stability of CrFeNi-based MPEAs such as $Cr_{0.6}$FeNiMn, equiatomic CrFeNiCoMn, and equiatomic CrFeNiCoPd against phase decomposition during high dose rate ion irradiation (>10^{-3} dpa/s). However, prior electron irradiation and limited thermal annealing studies found that these alloys are susceptible to phase decomposition. Therefore, further research was necessary to understand the equilibrium phases and kinetics of phase decomposition in these alloys at intermediate to high temperatures and the impact of phase decomposition on the development of irradiation damage. To address this knowledge gap, the microstructures of $Cr_{0.6}$FeNiMn and CrFeNiCo$Pd_{0.7}$ alloys at 500 °C were characterized after ion irradiation using lower dose rates (10^{-4}-10^{-5} dpa/s) to two doses (2 and 10 dpa), and the mechanisms of phase decomposition during long-term thermal aging of $Cr_{0.6}$FeNiMn at 500 °C were also studied.

Contrary to previous ion irradiation studies conducted at higher dose rates, both alloys exhibited irradiation-accelerated phase decomposition. In $Cr_{0.6}FeNiMn$, a high number density of homogeneously distributed nanometer-scale $L1_0$ Ni and Mn rich precipitates, along with fewer Cr rich precipitates, formed in the matrix, while in $CrFeNiCoPd_{0.7}$ decomposed into Pd-Fe rich and Co-Ni rich regions was observed. In addition, the significant presence of NiMn precipitates is likely to have played a role in the unexpectedly high density of dislocation loops observed, which in turn contributed to the decelerated rate of cavity swelling.

There is considerable potential for further research to expand upon the findings of this study and gain a deeper understanding of the role that coherent precipitates play in the evolution of dislocation loops and cavities in $Cr_{0.6}FeNiMn$. One potential avenue of investigation would be to examine the impact of the number density and size of NiMn-rich precipitates on the density and diameter of dislocation loops and cavities. This could be accomplished by irradiating a phase decomposed $Cr_{0.6}FeNiMn$ material and comparing the resulting data to that obtained from the present study. The phase decomposed $Cr_{0.6}FeNiMn$ alloy can be obtained by thermally aging two coarse grained samples at 500°C for 336 and 1008 hours, respectively, which would result in a homogenous distribution of NiMn-rich precipitates with different size distributions. These phase decomposed samples could then be subjected to irradiation conditions similar to those used in the current study, allowing for an observation of the effect of NiMn-rich precipitates of varying sizes and distributions on the evolution of dislocation loops and cavities. Such investigations could provide valuable insights into the development of irradiation tolerant materials.

8.4 Phase stability of CrFeNi-based MPEAs under thermal aging

During thermal aging at 500°C, $Cr_{0.6}$FeNiMn underwent phase decomposition characterized by two independent and parallel mechanisms: continuous precipitation through homogeneous nucleation and growth of NiMn precipitates within the matrix, and cellular precipitation initiating from grain boundaries and eventually sweeping through the entire material. The rapid and extensive transformation resulting from cellular precipitation led to the formation of three distinct phases within just nine weeks. These findings contribute to a better understanding of the equilibrium phases and their kinetics, as well as the mechanisms of phase decomposition in $Cr_{0.6}$FeNiMn.

We only had time to focus on $Cr_{0.6}$FeNiMn to provide context to the decomposition since under irradiation. Similar work is needed to understand how the CrFeNiCo$Pd_{0.7}$ decomposes under thermal aging condition. Furthermore, similar decomposition processes are expected in other CrFeNi-based alloys, warranting similar studies on alloys such as the Cantor composition. Comparing the aging responses of these different alloys could help us to understand the mechanisms that control the extent and kinetics of continuous and discontinuous precipitation in these alloys. Furthermore, complementing such microstructural studies with mechanical property measurements would be essential. We for example expect that for the case of the $Cr_{0.6}$FeNiMn alloy studied here, the continuous precipitation may improve mechanical properties through precipitation hardening, whereas the cellular precipitation could compromise the mechanical properties. Such a combined investigation could provide valuable insights into the design and development of new alloys with improved mechanical and irradiation resistance properties.

8.5 Effect of chemistry and dose rate on the microstructure of MPEAs under irradiation

Previous studies using ion irradiation have suggested that MPEAs have a higher resistance to swelling and reduced damage accumulation compared to stainless steels and simpler Ni-based concentrated alloys. However, these studies were conducted at very high dose rates ($>10^{-3}$ dpa/s), which can significantly affect cavity swelling and dislocation microstructure. To better understand the role of dose rate on dislocation loops and cavity swelling in MPEAs, pure Ni and seven Ni-based alloys with increasing compositional complexity were irradiated under ion irradiation at 500 ^{o}C using lower dose rates (10^{-4} – 10^{-5} dpa/s). The results indicated that the effect of chemistry on the density and size of dislocation loops in concentrated Ni-based alloys is more prominent at high dose rates ($>10^{-4}$ dpa/s), but becomes insignificant at 10^{-5} dpa/s. This may be due to the significant decrease in the defect production rate at lower dose rates, which prevents the localized 3-D interstitial migration in MPEAs from contributing to the nucleation of dislocation loops. At high dose rates ($>10^{-4}$ dpa/s), the lack of cavity swelling in the irradiated region is likely due to the high dislocation densities, which can act as sinks. However, at 10^{-5} dpa/s, the density of cavities becomes uniform in the irradiated region due to the significantly lower dislocation densities.

To further enhance the proposed hypotheses, this research can be expanded to incorporate simulation studies. This can be accomplished by utilizing density functional theory and molecular dynamics calculations to obtain the displacement energies of various atoms, defect migration energies for both interstitials and vacancies of all the elements involved, element-defect binding energies, and diffusion coefficients of all the elements. Subsequently, Monte Carlo simulations can be employed to simulate the dislocation and cavity evolution under a constant flux of defects, thereby substantiating the experimentally observed trends.

Appendices

Appendix A: Experimental Details

A1: Arc melting

Ni-based alloys were synthesized using an arc melting process in an MAM-1 arc melter. The required amounts of pure constituent metals (Cr, Fe, Ni, Co, Mn, and Pd with >99,9% purity) were measured and mixed to achieve the desired composition. The mixture was cleaned and sonicated with acetone and ethanol to remove any impurities. One cavity in the Cu stage of the arc melter was filled with the mixture, while another was filled with a pure Ti slug cleaned using the same procedure. After attaching the Cu stage to the arc melter, the chamber was evacuated with a roughing pump for 10 minutes before being purged with pure Ar gas to reach a pressure of 1 atm. This vacuum and purging sequence was repeated four times before leaving pure Ar gas in the chamber at 1 atm. The chiller was set to 21°C to cool down the stage while melting, and the Ti was melted first twice as an oxygen getter. The sample slugs were then melted for 30 seconds to form a cast bar. To ensure even melting, the cast bar was flipped and melted five more times. Finally, the obtained cast bars were cleaned with ethanol for further mechanical processing and heat treatments.

A2: Irradiation experiments

The cast bars were cut into 12x3x2 mm^3 bars using electrical discharge machine (EDM). These bars were encapsulated in quartz tubes filled with Argon gas at 1 atm. These tubes were put

in a vertical furnace and the samples were homogenized for 24 hrs. at 1100 ^{o}C followed by water quenching to ensure an equiaxed grain structure and a homogeneous chemistry. The homogenized samples were ground using SiC grinding papers with grits of 320, 600, 800, and 1200. After grinding, samples were electropolished using a twin jet electropolishing setup to remove the surface damage induced by grinding. The samples were held with a stainless-steel tweezer connected to a power supply, which served as the anode while a graphite bar was used for cathode. The electrolyte solution consisted of 7% perchloric acid plus 94% methanol. The electrolyte was maintained at roughly -50 °C using a cooling bath containing methanol, water, and dry ice pellets. To start the electropolishing, the sample surface facing the cathode was soaked into the electrolyte for 10 seconds at 50 V. A magnetic stirrer was used to constantly stir the electrolyte in order to refresh the electrolyte near the sample surface. After electropolishing, the sample was quickly removed from the electrolyte and rinsed with methanol to prevent further etching.

At least four samples were irradiated in each irradiation experiment. The electropolished samples were loaded on the irradiation stage with two dummy samples on each side with thermocouples welded on their surface to monitor the temperature during irradiation. A stainless-steel mask with 10x20 mm^2 opening was placed to hold the samples and define the irradiation area (Figure A 1). The irradiation experiments were conducted using a 6 MeV Fe^{3+} ions in a 1.7 MV Tandem accelerator in the Michigan Ion Beam Laboratory at the University of Michigan. After loading the stage in the beamline, laser was used to align the slits to allow the beam on the irradiation area. Before the irradiation, the stage was heated, and thermocouples were used to ensure 500 ^{o}C on the samples surface and were also used to calibrate the thermal camera (Figure A 2). During irradiation, the beam current was monitored to ensure the desired flux of ions.

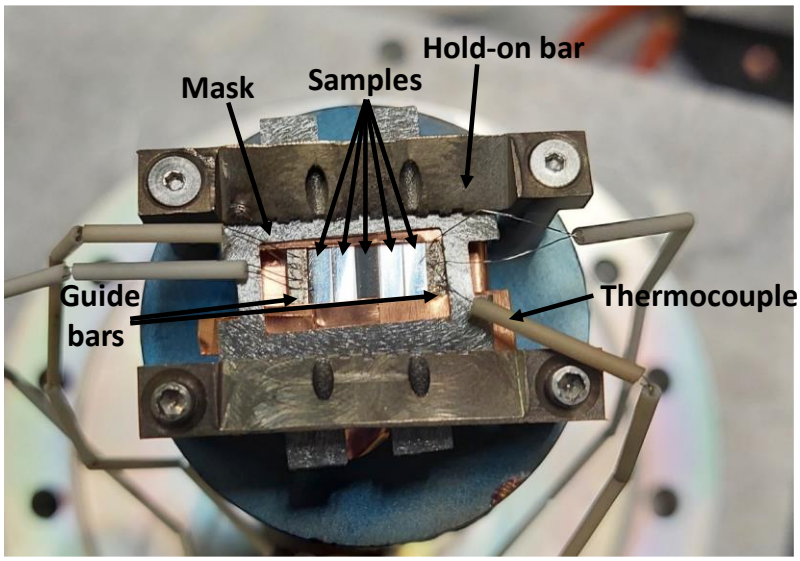

Figure A 1: Picture showing irradiation setup before the start of irradiation setups.

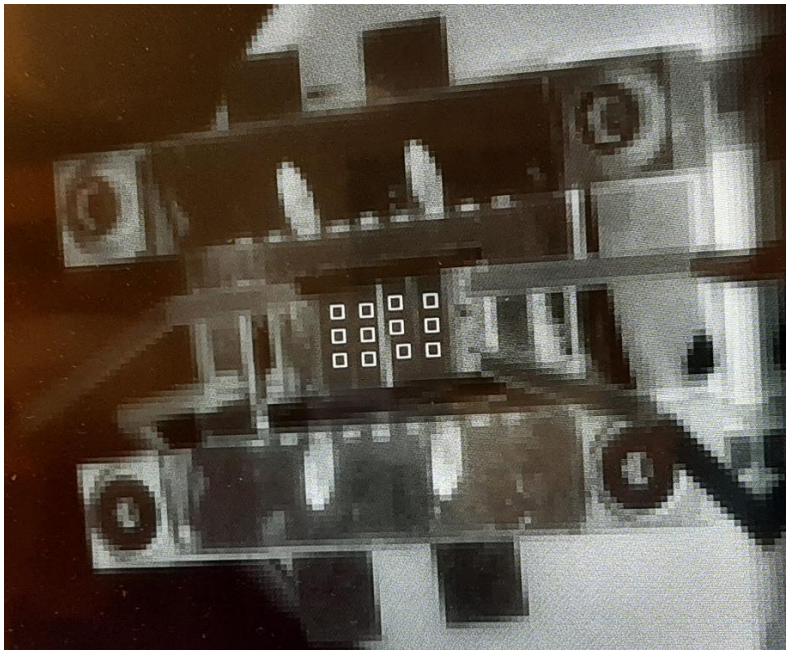

Figure A 2: Infrared image of the stage during irradiation experiment with area of interest (AOIs) to monitor the temperature.

To calculate the beam current at a given ion flux, Stopping and Range of Ions in Matter (SRIM) software was used. SRIM calculations were performed to estimate the damage profile in

Ni-based alloys (Figure A 3) using Kinchin-Pease mode with the atomic displacement energy of 40eV for all elements in the sample. A depth of 700 nm was chosen to accumulate the desired dose. The damage value (displacement/A^0/ion) obtained from SRIM at 700 nm was used to obtain the required beam current for a given ion flux using the following equation.

$$Beam\ current(A) =$$

$$\frac{Dose\ rate\ \left(\frac{dpa}{s}\right) \times atomic\ density\ \left(\frac{atoms}{cm^3}\right) \times ion\ charge(Q) \times irradaition\ area(cm^2)}{SRIM\ damage\ \left(\frac{diplacement}{Angstrom \times ion}\right)}$$

Irradiation was performed under a pressure below 10-7 torr using a raster-scanning mode with frequencies of ~220 Hz in the x-direction and ~2000 Hz in the y-direction. Once the desired dose was reached, the irradiation stage was quickly cooled using cold air to room temperature to avoid any thermal annealing effects.

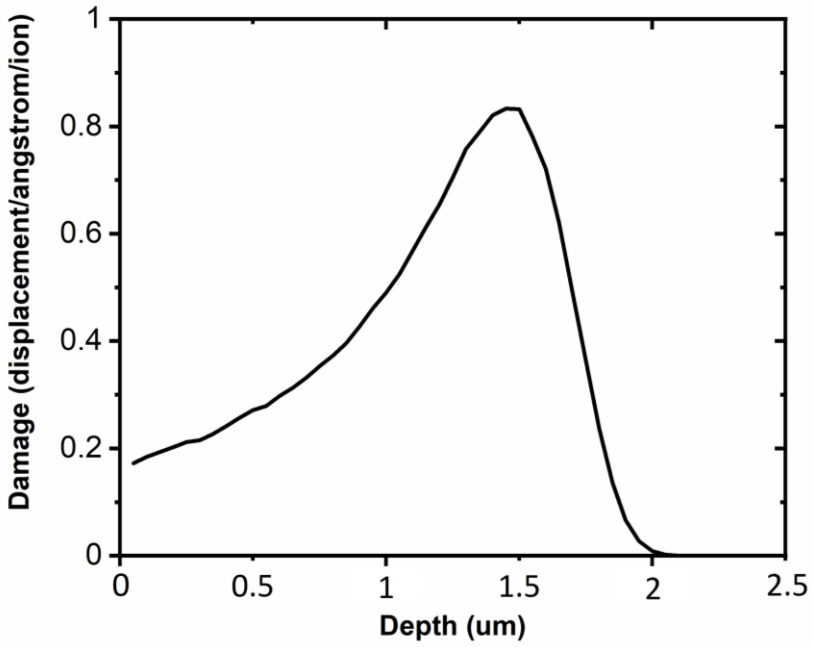

Figure A 3: Damage profile calculated using SRIM in $Cr_{0.5}FeNi$ using 6 MeV Fe^{3+} ions.

A3: Flash electropolishing for TEM samples

To get rid of the FIB induced damage in the TEM sample surface, flash electropolishing was used as the last step. FIB was used to thin the TEM lamella to a thickness of 200-250 nm. The procedure for flash polishing is similar to twin jet except a timer delay is needed to electropolish for time in milliseconds range. In addition, a gold tweezer is used instead of steel. The samples were electropolished for 100 ms and then imaged in the optical microscope. If the perforation between Pt layer and the sample is observed, the electropolishing is stopped otherwise continued in the increments of 30 ms until perforation was observed (Figure A 4).

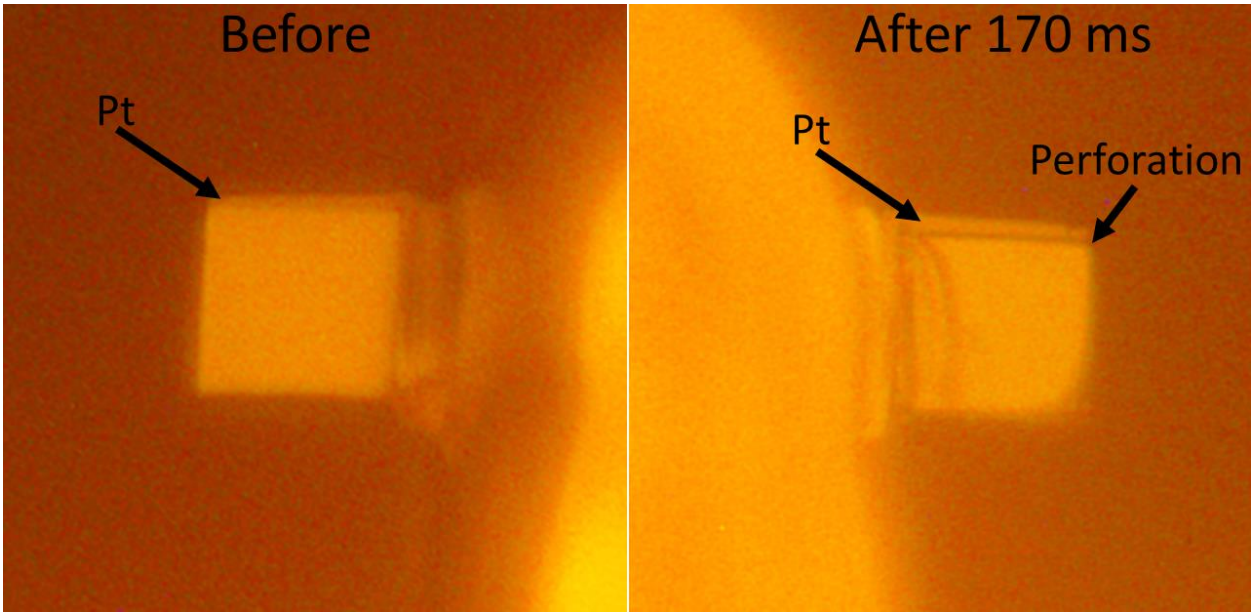

Figure A 4: Before and after flash electropolishing images of irradiated $Ni_{80}Mn_{20}$ sample

Appendix B: Supplementary Figures

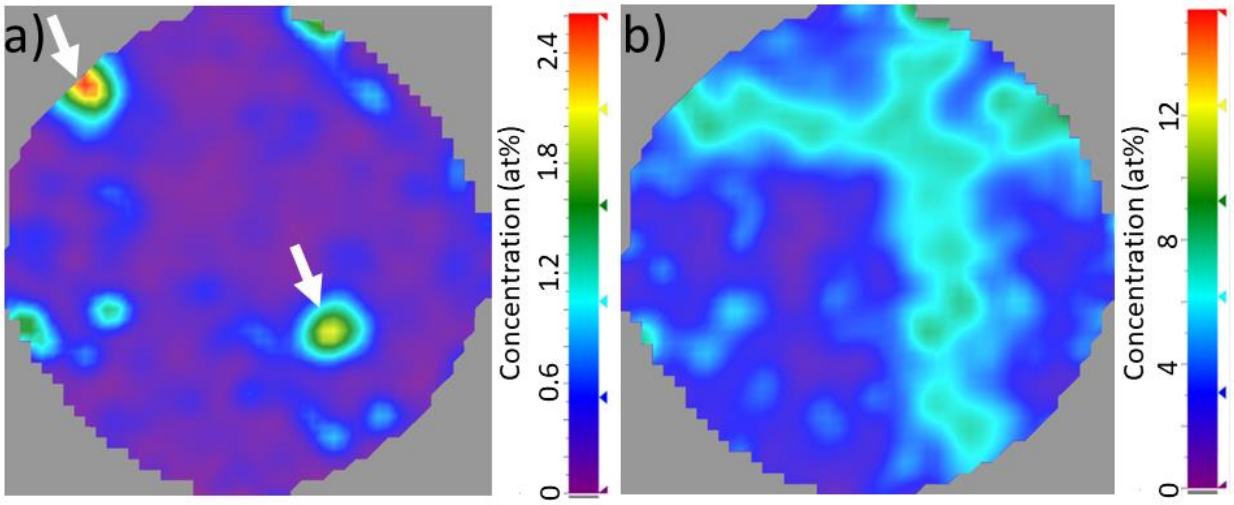

Figure B 1: Representative evaporation maps from CM7 tip1 obtained using 2D concentration plot along z-axis with 2 nm pixel size showing a) P distribution along poles (arrows), and b) Si distribution along poles.

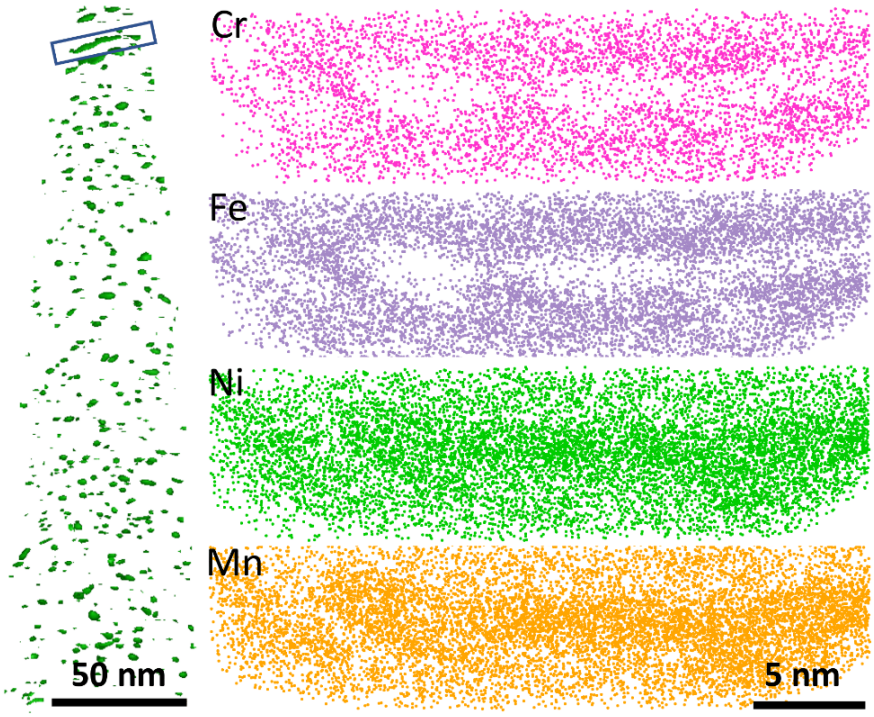

Figure B 2: APT reconstruction showing NiMn rich precipitates in the matrix and on dislocation (green isosurface 70 at. % Ni+Mn) after 60 hrs. at 500 ^{o}C in $Cr_{0.6}$FeNiMn. Element maps taken from highlighted region (blue) showing interconnected NiMn rich precipitates.

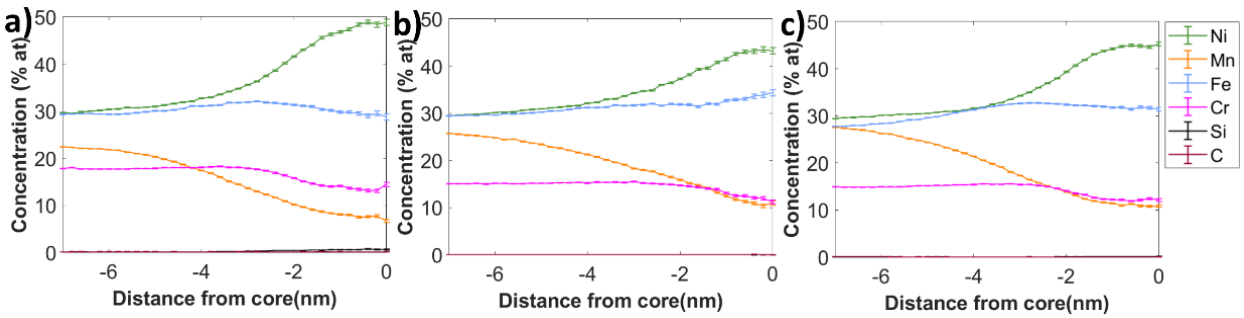

Figure B 3: Proxigram analysis showing concentration profile across dislocations at a) 2dpa using 10^{-4} dpa/s, b) 10 dpa using 10^{-4} dpa/s, and c) 2 dpa using 10^{-5} dpa/s in $Cr_{0.6}FeNiMn$.

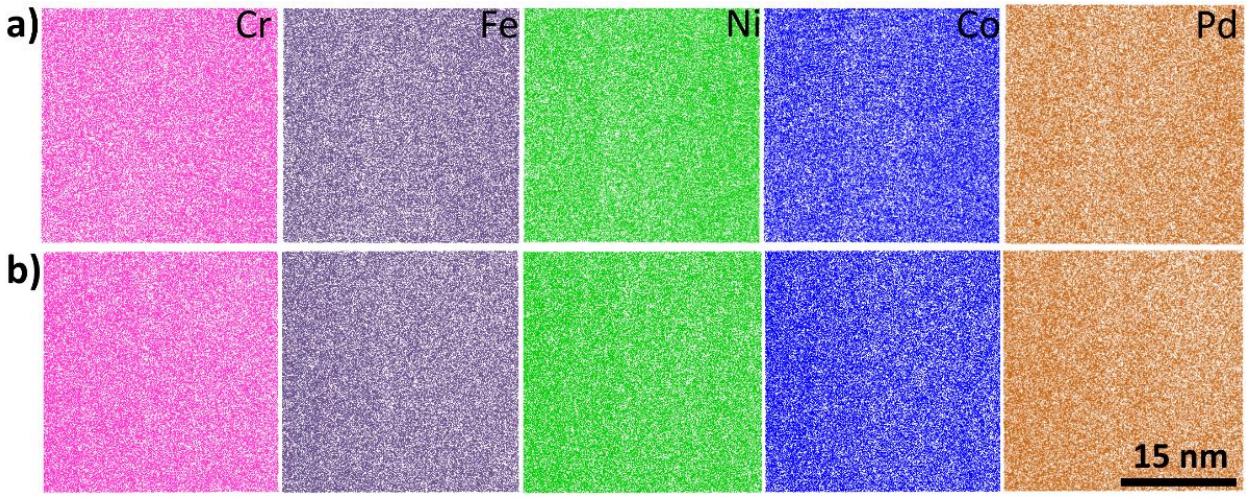

Figure B 4: APT element maps (30x30x5 nm^3) showing random distribution of alloying elements at 500 ^oC after a) 6 hrs., and b) 30 hrs. in $CrFeNiCoPd_{0.7}$.

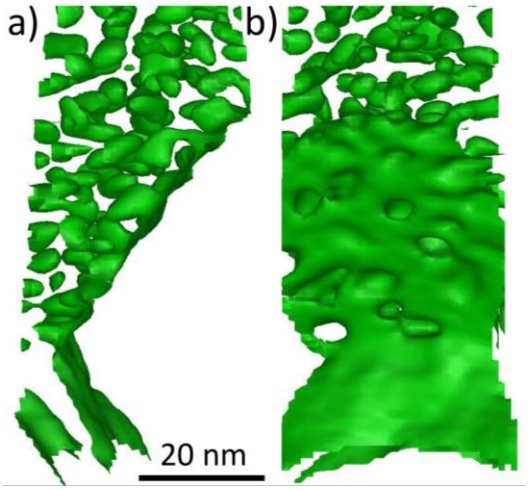

Figure B 5: a) Front and b) side view of NiMn-rich precipitates attached to the NiMn-rich phase at the reaction front after 1008 hrs. The iso concentration of 70 at. & (Ni+Mn) was used to draw isosurfaces.

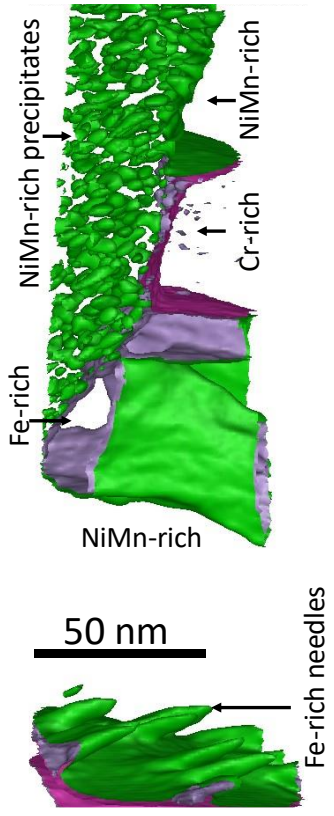

Figure B 6: Fe-rich fingers in the transformed region pointing in the opposite direction to the progression of reaction front after 1008 hrs. The iso concentration of 70 at. & (Ni+Mn) in green, 40 at. % in purple, and 40 at. % in pink were used to illustrate NiMn-rich phase, Fe-rich phase, and Cr-rich phase, respectively.

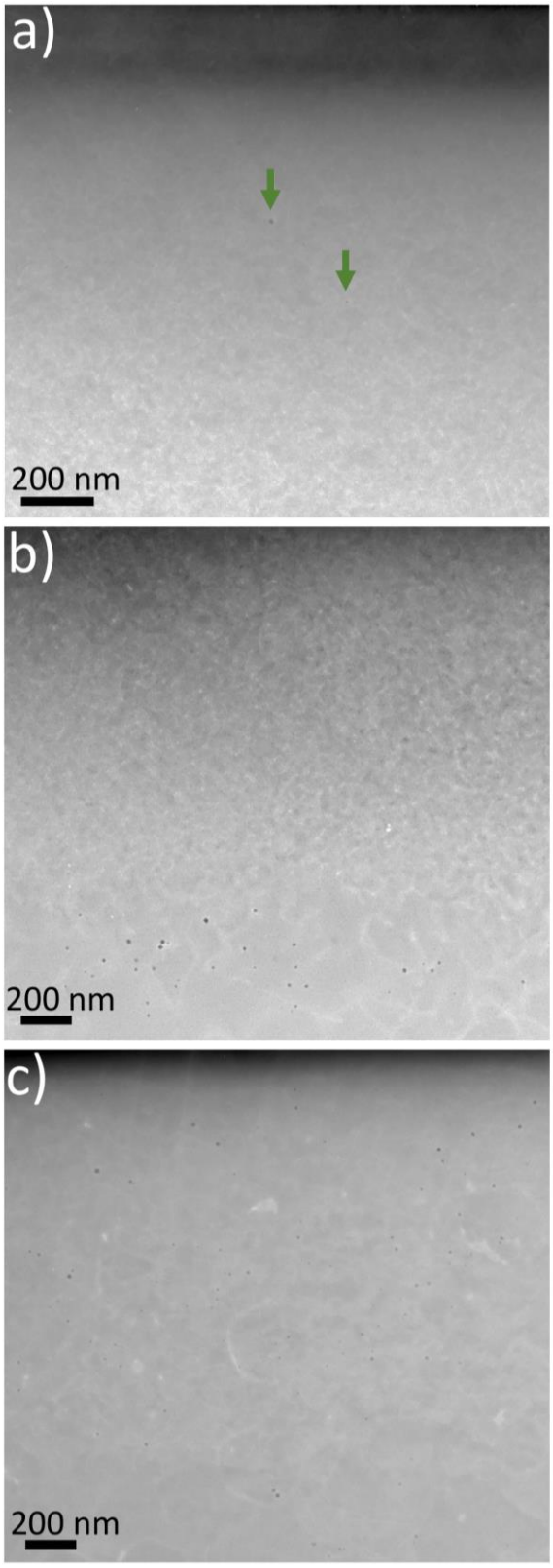

Figure B 7: STEM HAADF images showing different cavity distribution in the irradiated region equiatomic CrFeNiCoMn after a) 2 dpa, b) 10 dpa using 10^{-4} dpa/s, and 2 dpa using 10^{-5} dpa/s.

Figure B 8: Solute-decorated dislocation loops (using 50 at. % Ni isosurfaces) in $Cr_{0.5}FeNi$ at 10 dpa using 10^{-4} dpa/s at 500 ^{o}C.

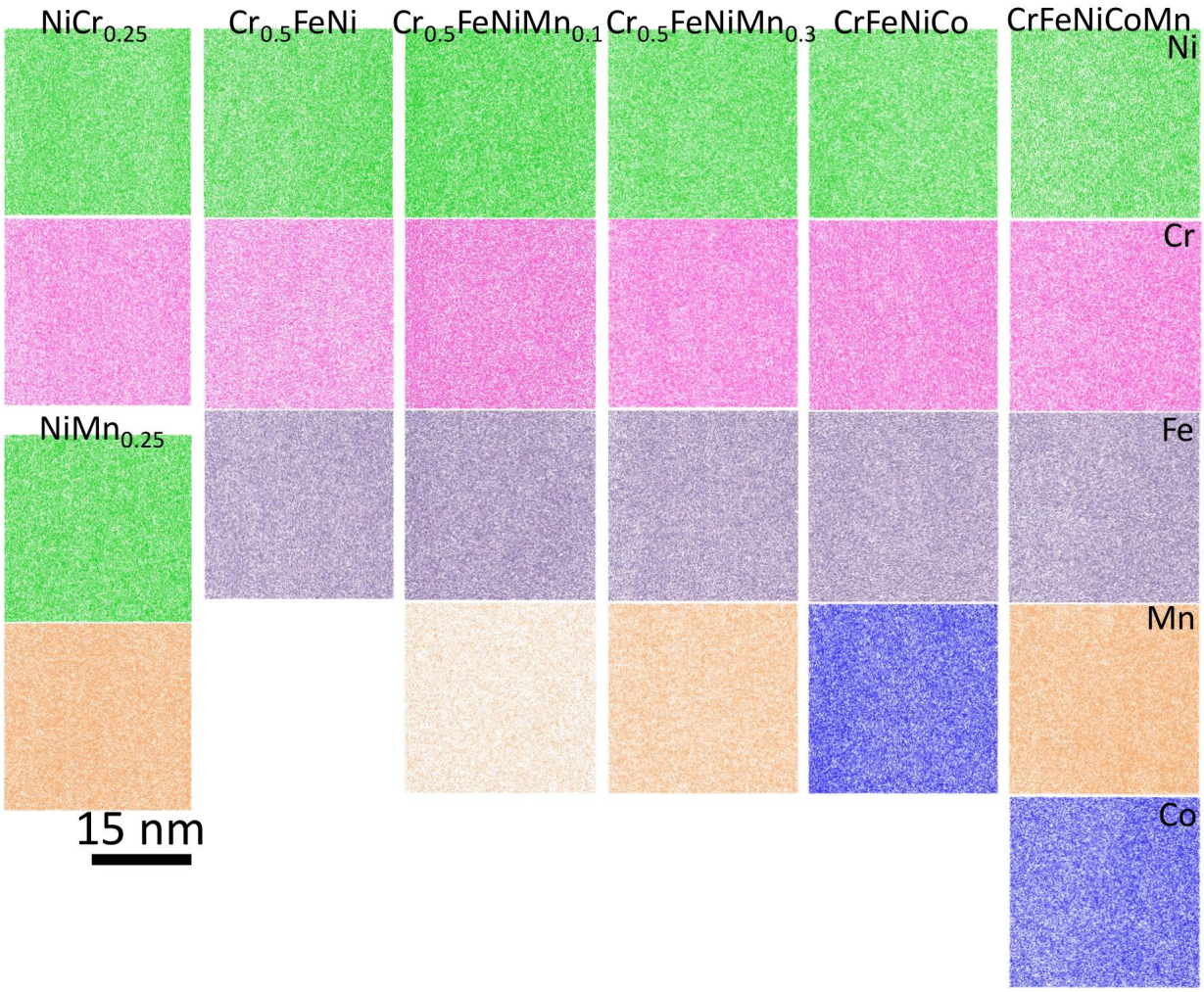

Figure B 9: APT element maps (30x30x10 nm^3) showing random distribution of alloying elements in all alloys at 500 ^oC, 2dpa using 10^{-5} dpa/s.

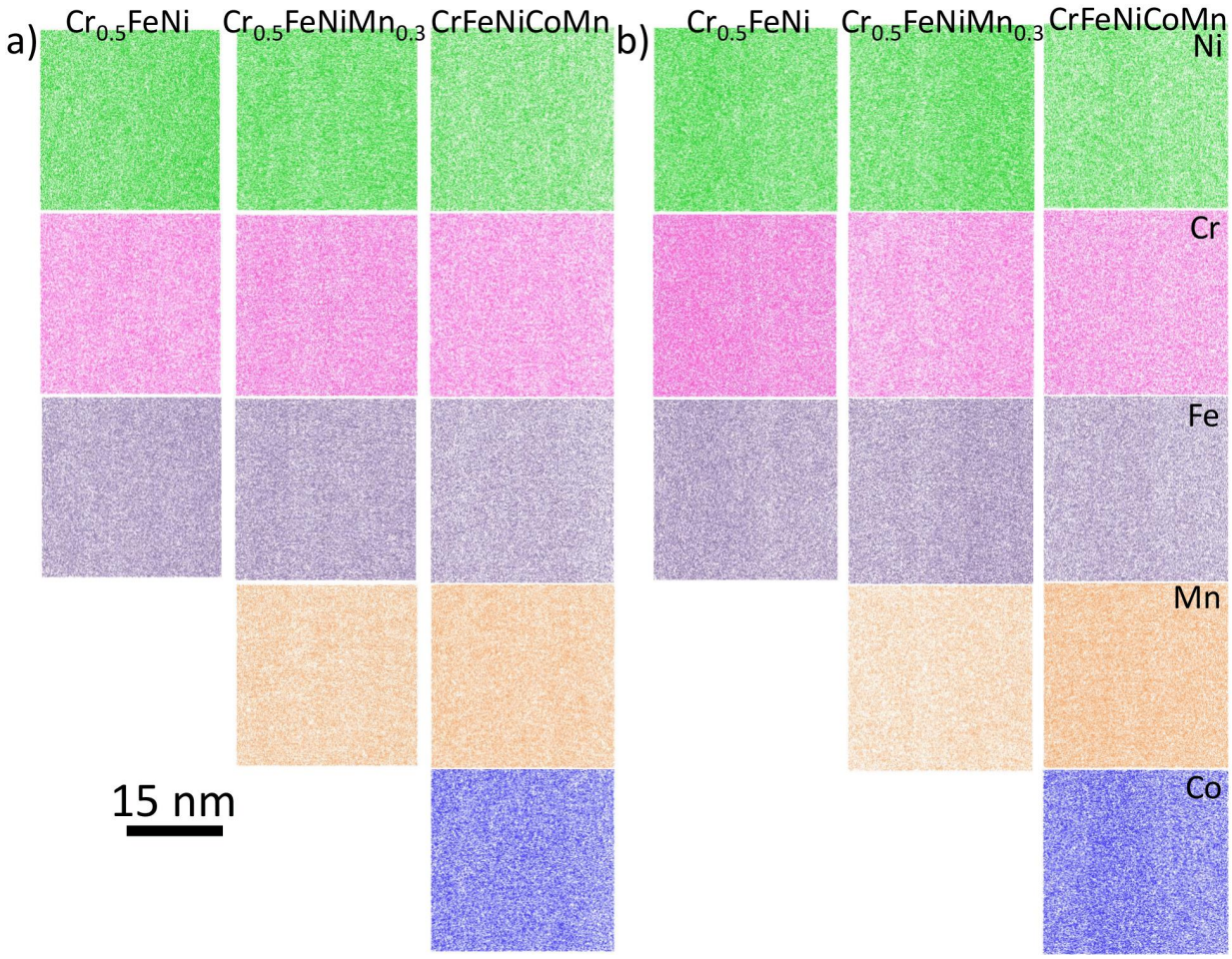

Figure B 10: APT element maps (30x30x10 nm^3) showing random distribution of alloying elements in all three alloys at 500 ^oC a) 10 dpa using 10^{-4} dpa/s and b) 2 dpa using 10^{-5} dpa/s.

Appendix C: Supplementary Tables

Table C 1**:** Number of MSN and P-MSN precipitates in the matrix, and precipitates on dislocation and the volume of tip in all samples.

Sample	**Precipitate type**	**Average Number of clusters**	**Volume of reconstruction (x 10^{-22} nm^3)**
CM3 Tip 1	MSN in the matrix	10	8.5
	P-MSN in the matrix	0	
	Precipitates on dislocation	50	
	Total	60	
CM3 Tip2	MSN in the matrix	30	6.5
	P-MSN in the matrix	0	
	Precipitates on dislocation	19	
	Total	49	
CM4	MSN in the matrix	21	2.1
	P-MSN in the matrix	8	
	Precipitates on dislocation	0	
	Total	29	
CM5 Tip1	MSN in the matrix	12	0.1
	P-MSN in the matrix	6	
	Precipitates on dislocation	0	
	Total	18	
CM5 Tip2	MSN in the matrix	31	2.4
	P-MSN in the matrix	25	
	P-MSN on dislocation	0	
	Total	56	
CM6 Tip1	MSN in the matrix	104	2.7
	P-MSN in the matrix	6	
	Precipitates on dislocation	0	
	Total	110	
CM6 Tip2	MSN in the matrix	572	22.9
	P-MSN in the matrix	30	
	Precipitates on dislocation	0	
	Total	602	
CM6 Tip3	MSN in the matrix	412	14.2
	P-MSN in the matrix	18	
	Precipitates on dislocation	20	
	Total	450	
CM7 Tip1	MSN in the matrix	206	8.3
	P-MSN in the matrix	58	
	Precipitates on dislocation	10	
	Total	274	
CM7 Tip2	MSN in the matrix	161	8.2
	P-MSN in the matrix	40	
	Precipitates on dislocation	27	
	Total	228	
CM7	MSN in the matrix	134	5.1

Tip3	P-MSN in the matrix	21	
	Precipitates on dislocation	20	
	Total	175	
CM7 Tip4	MSN in the matrix	241	15.5
	P-MSN in the matrix	100	
	Precipitates on dislocation	38	
	Total	379	
CM13 tip1	MSN in the matrix	10	2.5
	Cu-MSN in the matrix	26	
	Total	36	
CM13 tip2	MSN in the matrix	5	0.6
	Cu-MSN in the matrix	8	
	Total	13	
CM14 T16 IVAR	MSN in the matrix	16	4.6
	Cu-MSN in the matrix	27	
	P-MSN in the matrix	2	
	Cu-P-MSN in the matrix	3	
	Total	48	

References

[1] B.P. Schwartz, B.P. Schwartz, D. Randall, D. Randall, E. Summary, E. Summary, An Abrupt Climate Change Scenario and Its Implications for United States National Security, October. (2003) 1–22. https://doi.org/10.1128/JB.184.8.2167.

[2] C. Mora, D. Spirandelli, E.C. Franklin, J. Lynham, M.B. Kantar, W. Miles, C.Z. Smith, K. Freel, J. Moy, L. V. Louis, E.W. Barba, K. Bettinger, A.G. Frazier, J.F. Colburn IX, N. Hanasaki, E. Hawkins, Y. Hirabayashi, W. Knorr, C.M. Little, K. Emanuel, J. Sheffield, J.A. Patz, C.L. Hunter, Broad threat to humanity from cumulative climate hazards intensified by greenhouse gas emissions, Nat. Clim. Chang. 8 (2018). https://doi.org/10.1038/s41558-018-0315-6.

[3] Global Greenhouse Gas Emissions Data | US EPA, (n.d.). https://www.epa.gov/ghgemissions/global-greenhouse-gas-emissions-data (accessed September 20, 2021).

[4] N. Apergis, J.E. Payne, K. Menyah, Y. Wolde-Rufael, On the causal dynamics between emissions, nuclear energy, renewable energy, and economic growth, Ecol. Econ. 69 (2010) 2255–2260. https://doi.org/10.1016/j.ecolecon.2010.06.014.

[5] U.S. nuclear industry - U.S. Energy Information Administration (EIA), (n.d.). https://www.eia.gov/energyexplained/nuclear/us-nuclear-industry.php (accessed September 20, 2021).

[6] K. Ehrlich, J. Konys, L. Heikinheimo, Materials for high performance light water reactors, J. Nucl. Mater. 327 (2004) 140–147. https://doi.org/10.1016/J.JNUCMAT.2004.01.020.

[7] G. Locatelli, M. Mancini, N. Todeschini, Generation IV nuclear reactors: Current status and future prospects, Energy Policy. 61 (2013) 1503–1520. https://doi.org/10.1016/J.ENPOL.2013.06.101.

[8] P.J. Maziasz, J.T. Busby, Properties of austenitic steels for nuclear reactor applications, Compr. Nucl. Mater. 2 (2012) 267–283. https://doi.org/10.1016/B978-0-08-056033-5.00019-7.

[9] Integrity of Reactor Pressure Vessels in Nuclear Power Plants: Assessment of Irradiation Embrittlement Effects in Reactor Pressure Vessel Steels, International Atomic Energy Agency, Vienna, 2009. https://www.iaea.org/publications/7915/integrity-of-reactor-pressure-vessels-in-nuclear-power-plants-assessment-of-irradiation-embrittlement-effects-in-reactor-pressure-vessel-steels (accessed September 5, 2021).

[10] G.R. Odette, G.E. Lucas, Recent progress in understanding reactor pressure vessel steel embrittlement, Taylor & Francis, 1998. https://doi.org/10.1080/10420159808229676.

[11] G.R. Odette, T. Yamamoto, T.J. Williams, R.K. Nanstad, C.A. English, On the history and status of reactor pressure vessel steel ductile to brittle transition temperature shift prediction models, J. Nucl. Mater. 526 (2019) 151863. https://doi.org/10.1016/j.jnucmat.2019.151863.

[12] J.T. Busby, R.K. Nanstad, R.E. Stoller, Z. Feng, D.J. Naus, Materials Degradation in Light Water Reactors: Life After 60,???, (2008). https://doi.org/10.2172/938766.

[13] A. Ballesteros, E. Altstadt, F. Gillemot, H. Hein, J. Wagemans, J. Rouden, J. Barthelmes, K. Wilford, M. Serrano, M. Brumovsky, R. Chaouadi, S. Ortner, Monitoring radiation embrittlement during life extension periods, Nucl. Eng. Des. 267 (2014) 197–206. https://doi.org/10.1016/j.nucengdes.2013.11.068.

[14] M. Kirk, C. Santos, E. Eason, J. Wright, G.R. Odette, Updated Embrittlement Trend Curve for Reactor Pressure Vessel Steels, (2003).

[15] E. Eason, J. Wright, M.G. Odette, Improved Embrittlement Correlations for Reactor Pressure Vessel Steels., (1998). http://www.ntis.gov/ordernow (accessed March 8, 2022).

[16] E.D. Eason, G.R. Odette, R.K. Nanstad, T. Yamamoto, A physically-based correlation of irradiation-induced transition temperature shifts for RPV steels, J. Nucl. Mater. 433 (2013) 240–254. https://doi.org/10.1016/j.jnucmat.2012.09.012.

[17] E.D. Eason, G.R. Odette, R.K. Nanstad, T. Yamamoto, A Physically Based Correlation of Irradiation-Induced Transition Temperature Shifts for RPV Steels, (2007). https://doi.org/10.2172/941022.

[18] G.R. Odette, B.D. Wirth, D.J. Bacon, N.M. Ghoniem, Multiscale-Multiphysics Modeling of Radiation-Damaged Materials: Embrittlement of Pressure-Vessel Steels, MRS Bull. 26 (2001) 176–181. https://doi.org/10.1557/MRS2001.39.

[19] R.L. Klueh, D.S. Gelles, S. Jitsukawa, A. Kimura, G.R. Odette, B. Van der Schaaf, M. Victoria, Ferritic/martensitic steels - Overview of recent results, J. Nucl. Mater. 307–311 (2002) 455–465. https://doi.org/10.1016/S0022-3115(02)01082-6.

[20] A.A.F. Tavassoli, A. Alamo, L. Bedel, L. Forest, J.M. Gentzbittel, J.W. Rensman, E. Diegele, R. Lindau, M. Schirra, R. Schmitt, H.C. Schneider, C. Petersen, A.M. Lancha, P. Fernandez, G. Filacchioni, M.F. Maday, K. Mergia, N. Boukos, Baluc, P. Spätig, E. Alves, E. Lucon, Materials design data for reduced activation martensitic steel type EUROFER, J. Nucl. Mater. 329–333 (2004) 257–262. https://doi.org/10.1016/j.jnucmat.2004.04.020.

[21] R.L. Klueh, A.T. Nelson, Ferritic/martensitic steels for next-generation reactors, J. Nucl. Mater. 371 (2007) 37–52. https://doi.org/10.1016/j.jnucmat.2007.05.005.

[22] S.J. Zinkle, N.M. Ghoniem, Operating temperature windows for fusion reactor structural materials, Fusion Eng. Des. 51–52 (2000) 55–71. https://doi.org/10.1016/S0920-3796(00)00320-3.

[23] S. Ukai, M. Fujiwara, Perspective of ODS alloys application in nuclear environments, J. Nucl. Mater. 307–311 (2002) 749–757. https://doi.org/10.1016/S0022-3115(02)01043-7.

[24] R.L. Klueh, J.P. Shingledecker, R.W. Swindeman, D.T. Hoelzer, Oxide dispersion-strengthened steels: A comparison of some commercial and experimental alloys, J. Nucl. Mater. 341 (2005) 103–114. https://doi.org/10.1016/j.jnucmat.2005.01.017.

[25] S.J. Zinkle, Advanced materials for fusion technology, Fusion Eng. Des. 74 (2005) 31–40. https://doi.org/10.1016/j.fusengdes.2005.08.008.

[26] L.L. Snead, J.W. Klett, Ceramic composites for nuclear structural applications, Glob. 2003 Atoms Prosper. Updat. Eisenhowers Glob. Vis. Nucl. Energy. (2003) 1077–1078.

[27] L.L. Snead, T. Nozawa, M. Ferraris, Y. Katoh, R. Shinavski, M. Sawan, Silicon carbide composites as fusion power reactor structural materials, J. Nucl. Mater. 417 (2011) 330–339. https://doi.org/10.1016/j.jnucmat.2011.03.005.

[28] C. Sun, S. Zheng, C.C. Wei, Y. Wu, L. Shao, Y. Yang, K.T. Hartwig, S.A. Maloy, S.J. Zinkle, T.R. Allen, H. Wang, X. Zhang, Superior radiation-resistant nanoengineered austenitic 304L stainless steel for applications in extreme radiation environments, Sci. Rep. 5 (2015) 1–7. https://doi.org/10.1038/srep07801.

[29] S.J. Zinkle, H. Matsui, D.L. Smith, A.F. Rowcliffe, E. Van Osch, K. Abe, V.A. Kazakov, Research and development on vanadium alloys for fusion applications, J. Nucl. Mater. 258–263 (1998) 205–214. https://doi.org/10.1016/S0022-3115(98)00269-4.

[30] T. Muroga, J.M. Chen, V.M. Chernov, R.J. Kurtz, M. Le Flem, Present status of vanadium alloys for fusion applications, J. Nucl. Mater. 455 (2014) 263–268. https://doi.org/10.1016/j.jnucmat.2014.06.025.

[31] S. qin Xia, Z. Wang, T. fei Yang, Y. Zhang, Irradiation Behavior in High Entropy Alloys, J. Iron Steel Res. Int. 22 (2015) 879–884. https://doi.org/10.1016/S1006-706X(15)30084-4.

[32] V. V. Sagaradze, V.I. Shalaev, V.L. Arbuzov, B.N. Goshchitskii, Y. Tian, W. Qun, S. Jiguang, Radiation resistance and thermal creep of ODS ferritic steels, J. Nucl. Mater. 295 (2001) 265–272. https://doi.org/10.1016/S0022-3115(01)00511-6.

[33] Y. Zhang, K. Jin, H. Xue, C. Lu, R.J. Olsen, L.K. Beland, M.W. Ullah, S. Zhao, H. Bei, D.S. Aidhy, G.D. Samolyuk, L. Wang, M. Caro, A. Caro, G.M. Stocks, B.C. Larson, I.M. Robertson, A.A. Correa, W.J. Weber, Influence of chemical disorder on energy dissipation and defect evolution in advanced alloys, J. Mater. Res. 31 (2016) 2363–2375. https://doi.org/10.1557/jmr.2016.269.

[34] Y. Zhang, S. Zhao, W.J. Weber, K. Nordlund, F. Granberg, F. Djurabekova, Atomic-level heterogeneity and defect dynamics in concentrated solid-solution alloys, Curr. Opin. Solid State Mater. Sci. 21 (2017) 221–237. https://doi.org/10.1016/j.cossms.2017.02.002.

[35] T. Yang, C. Li, S.J. Zinkle, S. Zhao, H. Bei, Y. Zhang, Irradiation responses and defect behavior of single-phase concentrated solid solution alloys, J. Mater. Res. 33 (2018) 3077–3091. https://doi.org/10.1557/jmr.2018.285.

[36] K. Jin, H. Bei, Single-phase concentrated solid-solution alloys: Bridging intrinsic transport properties and irradiation resistance, Front. Mater. 5 (2018) 1–11. https://doi.org/10.3389/fmats.2018.00026.

[37] N. Soneda, Irradiation Embrittlement of Reactor Pressure Vessels (RPVs) in Nuclear Power Plants, Irradiat. Embrittlement React. Press. Vessel. Nucl. Power Plants. (2014) 1–409. https://doi.org/10.1016/C2013-0-17428-4.

[38] R. Xing, D. Yu, G. Xie, Z. Yang, X. Wang, X. Chen, Effect of thermal aging on mechanical properties of a bainitic forging steel for reactor pressure vessel, Mater. Sci. Eng. A. 720 (2018) 169–175. https://doi.org/10.1016/J.MSEA.2018.02.036.

[39] P.D. Styman, J.M. Hyde, K. Wilford, A. Morley, G.D.W. Smith, Precipitation in long term thermally aged high copper, high nickel model RPV steel welds, Prog. Nucl. Energy. 57 (2012) 86–92. https://doi.org/10.1016/j.pnucene.2011.10.010.

[40] G. Salje, M. Feller-Kniepmeier, M. Feller-Kniepmeier, The diffusion and solubility of copper in iron, J. Appl. Phys. 48 (2008) 1833. https://doi.org/10.1063/1.323934.

[41] L. Liu, K. Nishida, K. Dohi, A. Nomoto, N. Soneda, K. Murakami, Z. Li, D. Chen, N. Sekimura, Effects of solute elements on hardening and microstructural evolution in neutron-irradiated and thermally-aged reactor pressure vessel model alloys, J. Nucl. Sci. Technol. 53 (2016) 1546–1553. https://doi.org/10.1080/00223131.2015.1136902.

[42] D. Jain, D. Isheim, A.H. Hunter, D.N. Seidman, Multicomponent High-Strength Low-Alloy Steel Precipitation-Strengthened by Sub-nanometric Cu Precipitates and M2C Carbides, Metall. Mater. Trans. A. 47 (2016) 3860–3872. https://link.springer.com/article/10.1007/s11661-016-3569-5 (accessed August 5, 2021).

[43] S. Shu, N. Almirall, P.B. Wells, T. Yamamoto, G.R. Odette, D.D. Morgan, Precipitation in Fe-Cu and Fe-Cu-Mn model alloys under irradiation: Dose rate effects, Acta Mater. 157 (2018) 72–82. https://doi.org/10.1016/j.actamat.2018.07.017.

[44] P.B. Wells, T. Yamamoto, B. Miller, T. Milot, J. Cole, Y. Wu, G.R. Odette, Evolution of manganese-nickel-silicon-dominated phases in highly irradiated reactor pressure vessel steels, Acta Mater. 80 (2014) 205–219. https://doi.org/10.1016/j.actamat.2014.07.040.

[45] R. Monzen, K. Takada, C. Watanabe, Coarsening of Spherical Cu Particles in an a a-Fe Matrix, (2004).

[46] K. Osamura, Hiroshi Okuda Kazuo, Asano Michihiro Furusaka, K. Kishida, F. Kurosawa, Ry. UEMORl, D. Laboraotires, N. Steel Corporation, SANS Study of Phase Decomposition in Fe-Cu Alloy with Ni and Mn Addition, ISIJ Int. 34 (1994) 346–354. https://doi.org/10.2355/ISIJINTERNATIONAL.34.346.

[47] Q. Liu, J. Gu, W. Liu, On the role of Ni in Cu precipitation in multicomponent steels, Metall. Mater. Trans. A Phys. Metall. Mater. Sci. 44 (2013) 4434–4439. https://doi.org/10.1007/S11661-013-1933-2.

[48] L. Liu, K. Murakami, K. Dohi, K. Nishida, A. Nomoto, N. Soneda, Z. Li, N. Sekimura, Microstructural Evolution of Thermally Aged RPV Model Alloys by 3D Atom Probe, E-Journal Adv. Maint. 7 (2015) 117–121.

[49] A. Cerezo, S. Hirosawa, G. Sha, G. Smith, 3-D atomic-scale experimental and modelling studies of the early stages of precipitation, Solid-Solid Phase Transform. Inorg. Mater. 2005, Vol 1. (2005).

[50] A. Seko, N. Odagaki, S.R. Nishitani, I. Tanaka, H. Adachi, Free-Energy Calculation of Precipitate Nucleation in an Fe-Cu-Ni Alloy, Mater. Trans. 45 (2004) 1978–1981. https://doi.org/10.2320/MATERTRANS.45.1978.

[51] A.T. Al-Motasem, M. Posselt, F. Bergner, Nanoclusters in bcc-Fe containing vacancies, copper and nickel: Structure and energetics, J. Nucl. Mater. 418 (2011) 215–222. https://doi.org/10.1016/J.JNUCMAT.2011.07.002.

[52] P.D. Styman, J.M. Hyde, K. Wilford, D. Parfitt, N. Riddle, G.D.W. Smith, Characterisation of interfacial segregation to Cu-enriched precipitates in two thermally aged reactor pressure vessel steel welds, Ultramicroscopy. 159 (2015) 292–298. https://doi.org/10.1016/j.ultramic.2015.05.013.

[53] J. Buswell, C. English, W. Phythian, M. Hetherington, G. Smith, G. Worrall, An Analysis

of Small Clusters Formed in Thermally Aged and Irradiated FeCu and FeCuNi Model Alloys, (n.d.) 127–153. https://doi.org/10.1520/STP49447S.

[54] D. Isheim, R.P. Kolli, M.E. Fine, D.N. Seidman, An atom-probe tomographic study of the temporal evolution of the nanostructure of Fe–Cu based high-strength low-carbon steels, Scr. Mater. 55 (2006) 35–40. https://doi.org/10.1016/J.SCRIPTAMAT.2006.02.040.

[55] P.D. Styman, J.M. Hyde, A. Morley, K. Wilford, N. Riddle, G.D.W. Smith, The effect of Ni on the microstructural evolution of high Cu reactor pressure vessel steel welds after thermal ageing for up to 100,000 h, Mater. Sci. Eng. A. 736 (2018) 111–119. https://doi.org/10.1016/j.msea.2018.08.063.

[56] R. Prakash Kolli, D.N. Seidman, The temporal evolution of the decomposition of a concentrated multicomponent Fe–Cu-based steel, Acta Mater. 56 (2008) 2073–2088. https://doi.org/10.1016/J.ACTAMAT.2007.12.044.

[57] D. Isheim, M.S. Gagliano, M.E. Fine, D.N. Seidman, Interfacial segregation at Cu-rich precipitates in a high-strength low-carbon steel studied on a sub-nanometer scale, Acta Mater. 54 (2006) 841–849. https://doi.org/10.1016/J.ACTAMAT.2005.10.023.

[58] N. Almirall, P.B. Wells, S. Pal, P.D. Edmondson, T. Yamamoto, K. Murakami, G.R. Odette, The mechanistic implications of the high temperature, long time thermal stability of nanoscale Mn-Ni-Si precipitates in irradiated reactor pressure vessel steels, Scr. Mater. 181 (2020) 134–139. https://doi.org/10.1016/J.SCRIPTAMAT.2020.02.027.

[59] G.R. Odette, T. Yamamoto, P. Wells, N. Almirall, High Fluency Low Flux Embrittlement Models of LWR Reactor Pressure Vessel Embrittlement and a Supporting Database from the UCSB ATR-2 Irradiation Experiment, (2017) 89. https://doi.org/10.2172/1346148.

[60] W. Xiong, H. Ke, R. Krishnamurthy, P. Wells, L. Barnard, G.R. Odette, D. Morgan, Thermodynamic models of low-temperature Mn–Ni–Si precipitation in reactor pressure vessel steels, MRS Commun. 4 (2014) 101–105. https://doi.org/10.1557/mrc.2014.21.

[61] D.J. Sprouster, J. Sinsheimer, E. Dooryhee, S.K. Ghose, P. Wells, T. Stan, N. Almirall, G.R. Odette, L.E. Ecker, Structural characterization of nanoscale intermetallic precipitates in highly neutron irradiated reactor pressure vessel steels, Scr. Mater. 113 (2016) 18–22. https://doi.org/10.1016/j.scriptamat.2015.10.019.

[62] X. Yan, A. Grytsiv, P. Rogl, V. Pomjakushin, X. Xue, On the crystal structure of the Mn–Ni–Si G-phase, J. Alloys Compd. 469 (2009) 152–155. https://doi.org/10.1016/J.JALLCOM.2008.01.142.

[63] J. Millán, S. Sandlöbes, A. Al-Zubi, T. Hickel, P. Choi, J. Neugebauer, D. Ponge, D. Raabe, Designing Heusler nanoprecipitates by elastic misfit stabilization in Fe–Mn maraging steels, Acta Mater. 76 (2014) 94–105. https://doi.org/10.1016/J.ACTAMAT.2014.05.016.

[64] E.A. Marquis, J.M. Hyde, Applications of atom-probe tomography to the characterisation of solute behaviours, Mater. Sci. Eng. R Reports. 69 (2010) 37–62. https://doi.org/10.1016/J.MSER.2010.05.001.

[65] M. Guttmann, Temper embrittlement and ternary equilibrium segregation, Mater. Sci. Eng. 42 (1980) 227–232. https://doi.org/10.1016/0025-5416(80)90032-4.

[66] M. Guttmann, Equilibrium segregation in a ternary solution: A model for temper embrittlement, Surf. Sci. 53 (1975) 213–227. https://doi.org/10.1016/0039-6028(75)90125-

9.

[67] M. Guttmann, P. Dumoulin, M. Wayman, The thermodynamics of interactive co-segregation of phosphorus and alloying elements in iron and temper-brittle steels, Metall. Trans. A. 13 (1982) 1693–1711. https://doi.org/10.1007/BF02647825/METRICS.

[68] M. Perez, M. Dumont, D. Acevedo-Reyes, Implementation of classical nucleation and growth theories for precipitation, Acta Mater. 56 (2008) 2119–2132. https://doi.org/10.1016/J.ACTAMAT.2007.12.050.

[69] R.E. Stoller, G.R. Odette, B.D. Wirth, Primary damage formation in bcc iron, J. Nucl. Mater. 251 (1997) 49–60. https://doi.org/10.1016/S0022-3115(97)00256-0.

[70] G.R. Odette, G.E. Lucas, Embrittlement of nuclear reactor pressure vessels, JOM. 53 (2001) 18–22. https://doi.org/10.1007/s11837-001-0081-0.

[71] M.K. Miller, K.F. Russell, J. Kocik, E. Keilova, M.K. Miller, K.F. Russell, J. Kocik, E. Keilova, Embrittlement of low copper VVER 440 surveillance samples neutron-irradiated to high fluences, J. Nucl. Mater. 282 (2000) 83–88. https://doi.org/10.1016/S0022-3115(00)00240-3.

[72] M.K. Miller, A.A. Chernobaeva, Y.I. Shtrombakh, K.F. Russell, R.K. Nanstad, D.Y. Erak, O.O. Zabusov, Evolution of the nanostructure of VVER-1000 RPV materials under neutron irradiation and post irradiation annealing, J. Nucl. Mater. 385 (2009) 615–622. https://doi.org/10.1016/j.jnucmat.2009.01.299.

[73] H. Ke, P. Wells, P.D. Edmondson, N. Almirall, L. Barnard, G.R. Odette, D. Morgan, Thermodynamic and kinetic modeling of Mn-Ni-Si precipitates in low-Cu reactor pressure vessel steels, Acta Mater. 138 (2017) 10–26. https://doi.org/10.1016/j.actamat.2017.07.021.

[74] N. Almirall, P.B. Wells, T. Yamamoto, K. Wilford, T. Williams, N. Riddle, G.R. Odette, Precipitation and hardening in irradiated low alloy steels with a wide range of Ni and Mn compositions, Acta Mater. 179 (2019) 119–128.

[75] R.K. Nanstad, W.L. Server, M.A. Sokolov, G.R. Odette, N. Almirall, Some useful mechanical property correlations for nuclear reactor pressure vessel steels1, Am. Soc. Mech. Eng. Press. Vessel. Pip. Div. PVP. 6B-2018 (2018). https://doi.org/10.1115/pvp2018-84786.

[76] B.D. Wirth, G.R. Odette, W.A. Pavinich, G.E. Lucas, S.E. Spooner, Small angle neutron scattering study of Linde 80 RPV welds, ASTM Spec. Tech. Publ. (1999) 102–121. https://doi.org/10.1520/stp13860s.

[77] M.K. Miller, K.A. Powers, R.K. Nanstad, P. Efsing, Atom probe tomography characterizations of high nickel, low copper surveillance RPV welds irradiated to high fluences, J. Nucl. Mater. 437 (2013) 107–115. https://doi.org/10.1016/j.jnucmat.2013.01.312.

[78] Odette, G. R, Modeling irradiation embrittlement in reactor pressure vessel steels, (1998).

[79] On the character of nanoscale features in reactor pressure vessel steels under neutron irradiation - NASA/ADS, (n.d.). https://ui.adsabs.harvard.edu/abs/1998PhDT.....234W/abstract (accessed October 9, 2021).

[80] G.R. Odette, B.D. Wirth, A computational microscopy study of nanostructural evolution in irradiated pressure vessel steels, J. Nucl. Mater. (1997). https://doi.org/10.1016/S0022-3115(97)00267-5.

[81] G.R. Odette, Radiation Induced Microstructural Evolution in Reactor Pressure Vessel Steels, MRS Proc. 373 (1994) 137. https://doi.org/10.1557/PROC-373-137.

[82] P.D. Edmondson, M.K. Miller, K.A. Powers, R.K. Nanstad, Atom probe tomography characterization of neutron irradiated surveillance samples from the R. E. Ginna reactor pressure vessel, J. Nucl. Mater. 470 (2016) 147–154. https://doi.org/10.1016/j.jnucmat.2015.12.038.

[83] S. Connolly, J. Hyde, P. Pareige, D. Parfitt, P. Styman, the Effect of Irradiation Temperature on Precipitation in Rpv Steels, (2015).

[84] S. Shu, P.B. Wells, N. Almirall, G.R. Odette, D.D. Morgan, Thermodynamics and kinetics of core-shell versus appendage co-precipitation morphologies: An example in the Fe-Cu-Mn-Ni-Si system, Acta Mater. 157 (2018) 298–306. https://doi.org/10.1016/j.actamat.2018.07.037.

[85] N. Almirall, P.B. Wells, H. Ke, P. Edmondson, D. Morgan, T. Yamamoto, G.R. Odette, On the elevated temperature thermal stability of nanoscale Mn-Ni-Si precipitates formed at lower temperature in highly irradiated reactor pressure vessel steels, Sci. Rep. 9 (2019) 1–12. https://doi.org/10.1038/s41598-019-45944-z.

[86] C. Zhang, M. Enomoto, Study of the influence of alloying elements on Cu precipitation in steel by non-classical nucleation theory, Acta Mater. 54 (2006) 4183–4191. https://doi.org/10.1016/J.ACTAMAT.2006.05.006.

[87] B. Sonderegger, E. Kozeschnik, Generalized Nearest-Neighbor Broken-Bond Analysis of Randomly Oriented Coherent Interfaces in Multicomponent Fcc and Bcc Structures, Metall. Mater. Trans. A 2009 403. 40 (2009) 499–510. https://doi.org/10.1007/S11661-008-9752-6.

[88] M.K. Miller, K.F. Russell, M.A. Sokolov, R.K. Nanstad, APT characterization of irradiated high nickel RPV steels, J. Nucl. Mater. 361 (2007) 248–261. https://doi.org/10.1016/j.jnucmat.2006.12.015.

[89] Wirth BD, On the character of nanoscale features in reactor pressure vessel steels under neutron irradiation , University of California Santa Barbara, 1998. https://www.proquest.com/docview/304419730?pq-origsite=gscholar&fromopenview=true (accessed December 11, 2022).

[90] Mamivand Mahmood, Ke Huibin, Shu Shipeng, Morgan Dane, Light Water Reactor Sustainability Program Incorporation of copper-rich precipitation model into developed Ni-Mn-Si precipitate development models Milestone, Off. Nucl. Energy. (2016).

[91] F. Soisson, C.C. Fu, Cu-precipitation kinetics in α-Fe from atomistic simulations: Vacancy-trapping effects and Cu-cluster mobility, Phys. Rev. B - Condens. Matter Mater. Phys. 76 (2007) 214102. https://doi.org/10.1103/PHYSREVB.76.214102.

[92] G.R. Odette, T. Yamamoto, D. Klingensmith, On the effect of dose rate on irradiation hardening of RPV steels, Philos. Mag. 85 (2005) 779–797. https://doi.org/10.1080/14786430412331319910.

[93] H. Watanabe, S. Arase, T. Yamamoto, P. Wells, T. Onishi, G.R. Odette, Hardening and microstructural evolution of A533b steels irradiated with Fe ions and electrons, J. Nucl. Mater. 471 (2016) 243–250. https://doi.org/10.1016/j.jnucmat.2015.12.045.

[94] H. Watanabe, S. Masaki, S. Masubuchi, N. Yoshida, Y. Kamada, Radiation induced hardening of ion irradiated RPV steels, J. Nucl. Mater. 417 (2011) 932–935. https://doi.org/10.1016/j.jnucmat.2010.12.179.

[95] R.S. Nelson, J.A. Hudson, D.J. Mazey, The stability of precipitates in an irradiation environment, J. Nucl. Mater. 44 (1972) 318–330. https://doi.org/10.1016/0022-3115(72)90043-8.

[96] H.J. Frost, K.C. Russell, Particle stability with recoil resolution, Acta Metall. 30 (1982) 953–960. https://doi.org/10.1016/0001-6160(82)90202-4.

[97] C. Lu, Z. Lu, X. Wang, R. Xie, Z. Li, M. Higgins, C. Liu, F. Gao, L. Wang, Enhanced Radiation-tolerant Oxide Dispersion Strengthened Steel and its Microstructure Evolution under Helium-implantation and Heavy-ion Irradiation, Sci. Rep. 7 (2017) 1–7. https://doi.org/10.1038/srep40343.

[98] S. Shu, X. Zhang, J.A. Beach, P. Bellon, R.S. Averback, Irradiation-induced formation of nanorod precipitates in a dilute Cu-W alloy, Scr. Mater. 115 (2016) 155–158. https://doi.org/10.1016/j.scriptamat.2016.01.012.

[99] S. Shu, P. Bellon, R.S. Averback, Role of point-defect sinks on irradiation-induced compositional patterning in model binary alloys, 91 (2015) 214107. https://doi.org/10.1103/PhysRevB.91.214107.

[100] R.A. Enrique, P. Bellon, Compositional patterning in systems driven by competing dynamics of different length scale, Phys. Rev. Lett. 84 (2000) 2885. https://doi.org/10.1103/PhysRevLett.84.2885.

[101] M.K. Miller, B.D. Wirth, G.R. Odette, Precipitation in neutron-irradiated Fe-Cu and Fe-Cu-Mn model alloys: A comparison of APT and SANS data, Mater. Sci. Eng. A. 353 (2003) 133–139. https://doi.org/10.1016/s0921-5093(02)00679-2.

[102] F. Vurpillot, A. Bostel, E. Cadel, D. Blavette, The spatial resolution of 3D atom probe in the investigation of single-phase materials, Ultramicroscopy. 84 (2000) 213–224. https://doi.org/10.1016/S0304-3991(00)00035-8.

[103] F. Vurpillot, A. Bostel, D. Blavette, Trajectory overlaps and local magnification in three-dimensional atom probe, Appl. Phys. Lett. 76 (2000) 3127. https://doi.org/10.1063/1.126545.

[104] B. Gault, F. Danoix, K. Hoummada, D. Mangelinck, H. Leitner, Impact of directional walk on atom probe microanalysis, Ultramicroscopy. 113 (2012) 182–191. https://doi.org/10.1016/J.ULTRAMIC.2011.06.005.

[105] M.K. Miller, M.G. Hetherington, Local magnification effects in the atom probe, Surf. Sci. 246 (1991) 442–449. https://doi.org/10.1016/0039-6028(91)90449-3.

[106] D.W. Saxey, Correlated ion analysis and the interpretation of atom probe mass spectra, Ultramicroscopy. 111 (2011) 473–479. https://doi.org/10.1016/J.ULTRAMIC.2010.11.021.

[107] E.A. Marquis, F. Vurpillot, Chromatic Aberrations in the Field Evaporation Behavior of Small Precipitates, Microsc. Microanal. 14 (2008) 561–570. https://doi.org/10.1017/S1431927608080793.

[108] A.R. Waugh, E.D. Boyes, M.J. Southon, Investigations of field evaporation with a field-desorption microscope, Surf. Sci. 61 (1976) 109–142. https://doi.org/10.1016/0039-6028(76)90411-8.

[109] J. Takahashi, K. Kawakami, A quantitative model of preferential evaporation and retention for atom probe tomography, Surf. Interface Anal. 46 (2014) 535–543. https://doi.org/10.1002/SIA.5555.

[110] Y. Dong, A. Etienne, A. Frolov, S. Fedotova, K. Fujii, K. Fukuya, C. Hatzoglou, E. Kuleshova, K. Lindgren, A. London, A. Lopez, S. Lozano-Perez, Y. Miyahara, Y. Nagai, K. Nishida, B. Radiguet, D.K. Schreiber, N. Soneda, M. Thuvander, T. Toyama, J. Wang, F. Sefta, P. Chou, E.A. Marquis, Atom Probe Tomography Interlaboratory Study on Clustering Analysis in Experimental Data Using the Maximum Separation Distance Approach, Microsc. Microanal. 25 (2019) 356–366. https://doi.org/10.1017/S1431927618015581.

[111] M.K. Miller, E.A. Kenik, Atom probe tomography: a technique for nanoscale characterization, Microsc. Microanal. 10 (2004) 336–341. https://doi.org/10.1017/S1431927604040577.

[112] I. Ghamarian, E.A. Marquis, Hierarchical density-based cluster analysis framework for atom probe tomography data, Ultramicroscopy. 200 (2019) 28–38. https://doi.org/10.1016/j.ultramic.2019.01.011.

[113] J. Zelenty, A. Dahl, J. Hyde, G.D.W. Smith, M.P. Moody, Detecting Clusters in Atom Probe Data with Gaussian Mixture Models, Microsc. Microanal. 23 (2017) 269–278. https://doi.org/10.1017/S1431927617000320.

[114] W. Lefebvre, T. Philippe, F. Vurpillot, Application of Delaunay tessellation for the characterization of solute-rich clusters in atom probe tomography, (2010). https://doi.org/10.1016/j.ultramic.2010.11.034.

[115] P. Felfer, A. V. Ceguerra, S.P. Ringer, J.M. Cairney, Detecting and extracting clusters in atom probe data: A simple, automated method using Voronoi cells, Ultramicroscopy. 150 (2015) 30–36. https://doi.org/10.1016/J.ULTRAMIC.2014.11.015.

[116] D.B. Miracle, O.N. Senkov, A critical review of high entropy alloys and related concepts, Acta Mater. 122 (2017) 448–511. https://doi.org/10.1016/j.actamat.2016.08.081.

[117] K. Jin, C. Lu, L.M. Wang, J. Qu, W.J. Weber, Y. Zhang, H. Bei, Effects of compositional complexity on the ion-irradiation induced swelling and hardening in Ni-containing equiatomic alloys, Scr. Mater. 119 (2016) 65–70. https://doi.org/10.1016/j.scriptamat.2016.03.030.

[118] Y. Zhang, G.M. Stocks, K. Jin, C. Lu, H. Bei, B.C. Sales, L. Wang, L.K. Béland, R.E. Stoller, G.D. Samolyuk, M. Caro, A. Caro, W.J. Weber, Influence of chemical disorder on energy dissipation and defect evolution in concentrated solid solution alloys, Nat. Commun. 6 (2015) 1–9. https://doi.org/10.1038/ncomms9736.

[119] F. Granberg, K. Nordlund, M.W. Ullah, K. Jin, C. Lu, H. Bei, L.M. Wang, F. Djurabekova,

W.J. Weber, Y. Zhang, Mechanism of Radiation Damage Reduction in Equiatomic Multicomponent Single Phase Alloys, Phys. Rev. Lett. 116 (2016) 1–8. https://doi.org/10.1103/PhysRevLett.116.135504.

[120] W.Y. Chen, X. Liu, Y. Chen, J.W. Yeh, K.K. Tseng, K. Natesan, Irradiation effects in high entropy alloys and 316H stainless steel at 300 °C, J. Nucl. Mater. 510 (2018) 421–430. https://doi.org/10.1016/j.jnucmat.2018.08.031.

[121] M.A. Tunes, G. Greaves, H. Bei, P.D. Edmondson, Y. Zhang, S.E. Donnelly, C.G. Schön, Comparative irradiation response of an austenitic stainless steel with its high-entropy alloy counterpart, Intermetallics. 132 (2021) 107130.

[122] L. Yang, H. Ge, J. Zhang, T. Xiong, Q. Jin, Y. Zhou, X. Shao, B. Zhang, Z. Zhu, S. Zheng, X. Ma, High He-ion irradiation resistance of CrMnFeCoNi high-entropy alloy revealed by comparison study with Ni and 304SS, J. Mater. Sci. Technol. 35 (2019) 300–305. https://doi.org/10.1016/j.jmst.2018.09.050.

[123] M. Fedorov, J.S. Wróbel, A. Fernández-Caballero, K.J. Kurzydłowski, D. Nguyen-Manh, Phase stability and magnetic properties in fcc Fe-Cr-Mn-Ni alloys from first-principles modeling, Phys. Rev. B. 101 (2020) 174416. https://doi.org/10.1103/PHYSREVB.101.174416.

[124] M. Elbakhshwan, W. Doniger, C. Falconer, M. Moorehead, C. Parkin, C. Zhang, K. Sridharan, A. Couet, Corrosion and Thermal Stability of CrMnFeNi High Entropy Alloy in Molten FLiBe Salt, Sci. Rep. 9 (2019) 1–10. https://doi.org/10.1038/s41598-019-55653-2.

[125] C. Parkin, M. Moorehead, M. Elbakhshwan, X. Zhang, P. Xiu, L. He, M. Bachhav, K. Sridharan, A. Couet, Phase stability, mechanical properties, and ion irradiation effects in face-centered cubic CrFeMnNi compositionally complex solid-solution alloys at high temperatures, J. Nucl. Mater. 565 (2022) 153733. https://doi.org/10.1016/J.JNUCMAT.2022.153733.

[126] B. Schuh, F. Mendez-Martin, B. Völker, E.P. George, H. Clemens, R. Pippan, A. Hohenwarter, Mechanical properties, microstructure and thermal stability of a nanocrystalline CoCrFeMnNi high-entropy alloy after severe plastic deformation, Acta Mater. 96 (2015) 258–268. https://doi.org/10.1016/j.actamat.2015.06.025.

[127] N.D. Stepanov, D.G. Shaysultanov, M.S. Ozerov, S. V. Zherebtsov, G.A. Salishchev, Second phase formation in the CoCrFeNiMn high entropy alloy after recrystallization annealing, Mater. Lett. 185 (2016) 1–4. https://doi.org/10.1016/j.matlet.2016.08.088.

[128] P. Yu, N. Fan, Y. Zhang, Z. Wang, W. Li, R. Lupoi, S. Yin, Microstructure evolution and composition redistribution of FeCoNiCrMn high entropy alloy under extreme plastic deformation, Mater. Res. Lett. 10 (2022) 124–132. https://doi.org/10.1080/21663831.2021.2023678/SUPPL_FILE/TMRL_A_2023678_SM9574.DOCX.

[129] F. Otto, A. Dlouhý, K.G. Pradeep, M. Kuběnová, D. Raabe, G. Eggeler, E.P. George, Decomposition of the single-phase high-entropy alloy CrMnFeCoNi after prolonged anneals at intermediate temperatures, Acta Mater. 112 (2016) 40–52. https://doi.org/10.1016/j.actamat.2016.04.005.

[130] L. Li, Z. Li, A. Kwiatkowski da Silva, Z. Peng, H. Zhao, B. Gault, D. Raabe, Segregation-

driven grain boundary spinodal decomposition as a pathway for phase nucleation in a high-entropy alloy, Acta Mater. 178 (2019) 1–9. https://doi.org/10.1016/J.ACTAMAT.2019.07.052.

[131] Y.J. Li, A. Savan, A. Ludwig, Atomic scale understanding of phase stability and decomposition of a nanocrystalline CrMnFeCoNi Cantor alloy, Appl. Phys. Lett. 119 (2021) 201910. https://doi.org/10.1063/5.0069107.

[132] U. Lee, B. Straumal, N. Park, Dynamic precipitation of σ-phase and element partitioning in equiatomic CoCrFeMnNi high-entropy alloy, Mater. Sci. Eng. A. 804 (2021) 140739. https://doi.org/10.1016/J.MSEA.2021.140739.

[133] G. Spanos, W.T. Reynolds, Microstructure of Metals and Alloys, Phys. Metall. Fifth Ed. 1 (2014) 1073–1112. https://doi.org/10.1016/B978-0-444-53770-6.00010-1.

[134] D.A. Porter, K.E. Easterling, Phase transformations in metals and alloys, (2001) 514.

[135] W.R. Wang, W.L. Wang, S.C. Wang, Y.C. Tsai, C.H. Lai, J.W. Yeh, Effects of Al addition on the microstructure and mechanical property of AlxCoCrFeNi high-entropy alloys, Intermetallics. 26 (2012) 44–51. https://doi.org/10.1016/J.INTERMET.2012.03.005.

[136] C.J. Tong, Y.L. Chen, S.K. Chen, J.W. Yeh, T.T. Shun, C.H. Tsau, S.J. Lin, S.Y. Chang, Microstructure characterization of AlxCoCrCuFeNi high-entropy alloy system with multiprincipal elements, Metall. Mater. Trans. A Phys. Metall. Mater. Sci. 36 (2005) 881–893. https://doi.org/10.1007/S11661-005-0283-0/METRICS.

[137] Y. Zhang, Z. Chen, D. Cao, J. Zhang, P. Zhang, Q. Tao, X. Yang, Concurrence of spinodal decomposition and nano-phase precipitation in a multi-component AlCoCrCuFeNi high-entropy alloy, J. Mater. Res. Technol. 8 (2019) 726–736. https://doi.org/10.1016/J.JMRT.2018.04.020.

[138] A. Manzoni, H. Daoud, R. Völkl, U. Glatzel, N. Wanderka, Phase separation in equiatomic AlCoCrFeNi high-entropy alloy, Ultramicroscopy. 132 (2013) 212–215. https://doi.org/10.1016/J.ULTRAMIC.2012.12.015.

[139] D.B. Williams, E.P. Butler, Grain boundary discontinuous precipitation reactions, Http://Dx.Doi.Org/10.1179/Imtr.1981.26.1.153. 26 (2013) 153–180. https://doi.org/10.1179/IMTR.1981.26.1.153.

[140] L. Fan, T. Yang, J.H. Luan, Z.B. Jiao, Control of discontinuous and continuous precipitation of γ′-strengthened high-entropy alloys through nanoscale Nb segregation and partitioning, J. Alloys Compd. 832 (2020) 154903. https://doi.org/10.1016/J.JALLCOM.2020.154903.

[141] Y.L. Zhao, T. Yang, Y. Tong, J. Wang, J.H. Luan, Z.B. Jiao, D. Chen, Y. Yang, A. Hu, C.T. Liu, J.J. Kai, Heterogeneous precipitation behavior and stacking-fault-mediated deformation in a CoCrNi-based medium-entropy alloy, Acta Mater. 138 (2017) 72–82. https://doi.org/10.1016/J.ACTAMAT.2017.07.029.

[142] N. Baler, A. Godha, S.K. Makineni, On the discontinuous precipitation during recrystallization in a multicomponent alloy, Scr. Mater. 224 (2023). https://doi.org/10.1016/J.SCRIPTAMAT.2022.115133.

[143] S. Dasari, Y.J. Chang, A. Jagetia, V. Soni, A. Sharma, B. Gwalani, S. Gorsse, A.C. Yeh, R. Banerjee, Discontinuous precipitation leading to nano-rod intermetallic precipitates in an Al0.2Ti0.3Co1.5CrFeNi1.5 high entropy alloy results in an excellent strength-ductility

combination, Mater. Sci. Eng. A. 805 (2021) 140551. https://doi.org/10.1016/J.MSEA.2020.140551.

[144] Y.J. Chang, A.C. Yeh, The formation of cellular precipitate and its effect on the tensile properties of a precipitation strengthened high entropy alloy, Mater. Chem. Phys. 210 (2018) 111–119. https://doi.org/10.1016/J.MATCHEMPHYS.2017.09.057.

[145] T. Yang, Y.L. Zhao, L. Fan, J. Wei, J.H. Luan, W.H. Liu, C. Wang, Z.B. Jiao, J.J. Kai, C.T. Liu, Control of nanoscale precipitation and elimination of intermediate-temperature embrittlement in multicomponent high-entropy alloys, Acta Mater. 189 (2020) 47–59. https://doi.org/10.1016/J.ACTAMAT.2020.02.059.

[146] J.Y. He, H. Wang, Y. Wu, X.J. Liu, H.H. Mao, T.G. Nieh, Z.P. Lu, Precipitation behavior and its effects on tensile properties of FeCoNiCr high-entropy alloys, Intermetallics. 79 (2016) 41–52. https://doi.org/10.1016/J.INTERMET.2016.09.005.

[147] M. Wu, Z. Li, B. Gault, P. Munroe, I. Baker, The effects of carbon on the phase stability and mechanical properties of heat-treated FeNiMnCrAl high entropy alloys, Mater. Sci. Eng. A. 748 (2019) 59–73. https://doi.org/10.1016/J.MSEA.2019.01.083.

[148] B. Gwalani, S. Gorsse, V. Soni, M. Carl, N. Ley, J. Smith, A. V. Ayyagari, Y. Zheng, M. Young, R.S. Mishra, R. Banerjee, Role of copper on L12 precipitation strengthened fcc based high entropy alloy, Materialia. 6 (2019) 100282. https://doi.org/10.1016/J.MTLA.2019.100282.

[149] J.Y.C. Fang, W.H. Liu, J.H. Luan, T. Yang, Y. Wu, M.W. Fu, Z.B. Jiao, Competition between continuous and discontinuous precipitation in L12-strengthened high-entropy alloys, Intermetallics. 149 (2022) 107655. https://doi.org/10.1016/J.INTERMET.2022.107655.

[150] I. Manna, S.K. Pabi, W. Gust, Discontinuous reactions in solids, Int. Mater. Rev. 46 (2001) 53.

[151] K. Smidoda, W. Gottschalk, H. Gleiter, Diffusion in migrating interfaces, Acta Metall. 26 (1978) 1833–1836. https://doi.org/10.1016/0001-6160(78)90095-0.

[152] D. Welton, N. D'Souza, J. Kelleher, S. Gardner, Z.H. Dong, G.D. West, H. Dong, Discontinuous Precipitation in Ni-Base Superalloys During Solution Heat Treatment, Metall. Mater. Trans. A Phys. Metall. Mater. Sci. 46 (2015) 4298–4315. https://doi.org/10.1007/S11661-015-3046-6.

[153] A. Porter, B. Ralph, The recrystallization of nickel-base superalloys, J. Mater. Sci. 16 (1981) 707–713. https://doi.org/10.1007/BF02402788.

[154] P. Zięba, Recent Developments on Discontinuous Precipitation, Arch. Metall. Mater. 62 (2017) 955–968. https://doi.org/10.1515/AMM-2017-0138.

[155] L. Amirouche, M. Plapp, Phase-field modeling of the discontinuous precipitation reaction, Acta Mater. 57 (2009) 237–247. https://doi.org/10.1016/J.ACTAMAT.2008.09.015.

[156] S. Zhao, W.J. Weber, Y. Zhang, Unique Challenges for Modeling Defect Dynamics in Concentrated Solid-Solution Alloys, Jom. 69 (2017) 2084–2091. https://doi.org/10.1007/s11837-017-2461-0.

[157] C. Lu, T. Yang, K. Jin, N. Gao, P. Xiu, Y. Zhang, F. Gao, H. Bei, W.J. Weber, K. Sun, Y.

Dong, L. Wang, Radiation-induced segregation on defect clusters in single-phase concentrated solid-solution alloys, Acta Mater. 127 (2017) 98–107. https://doi.org/10.1016/j.actamat.2017.01.019.

[158] G.S. Was, Fundamentals of radiation materials science: Metals and alloys, second edition, Fundam. Radiat. Mater. Sci. Met. Alloy. Second Ed. (2016) 1–1002. https://doi.org/10.1007/978-1-4939-3438-6.

[159] Y. Li, C. Gao, J. Zeng, al -, H. Tezuka, K. Takahashi, J. Matsumoto, M.-H. Jung, H.-S. Choi -, V. V. Ovchinnikov, F.F. Makhin, V.I. Solomonov, F.F. Makhin'Ko, V.I. Solomonov, Thermal-spikes temperature measurement in pure metals under argon ion irradiation (E = 5-15 keV), J. Phys. Conf. Ser. 652 (2015) 012070. https://doi.org/10.1088/1742-6596/652/1/012070.

[160] K. Nordlund, F. Djurabekova, Multiscale modelling of irradiation in nanostructures, J. Comput. Electron. 13 (2014) 122–141. https://doi.org/10.1007/S10825-013-0542-Z.

[161] K. Jin, B.C. Sales, G.M. Stocks, G.D. Samolyuk, M. Daene, W.J. Weber, Y. Zhang, H. Bei, Tailoring the physical properties of Ni-based single-phase equiatomic alloys by modifying the chemical complexity, Sci. Rep. 6 (2016) 1–10. https://doi.org/10.1038/srep20159.

[162] M.H. Tsai, J.W. Yeh, High-Entropy Alloys: A Critical Review, Http://Mc.Manuscriptcentral.Com/Tmrl. 2 (2014) 107–123. https://doi.org/10.1080/21663831.2014.912690.

[163] Z. Fan, S. Zhao, K. Jin, D. Chen, Y.N. Osetskiy, Y. Wang, H. Bei, K.L. More, Y. Zhang, Helium irradiated cavity formation and defect energetics in Ni-based binary single-phase concentrated solid solution alloys, Acta Mater. 164 283–292. https://doi.org/10.1016/j.actamat.2018.10.040.

[164] S. Zhao, G.M. Stocks, Y. Zhang, Defect energetics of concentrated solid-solution alloys from ab initio calculations: Ni0.5Co0.5, Ni0.5Fe0.5, Ni0.8Fe0.2 and Ni0.8Cr0.2, Phys. Chem. Chem. Phys. 18 (2016) 24043–24056. https://doi.org/10.1039/c6cp05161h.

[165] S. Zhao, T. Egami, G.M. Stocks, Y. Zhang, Effect of d electrons on defect properties in equiatomic NiCoCr and NiCoFeCr concentrated solid solution alloys, Phys. Rev. Mater. 2 (2018) 1–8. https://doi.org/10.1103/PhysRevMaterials.2.013602.

[166] S. Zhao, Y. Osetsky, Y. Zhang, Preferential diffusion in concentrated solid solution alloys: NiFe, NiCo and NiCoCr, Acta Mater. 128 (2017) 391–399. https://doi.org/10.1016/j.actamat.2017.01.056.

[167] Y.N. Osetsky, L.K. Béland, R.E. Stoller, Specific features of defect and mass transport in concentrated fcc alloys, Acta Mater. 115 (2016) 364–371. https://doi.org/10.1016/J.ACTAMAT.2016.06.018.

[168] C. Lu, L. Niu, N. Chen, K. Jin, T. Yang, P. Xiu, Y. Zhang, F. Gao, H. Bei, S. Shi, M.R. He, I.M. Robertson, W.J. Weber, L. Wang, Enhancing radiation tolerance by controlling defect mobility and migration pathways in multicomponent single-phase alloys, Nat. Commun. 7 (2016) 1–8. https://doi.org/10.1038/ncomms13564.

[169] C. Lu, K. Jin, L.K. Béland, F. Zhang, T. Yang, L. Qiao, Y. Zhang, H. Bei, H.M. Christen, R.E. Stoller, L. Wang, Direct Observation of Defect Range and Evolution in Ion-Irradiated Single Crystalline Ni and Ni Binary Alloys, Sci. Rep. 6 (2016) 1–10.

https://doi.org/10.1038/srep19994.

[170] D. Gaertner, J. Kottke, G. Wilde, S. V. Divinski, Y. Chumlyakov, Tracer diffusion in single crystalline CoCrFeNi and CoCrFeMnNi high entropy alloys, J. Mater. Res. 33 (2018) 3184–3191. https://doi.org/10.1557/JMR.2018.162.

[171] S. V. Divinski, A. V. Pokoev, N. Esakkiraja, A. Paul, A Mystery of "Sluggish Diffusion" in High-Entropy Alloys: The Truth or a Myth?, Diffus. Found. 17 (2018) 69–104. https://doi.org/10.4028/WWW.SCIENTIFIC.NET/DF.17.69.

[172] J. Kottke, M. Laurent-Brocq, A. Fareed, D. Gaertner, L. Perrière, Ł. Rogal, S. V. Divinski, G. Wilde, Tracer diffusion in the Ni–CoCrFeMn system: Transition from a dilute solid solution to a high entropy alloy, Scr. Mater. 159 (2019) 94–98. https://doi.org/10.1016/J.SCRIPTAMAT.2018.09.011.

[173] D. Gaertner, K. Abrahams, J. Kottke, V.A. Esin, I. Steinbach, G. Wilde, S. V. Divinski, Concentration-dependent atomic mobilities in FCC CoCrFeMnNi high-entropy alloys, Acta Mater. 166 (2019) 357–370. https://doi.org/10.1016/J.ACTAMAT.2018.12.033.

[174] C. Zhang, F. Zhang, K. Jin, H. Bei, S. Chen, W. Cao, J. Zhu, D. Lv, Understanding of the Elemental Diffusion Behavior in Concentrated Solid Solution Alloys, J. Phase Equilibria Diffus. 38 (2017) 434–444. https://doi.org/10.1007/S11669-017-0580-5.

[175] K.Y. Tsai, M.H. Tsai, J.W. Yeh, Sluggish diffusion in Co-Cr-Fe-Mn-Ni high-entropy alloys, Acta Mater. 61 (2013) 4887–4897. https://doi.org/10.1016/j.actamat.2013.04.058.

[176] M. Vaidya, S. Trubel, B.S. Murty, G. Wilde, S. V. Divinski, Ni tracer diffusion in CoCrFeNi and CoCrFeMnNi high entropy alloys, J. Alloys Compd. 688 (2016) 994–1001. https://doi.org/10.1016/j.jallcom.2016.07.239.

[177] M. Vaidya, K.G. Pradeep, B.S. Murty, G. Wilde, S. V. Divinski, Bulk tracer diffusion in CoCrFeNi and CoCrFeMnNi high entropy alloys, Acta Mater. 146 (2018) 211–224. https://doi.org/10.1016/J.ACTAMAT.2017.12.052.

[178] M. Vaidya, K.G. Pradeep, B.S. Murty, G. Wilde, S. V. Divinski, Radioactive isotopes reveal a non sluggish kinetics of grain boundary diffusion in high entropy alloys, Sci. Reports 2017 71. 7 (2017) 1–11. https://doi.org/10.1038/s41598-017-12551-9.

[179] J. Dąbrowa, M. Danielewski, State-of-the-Art Diffusion Studies in the High Entropy Alloys, Met. 2020, Vol. 10, Page 347. 10 (2020) 347. https://doi.org/10.3390/MET10030347.

[180] W. Chen, L. Zhang, High-Throughput Determination of Interdiffusion Coefficients for Co-Cr-Fe-Mn-Ni High-Entropy Alloys, J. Phase Equilibria Diffus. 38 (2017) 457–465. https://doi.org/10.1007/S11669-017-0569-0.

[181] J. Dąbrowa, M. Zajusz, W. Kucza, G. Cieślak, K. Berent, T. Czeppe, T. Kulik, M. Danielewski, Demystifying the sluggish diffusion effect in high entropy alloys, J. Alloys Compd. 783 (2019) 193–207. https://doi.org/10.1016/J.JALLCOM.2018.12.300.

[182] A. Mehta, Y. Sohn, Interdiffusion, Solubility Limit, and Role of Entropy in FCC Al-Co-Cr-Fe-Ni Alloys, Metall. Mater. Trans. A Phys. Metall. Mater. Sci. 51 (2020) 3142–3153. https://doi.org/10.1007/S11661-020-05742-Z.

[183] Z. Zhang, D.E.J. Armstrong, P.S. Grant, The effects of irradiation on CrMnFeCoNi high-entropy alloy and its derivatives, Prog. Mater. Sci. 123 (2022) 100807.

https://doi.org/10.1016/j.pmatsci.2021.100807.

[184] T. ni Yang, C. Lu, G. Velisa, K. Jin, P. Xiu, Y. Zhang, H. Bei, L. Wang, Influence of irradiation temperature on void swelling in NiCoFeCrMn and NiCoFeCrPd, Scr. Mater. 158 (2019) 57–61. https://doi.org/10.1016/j.scriptamat.2018.08.021.

[185] P.R. Okamoto, L.E. Rehn, Radiation-induced segregation in binary and ternary alloys, J. Nucl. Mater. 83 (1979) 2–23. https://doi.org/10.1016/0022-3115(79)90587-7.

[186] A.J. Ardell, P. Bellon, Radiation-induced solute segregation in metallic alloys, Curr. Opin. Solid State Mater. Sci. 20 (2016) 115–139. https://doi.org/10.1016/j.cossms.2015.11.001.

[187] A.D. Marwick, Segregation in irradiated alloys: The inverse Kirkendall effect and the effect of constitution on void swelling, J. Phys. F Met. Phys. 8 (1978) 1849. https://doi.org/10.1088/0305-4608/8/9/008.

[188] N.A.P.K. Kumar, C. Li, K.J. Leonard, H. Bei, S.J. Zinkle, Microstructural stability and mechanical behavior of FeNiMnCr high entropy alloy under ion irradiation, Acta Mater. 113 (2016) 230–244. https://doi.org/10.1016/j.actamat.2016.05.007.

[189] J.J. Gao, B. Décamps, A. Fraczkiewicz, A.C. Bach, T. Jourdan, E. Meslin, Temperature effect on radiation-induced dislocation loops in a FCC high purity CrFeMnNi multi-principal element alloy, Materialia. 26 (2022). https://doi.org/10.1016/J.MTLA.2022.101580.

[190] M.R. He, S. Wang, S. Shi, K. Jin, H. Bei, K. Yasuda, S. Matsumura, K. Higashida, I.M. Robertson, Mechanisms of radiation-induced segregation in CrFeCoNi-based single-phase concentrated solid solution alloys, Acta Mater. 126 (2017) 182–193. https://doi.org/10.1016/j.actamat.2016.12.046.

[191] W.Y. Chen, J.D. Poplawsky, Y. Chen, W. Guo, J.W. Yeh, Irradiation-induced segregation at dislocation loops in CoCrFeMnNi high entropy alloy, Materialia. 14 (2020) 100951. https://doi.org/10.1016/j.mtla.2020.100951.

[192] Y. Tong, G. Velisa, S. Zhao, W. Guo, T. Yang, K. Jin, C. Lu, H. Bei, J.Y.P. Ko, D.C. Pagan, Y. Zhang, L. Wang, F.X. Zhang, Evolution of local lattice distortion under irradiation in medium- and high-entropy alloys, Materialia. 2 (2018) 73–81. https://doi.org/10.1016/j.mtla.2018.06.008.

[193] C. Parkin, M. Moorehead, M. Elbakhshwan, J. Hu, W.Y. Chen, M. Li, L. He, K. Sridharan, A. Couet, In situ microstructural evolution in face-centered and body-centered cubic complex concentrated solid-solution alloys under heavy ion irradiation, Acta Mater. 198 (2020) 85–99. https://doi.org/10.1016/j.actamat.2020.07.066.

[194] M.A. Tunes, H. Le, G. Greaves, C.G. Schön, H. Bei, Y. Zhang, P.D. Edmondson, S.E. Donnelly, Investigating sluggish diffusion in a concentrated solid solution alloy using ion irradiation with in situ TEM, Intermetallics. 110 (2019) 106461. https://doi.org/10.1016/j.intermet.2019.04.004.

[195] C. Lu, T. Yang, K. Jin, G. Velisa, P. Xiu, M. Song, Q. Peng, F. Gao, Y. Zhang, H. Bei, W.J. Weber, L. Wang, Enhanced void swelling in NiCoFeCrPd high-entropy alloy by indentation-induced dislocations, Mater. Res. Lett. 6 (2018) 584–591. https://doi.org/10.1080/21663831.2018.1504136.

[196] C. Li, X. Hu, T. Yang, N.K. Kumar, B.D. Wirth, S.J. Zinkle, Neutron irradiation response

of a Co-free high entropy alloy, J. Nucl. Mater. 527 (2019) 151838. https://doi.org/10.1016/j.jnucmat.2019.151838.

[197] N. Hashimoto, Y. Ono, Mobility of point defects in CoCrFeNi-base high entropy alloys, Intermetallics. 133 (2021) 107182. https://doi.org/10.1016/J.INTERMET.2021.107182.

[198] L. Debarberis, A. Kryukov, D. Erak, Y. Kevorkyan, D. Zhurko, Advanced method for WWER RPV embrittlement assessment, Int. J. Press. Vessel. Pip. 81 (2004) 695–701. https://doi.org/10.1016/J.IJPVP.2004.02.009.

[199] R. Chaouadi, R. Gérard, E. Stergar, W. Van Renterghem, Neutron irradiation hardening of chemically-tailored RPV steels with respect to Cu/P and Ni/Mn elements, J. Nucl. Mater. 519 (2019) 188–204. https://doi.org/10.1016/J.JNUCMAT.2019.03.030.

[200] C. English, S. Ortner, G. Gage, W. Server, S. Rosinski, Review of Phosphorus Segregation and Intergranular Embrittlement in Reactor Pressure Vessel Steels, Inst. Chem. Eng. Symp. Ser. (2001) 151–173. https://doi.org/10.1520/STP10531S.

[201] K. Hata, H. Takamizawa, T. Hojo, K. Ebihara, Y. Nishiyama, Y. Nagai, Grain-boundary phosphorus segregation in highly neutron-irradiated reactor pressure vessel steels and its effect on irradiation embrittlement, J. Nucl. Mater. 543 (2021) 152564. https://doi.org/10.1016/J.JNUCMAT.2020.152564.

[202] B. Bokstein, A.N. Khodan, M. V. Sorokin, A.O. Rodin, E.A. Syutkin, A. V. Khvan, D.A. Maltsev, Z. V. Bukina, M.A. Saltykov, B.A. Gurovich, A.I. Ryazanov, Kinetics of Phosphorus Segregation in the Grain Boundaries of VVER-1000 Pressure Vessel Steels, Defect Diffus. Forum. 375 (2017) 125–133. https://doi.org/10.4028/WWW.SCIENTIFIC.NET/DDF.375.125.

[203] Y. Nishiyama, K. Onizawa, M. Suzuki, Phosphorus Segregation and Intergranular Embrittlement in Thermally Aged and Neutron Irradiated Reactor Pressure Vessel Steels, J. ASTM Int. 4 (2007) 1–12. https://doi.org/10.1520/JAI100690.

[204] G.R. Odette, Modeling Irradiation Embrittlement in Reactor Pressure Vessel Steels, IAEA IRRWG-LMNPP-98-3, IAEA. (1998) 438.

[205] G.R. Odette, N. Almirall, P.B. Wells, T. Yamamoto, Precipitation in reactor pressure vessel steels under ion and neutron irradiation: On the role of segregated network dislocations, Acta Mater. 212 (2021) 116922. https://doi.org/10.1016/j.atamat.2021.116922.

[206] S. V. Fedotova, E.A. Kuleshova, D.A. Maltsev, M.A. Saltykov, Complex study of grain boundary segregation in long-term irradiated reactor pressure vessel steels, J. Nucl. Mater. 528 (2020) 151865.

[207] T. Toyama, Y. Nagai, A. Al Mazouzi, M. Hatakeyama, M. Hasegawa, T. Ohkubo, E. Van Walle, R. Gerard, Intergranular segregation in the pressure vessel steel of a commercial nuclear reactor studied by atom probe tomography, Mater. Trans. 54 (2013) 2119–2124. https://doi.org/10.2320/matertrans.M2013133.

[208] J.R. Hawthorne, An exploratory study of element interactions and composition dependencies in radiation sensitivity development: Final report, (1989). https://doi.org/10.2172/6183583.

[209] J.M. Steichen, J.A. Williams, Effect of strain rate and temperature on the tensile properties of irradiated ASTM A533-B steel, J. Nucl. Mater. 57 (1975) 303–311.

https://doi.org/10.1016/0022-3115(75)90214-7.

[210] D.P. Guillen, As-Run Thermal Analysis of the GTL-1 Experiment Irradiated in the ATR South Flux Trap, Eng. Calc. Anal. . (2011).

[211] J.W. Nielsen, As-Run Physics Analysis for the UCSB-1 Experiment in the Advanced Test Reactor, Eng. Calc. Anal. . (2015). http://www.inl.gov (accessed February 7, 2023).

[212] G. R. Odette, T. Yamamoto, P. B. Wells, N. Almirall, K. Fields, dGragg D., Nanstad R. K., Sokolov A., Robertson J. P., Update on the ATR–2 Reactor Pressure Vessel Steel High Fluence Irradiation Project, UCSB ATR-2 2016-1. (2016). https://lwrs.inl.gov/Materials Aging and Degradation/Update_on_the_High_Fluence_Advanced_Test_Reactor_2_Reactor_Pressure_Vessel_High_Fluence_Irradiation_Project.pdf (accessed January 29, 2023).

[213] K. Lindgren, K. Stiller, P. Efsing, M. Thuvander, On the Analysis of Clustering in an Irradiated Low Alloy Reactor Pressure Vessel Steel Weld, Microsc. Microanal. 23 (2017) 376–384. https://doi.org/10.1017/S1431927617000162.

[214] G.R. Odette, C.L. Liu, B.D. Wirth, On the Composition and Structure of Nanoprecipitates in Irradiated Pressure Vessel Steels, MRS Online Proc. Libr. 439 (1996) 457. https://doi.org/10.1557/proc-439-457.

[215] P.D. Edmondson, C.M. Parish, R.K. Nanstad, Using complimentary microscopy methods to examine Ni-Mn-Si-precipitates in highly-irradiated reactor pressure vessel steels, Acta Mater. 134 (2017) 31–39.

[216] S. Shu, B.D. Wirth, P.B. Wells, D.D. Morgan, G.R. Odette, Multi-technique characterization of the precipitates in thermally aged and neutron irradiated Fe-Cu and Fe-Cu-Mn model alloys: Atom probe tomography reconstruction implications, Acta Mater. 146 (2018) 237–252. https://doi.org/10.1016/j.actamat.2017.12.006.

[217] G. R. Odette, C. Cowan, Use of combined electrical resistivity and seebeck coefficient measurements to characterize solute redistribution under irradiation and thermal aging, Proc. 10th Int. Symp. Environ. Degrad. Mater. Light Water React. NACE. (2001). https://doi.org/10.1063/1.333084.

[218] J. Smith, A Comprehensive Combined Electrical Resistivity and Seebeck Coefficient Characterization of Precipitation and Hardening in Reactor Pressure Steels and Model Alloys, American Institute of Physics Inc., 2006. https://doi.org/10.1063/1.4812323.

[219] J. De Boor, E. Müller, Data analysis for Seebeck coefficient measurements, Rev. Sci. Instrum. 84 (2013). https://doi.org/10.1063/1.4807697/355394.

[220] H. Kaneko, T. Nishizawa, K. Tamaki, A. Tanifuji, Solubility of Phosphorus in α and γ ー Iron. , J. Japan Inst. Met. 29 (1965) 166–170. https://doi.org/10.2320/JINSTMET1952.29.2_166.

[221] J.H. Ke, H. Ke, G.R. Odette, D. Morgan, Cluster dynamics modeling of Mn-Ni-Si precipitates in ferritic-martensitic steel under irradiation, J. Nucl. Mater. 498 (2018) 83–88. https://doi.org/10.1016/j.jnucmat.2017.10.008.

[222] Appendix H To Part 50—Reactor Vessel Material Surveillance Program Requirements | NRC.gov, (n.d.). https://www.nrc.gov/reading-rm/doc-collections/cfr/part050/part050-apph.html (accessed August 15, 2022).

[223] N.T. Almirall, On the Role of Mn-Ni-Si Precipitation in Irradiated Reactor Pressure Vessel Steels: Implications to Life Extension and Advanced Damage Tolerant Alloys, UC Santa Barbara, 2021. https://escholarship.org/uc/item/5437q89j%0A (accessed October 31, 2021).

[224] R.K. Nanstad, G.R. Odette, N. Almirall, J.P. Robertson, W.L. Server, T. Yamamoto, P. Well, Effects of ATR-2 irradiation to high fluence on nine RPV surveillance materials, 2017.

[225] G.H. Kinchin, R.S. Pease, The displacement of atoms in solids by radiation, Reports Prog. Phys. 18 (1955) 1–51. https://doi.org/10.1088/0034-4885/18/1/301.

[226] M.K. Miller, K.F. Russell, Embrittlement of RPV steels: An atom probe tomography perspective, J. Nucl. Mater. 371 (2007) 145–160. https://doi.org/10.1016/j.jnucmat.2007.05.003.

[227] P. Auger, P. Pareige, M. Akamatsu, D. Blavette, APFIM investigation of clustering in neutron-irradiated Fe□Cu alloys and pressure vessel steels, J. Nucl. Mater. 225 (1995) 225–230. https://doi.org/10.1016/0022-3115(94)00522-2.

[228] R.G. Carter, N. Soneda, K. Dohi, J.M. Hyde, C.A. English, W.L. Server, Microstructural characterization of irradiation-induced Cu-enriched clusters in reactor pressure vessel steels, J. Nucl. Mater. 298 (2001) 211–224. https://doi.org/10.1016/S0022-3115(01)00659-6.

[229] J.H. Ke, B.W. Spencer, Cluster dynamics modeling of Mn-Ni-Si precipitates coupled with radiation-induced segregation in low-Cu reactor pressure vessel steels, J. Nucl. Mater. 569 (2022) 153910. https://doi.org/10.1016/j.jnucmat.2022.153910.

[230] E.A. Kuleshova, G.M. Zhuchkov, S. V. Fedotova, D.A. Maltsev, A.S. Frolov, I. V. Fedotov, Precipitation kinetics of radiation-induced Ni-Mn-Si phases in VVER-1000 reactor pressure vessel steels under low and high flux irradiation, J. Nucl. Mater. 553 (2021) 153091. https://doi.org/10.1016/j.jnucmat.2021.153091.

[231] E. Meslin, B. Radiguet, M. Loyer-Prost, Radiation-induced precipitation in a ferritic model alloy: An experimental and theoretical study, Acta Mater. 61 (2013) 6246–6254. https://doi.org/10.1016/j.actamat.2013.07.008.

[232] K. Fukuya, Current understanding of radiation-induced degradation in light water reactor structural materials, J. Nucl. Sci. Technol. 50 (2013) 213–254. https://doi.org/10.1080/00223131.2013.772448.

[233] E. Vincent, C.S. Becquart, C. Domain, Microstructural evolution under high flux irradiation of dilute Fe–CuNiMnSi alloys studied by an atomic kinetic Monte Carlo model accounting for both vacancies and self interstitials, J. Nucl. Mater. 382 (2008) 154–159. https://doi.org/10.1016/j.jnucmat.2008.08.019.

[234] E. Meslin, B. Radiguet, P. Pareige, C. Toffolon, A. Barbu, Irradiation-Induced Solute Clustering in a Low Nickel FeMnNi Ferritic Alloy, Exp. Mech. 51 (2011) 1453–1458. https://doi.org/10.1007/s11340-011-9476-1.

[235] N. Castin, G. Bonny, A. Bakaev, F. Bergner, C. Domain, J.M. Hyde, L. Messina, B. Radiguet, L. Malerba, The dominant mechanisms for the formation of solute-rich clusters in low-Cu steels under irradiation, Mater. Today Energy. 17 (2020) 100472.

https://doi.org/10.1016/J.MTENER.2020.100472.

[236] E. Kuleshova, I. Fedotov, D. Maltsev, S. Fedotova, G. Zhuchkov, A. Potekhin, Phase Formation Features of Reactor Pressure Vessel Steels with Various Ni and Mn Content under Conditions of Neutron Irradiation at Increased Temperature, Met. 2023, Vol. 13, Page 654. 13 (2023) 654. https://doi.org/10.3390/MET13040654.

[237] T.M. Whiting, D.J.M. King, M.R. Wenman, On the formation and structure of Mn-Ni-Si Γ2 precipitates in steels, J. Nucl. Mater. 542 (2020) 152429. https://doi.org/10.1016/J.JNUCMAT.2020.152429.

[238] B. Hu, Y. Du, J.J. Yuan, Z.F. Liu, Q.P. Wang, Thermodynamic reassessment of the Mn-Ni-Si system, J. Min. Metall. Sect. B Metall. 51 (2015) 125–132. https://doi.org/10.2298/JMMB141002015H.

[239] A. Jacob, C. Domain, G. Adjanor, P. Todeschini, E. Povoden-Karadeniz, Thermodynamic modeling of G-phase and assessment of phase stabilities in reactor pressure vessel steels and cast duplex stainless steels, J. Nucl. Mater. 533 (2020) 152091. https://doi.org/10.1016/J.JNUCMAT.2020.152091.

[240] A. Hosseinzadeh Delandar, O.I. Gorbatov, M. Selleby, Y.N. Gornostyrev, P.A. Korzhavyi, Ab-initio based search for late blooming phase compositions in iron alloys, J. Nucl. Mater. 509 (2018) 225–236. https://doi.org/10.1016/J.JNUCMAT.2018.06.028.

[241] D.J.M. King, P.A. Burr, S.C. Middleburgh, T.M. Whiting, M.G. Burke, M.R. Wenman, The formation and structure of Fe-Mn-Ni-Si solute clusters and G-phase precipitates in steels, J. Nucl. Mater. 505 (2018) 1–6. https://doi.org/10.1016/j.jnucmat.2018.03.050.

[242] G. Bonny, C. Domain, N. Castin, P. Olsson, L. Malerba, The impact of alloying elements on the precipitation stability and kinetics in iron based alloys: An atomistic study, Comput. Mater. Sci. 161 (2019) 309–320. https://doi.org/10.1016/J.COMMATSCI.2019.02.007.

[243] M.I. Pascuet, G. Monnet, G. Bonny, E. Martínez, J.J.H. Lim, M.G. Burke, L. Malerba, Solute precipitation on a screw dislocation and its effects on dislocation mobility in bcc Fe, J. Nucl. Mater. 519 (2019) 265–273. https://doi.org/10.1016/J.JNUCMAT.2019.04.007.

[244] P.D. Styman, J.M. Hyde, K. Wilford, G.D.W. Smith, Quantitative methods for the APT analysis of thermally aged RPV steels, Ultramicroscopy. 132 (2013) 258–264. https://doi.org/10.1016/j.ultramic.2012.12.003.

[245] Y. Matsukawa, T. Takeuchi, Y. Kakubo, T. Suzudo, H. Watanabe, H. Abe, T. Toyama, Y. Nagai, The two-step nucleation of G-phase in ferrite, Acta Mater. 116 (2016) 104–113. https://doi.org/10.1016/j.actamat.2016.06.013.

[246] B.M. Jenkins, J.O. Douglas, N. Almirall, N. Riddle, P.A.J. Bagot, J.M. Hyde, G.R. Odette, M.P. Moody, The effect of composition variations on the response of steels subjected to high fluence neutron irradiation, Materialia. 11 (2020) 100717. https://doi.org/10.1016/J.MTLA.2020.100717.

[247] K. Fukuya, K. Ohno, H. Nakata, S. Dumbill, J.M. Hyde, Microstructural evolution in medium copper low alloy steels irradiated in a pressurized water reactor and a material test reactor, J. Nucl. Mater. 312 (2003) 163–173. https://doi.org/10.1016/S0022-3115(02)01675-6.

[248] G. Martin, Phase stability under irradiation: Ballistic effects, Phys. Rev. B. 30 (1984) 1424–

1436. https://doi.org/10.1103/PhysRevB.30.1424.

[249] E. Meslin, B. Radiguet, P. Pareige, A. Barbu, Kinetic of solute clustering in neutron irradiated ferritic model alloys and a French pressure vessel steel investigated by atom probe tomography, J. Nucl. Mater. 399 (2010) 137–145. https://doi.org/10.1016/J.JNUCMAT.2009.11.012.

[250] U. Dahlborg, J. Cornide, M. Calvo-Dahlborg, T.C. Hansen, A. Fitch, Z. Leong, S. Chambreland, R. Goodall, Structure of some CoCrFeNi and CoCrFeNiPd multicomponent HEA alloys by diffraction techniques, J. Alloys Compd. 681 (2016) 330–341. https://doi.org/10.1016/J.JALLCOM.2016.04.248.

[251] A. Kamboj, E.A. Marquis, Effect of dose rate on the phase stability of a CrFeNiMn alloy, Scr. Mater. 215 (2022) 114697. https://doi.org/10.1016/J.SCRIPTAMAT.2022.114697.

[252] A. Fernández-Caballero, E. Bousser, S.M. Shubeita, P.T. Wady, Y. Gu, R. Krishna, M.J. Gorley, D. Nguyen-Manh, P.M. Mummery, E.J. Pickering, High-dose ion irradiation damage in Fe28Ni28Mn26Cr18 characterised by TEM and depth-sensing nanoindentation, Nucl. Mater. Energy. 28 (2021). https://doi.org/10.1016/j.nme.2021.101028.

[253] Anon., Standard practice for neutron radiation damage simulation by charged-particle irradiation, (1984). http://inis.iaea.org/Search/search.aspx?orig_q=RN:16071912 (accessed September 29, 2021).

[254] S.J. Zinkle, L.L. Snead, Opportunities and limitations for ion beams in radiation effects studies: Bridging critical gaps between charged particle and neutron irradiations, Scr. Mater. 143 (2018) 154–160. https://doi.org/10.1016/J.SCRIPTAMAT.2017.06.041.

[255] A. Schemer-Kohrn, M.B. Toloczko, Y. Zhu, J. Wang, D.J. Edwards, Removal of FIB Damage using Flash Electropolishing for Artifact-free TEM Foils, Microsc. Microanal. 25 (2019) 1606–1607. https://doi.org/10.1017/s1431927619008766.

[256] P. Xiu, H. Bei, Y. Zhang, L. Wang, K.G. Field, STEM Characterization of Dislocation Loops in Irradiated FCC Alloys, J. Nucl. Mater. 544 (2021) 152658. https://doi.org/10.1016/J.JNUCMAT.2020.152658.

[257] M. Calvo-Dahlborg, J. Cornide, U. Dahlborg, S. Chambreland, G.D. Hatton, A. Fones, Structural and Microstructural Characterization of CoCrFeNiPd High Entropy Alloys, Solid State Phenom. 257 (2017) 72–75. https://doi.org/10.4028/WWW.SCIENTIFIC.NET/SSP.257.72.

[258] M.S. Lucas, L. Mauger, J.A. Muoz, Y. Xiao, A.O. Sheets, S.L. Semiatin, J. Horwath, Z. Turgut, Magnetic and vibrational properties of high-entropy alloys, J. Appl. Phys. 109 (2011) 07E307. https://doi.org/10.1063/1.3538936.

[259] U. Dahlborg, J. Cornide, M. Calvo-Dahlborg, T.C. Hansen, Z. Leong, L. Asensio Dominguez, S. Chambreland, A. Cunliffe, R. Goodall, I. Todd, Crystalline Structures of Some High Entropy Alloys Obtained by Neutron and X-Ray Diffraction, AcPPA. 128 (2015) 552–557. https://doi.org/10.12693/APHYSPOLA.128.552.

[260] J. Cornide, M. Calvo-Dahlborg, S. Chambreland, L. Asensio Dominguez, Z. Leong, U. Dahlborg, A. Cunliffe, R. Goodall, I. Todd, Combined atom probe tomography and TEM investigations of CoCrFeNi, CoCrFeNi-Pdx (x = 0.5, 1.0, 1.5) and CoCrFeNi-Sn, Acta Phys. Pol. A. 128 (2015) 557–560. https://doi.org/10.12693/APHYSPOLA.128.557.

[261] L.K. Mansur, Theory of transitions in dose dependence of radiation effects in structural alloys, J. Nucl. Mater. 206 (1993) 306–323. https://doi.org/10.1016/0022-3115(93)90130-Q.

[262] L.K. Mansur, Void swelling in metals and alloys under irradiation: An assessment of the theory, Nucl. Technol. 40 (1978) 5–34. https://doi.org/10.13182/NT78-2.

[263] M.P. Surh, J.B. Sturgeon, W.G. Wolfer, Void nucleation, growth, and coalescence in irradiated metals, J. Nucl. Mater. 378 (2008) 86–97. https://doi.org/10.1016/J.JNUCMAT.2008.05.009.

[264] A. Hishinuma, Y. Katano, K. Shiraishi, Y.K. Ano, Surface Effect on Void Swelling Behavior of Stainless Steel, J. Nucl. Sci. Technol. 14 (1977) 664–672. https://doi.org/10.1080/18811248.1977.9730817.

[265] W.G. Wolfer, Advances in void swelling and helium bubble physics, J. Nucl. Mater. 122 (1984) 367–378. https://doi.org/10.1016/0022-3115(84)90626-3.

[266] P.T. Heald, M. V. Speight, Point defect behaviour in irradiated materials, Acta Metall. 23 (1975) 1389–1399. https://doi.org/10.1016/0001-6160(75)90148-0.

[267] D. Cui, Z. Cao, Y. Ding, Y. Li, G. Ran, Effect of dose rate on the characteristics of dislocation loops in palladium: In-situ TEM analysis during 30 keV H2+ irradiation, 150 (2023) 86–95. https://doi.org/10.1016/J.JMST.2022.12.013.

[268] G.S. Was, Dislocation Microstructure, Fundam. Radiat. Mater. Sci. (2017) 301–378. https://doi.org/10.1007/978-1-4939-3438-6_7.

[269] D. Chen, K. Murakami, H. Yang, L. Chen, H. Abe, Z. Li, N. Sekimura, Flux effects on point defect behavior by tracking loop evolution using combined irradiation method, Scr. Mater. 207 (2022) 114311. https://doi.org/10.1016/J.SCRIPTAMAT.2021.114311.

[270] S.A. Briggs, C.M. Barr, J. Pakarinen, M. Mamivand, K. Hattar, D.D. Morgan, M. Taheri, K. Sridharan, Observations of defect structure evolution in proton and Ni ion irradiated Ni-Cr binary alloys, J. Nucl. Mater. 479 (2016) 48–58. https://doi.org/10.1016/J.JNUCMAT.2016.06.046.

[271] P. Xiu, Y.N. Osetsky, L. Jiang, G. Velisa, Y. Tong, H. Bei, W.J. Weber, Y. Zhang, L. Wang, Dislocation loop evolution and radiation hardening in nickel-based concentrated solid solution alloys, J. Nucl. Mater. 538 (2020) 152247. https://doi.org/10.1016/J.JNUCMAT.2020.152247.

[272] T.R. Allen, J.T. Busby, G.S. Was, E.A. Kenik, On the mechanism of radiation-induced segregation in austenitic Fe-Cr-Ni alloys, J. Nucl. Mater. 255 (1998) 44–58. https://doi.org/10.1016/S0022-3115(98)00010-5.

[273] J. Dudala, J. Gilewicz-Wolter, Z. Stegowski, Simultaneous measurement of Cr, Mn and Fe diffusion in chromium-manganese steels, Nukleonika. 50 (2005) 67–71. http://inis.iaea.org/Search/search.aspx?orig_q=RN:38009123 (accessed December 2, 2021).

[274] L.J. Yu, E.A. Marquis, Precipitation in proton- and ion-irradiated Alloy 625 Plus, J. Nucl. Mater. 553 (2021) 153040. https://doi.org/10.1016/J.JNUCMAT.2021.153040.

[275] R.W. Harrison, A.W. Carruthers, J.A. Hinks, M.G. Burke, S.E. Donnelly, Cascade size and

dose rate effects on α′ precipitation in ion-irradiated Fe14Cr alloy, Scr. Mater. 172 (2019) 33–37. https://doi.org/10.1016/J.SCRIPTAMAT.2019.06.034.

[276] C. Wert, C. Zener, Interference of Growing Spherical Precipitate Particles, J. Appl. Phys. 21 (1950) 5–8. https://doi.org/10.1063/1.1699422.

[277] A. Kauffmann, M. Stüber, H. Leiste, S. Ulrich, S. Schlabach, D.V. Szabó, S. Seils, B. Gorr, H. Chen, H.J. Seifert, M. Heilmaier, Combinatorial exploration of the High Entropy Alloy System Co-Cr-Fe-Mn-Ni, Surf. Coatings Technol. 325 (2017) 174–180. https://doi.org/10.1016/J.SURFCOAT.2017.06.041.

[278] K. Arioka, Y. Iijima, T. Miyamoto, Rapid nickel diffusion in cold-worked type 316 austenitic steel at 360–5008°C, Int. J. Mater. Res. 108 (2017) 791–797. https://doi.org/10.3139/146.111542/MACHINEREADABLECITATION/RIS.

[279] T.F. Chen, G.P. Tiwari, Y. Iijima, K. Yamauchi, Volume and Grain Boundary Diffusion of Chromium in Ni-Base Ni-Cr-Fe Alloys, Mater. Trans. 44 (2003) 40–46. https://doi.org/10.2320/MATERTRANS.44.40.

[280] C.G. Ferguson, K.A. Christofidou, E.M. Hildyard, A.S. Wilson, N.G. Jones, H.J. Stone, On the continuous and discontinuous precipitation of the L12 phase in Cu-Ni-Al alloys, Materialia. 13 (2020) 100855. https://doi.org/10.1016/J.MTLA.2020.100855.

[281] A.N. Shiryayev, On The Statistical Theory of Metal Crystallization, Sel. Work. A. N. Kolmogorov. (1992) 188–192. https://doi.org/10.1007/978-94-011-2260-3_22.

[282] M. Avrami, Kinetics of Phase Change. II Transformation-Time Relations for Random Distribution of Nuclei, J. Chem. Phys. 8 (2004) 212. https://doi.org/10.1063/1.1750631.

[283] Reaction kinetics in processes of nucleation and growth | BibSonomy, (n.d.). https://www.bibsonomy.org/bibtex/e3bf174ae0d30d926bcb85c2c5bc410f (accessed March 30, 2023).

[284] S. Van der Zwaag, Kinetics of phase transformations in steels, Phase Transform. Steels. 1 (2012) 126–156. https://doi.org/10.1533/9780857096104.1.126.

[285] S. Baghsheikhi, Spinodal decomposition in the binary Fe-Cr system, (2009).

[286] T.R. Allen, J.I. Cole, C.L. Trybus, D.L. Porter, H. Tsai, F. Garner, E.A. Kenik, T. Yoshitake, J. Ohta, The effect of dose rate on the response of austenitic stainless steels to neutron radiation, J. Nucl. Mater. 348 (2006) 148–164.

[287] T. Okita, T. Kamada, N. Sekimura, Effects of dose rate on microstructural evolution and swelling in austenitic steels under irradiation, J. Nucl. Mater. 283–287 (2000) 220–223. https://doi.org/10.1016/S0022-3115(00)00355-X.

[288] J. Li, C. Zhang, Y. Yang, T. Wang, I. Martin-Bragado, Irradiation dose-rate effect in Fe-C system: An Object Kinetic Monte Carlo simulation, J. Nucl. Mater. 561 (2022). https://doi.org/10.1016/J.JNUCMAT.2022.153529.

[289] R. Schäublin, B. Décamps, A. Prokhodtseva, J.F. Löffler, On the origin of primary ½ a0 <111> and a0 <100> loops in irradiated Fe(Cr) alloys, Acta Mater. 133 (2017) 427–439. https://doi.org/10.1016/J.ACTAMAT.2017.02.041.

[290] M. Hernández-Mayoral, C. Heintze, E. Oñorbe, Transmission electron microscopy investigation of the microstructure of Fe–Cr alloys induced by neutron and ion irradiation

at 300 °C, J. Nucl. Mater. 474 (2016) 88–98. https://doi.org/10.1016/J.JNUCMAT.2016.03.002.

[291] M. Chiapetto, C.S. Becquart, L. Malerba, Simulation of nanostructural evolution under irradiation in Fe-9%Cr[sbnd]C alloys: An object kinetic Monte Carlo study of the effect of temperature and dose-rate, Nucl. Mater. Energy. 9 (2016) 565–570. https://doi.org/10.1016/J.NME.2016.04.009.

[292] C.D. Hardie, C.A. Williams, S. Xu, S.G. Roberts, Effects of irradiation temperature and dose rate on the mechanical properties of self-ion implanted Fe and Fe-Cr alloys, J. Nucl. Mater. 439 (2013) 33–40. https://doi.org/10.1016/J.JNUCMAT.2013.03.052.

[293] Y. Ding, G. Ran, Y. Li, Z. Cao, D. Cui, J. Huang, Z. Zhou, Effect of dose rate on dislocation loop evolution in tungsten: Combination of defect generation rate and elastic interaction, Scr. Mater. 222 (2023). https://doi.org/10.1016/J.SCRIPTAMAT.2022.115054.

[294] J.E. Westmoreland, J.A. Sprague, F.A. Smidt, P.R. Malmberg, Dose rate effects in nickel-ion-irradiated nickel, Http://Dx.Doi.Org/10.1080/00337577508237413. 26 (2006) 1–16. https://doi.org/10.1080/00337577508237413.

[295] G. Yang, Y. Wu, Y. Ding, Y. Li, Z. Cao, G. Li, D. Cui, K. He, X. Qiu, G. Ran, Effect of ion flux on one-dimensional migration of dislocation loops in Fe9Cr1.5W0.4Si F/M steel during in-situ Fe+ irradiation, J. Nucl. Mater. 579 (2023) 154412. https://doi.org/10.1016/J.JNUCMAT.2023.154412.

[296] G.S. Was, Irradiation-Induced Voids and Bubbles, Fundam. Radiat. Mater. Sci. (2017) 379–484. https://doi.org/10.1007/978-1-4939-3438-6_8.

[297] T. Okita, T. Sato, N. Sekimura, F.A. Garner, L.R. Greenwood, The primary origin of dose rate effects on microstructural evolution of austenitic alloys during neutron irradiation, J. Nucl. Mater. 307–311 (2002) 322–326. https://doi.org/10.1016/S0022-3115(02)01202-3.

[298] M.P. Surh, J.B. Sturgeon, W.G. Wolfer, Radiation swelling behavior and its dependence on temperature, dose rate, and dislocation structure evolution, J. Nucl. Mater. 336 (2005) 217–224. https://doi.org/10.1016/J.JNUCMAT.2004.09.016.

[299] T. ni Yang, C. Lu, G. Velisa, K. Jin, P. Xiu, M.L. Crespillo, Y. Zhang, H. Bei, L. Wang, Effect of alloying elements on defect evolution in Ni-20X binary alloys, Acta Mater. 151 (2018) 159–168. https://doi.org/10.1016/J.ACTAMAT.2018.03.054.

[300] T.N. Yang, The Effect of Principal Elements on Defect Evolution in Single-Phase Solid Solution Ni Alloys, (2018). http://deepblue.lib.umich.edu/handle/2027.42/149968 (accessed April 6, 2023).

[301] E.Y. Chen, C. Deo, R. Dingreville, R.E. Program, G.W. Woodruff, Irradiation resistance of nanostructured interfaces in Zr–Nb metallic multilayers, J. Mater. Res. 34 (2019) 2239–2251. https://doi.org/10.1557/JMR.2019.42.

[302] A. Chartier, C. Onofri, L. Van Brutzel, C. Sabathier, O. Dorosh, J. Jagielski, Early stages of irradiation induced dislocations in urania, Appl. Phys. Lett. 109 (2016) 181902. https://doi.org/10.1063/1.4967191.

[303] C.H. Woo, B.N. Singh, Production bias due to clustering of point defects in irradiation-induced cascades, Http://Dx.Doi.Org/10.1080/01418619208205596. 65 (2006) 889–912. https://doi.org/10.1080/01418619208205596.